Modeling and Simulation of Liquid Microlayer Formation and Evaporation in Nucleate Boiling using Computational Fluid Dynamics

by

Alexandre Nicolas Guion

Bachelor's Degree in Engineering, Supélec (2009)
Master's Degree in Engineering, Supélec (2011)
Master's Degree in Nuclear Engineering, Institut Nat. des Sci. et Tech. Nucléaires (2012)

Submitted to the Department of Nuclear Science and Engineering in Partial Fulfillment of the Requirements for the Degree of

DOCTOR OF PHILOSOPHY IN NUCLEAR SCIENCE AND ENGINEERING

at the

MASSACHUSETTS INSTITUTE OF TECHNOLOGY

June 2017

Signature of Author.....
Department of Nuclear Science and Engineering
April 28, 2017

Certified by .....
Jacopo Buongiorno
TEPCO Professor and Associate Department Head, Nuclear Science and Engineering
Director, Center for Advanced Nuclear Energy Systems (CANES)
Thesis Supervisor

Certified by .....
Stéphane Zaleski
Professor of Mechanics, Université Pierre et Marie Curie Paris 6
Head, Jean Le Rond d'Alembert Institute (UPMC & CNRS)
Thesis Co-Supervisor

Certified by .....
Shahriar Afkhami
Associate Professor of Mathematical Sciences, New Jersey Institute of Technology
Thesis Co-Supervisor

Certified by .....
Neil E. Todreas
KEPCO Professor of Nuclear Science and Engineering
Professor of Mechanical Engineering (Emeritus)
Thesis Reader

Certified by .....
Emilio Baglietto
Norman C. Rasmussen Associate Professor of Nuclear Science and Engineering
Thesis Reader

Accepted by.....
Ju Li
Battelle Energy Alliance Professor of Nuclear Science and Engineering
Professor of Materials Science and Engineering
Chairman, Department Committee on Graduate Students

Modeling and Simulation of Liquid Microlayer Formation and Evaporation in Nucleate Boiling using Computational Fluid Dynamics

by

Alexandre Nicolas Guion

Submitted to the Department of Nuclear Science and Engineering
on April 28, 2017, in partial fulfillment of the
requirements for the degree of
Doctor of Philosophy in Nuclear Science and Engineering

Abstract

The transport of latent heat makes boiling one of the most efficient modes of heat transfer, allowing a wide range of systems to improve their thermal performance, from microelectronic devices to nuclear power plants. In particular, Boiling Water Reactors (BWR) use boiling as the primary mode of heat transfer in the reactor core to accommodate very high heat fluxes. In Pressurized Water Reactors (PWR) subcooled flow boiling can occur in hot sub-channels.

As a bubble grows outside of a surface imperfection during nucleate boiling, viscous stresses at the wall can be strong enough to impede liquid motion and trap a thin liquid layer - referred to as microlayer, underneath the growing bubble. The contribution of microlayer evaporation to overall heat transfer and bubble growth can be large, in particular in the case of water[1]. In practice, numerical simulations of nucleate boiling resolve the macroscopic interface of the bubble and resort to subgrid models to account for the evaporation of the microlayer at the microscopic scale. The applicability of this subgrid modeling approach relies on the capacity to initialize the microlayer shape and extension, prior to its evaporation. However, existing models of microlayer formation are either physically incomplete[2] or purely empirical[3].

In this work, we first confirm through a sensitivity study the need for accurate modeling of microlayer formation to initialize boiling simulations and to reproduce physical boiling dynamics (a). Then, we build the first generally applicable model for microlayer formation through direct computations of the hydrodynamics of bubble growth at the wall for a wide range of conditions and fluids, including water at 0.101MPa (lab experiments) and 15.5MPa (PWR), capillary numbers $Ca \in [0.001;\ 0.1]$, and contact angles $\theta \in [10°;\ 90°]$ (b). In addition, we modify an existing experimental pool boiling setup to measure with unprecedented accuracy initial bubble growth rates needed to predict microlayer formation (c). Lastly, we develop a numerical procedure based on

hydrodynamics theories to obtain mesh-independent results in moving contact line simulations for a wide range of contact angles and viscosity ratios (d). In particular, we use direct computations of the transition to a Landau-Levich-Derjaguin film in forced dewetting to inform the onset of microlayer formation in nucleate boiling.

These contributions[(a) (b) (c) (d)] bridge a significant gap in our understanding of how boiling works and can be modeled at the microscopic scale, which represents a first step in designing surfaces with higher heat transfer performance and in building safer and more efficient energy systems.

[1]Gerardi et al., IJHMT, 53, 4185-4192, 2010
[2]Van Stralen et al., IJHMT, 18, 453- 467, 1975
[3]Sato and Niceno, J. Comp. Phys., 300, 20-52, 2015

Acknowledgments

• **Thesis committee:**

I have been privileged to receive advice, support and direction on a regular basis, from weekly meetings with Profs. Jacopo Buongiorno, Stéphane Zaleski and Shahriar Afkhami, and from bi-annual meetings with Profs. Neil Todreas and Emilio Baglietto. These technical meetings have helped me progress and refine my work in many ways. I am grateful for the opportunity I was given to receive such continued and broad support.

Prof. Jacopo Buongiorno: you have offered me an exceptional experience at MIT. First, you made sure I had constant technical support, either directly from you - remember deriving equations from first principles in your office? - or from others around you - the incredible number of trainings and workshops I had the chance to attend speaks volume about the amount of support you've offered me. You taught me to question results and to iterate quickly on new ideas. When there were many parameters to consider, you taught me to work systematically. To focus on research early on in the program, you advised me to take the qualifying exam in advance, and you gave me time and space to prepare. Thank you for always going the extra mile to provide the best possible support.
In addition, you made it possible for me to grow and progress in other areas. You supported me in joining the NSE communication lab. When I asked permission to take some time off from the lab and attend an intensive program at Harvard University, you replied: "This will be good for your career. You have my blessing" (01/04/2015). I couldn't be more grateful for the continued support you've offered me, not only on the technical side, but on the broader training experience as a whole.
Last, but not least, you have made every single meeting of the past six years enjoyable. Thank you for giving me the opportunity to work in such a fun, exciting, and stable environment.

Prof. Stéphane Zaleski: you have offered so much of your time and attention to my thesis work. In our first year working together, you repeatedly asked me to raise the bar, to do more, to do better. You taught me to try different things, and to iterate fast. You offered to take on additional tasks, and in particular to try to implement a joint Ph.D. with the ∂'Alembert Institute. You hosted me in Paris, many times. You included me in your group and you made it possible for me to make the most of this unique and incredible experience. You were instrumental in obtaining countless CPU hours on both OCCIGEN supercomputer and on babbage2 at ∂'Alembert. Last but not least, you brought Shahriar to our research group. Thank you Stéphane, I feel very privileged to have received so much of your time and support.

Prof. Shahriar Afkhami: you have contributed in many ways to my thesis work. First, thank you for supporting me though the hardships of moving contact simu-

lations. It has been a very challenging yet enriching experience for me. You have consistently encouraged me, while bringing a positive and motivating mindset to every single research meeting. I am very grateful for the support and the encouragement you've consistently offered me. Lastly, thank you for coordinating the visit to Princeton and the seminar with Prof. Howard Stone's group - this particular day remains one of my favorite memories of the doctorate.

Prof. Neil E. Todreas: thank you for accepting to join my thesis committee, and for actively contributing to my doctoral journey. It has been a privilege to have you in my thesis committee and I am very grateful for the time, advice and mentorship you've offered me. Thank you for giving me the opportunity to receive your help and support.

Prof. Emilio Baglietto: thank you for your encouragements and feedback throughout the PhD. You have consistently offered new perspectives and questions to help me make the most of the doctoral experience. Your feedback both at MIT and during conferences abroad have helped me progress my work. Thank you for joining my thesis committee.

• **Collaborators:**

MIT-NW12: I am grateful for the support I've received from the incredible community of people who shared the *iconic* NW12 building between April 2011 and April 2017: Dr. Dustin Langewisch, Dr. Enrique Lizarraga-Garcia, Dr. Gustavo Rabello dos Anjos, Dr. Giancarlo 'Carlito' Lenci, Dr. Ethan Bates, Dr. Koroush Shirvan, Dr. Lindsey Gilman, Dr. Bren Philips, Dr. Brittany Guyer, Dr. Despoina Chatzikyriakou, Dr. Riccardo Mereu, Dr. Gael Guedon, Dr. Gustavo Montoya, Dr. William Herbert, Etienne Demarly, Ravikishore Kommajosyula, Giulia Agostinelli, Ben Magolian, Rosie Sugrue, Sara Ferry, Abdulla Abdulaziz Alhajri, Sasha Angela Tan-Torres, Mariana Rodriguez Buno, Mike Acton, Carolyn Coyle, ...

MIT quals team: I would not have passed the qualifying exams in February 2013 without the support from this group of friends: Dr. Lulu Li, Dr. Will Boyd, Sam Shaner, David Bloore, Becky Romatosky, Dr. Alexandre Cooper, Dr. Ethan A Bates, Dr. Koroush Shirvan, Dr. Giancarlo Lenci, Sara Ferry, Rosie Sugrue,... Thank you!

∂'Alembert: Profs. Stéphane Zaleski and Jacopo Buongiorno made it possible for me to visit and work from the ∂'Alembert Institute multiple times between 2013 and 2017. During my visits there, I received help and support from: Dr. Stéphane Popinet, Dr. Daniel Fuster, Dr. Julien Philippi, Dr. Hervé Elettro, Dr. Augustin Paré, Dr. Cansu Ozhan, Dr. Luca Margheri, Dr. Virgile Meyer,... I am also very grateful for the support I received from the irreplaceable Simona Otarasanu, Olivier Labbey and Dr. Pascal Ray. Thank you for including me at ∂'Alembert and giving me the opportunity to make the most of it.

Green Lab: While simulations were running on the third floor of NW12, a group of experimentalists on the second floor gave me the opportunity to touch on the challenges of running experiments: Prof. Matteo Bucci, Dr. Reza Azizian, Dr. Thomas McKrell, Guanyu Su, Giacomo Saccone, Artyom Kossolapov, Dr. Mathias Trojer, Melanie Tetreault-Friend, Carolyn Coyle, Dr. Xili Duan, Dr. Bren Philips,... Thank you for making the Green Lab such a welcoming place to learn and try new things.

NSE Communication Lab: I am very grateful for the continued training and support I have received from the Comm Lab: Dr. Marina Dang, Jaime Goldstein, Mareena Robinson Snowden, Jake Jurewicz, Dr. John Hanson,... Thank you for helping others commmunicate better. Long live the Comm Lab!

NSE Staff: Thank you for making *everything* work smoothly during my years in NSE, from RA appointments, to prospectus and thesis requirements, petitions, travel reports, video conferences, thesis defense... Warm thank you to Heather Barry, Peter Brenton, Linda Arduino, Brandy Baker, Rachel Batista, Carolyn Carrington, Paula Cornelio, Valerie Censabella, Laura Guild, Lisa Magnano Bleheen, Clare Egan, and of course Nancy Iappini who always finds the best spots on campus for our annual NSE grad expo. Thank you all!

KHU collaborators: Prof Hyundae Kim and Satbyoul Jung have offered time and experimental data to support my work. Thank you for contributing to my doctorate.

EDF R&D and CEA: Without a doubt the best possible sponsors. Thank you for your financial and technical support throughout my doctorate. In particular, I want to sincerely thank Dr. Guillaume Bois, Dr. Mathieu Guingo, Dr. Jerome Lavieville, Dr. Stephane Mimouni, Dr. Marc Boucker, Bernard Salha, Michel Maschi, and Dr. Jan van der Lee for the direct feedback and encouragements they have generously provided during my Ph.D. I have been very fortunate to have met you.

ASCOMP (TransAT): Dr. Chidambaram Narayanan has provided technical support and assistance during the development of new capabilities in the commercial code TransAT. Thank you Chidu for your help.

MIT Faculty: I would like to thank the professors who provided technical training throughout the years of doctorate: Prof. Jacopo Buongiorno (course 22.06/22.312), Prof. Mujid Kazimi (course 22.312), Dr. Koroush Shirvan (course 22.312), Prof. Sidney Yip, Prof. Ju Li and Prof. Paola Capellaro (course 22.101), Prof. Emilio Baglietto (course 22.315), Prof. Pierre Lermusiaux (course 2.29), Prof. Kenneth Oye (course 17.310), Prof. Gilbert Strang (course 18.085), Dr. Michael V Hynes, Dr. Gordon E Kohse and Dr. Richard C Lanza (course 22.814), Dr. Maria Khotimsky (course 21F.613), William Boone Bonvillian (course 17.910), Joost Bonsen (course 11.S941), Dr. Brian Mandell (course HAK.T280).

• **Other groups**

MIT Club Francophone: Audren Cloitre, Beth M Hadley, Kelsey Jamieson, Zhuoxuan Li, Rami Abi Akl, Anne Collin, ... thank you for offering me the chance to contribute to our francophone group on campus, to provide an additional support system for students at MIT. Special thanks to Colin Codner (Student Activities and Finance) who supported us many times.

MIT GSW: Amy Yu, Rohit Singh, John Chisholm, Joost Bonsen, Mili Shah, Georgie Campbell, Wojtek Kalka, Rami Abi Akl, Aditi Gupta, Tom Luly, Abhishek Bajpayee, Vikash Kumar Mishra, Juanito 'El Toro de Murcia' Ruiz Ruiz, Ina Kundu, Bomy Lee, Felipe Oviedo, Shikhar Kumar, Ketan Makwana, Greg Batcheler, Christina Chase, Winnie Qiu, Tripti Somani, Vandana Dudhani, Ankita and Anuj Somani, Alex Guo, Amy Gao, Vivek Sivathanu, Julius Adebayo, David Ramsay, Charles Vitry, Anass Afilal, Bonnie Wong, Shailesh Mittal, Kevin Kung, Charles Plaisimond, Shrikanth Bolla, Subra Sundaram, Jesika Haria, Nell Watson, Magatte Wade, Ashok Rao, Christian Tidona, Ravi Mantha... Thank you for offering me the chance to contribute to MIT GSW in Morocco, Guatemala and India.

MIT Graduate Student Council & Sp1n DJs: Caleb Waugh, Ben Grena, Francky Dernoncourt,... Thank you for these memories together, they will live forever.

• **Friends and family:**

Palissy: les irremplaçables fils Rémi Cornière & Phil Morrain, Thuy-Vi N'Guyen, Arnaud Salaver, Marco Valente, Pierre Leocadio, Amandine Renould, Anne de Bortoli, Marion Martinet,... Les années passent. Samir Ismael. À quand la prochaine réunion?

Fermat & Supélec: l'inclassable Blériot Tcheeko, Greg Drouault & tous les Drouaults, Raphael Guterman, les Sono Supélec, Tonton Quentin Falières, Aude Marzuoli & Manu Boidot, les fistons César Martin, Maxime Laplanche, Edmond Chénel, Patxi Etche', Kaz, Florian Gain, Antoine Lafay, Greg Andre, la GRoTT: Vincent Gabou, Robin Michel, Thomas Hidden, Thomas-Siri Tornero, Gabriel Boya, Thierry Vallee & les Vallees, Mohamed Almechatt, Flo & Laura Hauer, KLT, Antoine Chenevier, Max Verger & les Vergers, Najib 'UEFA' El Omari, Anass & Halima Belmehdi, Charly & Charlotte Boyer, Xavier Campenon & les Campenons, Martha 'Gesellig' Deen, Aurelien Coquand, Gilles Vallier, Jeremy Heritier, Denis Janin, Jean-Lu Mazeau, Paulo Grenier, Marty, Slaan, Brunot Cauet, Youssef Sekkat, Lukette Marti, Michel Sancho... Vous savez entretenir la flamme et prendre soin des amis. Merci!

MIT: Enrique Lizarraga-Garcia, Jude Safo, Stephane Marcadet, Geoff Gunow, Rami Abi Akl, Juan Ruiz Ruiz, Reza Azizian, Omid 'Isfahaaan' Abari, Valentina & Giancarlo Lenci, Brittany Guyer, Wojtek 'Jedi Master' Kalka, Ferran Vidal, David

Colino, Alba Luengo, Alex & Claire Jacquillat, Carla Ferrer, Meryem Gonzalez, Aron Blaesi, Helena De Puix, Maite Pena, Majo Betancourt, Nina Panagiotidou, Noel Silva, Nuria Vila, Paolo Minelli, Roman Loonis, Varvara, Francesco Stefanelli, Remi Tachet, Roberto Sanchis, Spain@MIT, Philip Caplan, Anna Isabella Vaprio, Mounia Mostefaoui, Audren Cloitre, Katerina Markova, Julia Ipatova, Katia Paramonova, Michael Keating, Europeans@MIT, Rahul Srinivasan, Xavier Duportet, Christina Galonska, Emel Cankaya, Anna Turskaya, Giorgios Papachristoudis, Christos, Ivo Montenegro, Laura Popa, Mattia, Marga & Matteo Bucci, Tristan Giesa, Richard Bates, Ronan McGovern, Alex Gorlach,... And of course, Wellesley rising stars: Constance Gouelo & Kiara Daniela. Thank you all!

Boston FrenchCo Soccer Team: Jen, Fred & Max Bozec, Sarah & Bennie Tricot, Julien Pham, Theo Leclerc, Raph de Roubin, Antoine Perret, Cory Colman, Renaud, Aurelie & Stella Baguena, 'Kr kr kr' Dorochild, Anthony Leyme, Svetlana, Mr. Berose, Sarhane, Seb & Emilie Gelas, Paul Sammons, Nico Dioli, David & Nihan Veysset, Lolo Wesley Snipes, Jeremy Farmer, Patou, Junior, Roland Pilod, Ilyas & Soufiane Hasnaoui, Prasahnt Sivarajah, Seb Uzel, Pierre Dyer, Marylou Latrille, Gabie Pregernig, Morgan Meagher, Vincent Pons, Nick James, Serge Roux, Tu, Brendan, Max Silvera, Elison Matioli, Estelle Coneggo, Lilish, Benjamin Mailly, Baptiste Cesarini, Henri Vallet,... Merci les amis pour ces belles années ensemble! Champions du Bel Esprit....

American family: the Steins, the Rosens, the Millers, the Gunows, the Andrews, the Nuneses, the (one and only) Koroush Shirvan, the Flatters. Thank you for including me in your family circle throughout my doctorate. You made America feel like home.

Martha House: William Herbert, Benjamin Mailly Giachetti, Adrian 'Justaccio' Ramon, Samuel Humphry-Baker, Elison Matioli, Robert Wohl, Stephanie Rennesson, Lili Hannedouche, Sergio Castellanos, Thierry Leclerc, Remi Tachet, Sophie Hauser, Thomas Luypaert, Nicolas Aimon, Melissa Hanson, Dana Foarta, Katy Stout, Maria Kfoury, Felix Basset, Florent Cerruti, Jake & Georgina Flatter, Christopher de Vries, Azize Mohammed, Vivian Schafer, Andre de Haes, Andre Fialho, Fede & Caro Cismondi, Emily Lamont, James Furnival, Meryem Gonzalez, Aron Blaesi, Simon Muller. Gaz, George & Sam Herbert. Best years of my life. Thank you Will for making 216 Norfolk St a home for all of us.

Energy House: Evan Platt, Ian Miller, Matt Rosen, Abe Stein. Thank you brothers for an amazing last year of grad school together.

Famille: mon frère Vincent, mon père Guy, et ma grand-mère Arlette. Je vous aime, merci pour votre soutien.

Contents

List of Figures

List of Tables

Nomenclature

Acronyms

AZB Afkhami-Zaleski-Bussmann model

BWR Boiling Water Reactor

PWR Pressurized Water Reactor

Greek Symbols

α Thermal diffusivity (m^2/s)

α^* Wetted fraction underneath the bubble $(-)$

δ Microlayer thickness (m)

δ_0 Y-intercept of the linear microlayer thickess profile (m)

η Local thickness of the film near the contact line (m)

$\hat{\sigma}$ Accommodation coefficient $(-)$

κ Curvature of the liquid/vapor interface $(1/m)$

μ Dynamic viscosity $(Pa.s)$

ν Kinematic viscosity (m^2/s)

ϕ Gauge function $(-)$

ρ Density (kg/m^3)

σ Surface tension (N/m)

τ Time scale (s)

τ_w Wall shear stress (N/m^2)

θ Contact angle ($^\circ$)

θ_a Reference contact angle ($^\circ$)

θ_e Microscopic contact angle ($^\circ$)

θ_Δ Contact angle imposed at the wall where the computational mesh size is Δ ($^\circ$)

$\theta_{\mathrm{d}x}$ Contact angle imposed at the wall where the computational mesh size is $\mathrm{d}x$ ($^\circ$)

ζ Vertical distance of the interface from the contact line (m)

Roman Symbols

ΔT Wall superheat (K)

ℓ Reference length scale (m)

$\mathrm{d}x$ Computational mesh size (m)

$\mathrm{d}x_{macro}$ Computational mesh size away from the microlayer region and at the macroscopic liquid/vapor interface of the bubble (m)

$\mathrm{d}x_{micro}$ Computational mesh size in the microlayer region (m)

a Interfacial thermal resistance ($kg/m^2s - K$)

A_H Dispersion coefficient ($Pa.m^3$)

A_{bubble} Area underneath bubble (m^2)

b Interfacial thermal resistance ($kg/m^2s - K$)

Bo Bond number ($-$)

C Color function (Volume-of-Fluid) $(-)$

C Slope of microlayer central linear profile $(-)$

c Specific heat $(J/kg-K)$

C_0 Weighting coefficient $(-)$

C_∞ Asymptotic capillary number $(-)$

C_{ana} Slope of microlayer central linear profile obtained analytically $(-)$

C_{exp} Slope of microlayer central linear profile obtained experimentally $(-)$

Ca Capillary number $(-)$

D_h Hydraulic diameter (m)

f Bubble departure frequency $(1/s)$

G_v Volumetric source of vapor (kg/s)

H Control volume height (m)

h Specific enthalpy (J/kg)

h_∞ Stationary contact line height (m)

h_{CL} Contact line height (m)

h_{fg} Latent heat of vaporization (J/kg)

j_v Evaporation flux from the liquid microlayer to the vapor bubble (kg/m^2s)

k Thermal conductivity $(W/m-K)$

l_c Capillary length (m)

m'' Mass flux within the microlayer (kg/m^2s)

N_G Reynolds number based on the wavelength of gravity waves traveling at the same speed as the withdrawing plate $(-)$

N_{site} Nucleation site density $(1/m^2)$

Oh Ohnesorge number $(-)$

P Pressure (Pa)

q''' Volumetric heat generation (W/m^3)

q'' Heat flux (W/m^2)

R Radius (m)

r Radial coordinate, distance from the center of the bubble root or nucleation site (m)

R^* Gas constant $(J/kg-K)$

r_a Reference microscopic length scale (m)

r_c Characteristic length scale in microlayer formation (m)

r_d Dryout radius (m)

R_{eq} Equivalent bubble radius, as if the bubble was a sphere of identical volume (m)

r_{max} Outer edge radius of the bubble (m)

r_{min} Inner edge radius of the microlayer (m)

r_m Microscopic length (m)

r_{out} Outer edge radius of the microlayer (m)

Re Reynolds number $(-)$

T Temperature (K)

t Time (s)

t_c Time scale (s)

t_{cycle} Duration of boiling cycle (s)

u Specific internal energy (J/kg)

$U,\ v$ Velocity (m/s)

U_b Bubble growth rate (m/s)

$U_{b,\text{noflow}}$ Bubble growth rate in absence of external flow (m/s)

$U_{b,\text{withflow}}$ Bubble growth rate in presence of external flow (m/s)

V Volume (m^3)

V_s Withdrawing speed (m/s)

V_{flow} Characteristic velocity of external flow (m/s)

V_{ml} Volume of vapor resulting from complete evaporation of the liquid microlayer (m^3)

$v_{z,0}$ Shear velocity (m/s)

z Vertical coordinate $(-)$

Superscripts

* Dimensionless

Subscripts

0 Initial

ads Adsorbed

b Bubble

c	Characteristic
cl	Contact line
cr	Critical
f	Saturated liquid
g	Saturated vapor
i	Interface
k	Computational cell index k
l	Liquid
max	Maximum
ml	Microlayer
sat	Saturation
v	Vapor
w	Wall

Chapter 1

Motivation and background

1.1 Wide applicability of boiling heat transfer to improve thermal performance of various systems

The transport of latent heat makes boiling one of the most efficient mode of heat transfer, allowing a wide range of systems to improve their thermal performance, from nuclear power plants to microelectronic devices - see reviews [115], [68], [49]. Subcooled boiling heat transfer for example is able to accommodate very high heat fluxes, thus cooling components very efficiently.

Predicting boiling heat transfer has therefore garnered significant attention, but remains complicated by the need to consider phenomena occurring over multiple scales - see Figure 1-1, from the adsorbed liquid layer at the wall (nanometer scale: [14], [15]) up to the bubble diameter (millimeter scale: [101], [109], [52], [56], [36], [42], [45], [89], [119], [91]).

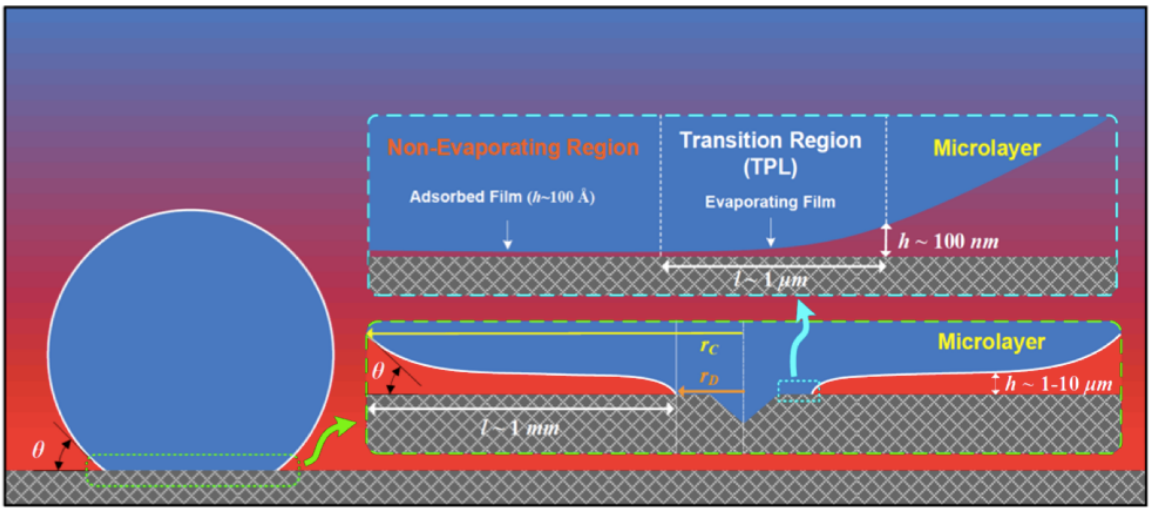

Figure 1-1: Multiple scales involved in nucleate boiling [65]

1.2 Overview of boiling phenomena

During nucleate boiling a bubble grows outside of a surface imperfection, referred to as cavity, and from a preexisting nucleus - an embryo of vapor initially trapped in that surface imperfection. Boiling starts at the wall when the local temperature is sufficiently high to allow the vapor bubble to exist and grow outside of the cavity and into the surrounding liquid.

At the inception of nucleate boiling at a cavity, the liquid in the vicinity of the heated wall is superheated and mass transfer occurs at the liquid-vapor interface of the bubble. The growth of the bubble is also fueled by the overpressure within the vapor, and impeded by the inertia of the liquid. During this initial phase of rapid growth, often referred to as the inertia-controlled phase of bubble growth, the bubble grows hemispherically [16] [32] - see Figure 1-2. In Figure 1-2(b), the bubble growth rate U_b based on bubble cross section area, bubble height, and bubble width are identical, confirming the assumption of an initial hemispherical growth.

As the bubble grows outside of the cavity, viscous stresses at the wall can be strong enough to impede liquid motion at the wall and trap a thin liquid layer - referred to as liquid microlayer, underneath the growing bubble - see experimental evidence in

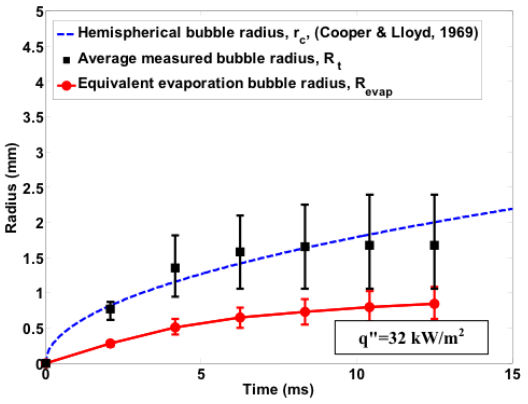

(a)

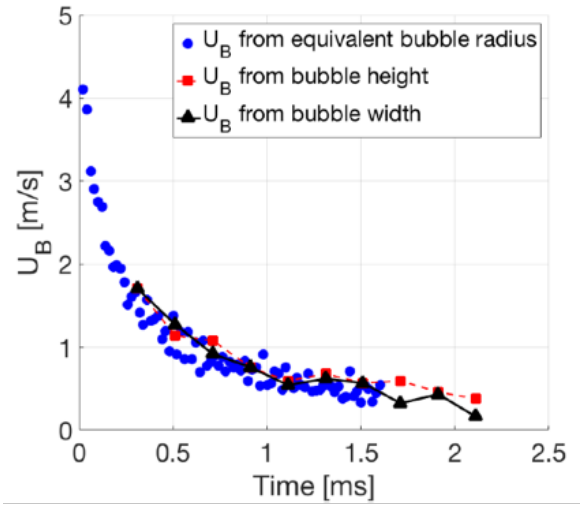

(b)

Figure 1-2: Experimental measurement of bubble radius as a function of time [32] compared with hemispherical bubble radius [16] (a), and bubble growth rate U_b as a function of time (b) (Courtesy of Prof. Hyungdae Kim), based on bubble cross section area, bubble height, and bubble width recorded by a High Speed Video camera on the side of the growing bubble. Fluid is DI water at saturation and atmospheric pressure.

[73], [37], [38], [41], [30], [43], [44], [55], [72], [34], [51], [31], [46], [47], [5], [113], [114], [118]. Bubble growth is then also fueled by the evaporation of the liquid microlayer - see overview of experimental results in Table 1.1. Once the bubble has reached a certain size, referred to as departure diameter, the bubble departs from its initial position at the heated wall and additional cooling mechanisms can occur.

1.3 Modeling of boiling heat transfer

In the past, various empirical correlations and mechanistic models have been proposed to describe and predict boiling heat transfer - see reviews [23], [68], [109]. A wide range of boiling surface geometries, materials, working fluids, and operating conditions have been investigated. In particular, heat partitioning models [44], [61], [33] provide a mechanistic description of the wall boiling phenomena: the total heat flux at the wall is divided into separate heat flux components that account for various modes of heat transfer at the wall, such as forced convection, evaporation, quenching, and sliding conduction.

Reference	Pressure	Fluid	Heat flux	Subcooling	Boiling surface temperature measured	Bubble radius measured	Microlayer thickness measured
(Moore, 1961)	0.101MPa	Water	~300 kW/m^2	0	YES	NO	NO
(Hendricks, 1964)	<0.1MPa	Water	~85 kW/m^2	10K	YES	NO	NO
(Hospeti, 1965)	0.101MPa	Sulfur-35 + calcium sulfate + water	Not reported	0	NO	NO	NO
(Cooper, 1969)	6.9-13.8 kPa	Toluene, Isopropyl alcohol	22.7 – 47.3 kW/m^2	0–10 K	YES	YES	NO
(Jawurek, 1969)	25 kPa	Methanol, Ethanol	70 kW/m^2	2-10	NO	NO	YES
(Foltz, 1970)	7- 28 kPa	Water	Not reported	50–70K	YES	NO	NO
(Judd, 1975)	50kPa	Dichloromethane	70 W/m^2	5-6K	NO	NO	YES
(Judd, 1976)	50kPa	Dichloromethane	25, 40, 60 kW/m^2	0-10K	NO	NO	NO
(Koffman, 1983)	0.101MPa	Water, ethanol	26, 200 kW/m^2	5–20 K	NO	NO	YES
(Golobic, 2009)	0.101MPa	Water	100 kW/m^2	0–10K	YES	NO	NO
(Moghaddam, 2009)	0.101MPa	FC-72	6-30 kW/m^2	0K	YES	NO	NO
(Gerardi, 2010)	0.101MPa	Water	1kW/m^2 to 1MW/m^2	0	YES	YES	NO
(Kim, 2011)	0.101MPa	Water	Not reported	Not reported	NO	NO	YES
(Gao, 2012)	100 kPa	Ethanol	32.4 kW/m^2	6K	NO	NO	YES
(Jung, 2014)	0.101MPa	Water	53 kW/m^2	3K	YES	YES	YES
(Jung, 2015)	0.101MPa	Water	53 kW/m^2	3K	YES	NO	YES
(Yabuki, 2016)	0.101MPa	Water	Not reported	0 – 30K	YES	NO	YES

Table 1.1: Experimental evidence and measurements of the liquid microlayer and its effect on boiling heat transfer

In this context, recent advanced diagnostics (IR, PIV, HSV, ...) provide new and highly-resolved experimental data that can inform and validate models or correlations describing each individual component of the wall heat flux, as they individually represent a single specific physical phenomenon at the wall - see review [11]. Through careful calibration and post-processing, it is possible to accurately measure the temperature and heat flux distributions on the boiling surface which reveals detailed features, including the effects of evaporation of the liquid microlayer [32], [52].
Depending on the fluid, flow and nucleation temperature, the contribution from microlayer evaporation to overall heat transfer and bubble growth can be large in the case of water [32] or relatively small in the case of refrigerants [52]. Typical microlayer models focus on evaporation at the Triple-Phase-Line region [22], [59], or in the extended microlayer region [36], [42], [90].
In practice, numerical simulations of boiling resolve the macroscopic liquid vapor interface of boiling bubbles, but typically resort to subgrid models to include contributions at the microscopic scale such as from evaporation of the microlayer, which requires initialization of the microlayer shape and extension.

1.4 Current gaps

Existing models of microlayer formation are either physically incomplete, e.g. do not include the effect of surface tension or contact angle [105], or are purely empirical [90]. The objective of the present work is to bridge this gap and build a generally applicable model for the formation of the microlayer.
Existing experimental data that directly measure microlayer thickness profiles [43], [55], [51], [46], [47] do not cover a wide range of fluids and surfaces, which makes it difficult to generate or validate a general model on microlayer formation. In practice, measurements of microlayer thickness profiles are mostly obtained at times where the microlayer has already started to evaporate, with little insight on its formation dynamics. Recent advances [114] in indirect measurements of microlayer thickness at short time scales can offer new insights and will be discussed.

1.5 Contributions

This work focuses on three main contributions: (1) assess the sensitivity of numerical simulations of nucleate boiling to the initial microlayer shape included as a subgrid source of vapor; (2) build a generally applicable model for microlayer formation, to be used during the initialization of boiling simulations; (3) provide a procedure for direct computations of moving contact lines and clarify the conditions under which the microlayer is expected to form.

1.6 Structure of the thesis

In this first chapter, we provide motivation and background information on boiling heat transfer, and the need for further modeling and simulation of the so-called liquid microlayer that forms and evaporates underneath a bubble.

In the second chapter, we present state-of-the-art methods to numerically simulate the various scales involved in nucleate pool boiling. We derive from first principles a model to account for the evaporation of the extended liquid microlayer underneath the bubble, and implement it as a subgrid source of vapor in a commercial code (TransAT). We show the dependence of the macroscopic bubble growth rate with the liquid microlayer shape initialized underneath the bubble. These results motivate the following chapter.

In the third chapter, we simulate with unprecedented accuracy the hydrodynamics of bubble growth at a wall, for the case of water at 0.101MPa to 15.5MPa, representative of lab experiments and pressurized water reactor conditions, using Gerris: an open source Navier-Stokes solver that implements the Volume-Of-Fluid interface tracking method. In particular, (i) we identify the minimum set of dimensionless parameters that controls the hydrodynamics of microlayer formation at a wall during nucleate pool boiling; (ii) we generate a large numerical database that resolves the

dynamics of microlayer formation for the conditions of interest; and (iii) we build a generally applicable model for microlayer formation, to be used during the initialization of boiling simulations. We obtain very good agreement with previous analytical and experimental results.

In the fourth chapter, we propose an experiment to measure bubble growth rates at small time scales, namely tens of micro-seconds, relevant to microlayer formation during pool boiling of water at 0.101MPa. We modify an existing pool boiling experiment set-up to specifically measure bubble dynamics at such short time scales, and compare results with existing models.

In the fifth chapter, we further investigate the numerical challenges associated with direct computations of moving contact lines and clarify the conditions, namely the critical capillary number, under which the microlayer is expected to form at a wall. More specifically, we perform a systematic study of the transition from a static meniscus to an entrained film in forced dewetting using Gerris. We use hydrodynamics theories of the moving contact line to model the critical capillary number for the dewetting transition, and provide a numerical procedure to obtain grid independent simulation results of moving contact lines using Gerris. We compare our results with other models and discuss the extension to dynamic contact angles.

In the sixth and last chapter, we conclude on the contributions of the present work and discuss potential future direction.

Chapter 2

Parametric study of boiling simulations

2.1 Motivation

Why simulate nucleate pool boiling?

In pressurized water reactors (PWR), subcooled flow boiling can occur in the so-called hot sub-channels, where temperatures at the surface of the fuel rods can locally exceed the saturation temperature and allow bubbles to grow outside of active cavities and surface imperfections of the fuel rods. Depending on the local conditions bubbles remain attached to the fuel rod surface or grow and detach from the surface.

Numerical simulations of single bubble growth in nucleate pool boiling represent a simplified first step towards modeling and simulating the complex industrial scenario of subcooled flow boiling in pressurized water reactors. In particular, we focus on the simulation of a single vapor bubble growing at a heated wall, under saturated pool boiling conditions at atmospheric pressure and test the applicability of current state-of-art numerical methods and models.

Why include microlayer evaporation?

Near the wall, fluid motion is impeded by viscous stresses, and a thin liquid film

forms underneath the bubble: the so-called liquid microlayer, first observed experimentally by Cooper and Lloyd [16]. As shown in Figure 1-1, the microlayer extends laterally from the root of the bubble (i.e. the location of the nucleation site) up to the macroscopic edge of the bubble (order of hundreds of μm or even mm for water at atmospheric pressure), and its height ranges between 1 to 10 μm.

Once formed, the microlayer starts to evaporate and effectively "retreats" towards the edge of the bubble, leaving behind a central dryout region. Figure 2-1 shows the dynamics of the microlayer for water bubbles at atmospheric pressure as measured by interferometry of visible light and infrared light. Note the time scale (order of milliseconds) and again the spatial scales (order of hundreds of m in the lateral direction and order of m in the vertical direction), i.e. the microlayer is a long and thin liquid film, which moves radially outward with speeds of the order of $0.05 - 0.20$ [m/s]. Obviously, these ranges depend on the fluid properties and the applied heat flux, but it is useful to keep these numbers in mind in the reminder of the discussion. Synchronized high-speed video and infrared video of steam bubble at atmospheric pressure growing on a sapphire wall [24] is shown in Figure 2-2.

In the microlayer region, high heat fluxes are achievable because of its small thickness. Once established, microlayer evaporation can contribute significantly to bubble growth. To illustrate this point, we approximate the microlayer as an axisymmetric wedge of maximum thickness δ_{max} and radius R; then the volume of vapor V_{ml} resulting from complete evaporation of the microlayer is:

$$V_{ml} = \frac{2}{3}\pi R^2 \delta_{max} \frac{\rho_l}{\rho_v} \tag{2.1}$$

which can be compared to the volume of vapor in the bubble (assumed hemispherical) above the microlayer itself:

$$V_b = \frac{2}{3}\pi R^3 \tag{2.2}$$

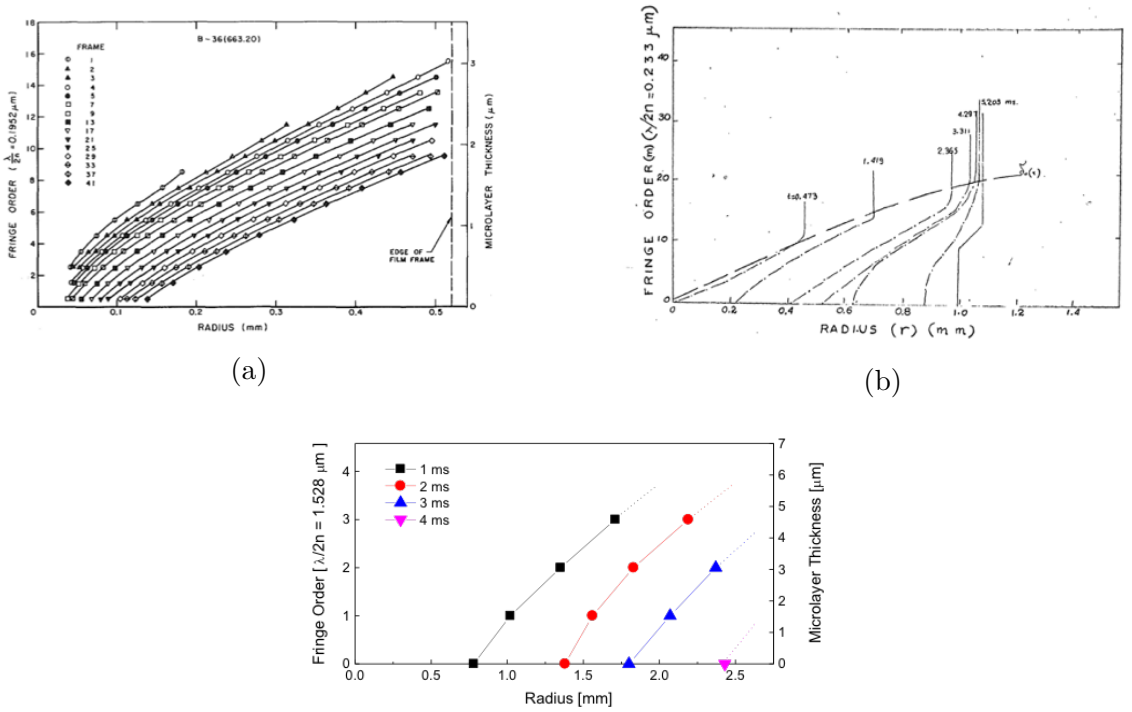

(a) (b) (c)

Figure 2-1: Time evolution of the microlayer underneath steam bubbles, as measured by light interferometry: (a) Visible light [55], (b) Visible light [43] and (c) Infrared light [51]. "Radius" is the radial distance from the center of the bubble base, i.e. distance from the nucleation site. Note the scale for the X-axis is mm while that of the Y-axis is μm.

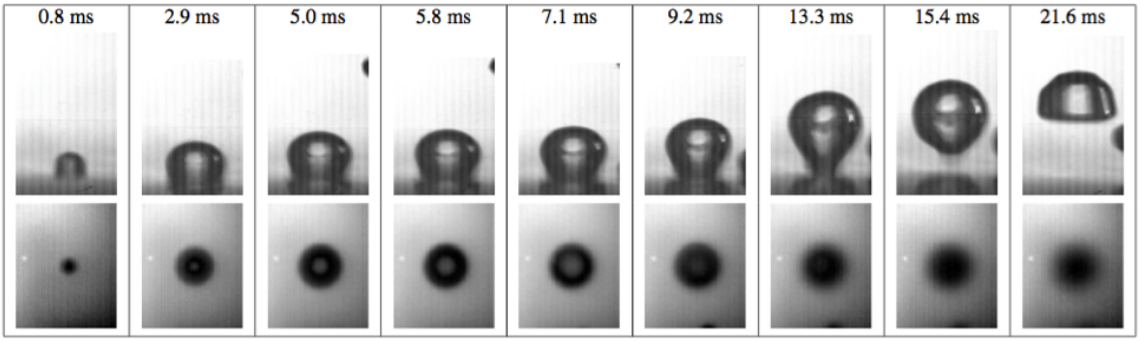

Figure 2-2: Synchronized high-speed video and infrared video of steam bubble at atmospheric pressure growing on a sapphire wall [24]. The top sequence is a lateral view of the bubble, the bottom sequence is the two-dimensional temperature distribution on the sapphire surface underneath the bubble. The nucleation temperature for this bubble was 109°C, the bubble departure occurred at about 14.7ms after nucleation with a departure diameter of 3.7mm.

Taking the ratio of the two, we get:

$$V_{ml}/V_b = \frac{\delta_{max}}{R}\frac{\rho_l}{\rho_v} \approx 6 \tag{2.3}$$

for steam bubble at 0.101MPa.

This result indicates that there is plenty of liquid to contribute to bubble growth. The actual contribution of microlayer evaporation to bubble growth is the subject of debate in the literature. Kim [52] concluded that microlayer evaporation contributes no more than 25% to the overall heat transfer, while Gerardi [32] showed that for steam bubbles microlayer evaporation accounted for the majority of the bubble growth.

The importance of the microlayer depends strongly on the fluid, i.e., fluids with low surface tension and viscosity (e.g. refrigerants or water itself at high pressure) tend to have much thinner microlayers, thus diminishing the importance of the microlayer contribution to bubble growth.

2.2 Numerical simulations of nucleate boiling

Numerical simulation of nucleate boiling using interface tracking methods, has gained momentum in the last decade because of its potential to generate insight into physical phenomena (e.g. bubble merging, microconvection, condensation, turbulence/bubble interaction, etc.) that are generally difficult to probe experimentally. We here list leading studies: [23], [76], [109], [98], [78], [20], [99], [58], [59], [81], [83], [56], [77], [80], [66],[57], [60], [21], [88], [62], [90], [91]. While Ose and Kunugi, Mukherjee and Kandlikar, Narayanan et al. do not consider the microlayer in their analysis at all, all others employ a subgrid models. Subgrid models account for the effects of microlayer evaporation on bubble growth, in lieu of resolving the microlayer region explicitly, which decreases the computational cost of the simulation. Examples of the subgrid

models considered in these studies are shown in Figure 2-3.

2.3 Governing equations

We consider an axisymmetric microlayer underneath a bubble growing at a heated wall, as shown in Figure 2-4. Here the thickness of the microlayer at any given location r (distance from the center of the bubble root or nucleation site) is δ, the mass flux within the microlayer is $m^{"}$, the evaporation flux is j_v and the heat flux from the wall is $q^{"}$. We write equations expressing the conservation of mass, energy and momentum, as well as a closure relation for the interfacial temperature. Note that H is the (arbitrary) height of the control volume, and it will wash out of the equations.

2.3.1 Conservation of Mass

$$\begin{aligned}\frac{\partial}{\partial t}\{2\pi r\mathrm{dr}\delta\rho_l + 2\pi r\mathrm{dr}(H-\delta)\rho_v)\} = -j_v 2\pi r\mathrm{dr} + ... \\ ... + m^{"}2\pi r\delta(r) - m^{"}(r+dr)2\pi(r+dr)\delta(r+dr)\end{aligned} \tag{2.4}$$

which becomes

$$\frac{\partial}{\partial t}\{\delta\rho_l + (H-\delta)\rho_v\} = -j_v - \frac{1}{r}\frac{\partial}{\partial r}\{m^{"}r\delta\} \tag{2.5}$$

2.3.2 Conservation of Energy

$$\begin{aligned}\frac{\partial}{\partial t}\{2\pi r\mathrm{dr}\delta\rho_l u_l + 2\pi r\mathrm{dr}(H-\delta)\rho_v u_v\} = q^{"}2\pi r\mathrm{dr} - j_v 2\pi r\mathrm{dr}h_v + ... \\ ... + m^{"}2\pi r\delta(r)h_l(r) - m^{"}2\pi(r+dr)\delta(r+dr)h_l(r+dr)\end{aligned} \tag{2.6}$$

which becomes

$$\frac{\partial}{\partial t}\{\delta\rho_l u_l + (H-\delta)\rho_v u_v\} = q^{''} - j_v h_v - \frac{1}{r}\frac{\partial}{\partial r}\{m^{"}r\delta h_l\} \tag{2.7}$$

2.3.3 Conservation of Momentum: radial component

Assuming 1D flow in the microlayer and using the lubrication approximation in the Navier-Stokes equations, the average mass flux in the microlayer can be related to

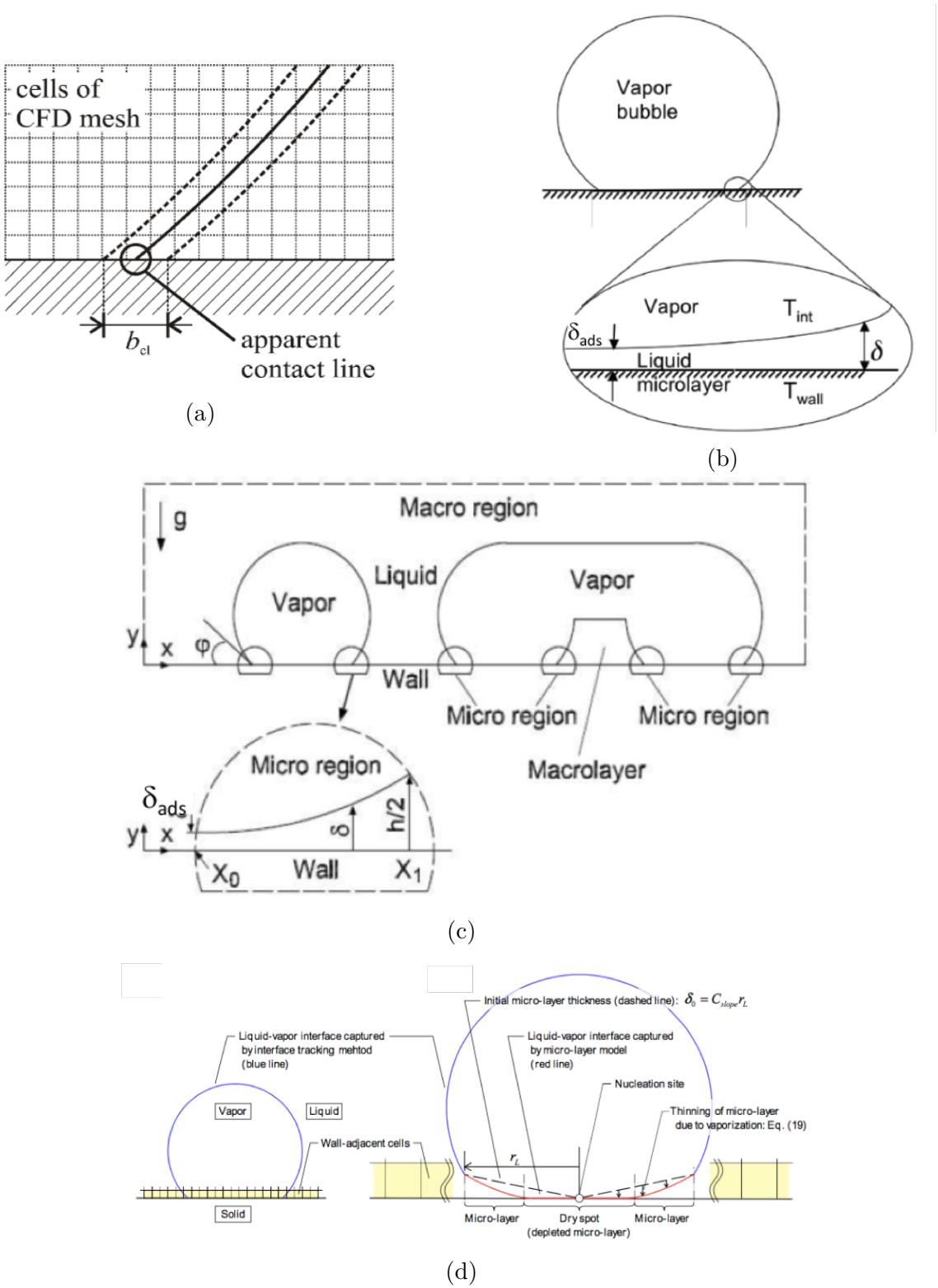

Figure 2-3: Microlayer region as modeled by (a) Kunkelmann and Stephan [56] (b) Juric et al. [48] (c) Son and Dhir [99], and (d) Sato and Niceno [91]. Note that only the short Triple Phase Line (TPL) transition region is considered in (a), (b), (c), while the microlayer is coarsely represented in (d), with an empirical slope C_{exp}.

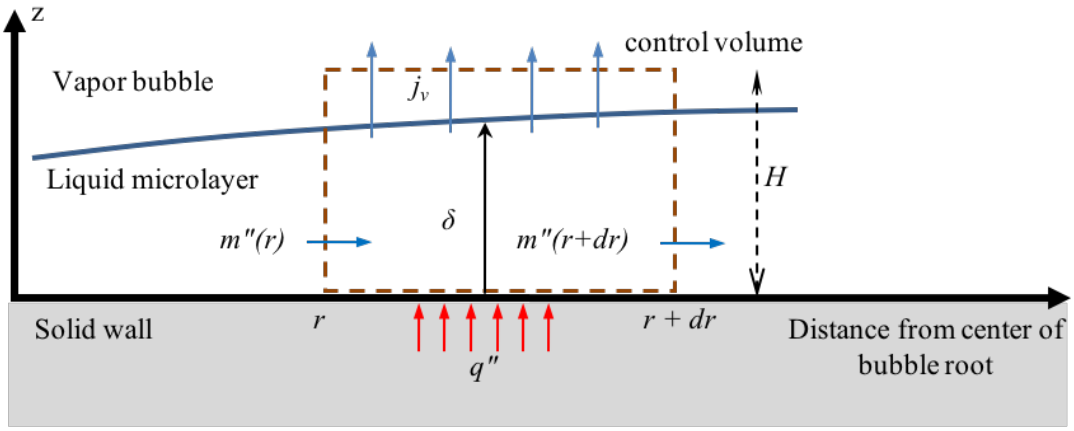

Figure 2-4: Geometry and key quantities for microlayer analysis

the pressure gradient as follows:

$$m^{"} = -\frac{1}{3\nu_l}\frac{\partial P_l}{\partial r}\delta^2 \tag{2.8}$$

2.3.4 Conservation of Momentum, axial-component (Force Balance at the Vapor-Liquid Interface)

The pressure in the microlayer may differ from that in the vapor above it because of long range molecular interactions (disjoining pressure) between the wall and the liquid, curvature effects and vapor recoil:

$$P_v - P_l = -\frac{A_H}{\delta^3} - \sigma\kappa + \left\{\frac{1}{\rho_g} - \frac{1}{\rho_f}\right\} j_v^2 \tag{2.9}$$

where A_H is the dispersion coefficient relating the disjoining pressure to the microlayer thickness, σ is the surface tension coefficient and κ is the curvature:

$$\kappa = \frac{\partial^2\delta}{\partial r^2} \Big/ \left\{1 + \left(\frac{\partial\delta}{\partial r}\right)^2\right\}^{2/3} + \frac{\partial\delta}{\partial r} \Big/ \left\{r\left[1 + \left(\frac{\partial\delta}{\partial r}\right)^2\right]^{1/2}\right\} \tag{2.10}$$

The third term on the RHS of Eq. (2.9) represents the vapor recoil pressure.

2.3.5 Interfacial Thermal Resistance

It is generally assumed that the interface temperature can differ from the saturation temperature at the vapor pressure. Wang et al. [108] showed that the linearized approximation of [110] accurately captures the interfacial thermal resistance effect over a large range of conditions:

$$j_v = a(T_i - T_v) + b(P_l - P_v) \tag{2.11}$$

where

$$a = \frac{\hat{\sigma}}{2-\hat{\sigma}} \frac{1}{\sqrt{2\pi R^* T_i}} \frac{P_v h_{fg}}{R^* T_i T_v} \tag{2.12}$$

$$b = \frac{\hat{\sigma}}{2-\hat{\sigma}} \frac{1}{\sqrt{2\pi R^* T_i}} \frac{P_v}{\rho_l R^* T_i} \tag{2.13}$$

with $\hat{\sigma} \approx 1$ and R^* is the gas constant for the fluid of interest (e.g. 462 J/kg-K for water). Therefore Eq. (2.11) is adopted hereafter. The following assumptions are made to simplify the mass and energy equations:

- Heat transfer within the microlayer is purely by conduction: $q^{"} = \frac{k_l}{\delta}(T_w - T_i)$
- Both phases (vapor and liquid) are treated as incompressible fluids, i.e. ρ_v and ρ_l are constant in time and space.
- The vapor is assumed to be saturated at the pressure of the bubble ($T_v = T_{sat}$), thus $\rho_v = \rho_g$, $u_v = u_g$, $h_v = h_g$
- The liquid is modestly superheated at average temperature $T_l = \frac{T_w + T_i}{2}$, and pressure P_l. Therefore, $\rho_l \approx \rho_f$, $u_l = u_f + c_l(T_l - T_{sat})$ and $h_l = h_f + c_l(T_l - T_{sat}) + \{P_l - P_v\}/\rho_f$

Which yields the following set of equations:

$$(\rho_f - \rho_g)\frac{\partial \delta}{\partial t} = -j_v - \frac{1}{r}\frac{\partial}{\partial r}\{m^{"} r\delta\} \tag{2.14}$$

$$j_v = \left(\frac{\rho_f - \rho_g}{\rho_f}\right)\left(\frac{k_l}{\delta}(T_w - T_i) - \left\{\frac{\rho_g}{\rho_f - \rho_g}[h_{fg} - c_l(T_l - T_{sat})] + ... \right.\right.$$
$$\left.\left. ... + \quad \frac{P_l - P_v}{\rho_f}\right\}\frac{1}{r}\quad\frac{\partial}{\partial r}[m^{"} r\delta]\right) / \left(h_{fg} - c_l(T_l - T_{sat})\right) \tag{2.15}$$

$$P_v - P_l = -\frac{A_H}{\delta^3} - \sigma\kappa + \left\{\frac{1}{\rho_g} - \frac{1}{\rho_f}\right\} j_v^2 \tag{2.16}$$

$$m^{"} = -\frac{1}{3\nu_l}\frac{\partial P_l}{\partial r}\delta^2 \tag{2.17}$$

$$j_v = a(T_i - T_v) + b(P_l - P_v) \tag{2.18}$$

Equations (2.14), (2.15), (2.16), and (2.17) represent, respectively, the conservation of mass, energy, momentum (z-component) and momentum (r-component) in the microlayer, while Eq. (2.25) represents the interfacial thermal resistance on the surface of the microlayer. Equations (2.14) through (2.25) constitute a system of five PDEs, from which the five unknown functions $\delta(r,t)$, $j_v(r,t)$, $m^{"}(r,t)$, $P_l(r,t)$, and $T_i(r,t)$ can be found, if the appropriate initial and boundary conditions are specified along with the values of all transport and thermodynamic properties present in the equations. Note that T_w, P_v and T_{sat} are typically given as inputs to the problem. These PDEs can be considered the starting point of all analyses of the microlayer region.

2.4 Triple Phase Line (TPL) region - also referred to as contact line region

Typically, the following simplifying assumptions are made for the TPL region [29], [56]:

- Since the TPL region is very short (order of 1 μm or less), the microlayer in this region can be considered planar. Therefore, the $1/r$ factor disappears from the last term on the RHS of Eq. (2.14) and (2.15); moreover, the second radius of curvature is assumed to be zero thus

$$\kappa \approx \frac{\partial^2\delta}{\partial r^2} / \left\{1 + \left(\frac{\partial\delta}{\partial r}\right)^2\right\}^{2/3} \tag{2.19}$$

- The TPL region is quasi-static. This assumption is never justified in the literature and it leads to the incorrect conclusion that evaporation from the TPL region is important, whereas in fact it is evaporation from the extended microlayer region that determines the motion of the dry spot underneath the bubble, as will be shown below.

- In Eq. (2.16) the vapor recoil term is typically neglected with respect to the surface tension and disjoining pressure terms, without a compelling justification.

- The liquid superheat is relatively small:

$$\frac{c_l(T_l - T_{sat})}{h_{fg}} << 1 \tag{2.20}$$

- The vapor density is much lower than the liquid density:

$$\frac{\rho_g}{\rho_f} << 1 \tag{2.21}$$

Equations (2.14), (2.15), (2.16), (2.17) and (2.25) become, respectively:

$$j_v = -\frac{\mathrm{d}}{\mathrm{d}r}[m^{"}\delta] \tag{2.22}$$

$$P_l - P_v = -\frac{A_H}{\delta^3} - \sigma\frac{\partial^2\delta}{\partial r^2}/\left\{1 + \left(\frac{\partial\delta}{\partial r}\right)^2\right\}^{2/3} \tag{2.23}$$

$$m^{"} = -\frac{1}{3\nu_l}\frac{\partial P_l}{\partial r}\delta^2 \tag{2.24}$$

$$j_v = a(T_i - T_v) + b(P_l - P_v) \tag{2.25}$$

If T_i, , P_l and j_v are eliminated from these equations, a single, highly non-linear, 4th-order ODE for the microlayer thickness is obtained:

$$f\left(\delta, \frac{\mathrm{d}\delta}{\mathrm{d}r}, \frac{\mathrm{d}^2\delta}{\mathrm{d}r^2}, \frac{\mathrm{d}^3\delta}{\mathrm{d}r^3}, \frac{\mathrm{d}^4\delta}{\mathrm{d}r^4}\right) = 0 \tag{2.26}$$

Solution of this ODE requires specification of four boundary conditions. Since the TPL region starts from the nanosize adsorbed layer, which is flat, the natural boundary conditions at the edge of the TPL are:

$$\delta = \delta_{ads},\ \frac{\mathrm{d}\delta}{\mathrm{d}r} = 0,\ \frac{\mathrm{d}^2\delta}{\mathrm{d}r^2} = 0,\ \frac{\mathrm{d}^3\delta}{\mathrm{d}r^3} = 0 \tag{2.27}$$

where δ_{ads} is the thickness of the adsorbed layer. However, with these boundary conditions the ODE yields the trivial solution $\delta = \delta_{ads}$ for any r. Therefore, researchers have resorted to perturbing the boundary conditions according to the following 'trial and error' approach: a small arbitrary positive curvature or a small arbitrary positive slope at $r = 0$ is assumed, and the ODE is repeatedly solved until the microlayer thickness at the bubble outer edge matches the macroscopic liquid-vapor interface calculated by DNS (Dhir [22] also imposes (without justification) a zero curvature as boundary condition at the outer edge of the microlayer.). Examples of solutions so obtained are shown in Figure 2-5. Wang et al. [108] also proposed an analytical approximation of their TPL solutions. Note that Eq. (2.26) is an extremely stiff ODE, which is sensitive to the boundary conditions; therefore, the reliability of this perturbation approach is generally open to question. Moreover, no validation of these solutions is presented in the papers reporting the results. Finally, all the solutions presented in Figure 2-5 seem to diverge rapidly with r, which is in contrast with the experimental data showing a microlayer region that is thin and long and with (small) negative curvature (Figure 2-1). In addition to the shortcomings described above, the whole effort about this very short TPL region seems somewhat futile, since the TPL does not really affect the evolution of the extended microlayer.

2.5 Extended microlayer region

2.5.1 Simplifications of general governing equations

The extended microlayer region is essentially a long and flat liquid film for which the following simplifying assumptions can be made:

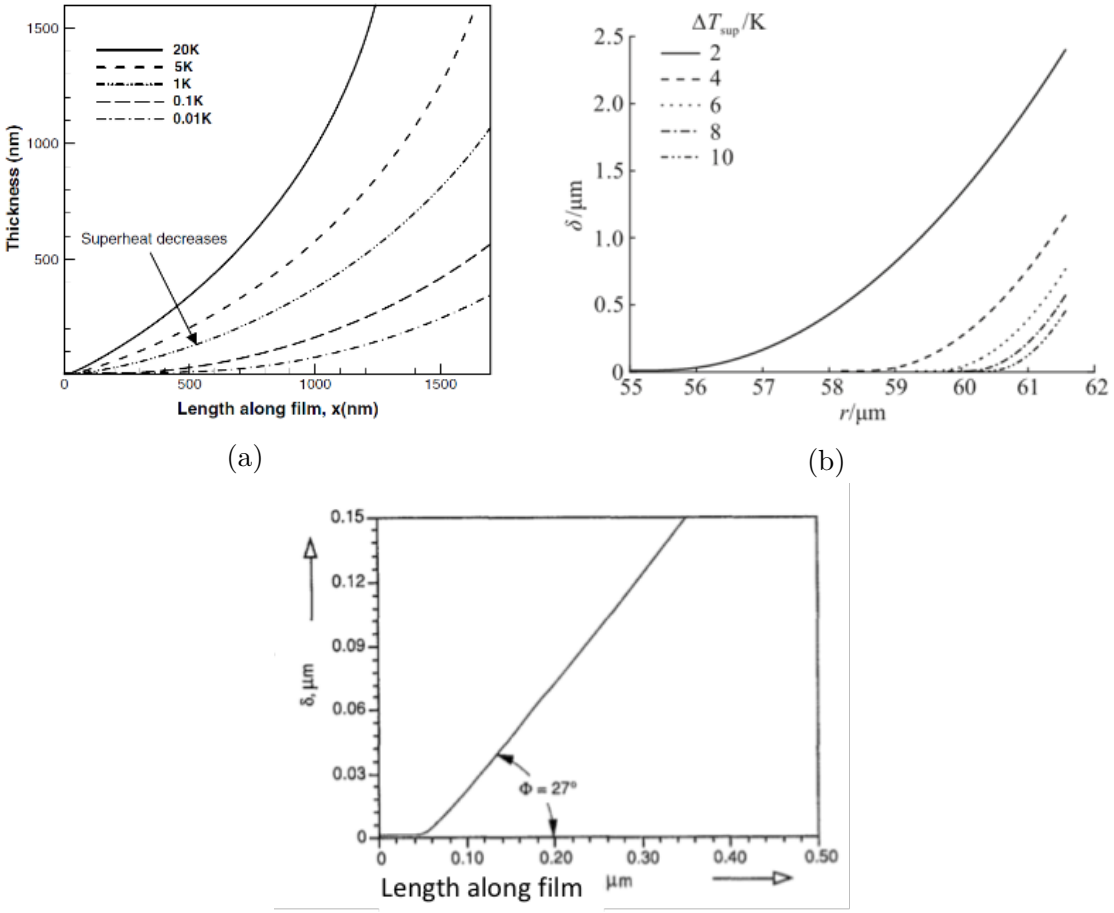

Figure 2-5: Microlayer thickness in the TPL region, as calculated by (a) Wang et al. [108], (b) Christopher and Zhang [13] and (c) Stephan and Hammer [100]. Note the radial extension of the TPL region is order of 1 μm or less. Also, note the contradictory superheat trend of the curves in (a) and (b).

- Negligible curvature ($\kappa \approx 0$). Visual inspection of the experimentally measured microlayer profiles (Figure 2-1) suggests the microlayer curvature is very low. An approximate estimate is $\kappa \approx 3m^{-1}$, which results in a very small pressure difference of $\sigma\kappa \approx 0.17Pa$.

- Negligible disjoining pressure. Disjoining pressure arises from attractive forces between molecules in the fluid and molecules in the solid wall. These forces typically have a range of a few molecular diameters, which in the case of water is order of $0.3nm$. Thus, disjoining pressure effects can be safely neglected for films $> 10nm$, such as the extended microlayer region of interest here.

- Negligible vapor recoil pressure. Assuming an evaporation mass flux in the microlayer region for water at atmospheric pressure of $0.3kg/m^2s$ (as estimated in the introduction, the vapor recoil pressure is a miniscule $10^{-4}Pa$.

- Negligible interfacial resistance ($T_i = T_{sat}$). For water $a \approx 6.8kg/m^2s\text{-}K$ and assuming again an evaporation mass flux of $0.3kg/m^2s$, the difference between T_i and T_{sat} is order of $j_v/a \approx 0.04K$, which is completely negligible.

- The liquid superheat is relatively small:

$$\frac{c_l(T_l - T_{sat})}{h_{fg}} << 1 \tag{2.28}$$

Under these assumptions, the liquid pressure is equal to the vapor pressure and the temperature of the interface is equal to the saturation temperature, thus the equations simplify dramatically: in particular, it immediately follows that $m" = 0$, i.e. there is no flow within the microlayer (which implies that the lateral retreat of the microlayer is primarily due to microlayer evaporation, not liquid flow). The system of PDEs reduces to the following two simple equations:

$$(\rho_f - \rho_g)\frac{\partial \delta}{\partial t} = -j_v \quad \text{(mass)} \tag{2.29}$$

$$j_v = \frac{\rho_f - \rho_g}{\rho_f} \frac{k_l(T_w - T_{sat})}{h_{fg}\delta} \quad \text{(energy)} \tag{2.30}$$

Eliminating j_v from the above equations, a single equation that governs the time-evolution of the microlayer thickness is obtained:

$$\frac{\partial \delta}{\partial t} = -\frac{k_l(T_w - T_{sat})}{\rho_f h_{fg}\delta} \tag{2.31}$$

which is readily integrated to give:

$$\delta^2(r,t) = \delta_0^2(r) - \int_0^t \frac{k_l(T_w - T_{sat})}{\rho_f h_{fg}} \mathrm{d}t \tag{2.32}$$

where $\delta_0(r) = \delta(r, t = 0)$ is the initial microlayer profile. In particular, for a fixed wall temperature T_w, we have:

$$\delta(r,t) = \sqrt{\delta_0^2(r) - \int_0^t \frac{k_l(T_w - T_{sat})}{\rho_f h_{fg}} \mathrm{d}t} \tag{2.33}$$

Representative examples of the microlayer evolution calculated from Eq. (2.33) are shown in Figure 2-6(a)(b). It can be seen that the microlayer moves radially outward due to evaporation, as expected. The microlayer radial speed can be extracted from the simulation and is shown in Figure 2-6(c), and in Figure 2-8. Interestingly, if the initial microlayer shape is proportional to $\sqrt{r}$: $\delta_0(r) = \delta_{max}\sqrt{\frac{r}{R}}$, the microlayer speed is constant in time. In fact, it is possible to derive an analytical expression for the microlayer speed. Let $r_d = r_d(t)$ denote the dryout radius, i.e., the location of the microlayer edge at which $\delta(r_d(t), t) = 0$. Taking $r = r_d(t)$ in Eq. (2.32) and differentiating with respect to t gives:

$$\frac{\mathrm{d}}{\mathrm{d}t}\delta_0^2(r_d(t)) = \frac{\mathrm{d}\delta_0^2}{\mathrm{d}r}\frac{\mathrm{d}r_d}{\mathrm{d}r} = \frac{2k_l(T_w(r_d(t)) - T_{sat})}{\rho_f h_{fg}} \tag{2.34}$$

Defining $v_{ml} = \dfrac{\mathrm{d}r_d}{\mathrm{d}r}$ to be the microlayer velocity, we have:

$$v_{ml} = \left(\frac{2k_l(T_w(r_d(t)) - T_{sat})}{\rho_f h_{fg}}\right) / \left(\frac{\mathrm{d}\delta_0^2}{\mathrm{d}r}\right) \tag{2.35}$$

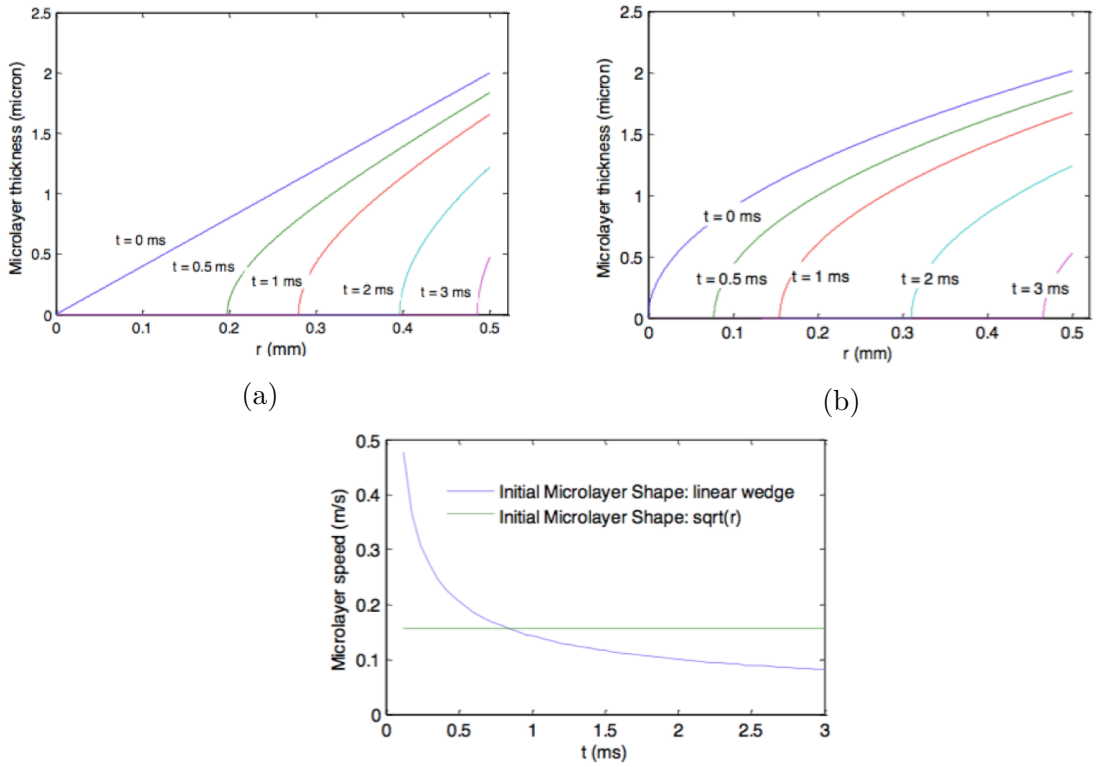

Figure 2-6: Spatial and temporal evolution of microlayers of $2\mu m$ maximum initial thickness and $500\mu m$ extension under a vapor bubble. The initial shape of the microlayer is assumed to be (a) linear wedge or (b) square root of r. (c) Microlayer speed as a function of time. The fluid is water at atmospheric pressure; Wall superheat $T_w - T_{sat}$=2K.

Assuming the wall superheat $T_w - T_{sat}$ to be constant, the microlayer velocity will be constant whenever:

$$\frac{\mathrm{d}}{\mathrm{d}t}\delta_0^2 = C^{te} \Rightarrow \delta_0(r) = \delta_{max}\sqrt{r/R} \tag{2.36}$$

in which case:

$$v_{ml} = \frac{2k_l(T_w(r_d(t)) - T_{sat})R}{\rho_f h_{fg}\delta_{max}^2} \tag{2.37}$$

2.5.2 Preliminary tests

The experimental configuration of Kim and Buongiorno [51] is reproduced to solve the conjugate heat transfer between the liquid microlayer and the silicon wafer heater used in those experiments. The computational domain is limited to the heater itself underneath the microlayer region (cylinder of height $H_w = 380\mu m$ and radius $R_s = 600\mu m$). The heat generation rates per unit surface area and volume of the heater are $q_w^{"} = 50kW/m^2$ and $q^{'''} = q_w^{"}/H_w = 132MW/m^3$, respectively. The initial temperature field within the heater is assumed to be uniform and equal to $T_{sat} + T_0$, with T_0 assumed to be a reasonable $5°C$ - unfortunately the actual value of T_0 is not available from the experimental data. A finite difference solution scheme was used to solve the heat equation in the heater:

$$\frac{\partial T}{\partial t} = \alpha_w \nabla^2 T + \frac{q^{'''}}{\rho_w c_w} \tag{2.38}$$

in cylindrical coordinates and the microlayer equation Eq. (2.31), both in space and time. The boundary conditions were as follows: zero heat flux at the centerline, at the bottom and at the outer-edge of the cylindrical domain. Also, the heat flux was set equal to:

$$q^{"} = \frac{k_l(T_w - T_{sat})}{\delta} \tag{2.39}$$

at the wall where the microlayer is present (with δ found from Eq. (2.31)) and zero where the wall is dry. The output of the calculation is the coupled time-dependent temperature distribution within the heater and the time-dependent microlayer profile above it; they are shown in Figure 2-7. The behavior of the solution is consistent with the experimentally observed behavior, i.e. the microlayer moves outward (compare to Figure 2-1) and creates a temperature minimum that also moves outward (compare to Figure 2-2). Post-processing of Figure 2-7(a) yields the microlayer outward speed, which is shown in Figure 2-8. The predicted speed is definitively in the correct range of experimental values however it slows down faster than in the experiments. The discrepancy may be due to an inaccurate guess of ΔT_0 (i.e. the actual ΔT_0 in the

heater may be higher than 5°C), or to the zero heat flux boundary condition at the outer boundary of the domain, which tends to underestimate the thermal capacity of the heater. In fact, post-processing of the temperature distribution within the heater reveals the presence of strong radial conduction heat fluxes within the heater (see Figure 2-9). The convergence of the results is confirmed - see Figure 2-10.

Finally, similar, reasonably good results were found when the model was applied to the data of Koffman and Plesset [55] (Figure 2-11). To reproduce their experimental setup, we estimated their SnO_2 coating thickness $d_{SnO_2} \approx 30\mu m$ from its measured resistance ($10-30\Omega$). Its specific heat was estimated from Dulong and Petite's simple model (Debye theory). Pyrex glass properties were found in the literature.

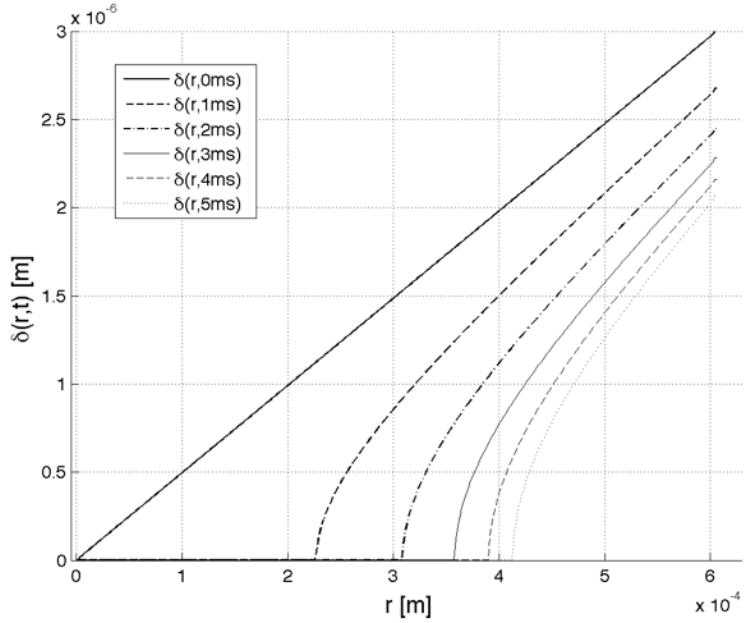

(a)

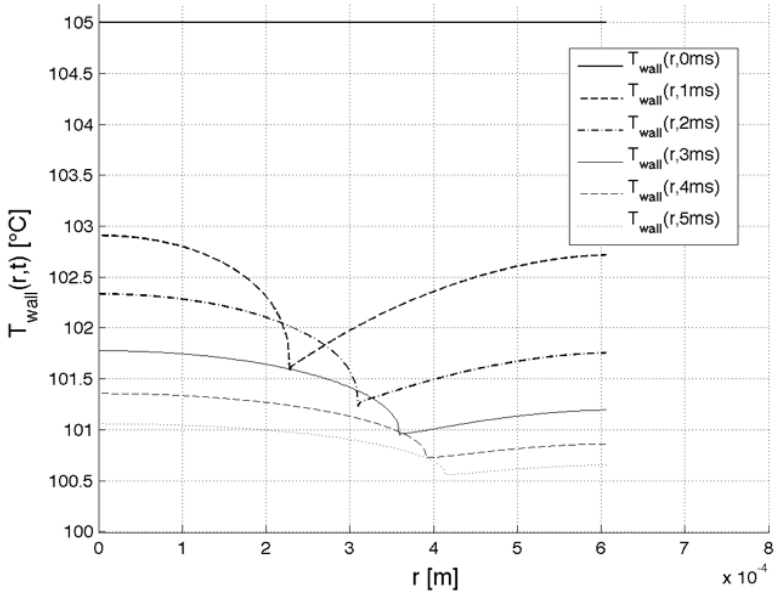

(b)

Figure 2-7: Evolution of (a) microlayer of maximum initial thickness $3\mu m$ and extension $600\mu m$, and (b) wall temperature profiles of initial superheat $\Delta T_0 = 5°\text{C}$.

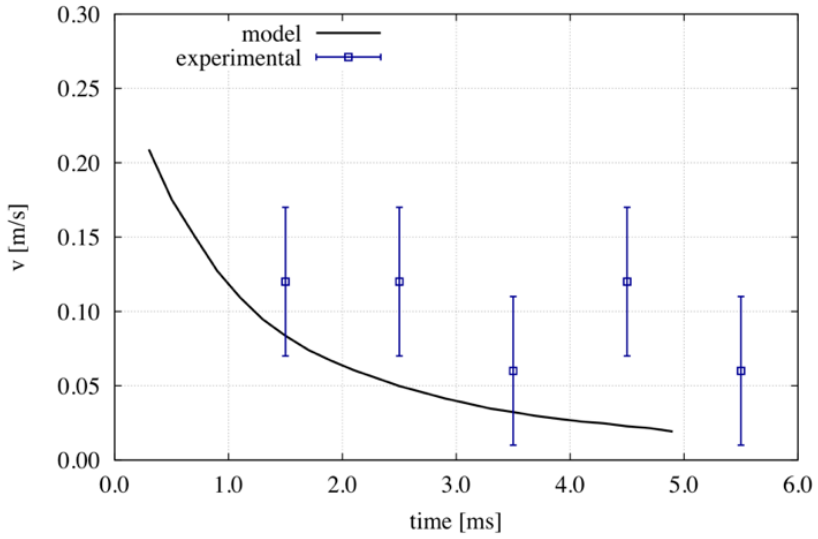

Figure 2-8: Temporal evolution of predicted and experimental microlayer speed [m/s]; experimental results from Kim and Buongiorno [51]

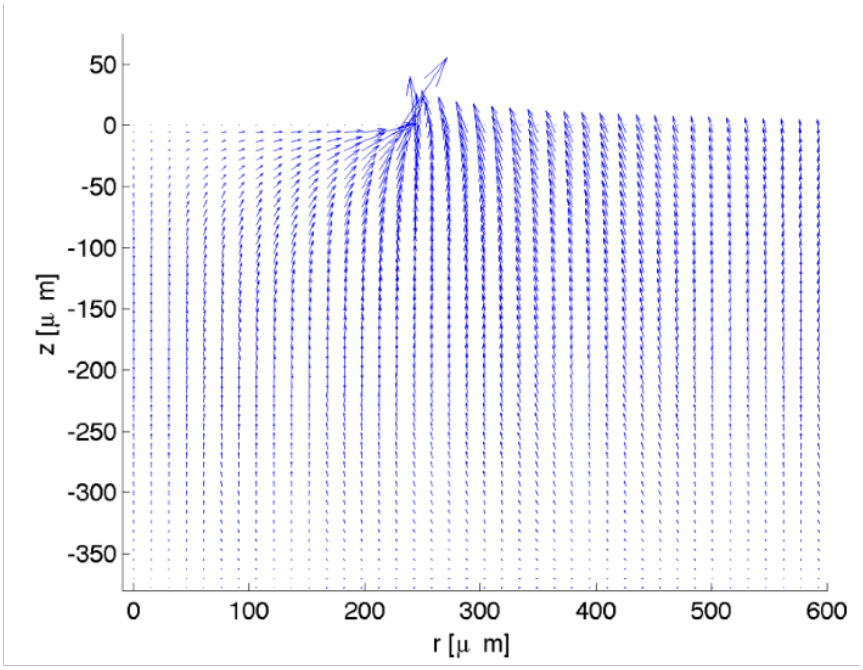

(a)

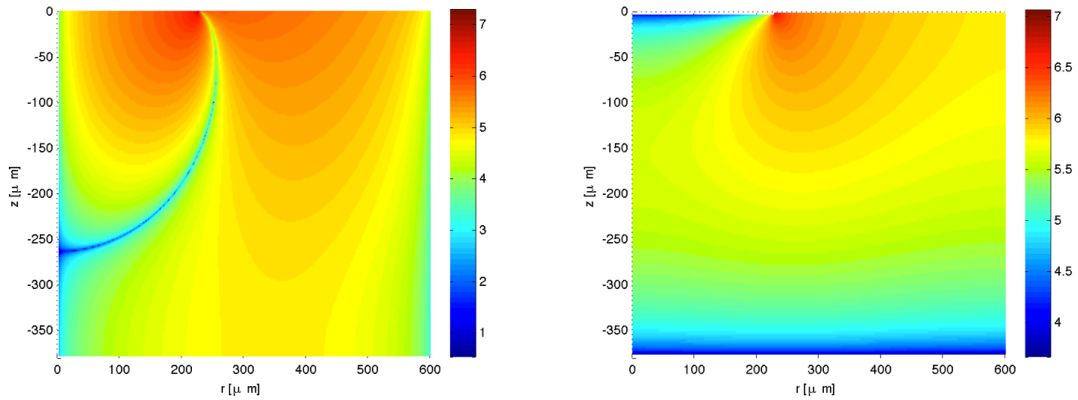

(b) (c)

Figure 2-9: Spatial distribution of the heat flux (a), within the heater at $t = 1ms$ after the beginning of microlayer's evaporation). Log-10 of absolute values (in W/m^2) of r-component (b) and z-component (c) of the heat flux are also reported (see colorbar), over the whole computational domain (maximum initial thickness $3\mu m$ and $600\mu m$ extension; initial superheat $\Delta T_0 = 5°C$ above the saturation temperature at atmospheric pressure). Discretization: $\mathrm{d}r = \mathrm{d}z = 1.9\mu m,\ \mathrm{d}t = 7ns$.

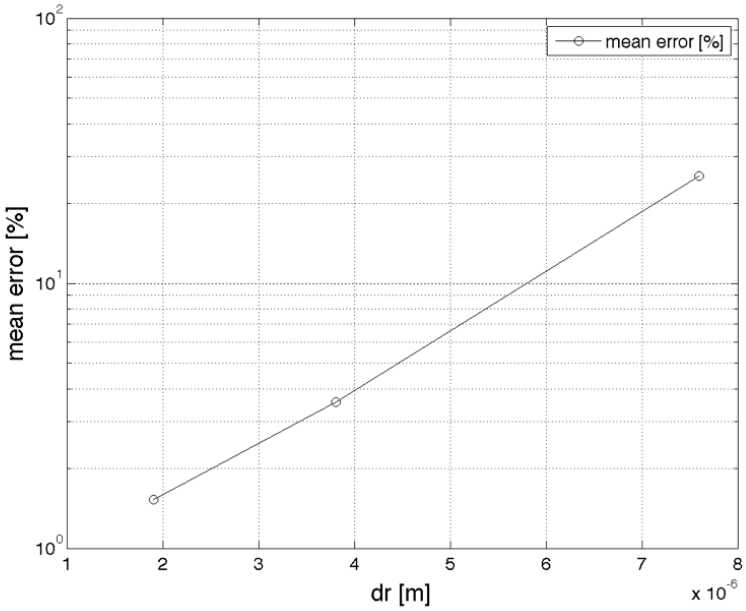

Figure 2-10: Second order convergence with grid size is obtained for the mean error in the computed microlayer thickness ($\mathrm{d}r = 1.9,\ 3.8$ and $7.6\mu m$ vs reference calculation $dr = 0.475\mu m$). In all cases, $\mathrm{d}z = \mathrm{d}r$, and $\mathrm{d}t$ is given by stability criterion.

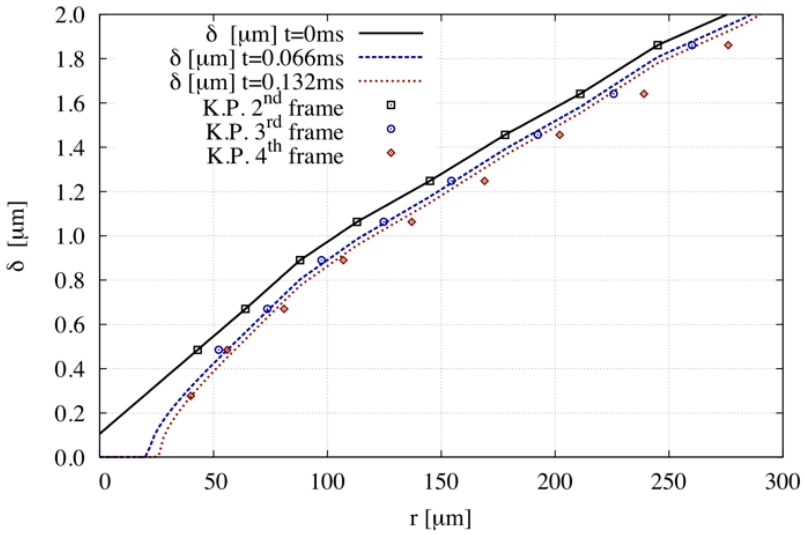

Figure 2-11: Temporal evolution of microlayer of initial thickness taken from the second frame of Koffman and Plesset [55] results for water, with initial superheat $\Delta T_0 = 7°\text{C}$ (guessed), mean wall heat flux of $204 kW/m^2$. The SnO_2 coating thickness was guessed to be $30 \mu m$ from its overall resistance; the Pyrex glass substrate thickness was $3.2 mm$.

2.6 Implementation of subgrid model for micro-layer evaporation in commercial software (TransAT)

2.6.1 Computational framework

TransAT is a commercial finite-volume code that solves the Navier-Stokes equations on structured meshes, using the one-fluid formulation approach:

$$\rho\left(\frac{\partial\vec{u}}{\partial t}+\nabla.\vec{u}\vec{u}\right)=-\nabla P+\nabla\ .\ (2\mu\bar{D})+\rho\vec{g}+\sigma\kappa(\Psi)\delta(\Psi)\nabla(\Psi)+\vec{F}_{external} \tag{2.40}$$

with

$$\kappa(\Psi)=\nabla\ .\ \left(\frac{\nabla\Psi}{|\nabla\Psi|}\right) \tag{2.41}$$

The flow is described by a single fluid of variable material properties based on a color function Psi, also referred to as the Level-Set (LS) function:

$$\rho(\Psi)=\rho_1+(\rho_1-\rho_2)H(\Psi),\ \mu(\Psi)=\mu_1+(\mu_1-\mu_2)H(\Psi) \tag{2.42}$$

where H is a smoothed Heaviside function defined as:

$$\begin{aligned} H(\Psi)&=0,\ \text{if}\ |\Psi|>\epsilon \\ H(\Psi)&=\frac{1}{2}\left(1+\frac{\Psi}{\epsilon}+\frac{sin(\pi\Psi/\epsilon)}{\pi}\right),\ \text{otherwise} \end{aligned} \tag{2.43}$$

where ϵ is referred to as interface thickness;

$$\nabla\vec{u}=0 \tag{2.44}$$

This function Ψ has a value of zero at the interface, and is negative in one fluid and positive in the other (the two fluids being considered are immiscible throughout the study). The Level-Set function is advected by the flow, and influenced by mass

transfer $\dot{m}$ at the interface:

$$\frac{\mathrm{d}\Psi}{\mathrm{d}t} + \vec{u} \; . \; \nabla\Psi = \dot{m}/\rho|\nabla\Psi| \tag{2.45}$$

TransAT implements a second order heat flux model to obtain grid convergence results for simulations with phase change and mass transfer across the interface.

2.6.2 Verification of numerical methods used in TransAT

Verification of the numerical methods employed in TransAT was provided by C. Narayanan et al. [79].

2.6.3 Verification of correct implementation of new subgrid model in TransAT

- Preliminary work to identify a suitable numerical scheme to compute the evaporative mass flux from microlayer evaporation.

  The subgrid model for microlayer evaporation is written as:

$$\frac{\partial\delta}{\partial t} = -\frac{k_l \Delta T}{\rho_f h_{fg} \delta} \tag{2.46}$$

  where δ is the microlayer thickness and $\Delta T = T_w - T_{sat}$ is the local wall superheat, which can be solved to find the evolution of the microlayer profile. However, the parameter of interest for the subgrid model in TransAT is the evaporative mass flux j_v from the microlayer. If S_k is the evaporating surface between a radial position r_k and a position r_{k+1} (note we consider axisymmetric bubbles in the pool boiling situation), then the mass flux becomes:

$$j_{v,k} = \frac{\rho_f}{S_k}\left|\frac{\partial V_{micro,k}}{\partial t}\right| = \frac{\rho_f}{S_k}\left|\frac{\partial}{\partial t}\left(\int_{r_k}^{r_{k+1}} 2\pi r \delta \mathrm{d}r\right)\right| \tag{2.47}$$

  where we use a linear description for the initial microlayer profile, for which an analytical solution exists, and where its slope C becomes a parameter of the

simulation:

$$\delta(r, t = 0) = \delta_0 + C\ r \tag{2.48}$$

with δ_0 the so-called absorbed layer thickness under which the microlayer can no longer evaporate because of long-range (Van Der Walls) molecular forces. δ_0 is orders of nanometers and has no effect on the resolution of the microlayer.

There are at least two methods to add the contribution from microlayer evaporation to the global bubble growth: (i) compute the evaporative mass flux directly as:

$$j_{v,k} = \frac{k_l \Delta T}{h_{fg} \delta_k} \tag{2.49}$$

and then integrate the flux over the whole microlayer surface area S, or (ii) compute the rate of decrease of the total microlayer volume $\dot{V}_{micro}$ (Eq. (2.46) integrated over the whole microlayer surface). Both methods are equivalent in meaning, but not in the calculation scheme. The second method is more convenient. To verify that the method is accurate, we tested its performance for the simple case of a constant wall superheat ΔT for which an analytical solution of Eq. (2.46) exists:

$$\delta(r, t) = \sqrt{\delta_0^2(r) - \frac{2 k_l \Delta T}{\rho_f h_{fg}} t} \tag{2.50}$$

which therefore allows for an analytical integration of Eq. (2.49). The numerical scheme computes the total microlayer volumes at each time step and then its rate of change during dt:

$$\dot{V}_{micro} = \frac{V_{micro}(t + \mathrm{d}t) - V_{micro}(t)}{\mathrm{d}t} \tag{2.51}$$

The evaporative mass flux is plotted as a function of time in Figure 2-12, where j_v is calculated from both analytical and numerical integration schemes (dt = $0.2ms$, dr = $12.5nm$). From the upper schemes implementation (trapezoidal

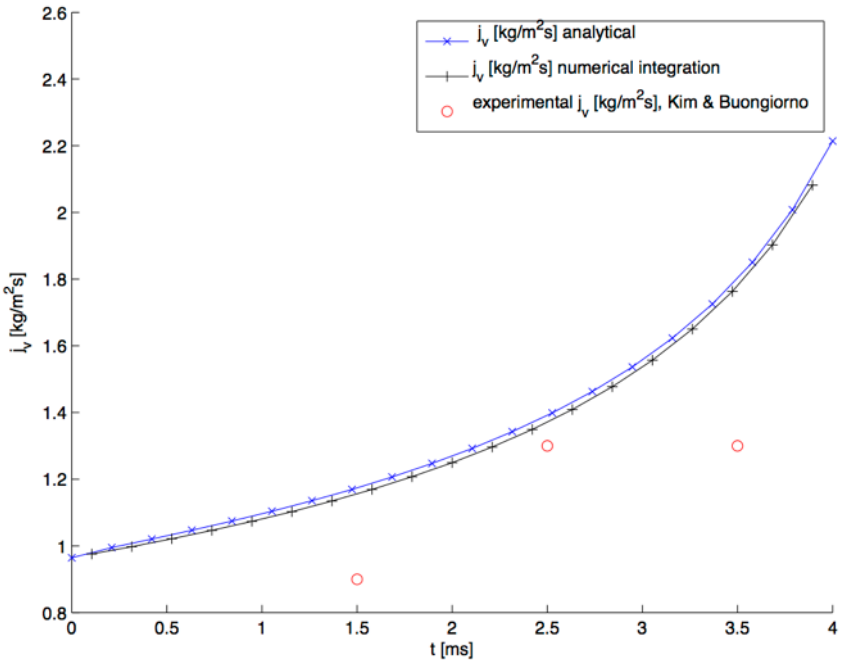

Figure 2-12: Evaporative mass flux as a function of time, calculated from both analytical and numerical integration schemes ($\mathrm{d}t = 0.2ms$, $\mathrm{d}r = 12.5nm$). Experimental results [51] are also plotted as reference to show consistent order of magnitude.

rule for integration) we expect a first order convergence of the results, also confirmed by the mesh convergence study reported in Figure 2-13.

- Subgrid model implementation in TransAT ensures fine resolution of microlayer evaporation at the subgrid scale. Specific tests follow.

  The subgrid model for microlayer evaporation locally couples microlayer thickness with wall temperature. It requires declaring and manipulating two arrays storing those two variables at the wall. For a typical mesh size of $50\mu m$ used in boiling simulations, the microlayer thickness varies significantly. We therefore allow the subgrid implementation to define subgrid points within each existing TransAT cell at the wall. The algorithm is described in Figure 2-14: variables are loaded at mesh cells located at the wall. Each cell from TransAT is divided into subcells. For all subcells, wall temperature and microlayer thickness from the previous time step (or the initialization step) are used to compute a

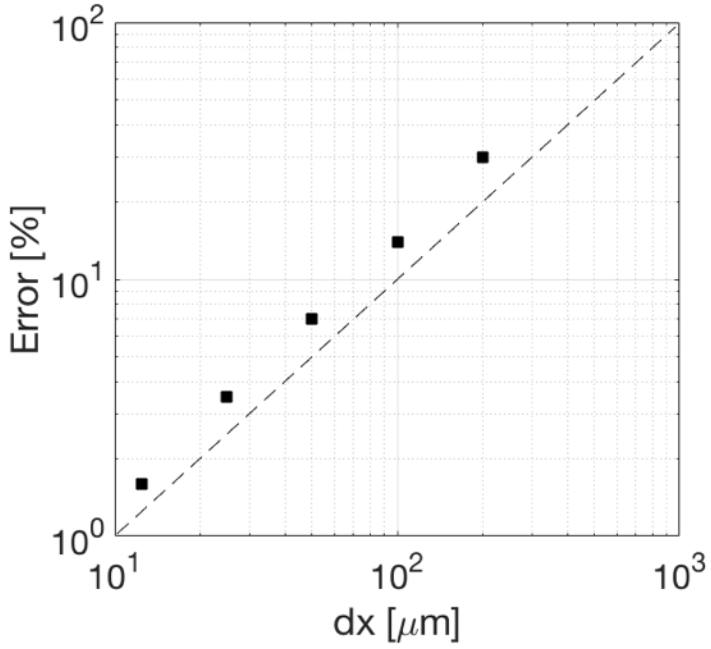

Figure 2-13: Mesh convergence of the numerical integration scheme proposed to compute

local evaporative mass flux and update microlayer thickness. Summing up all subcells evaporative mass flux over one TransAT cell provides an estimate of the average mass flux in that TransAT cell at the wall. The solver ensures the conservation of energy, and the wall temperature is updated before going to the next time step. Actual user-defined functions used are provided in Appendix A. We then test the implementation of the model. All of the three cases rely on the boundary conditions shown in Figure 2-15, to reproduce saturated pool boiling conditions. For simplicity, the temperature at the wall surface is fixed at a given superheat of 10K.

- Specific tests: simulations with initial liquid microlayer of linear shape validate the implementation of the subgrid model accounting for microlayer evaporation in the case of constant wall superheat for which an analytical solution exists. We initialize the shape of the liquid microlayer to be linear, with a thickness varying from $1.7nm$ up to $500nm$, and extending from the bubble root ($r = 0$) up to a radial distance of $500\mu m$ (the slope $C = 0.001$ [-]). Reference properties

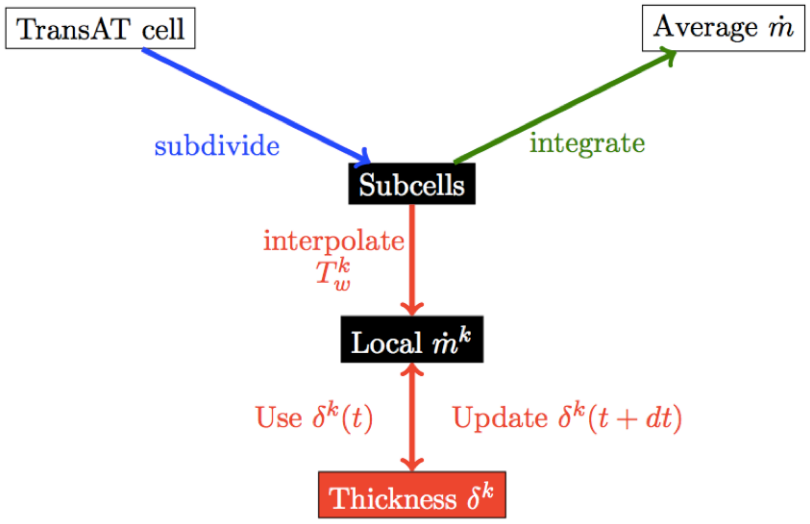

Figure 2-14: Sketch of the implementation scheme for the microlayer evaporation model as a subgrid model in TransAT.

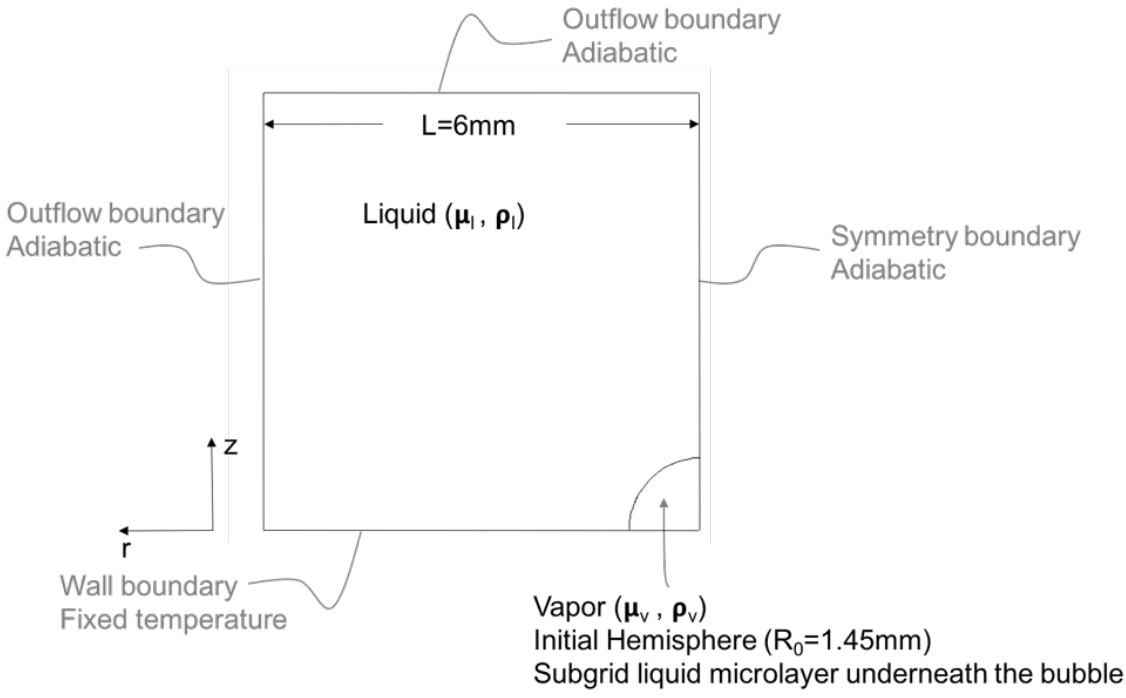

Figure 2-15: Sketch of the computational domain and boundary condition to test the subgrid implementation.

Table 2.1: Reference properties of the nucleate boiling simulations performed

Properties	Water	Steam
$\rho\ (kg/m^3)$	958	0.6
$\mu\ (Pa.s)$	2.8e-4	1.2e-5
$\lambda\ (W/mK)$	0.681	0.025
$c_p\ (J/kgK)$	4218	2034
$h_{fg}\ (J/kg)$	$2.257e+6$	
$T_{sat}\ (K)$	373.15	
$T_n\ (K)$	382.15	
$\sigma\ (N/m)$	0.059	
$g\ (m/s^2)$	9.81	
$R_0\ (\mu m)$	100	

of the nucleate boiling simulations presented in this section and next, including fluid properties, are given in Table 2.1.

Such thin layer completely evaporates within $0.04ms$. The simulated time evolution of the thickness matches the analytical prediction, as shown in Figure 2-16: perfect agreement is shown for example at half time to dry-out (simulation is in green, analytical solution is in black). In Figure 2-16, the simulated profile using only 1 single subgrid point per TransAT cell is able to recover the microlayer geometry, except in the bended region of lowest thickness. A coarse resolution in microlayer geometry results in a coarse estimate of the actual evaporative mass flux. Based on the numerical scheme we chose to integrate the actual microlayer volume at a given time step, such coarse resolution results in an over estimation of the actual evaporative mass flux, as illustrated in Figure 2-17: in the case of a coarse subgrid discretization (1 subgrid point per TransAT cell, in magenta), a higher equivalent bubble radius is obtained - more vapor was fueled from the subgrid microlayer to the macroscopic bubble. Finer subgrid resolution of the microlayer geometry (100 subgrid points per TransAT cell, in grey) allows to better capture the evaporative mass flux that comes from the subgrid microlayer evaporation.

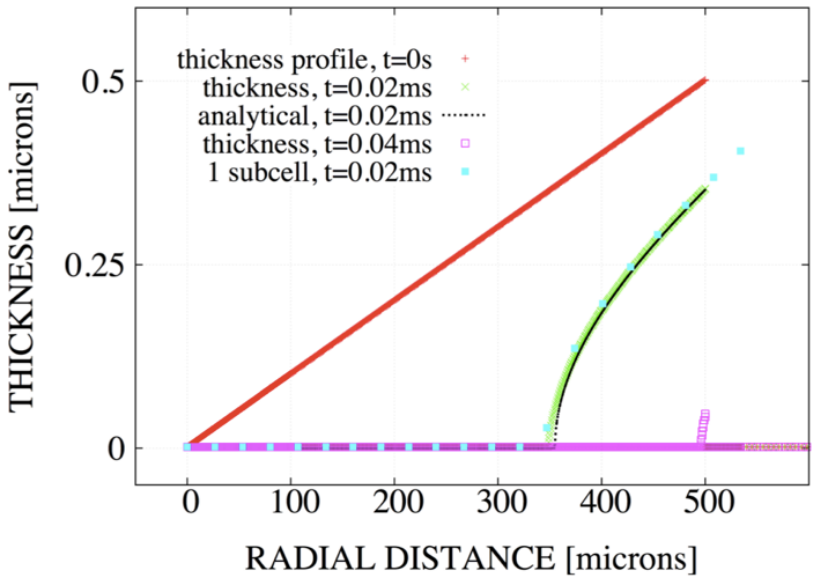

Figure 2-16: Plot of microlayer thickness profiles simulated using 100 subgrid points per TransAT cell at the wall: initially at t=0ms (in red), right before dry-out at $t = 0.04ms$ (in magenta), and half time to dry-out at $t = 0.02ms$ (in green). A constant wall superheat is imposed at $10K$. An analytical solution exists and is plotted for comparison at half time to dry-out (in black). Also at half dry-out is plotted (in light blue) with dots the simulated profile using only 1 single subgrid point per TransAT cell.

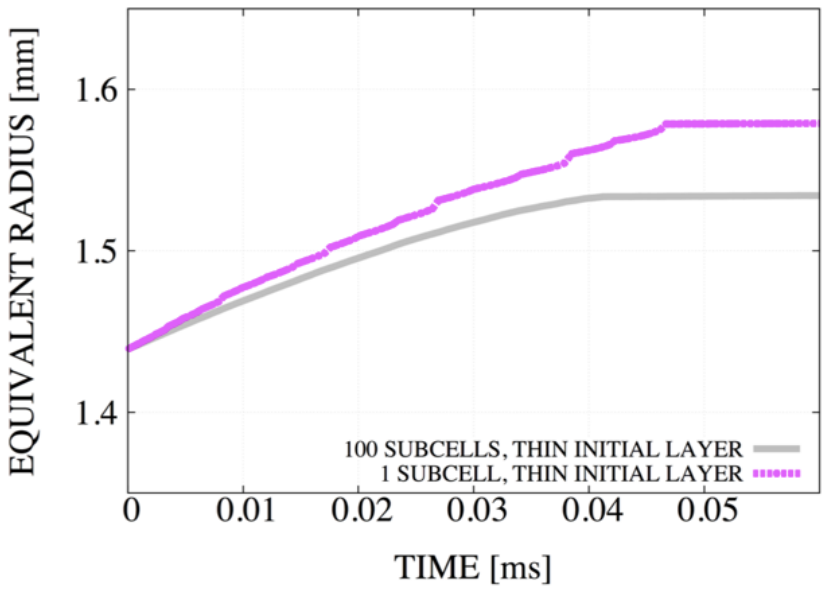

Figure 2-17: Plot of equivalent bubble radius as a function of time comparing the use of 1 subgrid point per TransAT cell (in magenta) and 100 subgrid points per TransAT cell (in grey) are used.

2.6.4 Sensitivity study on initial microlayer shape and its effect on initial bubble growth rates

We now proceed to two sensitivity tests: the first test at fixed extension radius but varying slopes C, hence varying liquid volumes, and the second test at fixed liquid volume but varying slopes and extension radius.

Simulations with initial microlayers of fixed extension radius but varying slopes show strong dependence of initial bubble growth rate with initial shape of the microlayer. We perform two simulations of nucleate boiling for which we initialize the shape of the liquid microlayer to be linear, with an extension radius of $500\mu m$, and slopes C of 0.001 and 0.004, respectively - see Figure 2-18. Simulated equivalent radius are plotted as a function of time in Figure 2-19: the change in slope corresponds again to the change of dominant evaporation mode driving bubble growth, from rapid growth due to microlayer evaporation to slow growth due to evaporation at the bubble cap only after microlayer dry-out. Analytical predictions

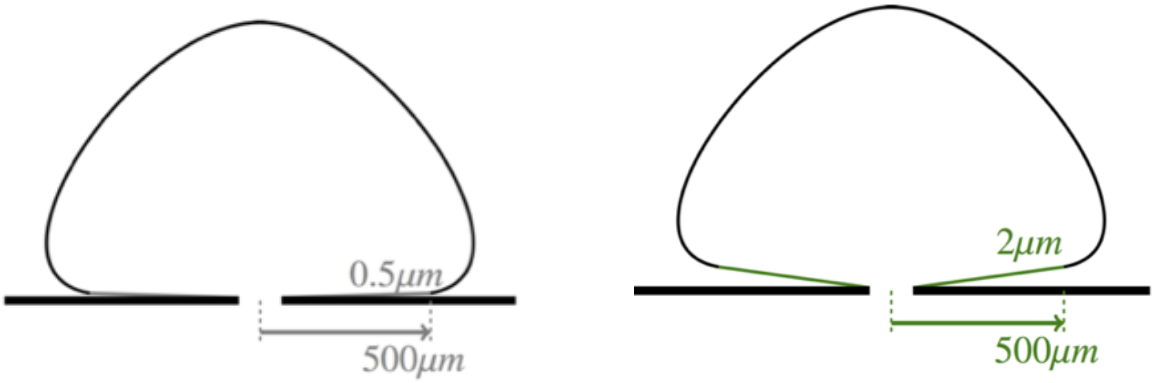

(a) (b)

Figure 2-18: Sketch (not at scale) of initial microlayer profile characteristics used in the used to test the sensitivity of initial bubble growth rates with microlayer shapes at fixed extension radius. Linear profiles extending from $1.7nm$ up to $500nm$ (a) and $2\mu m$ (b) from the bubble root up to a radial distance of $500\mu m$ (slopes C of 0.001 and 0.004 respectively).

of times of dry-out ($0.04ms$ and $0.63ms$, respectively) for the two layers, computed from:

$$t_{dryout} = \rho_l h_{fg} \frac{(\delta_0 + Cr_{max})^2}{2k_l \Delta T} \tag{2.52}$$

are added to the plot to show perfect agreement between simulated and analytical microlayer behaviors in the case of constant wall superheat - see Figure 2-19. Note in Figure 2-19 that analytical predictions of times of dryout are also indicated for reference. The abrupt change in bubble growth rates at this particular dryout time indicates the complete evaporation (dryout) of the initial liquid microlayer. Past this dryout, bubble growth is only fueled by mass transfer across its macroscopic interface, and its growth rate is significantly diminished. In addition, and as expected, the thinner layer evaporates more rapidly - the conduction heat flux through the layer being proportional to the inverse of the liquid thickness, hence the evaporation from the thinner layer fuels bubble growth more intensively than the thicker layer, as illustrated in the presented results by the increased initial bubble growth rate in the thinner layer case. However, at fixed extension radius, the volume of liquid in the thinner layer is much less than in the thicker layer, and the thinner layer dries out sig-

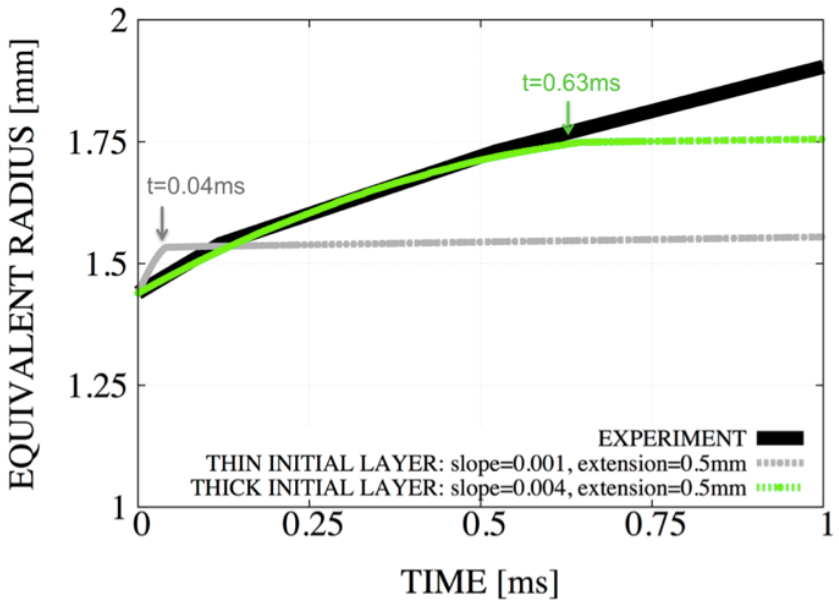

Figure 2-19: Plot of equivalent bubble radius as a function of time. The wall superheat is maintained constant ($10K$). Two initial shapes of microlayer with different slopes C, 0.001 (in grey) and 0.04 (in green), respectively, but with similar extension radius of $500\mu m$, and 100 subgrid points per TransAT cell. Experimental result is also plotted for reference (black line) [24]. Analytical prediction of times of dryout are also indicated for reference. The abrupt change in bubble growth rates indicate the dryout of the initial liquid microlayer. Past this dryout, bubble growth is only fueled by mass transfer across its macroscopic interface.

nificantly faster: within $0.04ms$ (vs. $0.63ms$ for the thicker case). Also note that the thicker layer proposed is able to reproduce experimental bubble growth rates. Once the liquid microlayer is fully evaporated, the only mechanism fueling bubble growth is the mass transfer at the bubble cap, which fuels bubble growth at a significantly lower rate. Lastly, these results are obtained at fixed wall temperature and do not take into account the cooling of the wall due to microlayer evaporation. A conjugate heat transfer simulation is expected to show a slowdown in microlayer evaporation due to a local decrease of the wall superheat in the vicinity of the contact line where the microlayer thickness is the smallest, and where the evaporation heat flux is the highest.

Simulations with initial microlayers of fixed volumes but varying slopes (and extension radius) confirm strong dependence of initial bubble growth

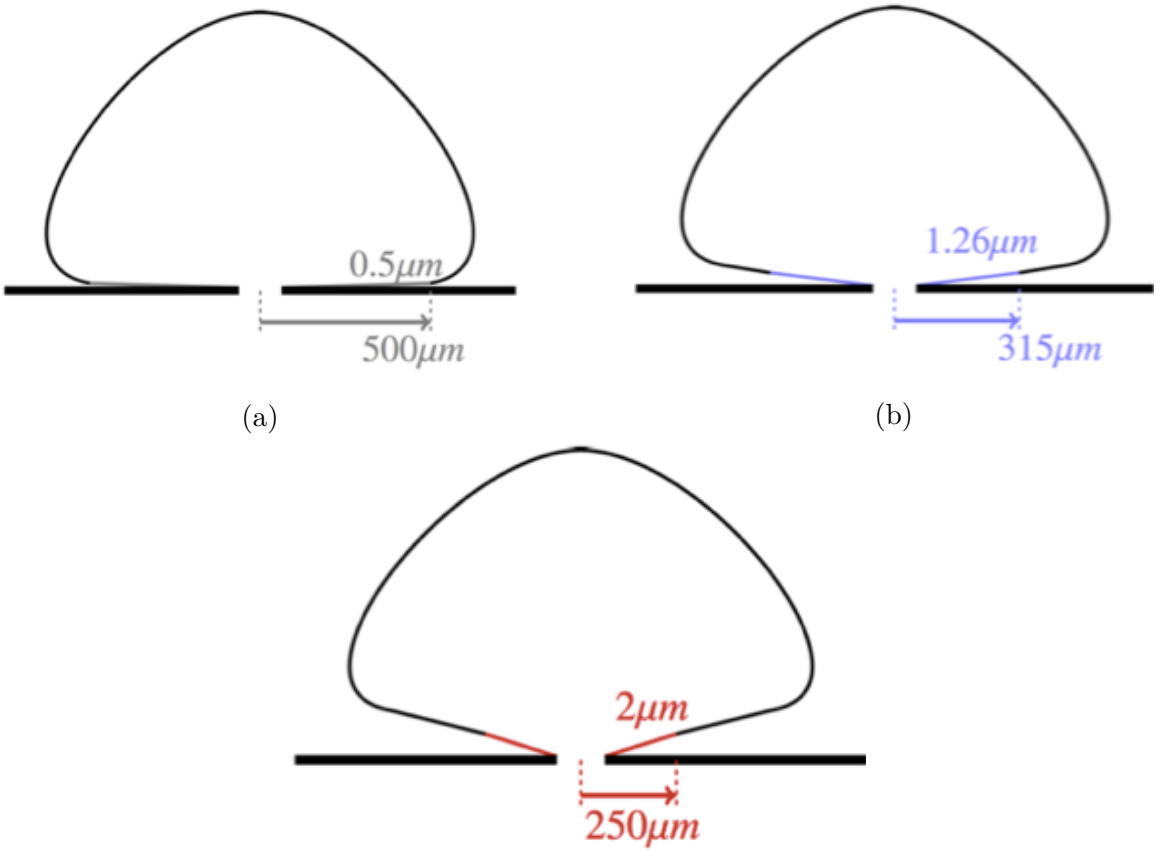

Figure 2-20: Sketch (not at scale) of initial microlayer profiles with fixed volumes but varying slopes C: 0.001 (a), 0.004 (b) and 0.008 (c).

rate with initial shape of the microlayer. We perform three simulations of nucleate boiling for which we initialize the shape of the liquid microlayer to be linear, with different slopes C: 0.001, 0.004 and 0.008, respectively, but same volumes. We adjust the extension radius of the initial liquid microlayer to ensure same volume of liquid is initialized at the subgrid scale - see Figure 2-20. Analytical predictions of times of dry-out (0.04ms, 0.25ms and 0.63ms, respectively) for the three cases of increasing slopes are added to the plot of equivalent radius as a function of time in Figure 2-21, and show perfect agreement between simulated and analytical microlayer behaviors in the case of constant wall superheat. The plot also shows identical contribution to bubble growth from all three microlayers, as their identical initial liquid volume

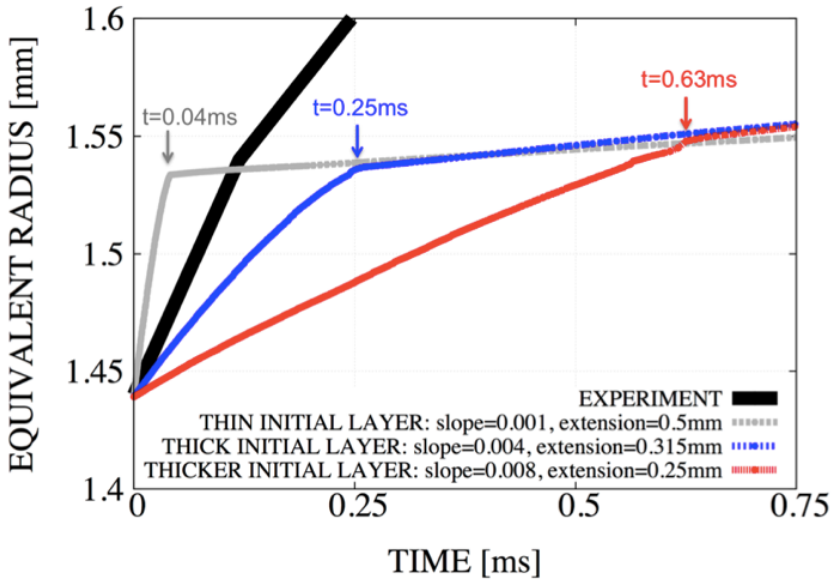

Figure 2-21: Plot of equivalent bubble radius as a function of time. The wall superheat is maintained constant ($386K$). Three initial shapes of microlayer with different slopes C, 0.001 (in grey), 0.04 (in blue) and 0.008 (in red), respectively, but with same volume, and 100 subgrid points per TransAT cell. Experimental result is also plotted for reference (black line) [24]. Analytical prediction of times of dryout are also indicated for reference. The abrupt change in bubble growth rates indicate the dryout of the initial liquid microlayer. Past this dryout, bubble growth is only fueled by mass transfer across its macroscopic interface.

provides an identical volume of vapor to the bubble. The different initial shape affects growth rates: a thinner microlayer evaporates faster than a thicker one due to inverse dependence of conduction heat flux to the layer thickness.

2.7 Relative importance of microlayer evaporation in total wall heat transfer and bubble growth dynamics

2.7.1 A general figure of merit

During one boiling cycle, the liquid microlayer evaporates at the wall, extracting an energy E_{micro} defined as:

$$E_{micro} = \rho_l V_{ml} h_{fg} \tag{2.53}$$

with ρ_l the liquid water density, V_{ml} the liquid microlayer volume (see next chapter), and h_{fg} the latent heat. While the boiling cycle lasts t_{cycle} defined as:

$$t_{cycle} = 1/f \tag{2.54}$$

with f the bubble departure frequency, a total energy E_{tot} is transferred though the wall and to the liquid:

$$E_{tot} = q^{''} A_{bubble} t_{cycle} \tag{2.55}$$

with $q^{''}$ the wall heat flux, and $A_{bubble} = \pi(D_w/2)^2$ the area underneath the bubble, and D_w the bubble departure diameter. The dimensionless ratio E^*:

$$E^* = \frac{E_{micro}}{E_{tot}} = \frac{\rho_l V_{ml} h_{fg}}{q'' A_{bubble} t_{cycle}} \tag{2.56}$$

quantifies the relative importance of microlayer evaporation in wall heat transfer where boiling occurs. We here make no assumption on the coupling between heat flux and bubble departure frequency, and calculate the dimensionless ratio E^* for a wide range of heat fluxes and bubble departure frequencies - see Figure 2-22, for a typical superheat of 10K, and no subcooling. We conclude that microlayer evaporation can be a dominant component of wall heat heat transfer when:

- boiling cycles are short (see solid line in Figure 2-22: $f = 200\ (1/s)$, $t_{cycle} =$

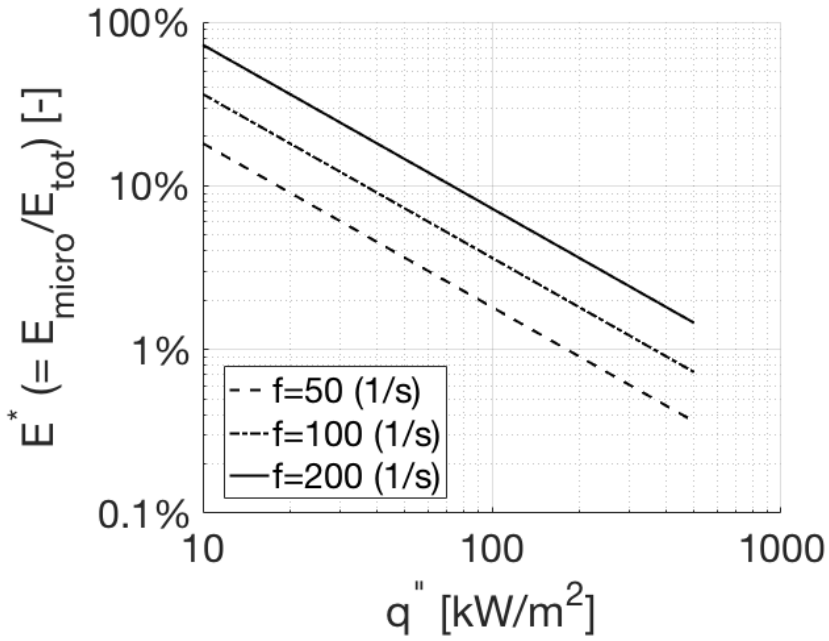

Figure 2-22: Plot of the dimensionless ratio $E^* = E_{micro}/E_{tot}$, defined as the ratio between the total energy extracted from the wall to evaporate the liquid microlayer, and the total energy transferred at the wall underneath the bubble during one boiling cycle. The ratio is plotted for a wide range of heat fluxes $q" \in [10;\ 500]$ (kW/m^2), and various bubble departure frequencies $f \in \{50,\ 100,\ 200\}$. A typical superheat of 10K and no subcooling are assumed.

$5ms$)

- heat fluxes are low: most of the energy available at the wall is then captured by the evaporation of the liquid microlayer

Conversely, we conclude that microlayer evaporation can be a relatively small component of wall heat heat transfer when:

- boiling cycles are long (see dashed line in Figure 2-22: $f = 50\ (1/s)$, $t_{cycle} = 20ms$)

- heat fluxes are high (see $q" \geq 100kW/m^2$ in Figure 2-22): the total energy available at the wall during t_{cycle} is increased while the energy captured by the evaporation of the liquid microlayer remains the same, hence reduction in E^*.

Lastly, note that one can extend the results presented here to a broader A_{bubble} noted $A_{bubble,2}$ defined across the wall surface:

$$A_{bubble,2} = 1/N_{site} \tag{2.57}$$

with N_{site} the nucleation site density (in $1/m^2$). As a result, the ratio E_2^* considered across the wall surface can be written as:

$$E_2^* = E^* \frac{A_{bubble}}{A_{bubble,2}} = N_{site} A_{bubble} E^* \tag{2.58}$$

For low nucleation site densities, $\frac{A_{bubble}}{A_{bubble,2}} << 1$ and $E_2^* << E^*$. In contrast, for large nucleation site densities $\frac{A_{bubble}}{A_{bubble,2}} \sim 1$ and $E_2^* \sim E^*$. Correlations for N_{site} and t_{cycle}, as functions of heat flux and subcooling for example, can be used in the proposed model here, to conclude on exact contributions to total wall heat transfer at the scale of one bubble (E^*), or at the scale of the entire surface (E_2^*).

2.7.2 A comparative study of microlayer evaporation contribution for the cases of water and refrigerant FC-72 at 0.101MPa.

Gerardi [32] concludes from his experimental measurements in pool boiling conditions that the contribution of microlayer evaporation to overall heat transfer and bubble growth can be large in the case of water at 0.101MPa, while Kim [52] concludes that the contribution can be small in the case of refrigerant FC-72 at 0.101MPa. In Table 2.2, we gather relevant saturation properties of the two fluids (water and FC-72) at 0.101MPa. The range of wall superheats: 1K-10K is representative of boiling of both water [32] and FC-72 [75]. In the next chapter, we provide a general model for the shape of the liquid microlayer. We here use that model to compute the ranges of slopes C of the microlayer for both fluids, FC-72 and water. A bubble radius $R_b = 0.5mm$ is representative of boiling in lab conditions. We obtain similar microlayer slopes for

Table 2.2: Water and FC-72 saturation properties at 0.101MPa

Properties at saturation / Fluids	FC-72	Water
T_{sat} (°C)	56	100
Liquid dynamic viscosity (kg/ms)	0.45e-3	0.28e-3
Liquid density (kg/m^3)	1620	958
Vapor density (kg/m^3)	13.01	0.6
Density ratio ρ_l/ρ_v (-)	0.12e3	0.16e4
Latent heat (J/kg)	0.85e5	0.22e7
Liquid thermal conductivity (W/mK)	0.54e-1	0.6

Table 2.3: Slopes C of FC-72 and water microlayers at 0.101MPa, for representative wall superheats of 1K and 10K.

Fluid / ΔT	$\Delta T = 1K$	$\Delta T = 10K$
FC-72	$C = 0.012$ $(-)$	$C = 0.007$ $(-)$
water	$C = 0.011$ $(-)$	$C = 0.006$ $(-)$

both fluids, see Table 2.3. This results can be anticipated as FC-72 and water have similar liquid viscosity and density, and similar growth rates. Details regarding the model and how to use it can be found in the next chapter. For a range of typical microlayer shapes, namely slopes in 0.001, 0.010 [-], and a typical extension radius of $0.500mm$, we calculate three figures of merit to assess the contribution of microlayer evaporation to overall heat transfer and bubble growth for both fluids at 0.101MPa:

1. Duration t_{dryout} of microlayer evaporation until it dries out, in (s), defined in Eq. (2.52)

2. Volume V_{ml} of vapor fueled from the evaporation of the liquid microlayer to the bubble, in (m^3), defined in Eq. (2.1)

3. Average heat flux $< Q" >$ in (W/m^2) at the wall due to microlayer evaporation (averaged throughout the duration of the evaporation t_{dryout} and over the initial evaporating surface S_{micro} of the liquid microlayer of initial volume V_{micro} defined as:

$$< Q" >= \frac{\rho_l \, V_{micro} \, h_{lv}}{S_{micro} \, t_{dryout}} \tag{2.59}$$

For the range of microlayer slopes considered here - see Table 2.3, we compute all three figures of merit - see Table 2.4:

1. Liquid microlayers of water and FC-72 evaporate within similar time scales tdryout, given same initial superheat and shape. The ratio of their respective time scales in the cases studied here is found to be 1.4, e.g. of the order of unity.

2. Liquid microlayers of water contribute much more than liquid microlayers of FC-72 to overall bubble growth: the ratio of the respective volumes of vapor generated throughout the evaporation of the microlayer, which fuels bubble growth, is found to be 12.8, which 1) reveals an order of magnitude difference between water and FC-72 results in the cases studied here. Another way to present this result is to note that the ratio of average vapor production rates $< \frac{\mathrm{d}V_{ml}}{\mathrm{d}t} >$ defined as:

$$< \frac{\mathrm{d}V_{ml}}{\mathrm{d}t} >= V_{ml}/t_{dryout} \tag{2.60}$$

   between the two fluids is of the order of 10, which reveals that liquid water microlayers fuel bubble growth much faster than FC-72 liquid microlayer, while the duration of evaporation for both fluids is of same order of magnitude.

3. Liquid microlayers of water contribute much more than liquid microlayers of FC-72 to overall heat transfer at the wall underneath bubbles: the ratio of the respective averaged wall heat fluxes in the cases studied here is found to be 11.1, which reveals an order of magnitude difference between water and FC-72 results.

In the previous subsection 2.6.4, we conclude that simulations of saturated nucleate boiling of water at 0.101MPa reveal that microlayer evaporation contribute significantly to overall heat transfer and bubble growth. In this section, the comparative study shows that fluid properties control the extent of the contribution of microlayer evaporation to overall heat transfer and bubble growth, and in particular, that liquid microlayers of FC-72 are expected to contribute much less to wall heat transfer and bubble dynamics than liquid microlayers of water at 0.101MPa. These

Table 2.4: Comparison of the contribution of microlayer evaporation to overall heat transfer and bubble growth between water and FC-72 at 0.101MPa. A typical initial superheat of 10K is assumed for both fluids.

		Microlayer shape (slope C, radius $0.5mm$)	
Figure of merit	Fluid	C=0.001	C=0.01
t_{dryout}	water	0.04 (ms)	4.4 (ms)
	FC 72	0.03 (ms)	3.3 (ms)
	ratio	**1.4 (−)**	**1.4 (−)**
V_{ml}	water	0.42 (mm^3)	4.2 (mm^3)
	FC 72	0.03 (mm^3)	0.33 (mm^3)
	ratio	**12.8 (−)**	**12.8 (−)**
$< Q" >$	water	16 (MW/m^2)	1.6 (MW/m^2)
	FC 72	1.4 (MW/m^2)	0.14 (MW/m^2)
	ratio	**11.1 (−)**	**11.1 (−)**

results are consistent with experimental conclusions from Gerardi [32] and Kim [52].

2.8 Conclusions

Numerical simulations of single bubble growth in nucleate pool boiling represent a simplified first step towards modeling and simulating the complex industrial scenario of subcooled flow boiling in pressurized water reactors. In particular, we focus on the simulation of a single vapor bubble growing at a heated wall, under saturated pool boiling conditions at atmospheric pressure.

Our results confirm the strong sensitivity of simulated bubble growth rates with initial microlayer shape and extension in boiling simulations. This conclusion motivates the next section, which aims at bridging the current gap in modeling microlayer formation.

Chapter 3

Direct computations of bubble growth hydrodynamics at a wall and microlayer formation

3.1 Problem statement and dimensional analysis

We consider the first tens to hundreds of microseconds of growth of a steam bubble which expands at a rate U_b near the wall of a pool of initially stagnant liquid. We take advantage of the symmetry of the growth and consider the problem to be axisymmetric. Ten physical variables are involved in describing the hydrodynamics of microlayer formation:

- μ_l, μ_v: liquid and vapor viscosities, resp.
- ρ_l, ρ_v: liquid and vapor densities, resp.
- σ: surface tension
- U_b: bubble growth rate, the velocity at which the liquid vapor interface moves into the surrounding liquid
- θ_{dx}: microscopic contact angle at scale dx, between the liquid vapor interface and the wall, and at a given reference length scale dx.

- r: radial distance from bubble root
- t: time
- δ: unknown local thickness of the liquid microlayer forming at the wall

Altogether, these ten variables involve three physical dimensions: mass, length, and time. Therefore, we obtain that 10-3=7 dimensionless Pi-groups that can fully describe the microlayer formation. The seven proposed dimensionless Pi-groups are:

$$\Pi_1 = \delta/r_c = \delta^* \tag{3.1}$$

$$\Pi_2 = \mu_l/\mu_v \tag{3.2}$$

$$\Pi_3 = \rho_l/\rho_v \tag{3.3}$$

$$\Pi_4 = r/r_c = r^* \tag{3.4}$$

$$\Pi_5 = t/t_c = t^* \tag{3.5}$$

$$\Pi_6 = \theta_{\mathrm{dx}} \tag{3.6}$$

$$\Pi_7 = Ca = \mu_l U_b/\sigma \tag{3.7}$$

$$\tag{3.8}$$

where the intrinsic reference length and time scales r_c and t_c were defined as follows:

$$r_c = \sigma/(\rho_l U_b^2) \tag{3.9}$$

$$t_c = r/U_b = \sigma/(\rho_l U_b^3) \tag{3.10}$$

Buckingham's Pi Theorem [10] ensures that such Pi-groups are related by a unique functional form, which can be written as follows:

$$\delta/r_c = f(\mu_l/\mu_v, \rho_l/\rho_v, r/r_c, t/t_c, Ca, \theta_{\mathrm{dx}}) \tag{3.11}$$

In this study we have performed numerical simulations of microlayer formation to quantify the above function. In Table 3.1, we report the relevant parameter space for

Application / $\Pi - group$	μ_l/μ_v	ρ_l/ρ_v	Ca	θ_{dx}
Lab experiment (water, 0.101 MPa)	23.3	1650	0.005-0.1	0-90°
Pressurized Water Reactors (water, 15.5 MPa)	3.2	5.9	0.001-0.1	0-90°

Table 3.1: Parameter space for the conditions of interest

liquid water boiling in lab and industrial conditions (Pressurized Water Reactors, or PWR). This parameter space is discretized as shown in Table 3.2 gathering parameters of all simulations presented in this paper. The range of capillary number Ca is obtained from water properties at saturation (μ_l and σ) for both pressures, and estimates of bubble growth rates U_b from [71], including a range of cavity mouth radius r_b:

$$U_b = \sqrt{\pi h_{fg} \rho_v \Delta T_{sat} / (7 \rho_l T_{sat})} \tag{3.12}$$

where ΔT_{sat} is the so-called wall superheat at the inception of boiling:

$$\Delta T_{sat} = 2\sigma T_{sat} / (r_b \rho_v h_{fg}) \tag{3.13}$$

3.2 Computational framework

3.2.1 Gerris Flow Solver

A myriad of methods are available today to simulate two phase flow while tracking the interface between two fluids: Lagrangian moving mesh methods, Eulerian methods and Lagrangian/Eulerian methods - see review in Figure 3-1 [50]. The Volume-Of-Fluid (VOF) method and the Level-Set methods have been predominantly used and tested in the literature. The VOF method [93] tracks the interface using a color function C that represents the volume fraction of one phase in each cell of the

Table 3.2: Summary of simulation parameters for all results presented in this work.

SET UP	Side L [μm] of domain (LxL)	Initial bubble radius [μm]	Reference length and time scales (r_c [μm], tc [μs])	Finest mesh size dx_{micro} [μm]	Coarsest mesh size dx_{macro} [μm] (at the interface	Coarsest mesh size dx_{coarse} [μm] (away from the interface)	μ_l/μ_v [-]	ρ_l/ρ_v [-]	Ca [-]	t* [-]	θ_{dx} [°] (dx_{micro})
A	512	32	(1, 1)	(0.25, 0.5, 1.0, 2.0)	(0.25, 0.5, 1.0, 2.0)	16	2	2	5.000	2	N/A
B	128	10	(0.32, 0.07)	(1/32, 1/16, 1/8, 1/4)	(1, 1, 1, 1)		3.2	5.8	0.080	0-1E2	10
C				(1/4, 1/4, 1/4)	(1/4, 1/2, 1)						
D				(1/32, 1/16, 1/8, 1/4)	(1,1,1,1)					0-5E3	10, 15, 20, 25, 30, 35, 40, 45, 50, 55, 60, 65, 70, 75
E											18.5, 20.5, 22.0, 23.5
F	64	5	(0.32, 0.07)	1/4	1	1	(3.2, 23.3, 3.2, 3.2)	(5.8, 5.8, 1650, 5.9)	1.000	0-1E2	50
G	500	6.4	(0.1, 0.05)	0.1	0.4	3.2	23.3	5.8	(0.200, 0.020)	0-5E3	(25, 85)
H									(0.002, 0.004, 0.008, 0.01, 0.02, 0.04, 0.08, 0.1, 0.2, 0.4, 0.8, 1.0)		20, 25, 30, 35, 40, 45, 50, 55, 60, 65, 70, 75, 80, 85
I									(0.002,		90
J									0.004,		40, 60, 80
K									0.006, 0.008, 0.01, 0.02, 0.04,		30, 35, 40, 45, 50, 55, 60, 65, 70, 75, 80, 85, 90
L									0.06, 0.08, 0.1, 0.2, 0.4, 0.6, 0.8, 1.0)		90
M	768	16	(1, 0.2)	1/32	1	8			(0.001 0.002 0.003 0.004 0.005 0.006 0.007 0.008 0.009 0.01 0.02 0.03 0.04 0.05 0.06 0.07 0.08 0.09 0.1)	0-200	10

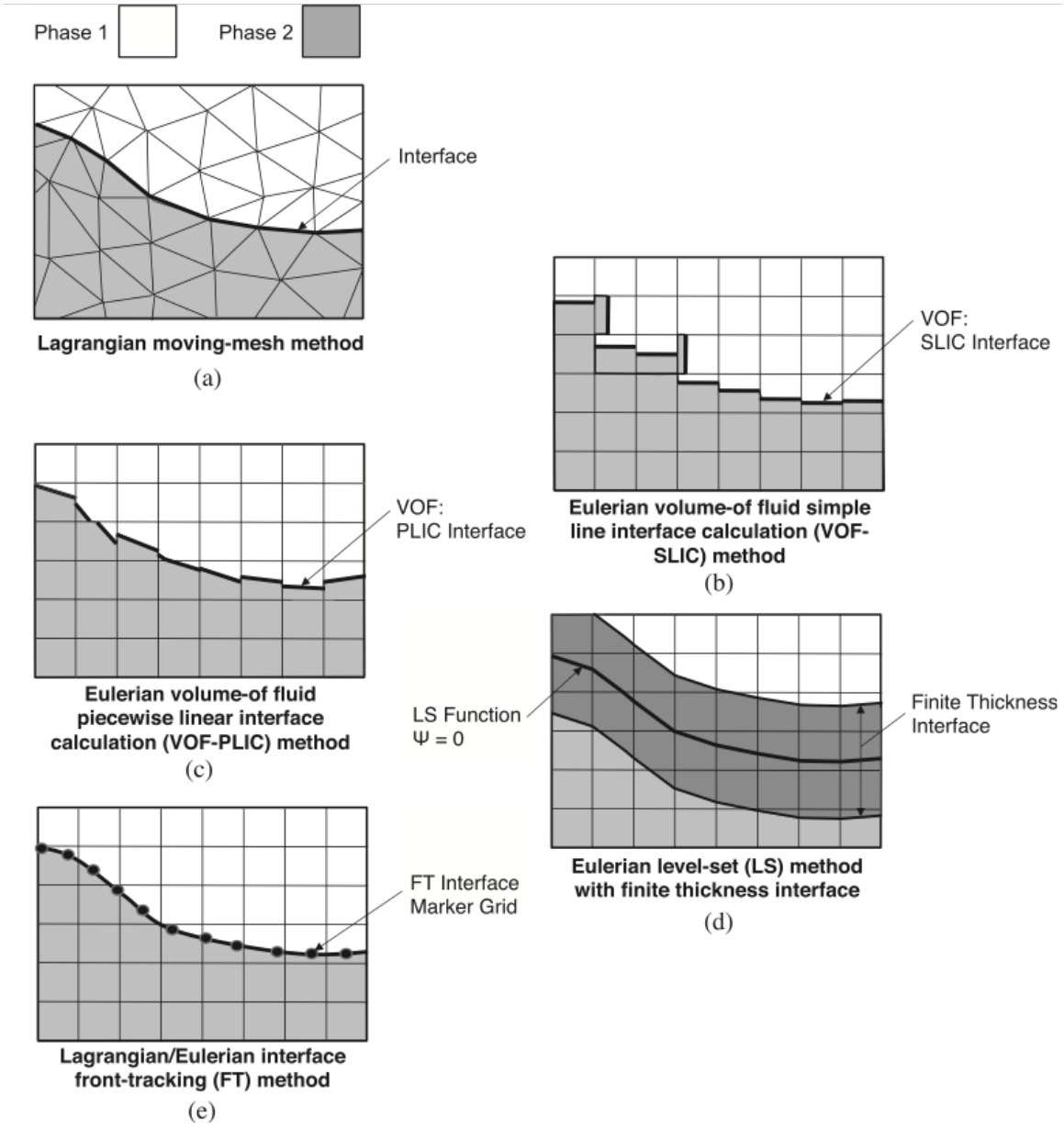

Figure 3-1: Review of interface tracking methods used in two-phase flow simulations [50]

computational domain. Starting from an initial distribution, the color function C is then advected by the flow:

$$\partial C/\partial t + \vec{u}.\nabla C = 0 \tag{3.14}$$

No mass transfer at the interface is considered. Interface reconstruction schemes such as the Simple Line Interface Calculation (SLIC) [82] or the Piecewise Linear Interface Calculation (PLIC) [117] allow capturing the interface sharply. The Gerris Flow Solver [85] (gfs.sourceforge.net/) solves the incompressible Navier-Stokes equations, and implements the VOF method to track the interface and compute the surface tension force:

$$\rho(\partial\vec{u}/\partial t + \vec{u}.\nabla\vec{u}) = -\nabla P + \nabla.(2\mu\bar{\bar{D}}) + \sigma\kappa\delta_s\vec{n} + \vec{F}_{external} \tag{3.15}$$

$$\partial\rho/\partial t + \nabla.(\rho\vec{u}) = 0 \tag{3.16}$$

$$\nabla.\vec{u} = 0 \tag{3.17}$$

With:
$D_{ij} = 1/2(\partial u_j/\partial x_i + \partial u_i/\partial x_j)$,
$\rho = C\rho_1 + (1-C)\rho_2$,
$\mu = C\mu_1 + (1-C)\mu_2$

$$\partial C/\partial t + \nabla.(C\vec{u}) = 0 \tag{3.18}$$

The computational domain in Gerris is spatially discretized using quad/octrees, which allows refining specific regions in space while coarsening others. In this work, we typically refine in the vicinity of the wall and at the interface to resolve microlayer formation, while coarsening away from the wall and the bubble interface where such refinement is not necessary.

3.2.2 Simulation strategy

Assumptions made in this work

In this work, we focus on the initial rapid phase of bubble growth that lasts tens of microseconds and during which the microlayer forms at the wall, over hundreds of microns in radial extension (typical bubble growth rates: 5-10 m/s in lab experiments with water). In particular, we only consider the hydrodynamics of microlayer formation, and neglect thermal effects. Part of the liquid layer that forms at the wall may also evaporate during such short time scale, hence affecting its shape over time. Based on a typical wall superheat at the wall of 10K observed experimentally at atmospheric pressure, we evaluate the relative change in liquid layer thickness due to evaporation from pure conduction through the liquid layer, for various growth times, and various layer thicknesses - see Figure 3-2. For typical growth rates of 5-10m/s, relevant growth times are in the range of 25 to 50μs to obtain extension radiuses in the range of 100-500μm. The extended microlayer is typically reported with a thickness of the order of 1-5 μm. Based on evaporation from pure conduction during such time scales, 10% or less of the thickness of the extended microlayer would be affected. Therefore, thermal effects, including the effect of mass transfer, on the motion of the contact line at short time scales - see for example [87], are not included in the scope of the present work. Mesh dependence of moving contact lines simulations with grid size [74], [112], [3] is reported elsewhere [1].

Time-dependent volumetric source of vapor in the vapor phase

We include a time-dependent volumetric source of vapor within the vapor phase to reproduce the growth observed in lab experiments. The source of vapor fuels bubble growth uniformly inside the bubble, and pushes the macroscopic liquid vapor interface at the desired rate U_b, hence reproducing the hydrodynamics of hemispherical bubble growth at the wall. A time-dependence of the source is necessary to reproduce the sustained growth of the bubble as its volume increases. For a given constant bubble growth rate U_b ($U_b = dR_b/dt$) during the initial inertia-controlled phase of

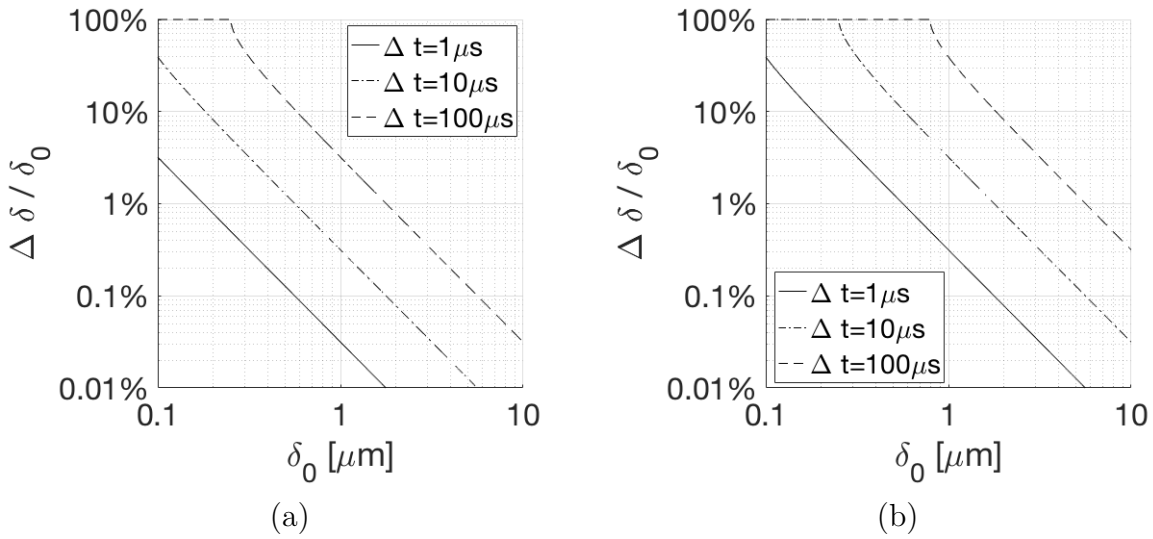

Figure 3-2: Fraction of microlayer thickness [%] that evaporates, for various growth times: $1\mu s$ (solid line), $10\mu s$ (dash-dotted line), $100\mu s$ (dashed line), and various layer thicknesses δ_0 (x-axis). The wall superheat is fixed to typical values of 1K (a) and 10K (b).

bubble growth, one can compute the volumetric growth rate dV_b/dt of the equivalent hemispherical bubble as follows:

$$dV_b/dt = 2\pi R_b^2(dR_b/dt) = 2\pi R_b^2 U_b \tag{3.19}$$

The rate of change of the equivalent hemispherical bubble dV_b/dt is obtained by imposing a volumetric source term G_v in the vapor phase of volume V_b:

$$G_v V_b = dV_b/dt \tag{3.20}$$

Rearranging Eq. 3.20 we obtain an explicit expression for the volumetric source term Gv to impose in the vapor phase:

$$G_v = (dV_b/dt)/V_b = 3U_b/(R_{b,0} + U_b t) \tag{3.21}$$

Note the volumetric source term G_v is uniform in space within the vapor phase at all times, yet time dependent, and function of three parameters: the bubble growth

rate U_b known from experiments or derived from Mikic's theory [71], the initial bubble radius $R_{b,0}$ prescribed during the initialization of the numerical simulation, and the physical time t. Another method was also investigated and is reported in Appendix B.

3.2.3 Method verification in the absence of a wall (spherical bubble growth)

The implementation of the volumetric source term in axisymmetric configuration in Gerris is verified for the special case of a spherical bubble growth in a (semi)-infinite medium - see Figure 3-3 (Setup A, Table 3.2). The volume and shape of the bubble can be compared to its simple analytical and spherical reference. Second order convergence with grid size is obtained - see Figure 3-5.

3.2.4 Method verification in the presence of a wall (hemi-spherical bubble growth)

We also verify the convergence of the proposed method in the presence of a wall - see Figure **??**. Two figures of merit are considered: the shape of the liquid microlayer forming at the wall, and the macroscopic bubble growth rate obtained from imposing the volumetric source of vapor inside the bubble. Four simulations of bubble growth at a wall are reported here (Setup B, Table 3.2), with increased refinement in the microlayer region: $\mathrm{dx}_{micro}/R_{b,0}$= 1/40, 1/80, 1/160, 1/320 ($R_{b,0} = 10\mu m$, the initial bubble radius), specifically in a band of $4\mu m$ at the wall. Refinement elsewhere at the interface is kept identical: $\mathrm{dx}_{macro}/R_{b,0}$=1/10. All four simulations yield identical macroscopic bubbles shapes - see Figure 3-8(a). In Figure 3-8(b), the microlayer shape converges to a single profile as we refine the mesh in the microlayer region, from dx_{micro}=250nm down to 125nm, 62.5nm, and 31.25nm.

With such refinement dx_{macro} at the macroscopic interface, the bubble growth rate obtained numerically is 4.87m/s (vs 5.0m/s), a 2.6% difference between desired and

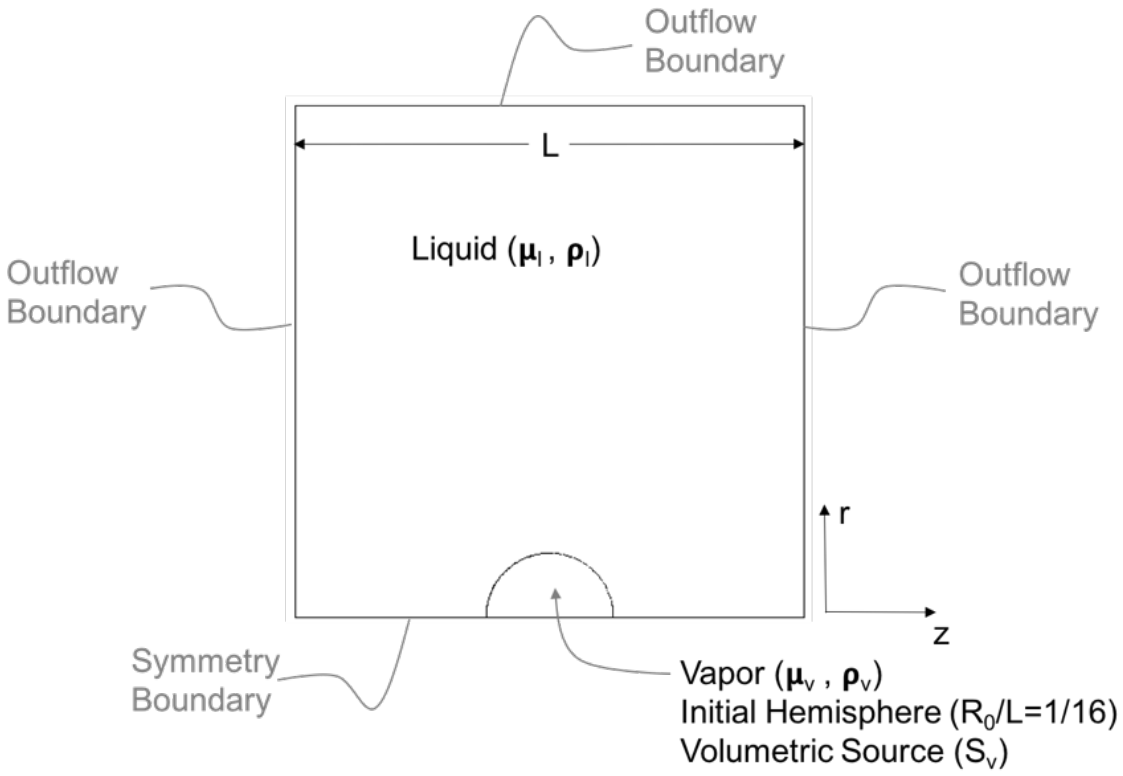

Figure 3-3: Computational domain to verify correct implementation of the volumetric source of vapor to control the macroscopic growth of the bubble in the absence of a wall

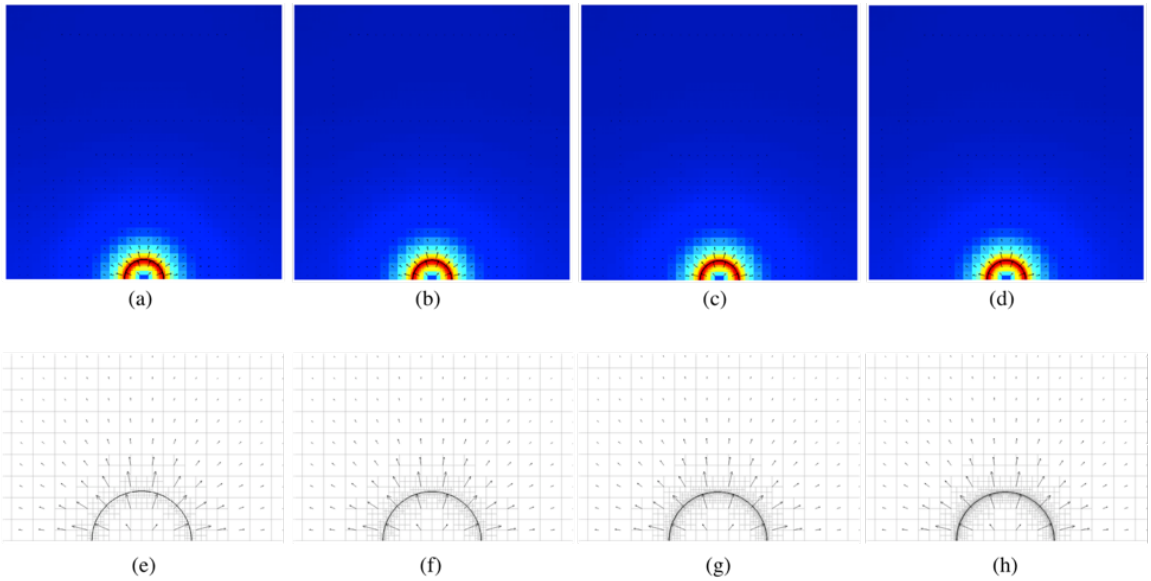

Figure 3-4: Norm of velocity (top row): red is U_b, blue is 0 [m/s]. Mesh and velocity field (bottom row), in the vicinity of the wall confirm spherical growth. Four levels of refinement at the interface are used: from coarse (left column) to very refined (right). (Setup A, Table 3.2)

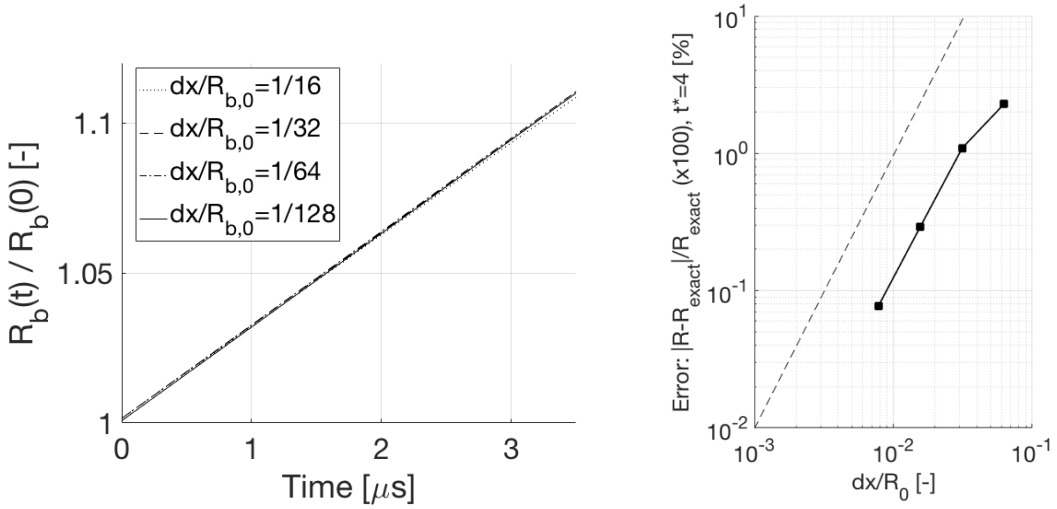

(a) (b)

Figure 3-5: Bubble radius R_b as a function of time (a), for three refinements at the interface: dx/R$_b$(t = 0)=1/16, 1/32, 1/64, 1/128. Second order convergence is obtained as we refine the mesh (b), using the proposed volumetric source in the vapor phase to drive bubble growth at rate U$_b$. (Setup A, Table 3.2)

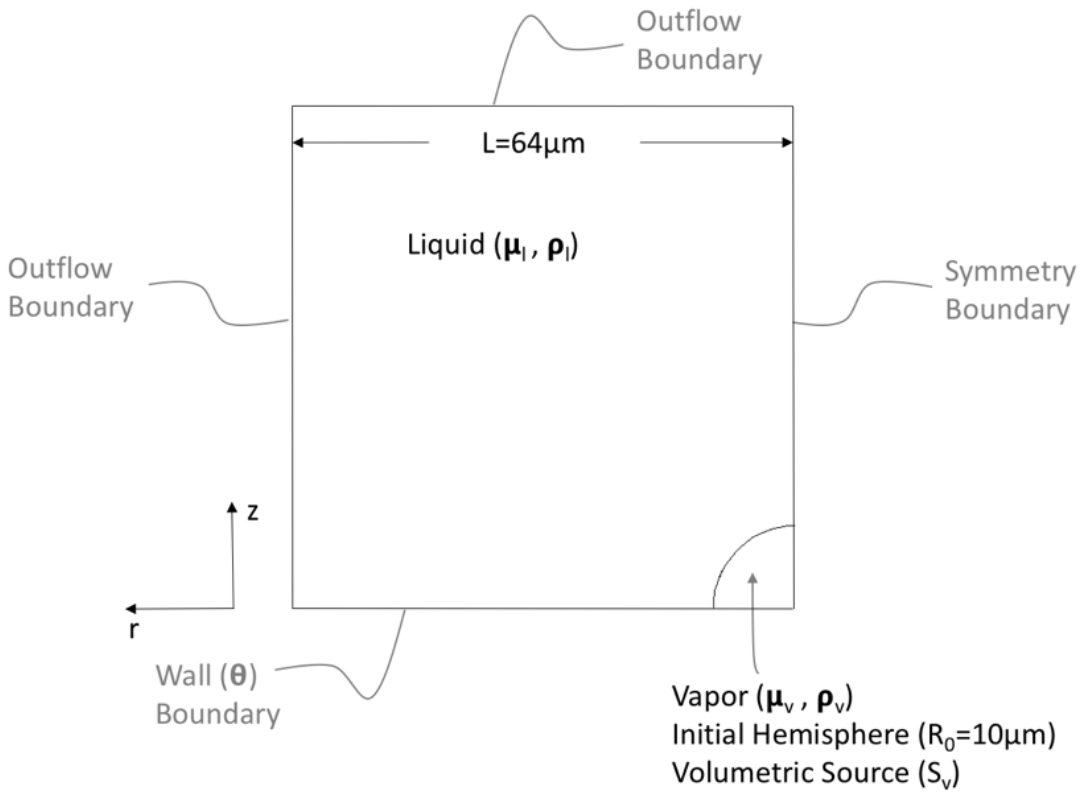

Figure 3-6: Computational domain to verify correct implementation of the volumetric source of vapor to control the macroscopic growth of the bubble in the presence of a wall.

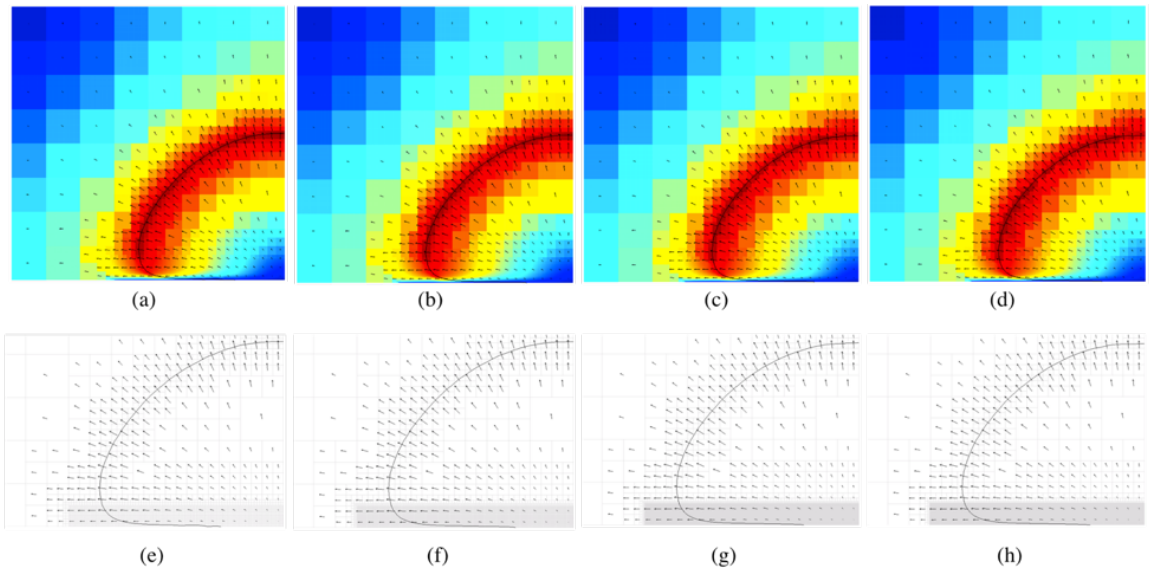

Figure 3-7: Norm of velocity (top row): red is U_b, blue is 0 [m/s]. Mesh and velocity field (bottom row), in the vicinity of the wall. Four levels of refinement at the interface are used: from coarse (left column) to very refined (right): dx/Rb0=1/40 (a)(e), 1/80 (b)(f), 1/160, 1/320. (Setup B, Table 3.1).

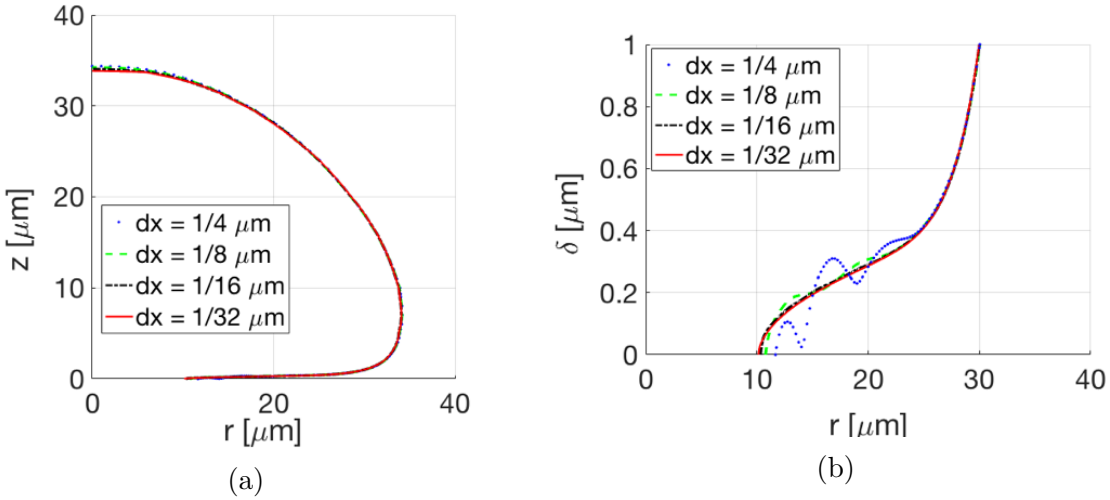

(a) (b)

Figure 3-8: Axisymmetric shapes of the macroscopic bubble (a) and liquid microlayer (b) obtained in four simulations of bubble growth at a wall, with increased refinement in the microlayer region (band of 4microns at the wall of increased refinement: $dx_{micro}/R_{b,0}$= 1/40, 1/80, 1/160, 1/320), while the refinement elsewhere at the interface is kept identical ($dx_{macro}/R_{b,0}$=1/10, $R_{b,0} = 10\mu m$). (Setup B, Table 3.2)

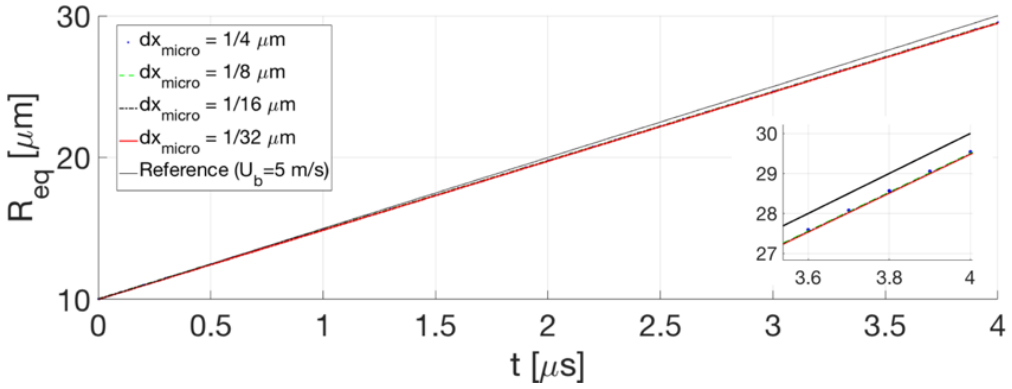

Figure 3-9: Equivalent bubble radius as a function of time for four simulations of bubble growth at a wall, with increased refinement in the microlayer region (band of 4microns at the wall of increased refinement: $\mathrm{dx}_{micro}/R_{b,0}$= 1/40, 1/80, 1/160, 1/320), while the refinement elsewhere at interface is kept identical ($\mathrm{dx}_{macro}/R_{b,0}$=1/10, $R_{b,0} = 10\mu m$). (Setup B, Table 3.1)

numerically obtained growth rates - see Figure 3-9.

The error in bubble growth rate can be reduced by further refinement at the macroscopic interface - see Figure 3-10. First order convergence with grid size at the bubble interface is obtained - see Figure 3-11.

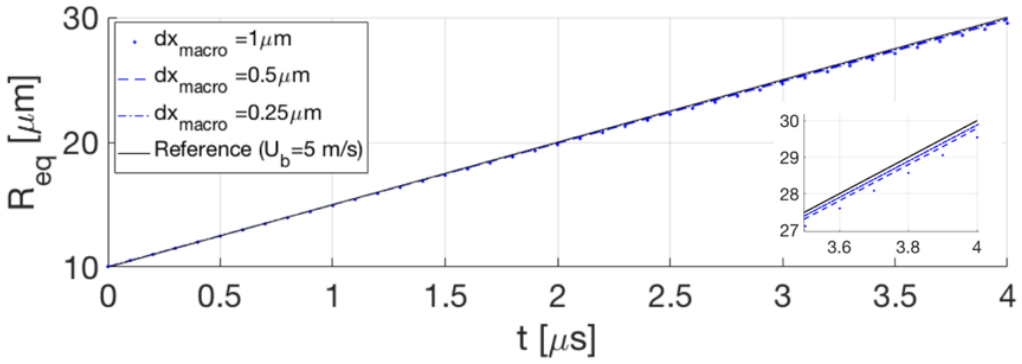

Figure 3-10: Equivalent bubble radius as a function of time for three simulations of bubble growth at a wall, with increased refinement in the macroscopic region of the interface (away from a band of 4microns at the wall of refinement $dx_{micro}/R_{b,0}$=1/40): $dx_{macro}/R_{b,0}$=1/10, 1/20, 1/40 ($R_{b,0} = 10\mu m$). (Setup C, Table 3.2)

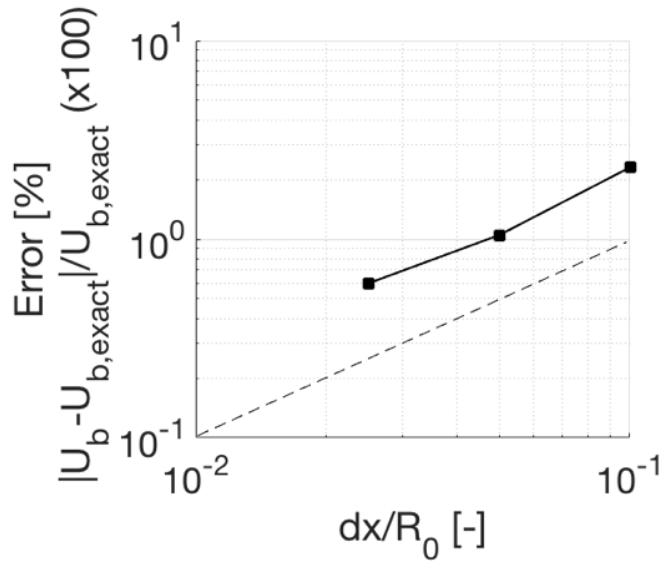

Figure 3-11: Convergence of the error in apparent bubble growth rate with refinement of the mesh at the interface (solid dot). First order convergence is obtained (dashed line). (Setup C, Table 3.2)

3.3 Qualitative results

3.3.1 Multi-scale modeling

Four regions (and scales) can be identified based on the curvature κ of the interface - see Figure 3-12 below:

1. the contact line region where the interface meets the wall (negative curvature)

2. the central linear region of the liquid microlayer (≈ zero curvature)

3. the transition region from the central linear region to the macroscopic bubble (maximum curvature)

4. the macroscopic hemispherical bubble cap (uniform curvature along the interface)

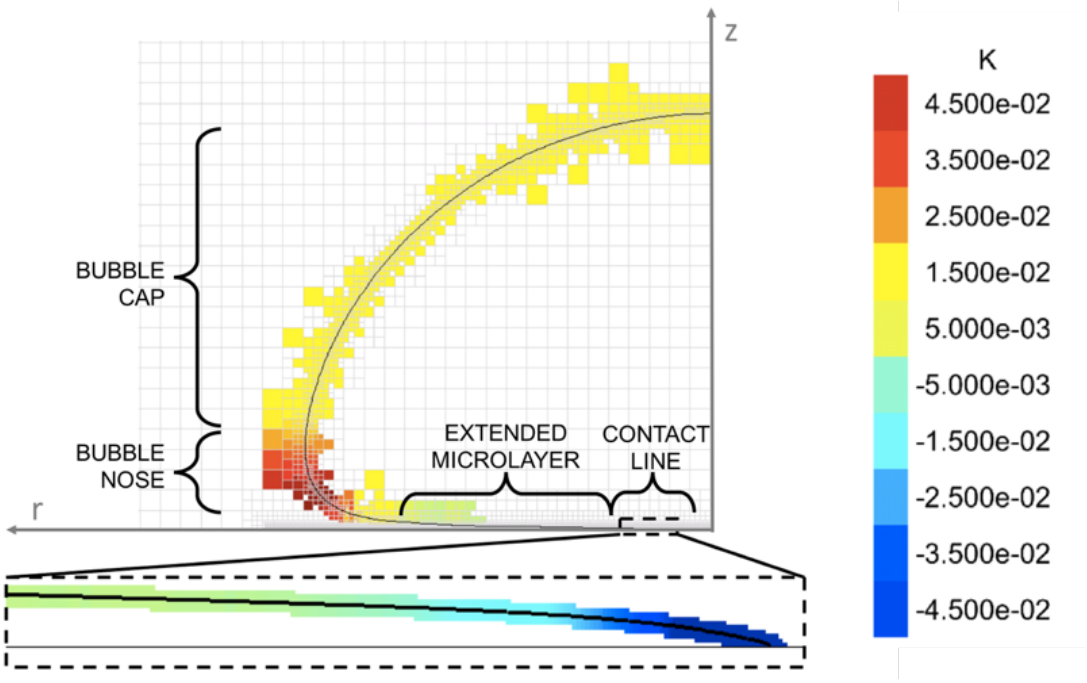

Figure 3-12: Typical axisymmetric shape of a growing bubble at a wall. Interface is solid black line. Curvature κ is given by the colormap: blue in the contact line region is negative curvature (minimum reached at the contact point κ=-0.66 $[1/\mu m]$), green in the central linear region is approaching zero curvature ($\kappa \approx 10^{-3}$ $[1/\mu m]$), red at the bubble nose is maximum curvature ($\kappa = 5.8\ 10^{-2}$ $[1/\mu m]$), and yellow is the uniform curvature along the interface at the bubble cap as the bubble grows hemispherically ($\kappa \approx 1.510^{-2}$ $[1/\mu m]$). The range used in the color map does not reflect the maximum positive value and minimum negative value taken by the curvature, but rather is centered around 0 to allow easier identification of all four regions, also denoted in the image with direct labeling.

3.3.2 Reducing the parameter space

The fluid of interest is water, used as a coolant in PWRs (15.5 MPa), but also in lab experiments (0.101 MPa). The parameter space in Table 3.1 gives ranges for all dimensionless groups in both conditions, namely density ratio, viscosity ratio, capillary number, and contact angle.

The viscosity ratio varies between 3.2 and 23.3 (-), while the density ratio varies between 5.9 and 1650 (-). We perform simulation with all four bounding values for both viscosity and density ratios.

The computational domain used is identical as the one shown in Figure 3-6, except the size of the computational domain is increased to $128\mu m$ (Setup F, Table 3.2). The finest mesh size is 250nm ($\mathrm{d}x_{micro}/R_{b,0} = 1/40$) and is imposed at the interface. Elsewhere in the domain, the largest mesh size is coarsened up to 16mum away from the interface.

We note the weak dependence of the microlayer shape within both ranges of interest of viscosity and density ratios - see Figure 3-13(a) and (b). This is expected since the properties of the liquid phase affect the hydrodynamics of this problem much more than those of the vapor phase, which in practice can be considered as an inviscid and massless fluid.

Therefore, in the rest of the study, we will no longer consider the dependence of the microlayer formation on the viscosity and density ratios, which greatly simplifies to:

$$\delta^* = f(r^*, t^*, Ca, \theta_{\mathrm{d}x}) \tag{3.22}$$

3.3.3 Physical justification of trends observed

Before exploring the parameter space of interest - Table 3.1, we first analyze trends on a small sample of capillary numbers and contact angles: $Ca \in \{0.02,\ 0.2\}$ and $\theta_{\mathrm{d}x} \in \{25^\circ,\ 85^\circ\}$ ($\mathrm{d}x = 100nm$), for times $t^* \in \{250,\ 1000\}$. Dimensionless times are picked here to be representative of microlayer thickness profiles reported in most

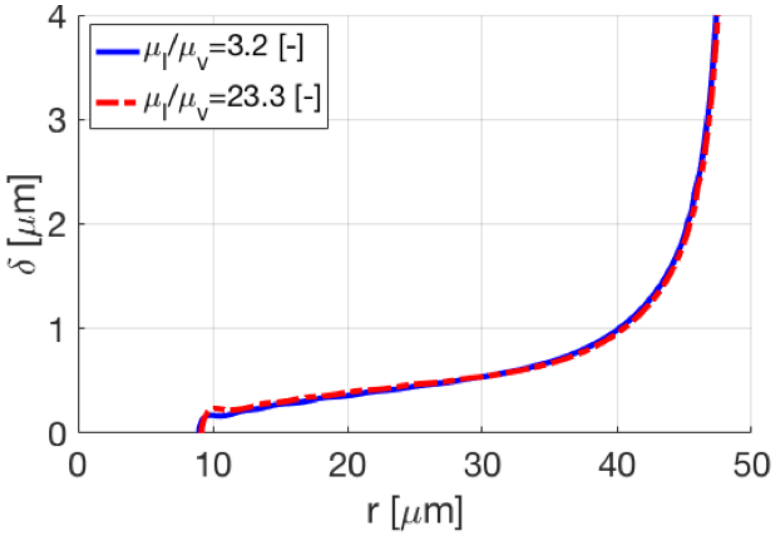

(a)

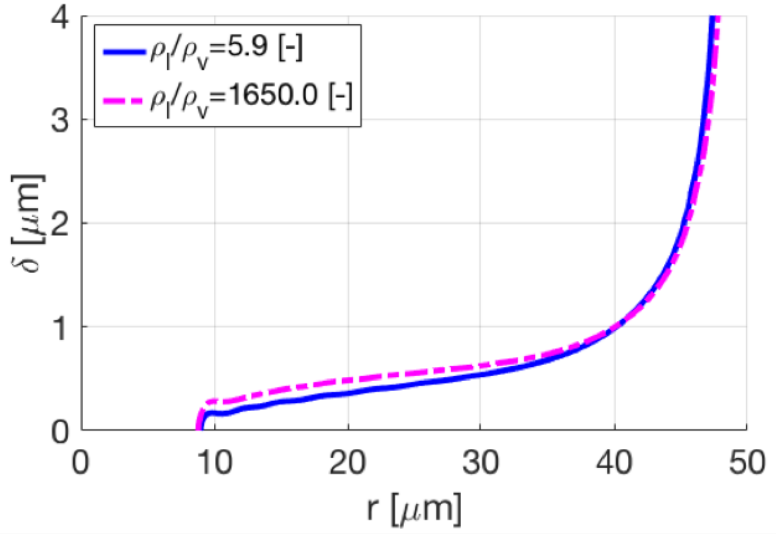

(b)

Figure 3-13: Microlayer shapes for the bounding values of viscosity ratio (a) and density ratio (b). Simulation properties: Ca=1.0, $\theta_{\mathrm{d}x} = 50°$ ($\mathrm{d}x = 250nm$), (Setup F, Table 3.2)

recent experiments (Reference: unpublished work from Jung and Kim, 2016). All eight simulation results are presented in Figure 3-14.

The size of the computational domain is increased to $500\mu m$, the initial bubble radius is $6.4\mu m$ ($R_{b,0}/r_c = 64$, $r_c = 0.1\mu m$). The finest mesh size is of $100nm$ ($\mathrm{d}x_{micro}/R_{b,0} = 1/64$) and is imposed in a band of $4\mu m$ of thickness at the wall. Elsewhere at the interface, the mesh size is four times larger ($\mathrm{d}x_{macro}/R_{b,0} = 1/16$) (Setup G, Table

3.2).

Fluid properties are fixed in the range of interest. Trends are discussed in Table 3.3, for each of the dimensionless groups Ca, θ_{dx}, and t^*.

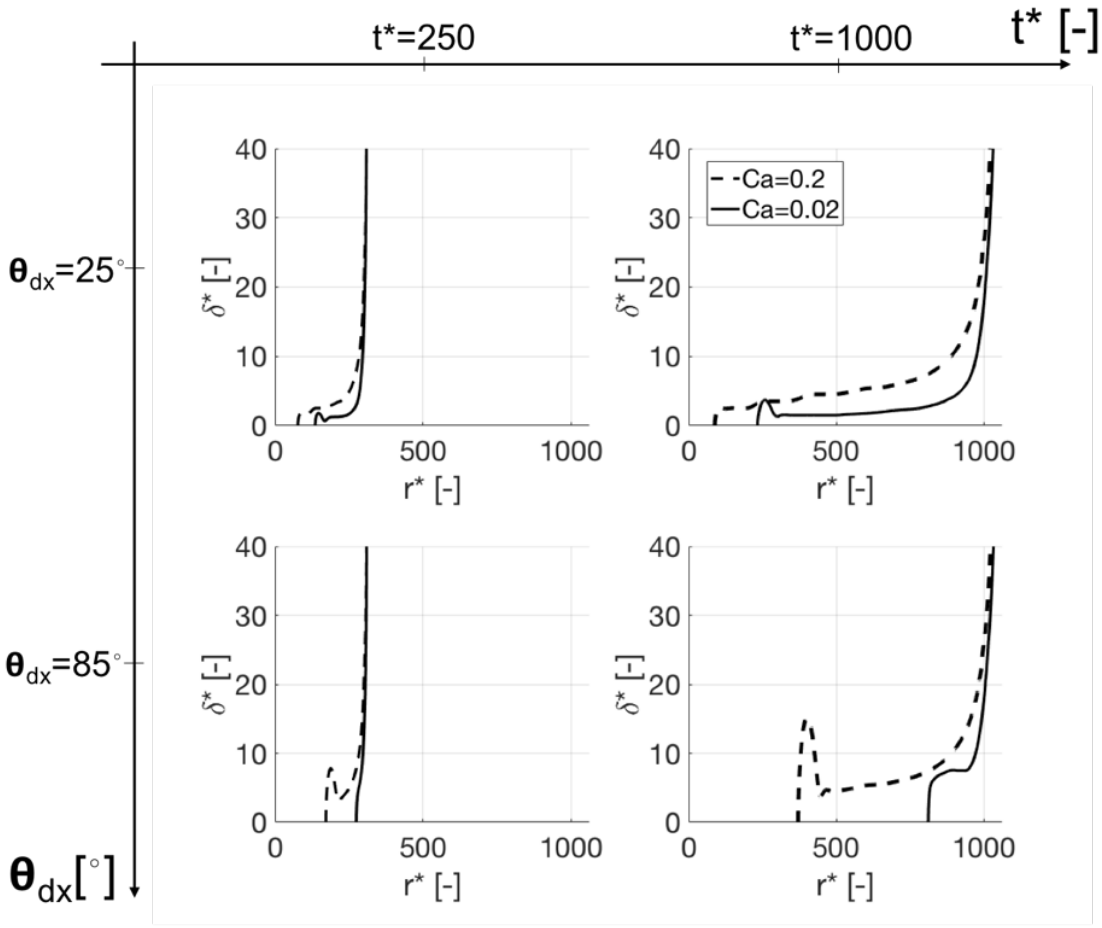

Figure 3-14: Typical microlayer shapes: $\delta^* = f(r^*)$, for fixed combinations of (Ca, θ_{dx}, t^*) Top row corresponds to $\theta_{dx} = 25°$ ($dx = 100nm$), bottom row to $\theta_{dx} = 85°$ ($dx = 100nm$). Left column corresponds to $t^* = 250$, right column to $t^* = 1000$. Two capillary numbers are shown for each panel: $Ca = 0.2$ (dash line), and $Ca = 0.02$ (solid line). In all simulations, reference length scale $r_c = 0.1\mu m$, and reference time scale $t_c = 0.050\mu s$. (Setup G, Table 3.2).

3.3.4 Self-similarities in the central region (micron-scale)

In the central region, we find the microlayer shape to be linear of slope C (-) decreasing with the square root of time - see Figure 3-16. Consequently, self-similar profiles in the

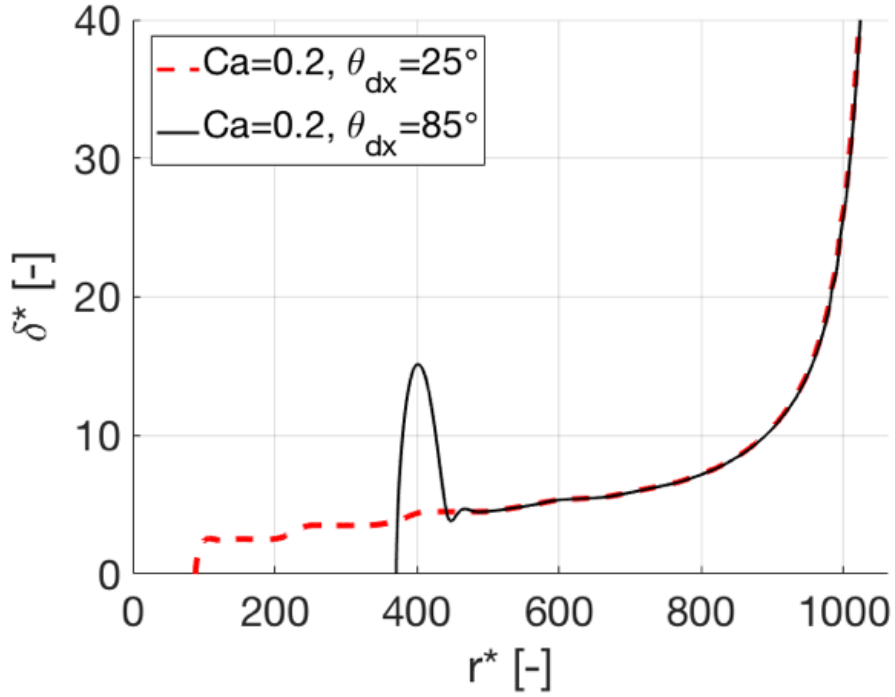

Figure 3-15: Typical microlayer axisymmetric shapes: $\delta^* = f(r^*)$, for t^*=1000, Ca=0.2, and θ_{dx}=25° (red dashed line), and θ_{dx}=85° (solid black line). dx^*=1 (-) in the band $\delta^* < 40$ (-). $r_c = 0.1\mu m$, $t_c = 0.050\mu s$. Away from the bulge region, both shapes are identical. (Setup G, Table 3.2).

Π-GROUP	OBSERVATION	PHYSICAL JUSTIFICATIONS
Capillary number Ca	Higher Ca yields thicker microlayer (for a given contact angle and time).	At higher capillary number, higher expansion velocity and/or viscosity yield higher viscous stresses near the wall, which result in higher entrainment of liquid in the microlayer. To illustrate this point, we note in an earlier work where the surface tension force dominates over viscous stresses, Bretherton (Bretherton, 1961) investigated the formation of a thin liquid film when a bubble moves at small Ca in a capillary tube and obtained the dimensionless thickness of the thin liquid layer left between the bubble and the wall to increase with increasing Ca ($Ca^{2/3}$ scaling law).
Contact angle θ_{dx} (at scale dx_{micro})	i. Higher contact angle reduces the wetted fraction underneath the bubble (for a given capillary number and time) ii. Higher contact angle does not affect the slope of the central region away from the bulge, provided the central region is formed - see Figure **??**	i. The radial component of the surface tension force applied to the liquid wedge ($\sigma\ \kappa cos(\theta)$, with θ contact angle, and $\kappa < 0$ at the contact line) decreases in magnitude for increasing contact angle. As a result, the contact line moves faster at higher contact angles, and the wetted fraction underneath the bubble is reduced. ii. The expansion of a circular hole in a viscous sheet of liquid has been thoroughly investigate: [103], [8], [92], [35], [4]. For low Ohnesorge numbers ($Oh = \mu_l/\sqrt{\delta\rho_l\sigma}$)), fluid motion is concentrated near the tip of the hole where fluid builds up in a so-called bulge or rim, while the rest of sheet is not affected. Three regimes are identified: $Oh < 0.1$, $Oh \in [0.1;\ 10]$, and $Oh > 10$. As Oh increases, the capillary waves found at the tip disappear through the action of viscosity. In the cases shown in Figure **??**, the thickness of the film is in the range of $1\mu m$ to $7\mu m$, and Oh ranges from 0.002 to 0.04. All simulation results are in the first regime where capillary waves are expected in the vicinity of the tip, and damped away from the tip due to viscous effect, leaving the rest of the extended liquid layer unaffected by the motion at the rim.
Dimensionless time t^*	The slope of the central linear region of the liquid microlayer decreases over time	The curvature at the rim, and thus the resulting capillary pressure at the rim, pushes the liquid outwards and depletes the liquid microlayer with time.

Table 3.3: Qualitative results: typical microlayer results $\delta^* = f(r^*)$, for fixed combinations of ($\theta_{\mathrm{d}x}$, Ca, t^*). Trends observed and physical justifications.

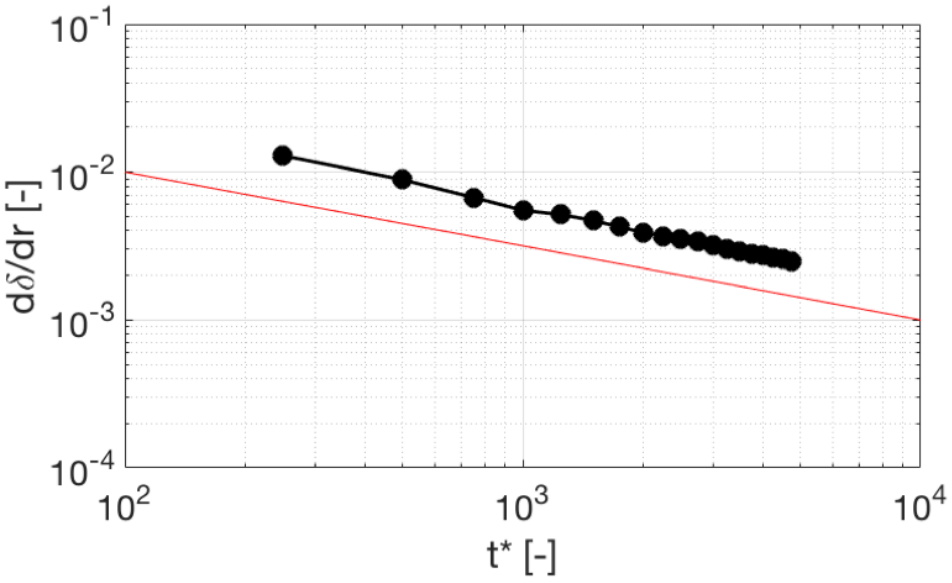

Figure 3-16: Time-evolution of the slope of central linear region of the microlayer: $d\delta^*/dr^* = d\delta/dr = f(t^*)$ (black dots), for Ca=0.2, θ_{dx}=25°(dx=100nm), and $t^* \in [250; 5000]$. $1/\sqrt{t^*}$ scaling added for reference (red line). (Setup G, Table 3.2).

central region of the microlayer (micron scale) are obtained in Figure 3-17 showing $\delta^*/\sqrt{t^*} = f(r^*/t^*)$, for Ca=0.020 in Fig. 3-17c and Ca=0.2 in Fig. 3-17d, times $t^* \in [250, 5000]$, and $\theta_{\mathrm{d}x}$=25°(dx=100nm).

3.3.5 Self similarities in the bulge region (sub-micron to micron scale)

In all four conditions in Figure 3-14, we note the formation of a bulge at the inner edge of the microlayer, where the surface tension force acts against the viscous force at the wall and pushes the contact line outwards, similar to the classic hole expansion problem [92]. As consequence to this dewetting process, fluid builds up and forms the observed bulge at the inner edge of the microlayer. It is particularly apparent for the cases CASE1: {Ca=0.020, θ_{dx}=25°(dx=100nm)}, and CASE2: {Ca=0.200, θ_{dx}=85° (dx=100nm)}, where the bulge fully forms within $t^* < 1000$ as shown in Figure 3-14.

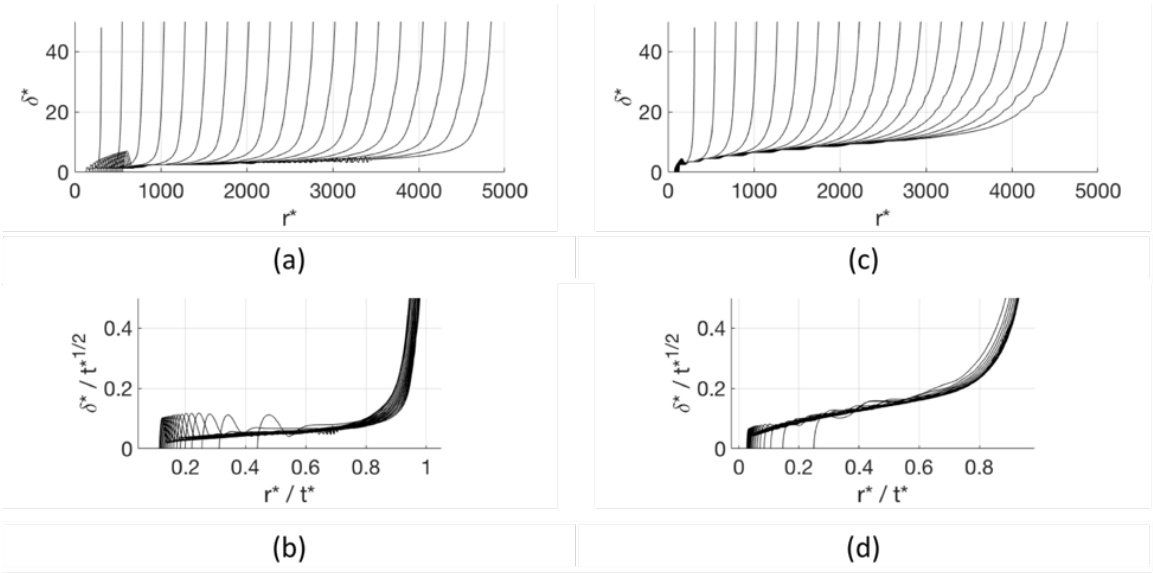

Figure 3-17: Axisymmetric profiles in the microlayer region: $\delta^* = f(r^*)$ for Ca=0.020 (a) and Ca=0.2 (c), for times $t^* \in [250, 5000]$ (profiles move outwards as time t^* increases), θ_{dx}=25deg. Self-similar profiles in the central region of the microlayer (micron scale): $\delta^*/\sqrt{t^*} = f(r^*/t^*)$ for Ca=0.020 (c) and Ca=0.2 (d), for times $t^* \in [250, 5000]$, $\theta_{\mathrm{dx}} = 25°$ (Setup G, Table 3.2).

CASE1 and CASE2 are analyzed in more details in Figures 3-18 and 3-19, respectively, for times $t^* \in [500; 2500]$. Time series are shown in Figure 3-18(a) and 3-19(a). The definition of so-called top location and neck location at the bulge are shown in Figure 3-18(b) and Figure 3-19(b), and self-similar profiles at the submicron to micron scale of the bulge are shown in Figure 3-18(c) and Figure 3-19(c), respectively. The definition of these two scaling parameters is sufficient to obtain self-similar profiles of the bulge.

At high Ca and low contact angle, the bulge barely forms as the contact line does not move significantly, hence only collecting a limited amount of liquid in the rim. At low Ca and high contact angle, the bulge barely forms as the contact line tends to move as fast as the edge of the macroscopic bubble, leaving no microlayer behind.

Variations of the self-similar shape with contact angle is reported in Figure 3-20 for reference. A systematic quantitative assessment of the wetted fraction underneath

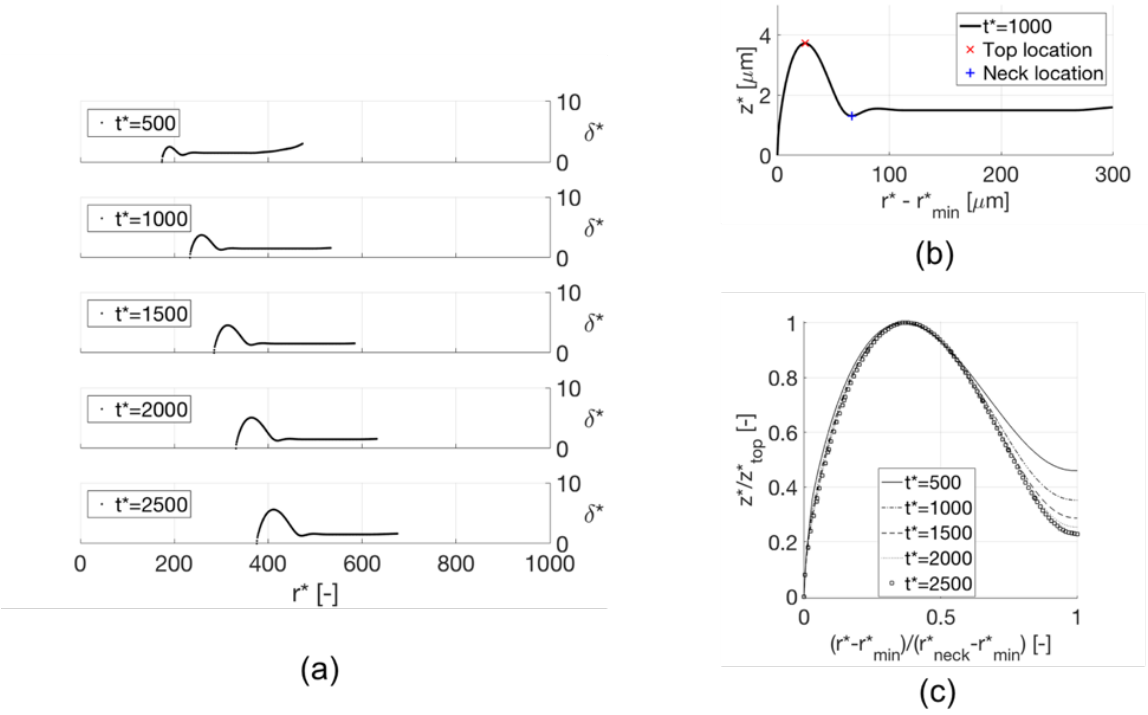

Figure 3-18: Details on bulge formation at low Ca, low contact angle: time series (a), definition of top location and neck location at the bulge (b), and self-similar profiles at the submicron to micron scale of the bulge (c), for Ca=0.020, θ_{dx}=25°dx=100nm), $t^* \in [500, 2500]$. (Setup G, Table 3.2).

the bubble is discussed in the following section.

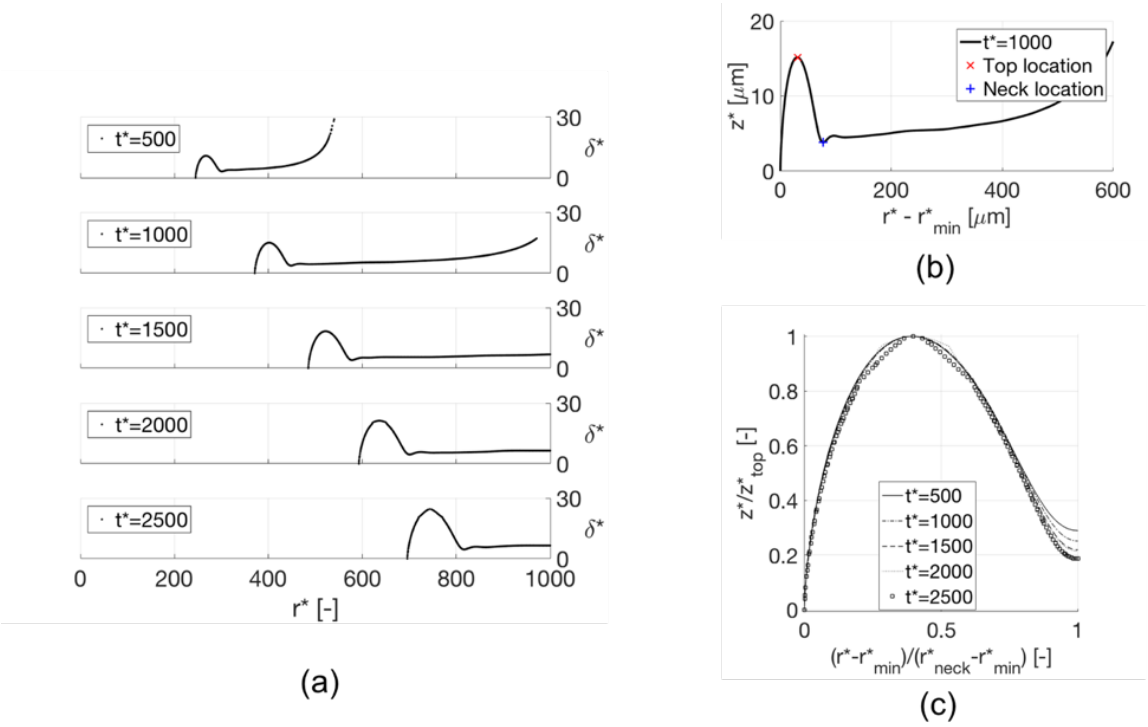

Figure 3-19: Details on bulge formation at low Ca, low contact angle: time series (a), definition of top location and neck location at the bulge (b), and self-similar profiles at the submicron to micron scale of the bulge (c), for Ca=0.200, θ_{dx}=85°(dx=100nm), $t^* \in [500, 2500]$. (Setup G, Table 3.2).

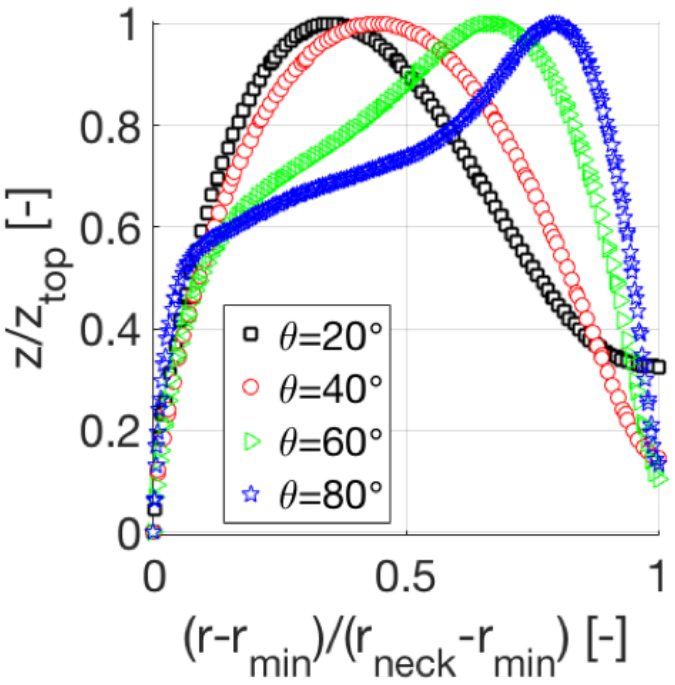

Figure 3-20: Self-similar profiles at the submicron to micron scale of the bulge for Ca=0.020 for and different angles θ_{dx}=20° (black square), 40° (red circle), 60° (green triangle) and 80° (blue star), dx=100nm, t^*=2500. (Setup G, Table 3.2).

3.4 Systematic study and microlayer formation model

We consider the extended microlayer region [36] that predominantly contributes to wall heat flux underneath the bubble during nucleate boiling, where the layer is very thin (of the order of few microns or less), and very long in the radial direction (hundreds of microns). The extended microlayer region extends from a bulge at the inner edge of the microlayer up to the bubble nose where the curvature peaks, and from which the thickness increases very rapidly, hence contributing much less to the wall heat flux (conduction heat flux through the liquid layer: $q'' \propto 1/\delta$). The shape of the extended microlayer in the central region is found to be linear: $\delta^* = \delta_0^* + Cr^*$, with δ_0^* the y-intercept of the linear thickness profile, and C the slope.

To obtain a generally applicable model for microlayer formation, three characteristics need to be modeled as a function of (Ca, θ_{dx}, t^*): (i) the position of the inner edge of

the microlayer r_{min}, or similarly since the extension radius of the macroscopic bubble r_{max} is known, the wetted fraction underneath the bubble $\alpha^* = (1 - r_{min}/r_{max})$, (ii) the linear shape of the extended microlayer, and (iii) the extension radius of the microlayer.

3.4.1 Wetted fraction underneath the bubble

Map of $\alpha^* = (1 - r_{min}/r_{max}) = f(\theta_{\mathbf{dx}}, t^*, Ca)$

We here systematically report the wetted fraction underneath the bubble for a wide range of parameters covering the parameter space of interest (Setup H, Table 3.2). We report contours of the wetted fraction at times t^*=100, 500, 1000, in Figures 3-21, 3-22, and 3-23, respectively. Physical justifications are provided below:

- Time-dependence: for all (θ_{dx}, Ca) considered, α^* increases over time. As the bubble grows, the capillary number of the contact line Ca_{cl} is always smaller than the capillary number of the macroscopic bubble Ca - see Figure 3-25, hence the increase of wetted fraction underneath the bubble.

- Ca-dependence: for all (θ_{dx}, t^*) considered, α^* increases with higher Ca. The dimensionless velocity of the contact line $U^*_{cl}(=Ca_{cl}/Ca)$ decreases as Ca increases - see Figure 3-26, hence the increase of wetted fraction underneath the bubble.

- θ_{dx}-dependence: for all (Ca, t^*) considered, α^* decreases with higher contact angle. The radial component of the surface tension force applied to the liquid wedge decreases in magnitude for increasing contact angle, hence reducing the wetted fraction underneath the bubble.

Systematic quantification of Ca_{cl}=f($\theta_{\mathbf{dx}}$, t^*, Ca), the capillary number associated with contact line motion.

- Scaling of Ca_{cl} with Ca for θ_{dx}=90° (dx=100nm).

  Past an initial transient, and for the case of θ_{dx}=90° (dx=100nm), the rim at

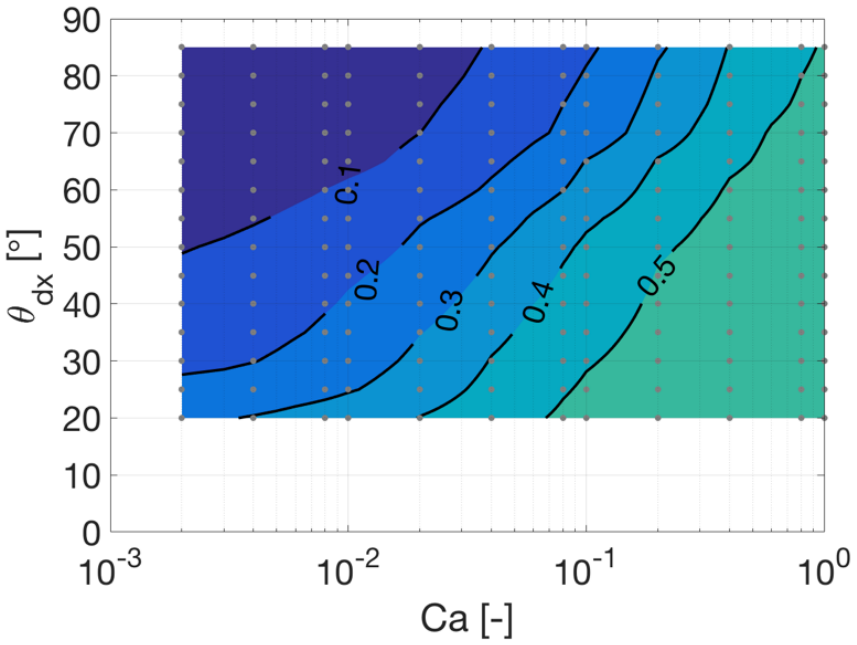

Figure 3-21: Wetted fraction contours α^*=0.1, 0.2, 0.3, 0.4, 0.5 in the (θ_{dx}, Ca) space $t^* = 100$. Simulated conditions are designated by round grey dots. (Setup H, Table 3.2)

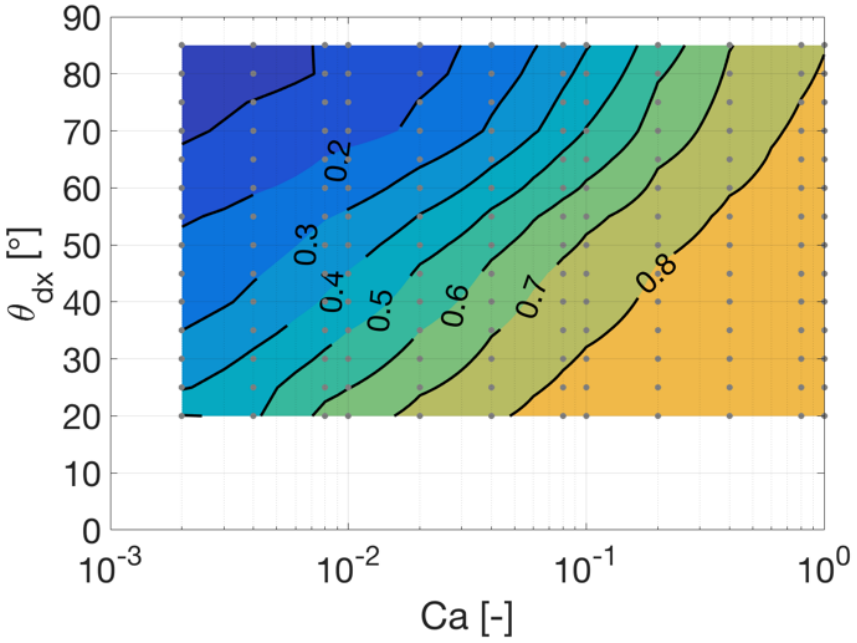

Figure 3-22: Wetted fraction contours α^*= 0.2, 0.3, 0.4, 0.5, 0.6, 0.7, 0.8 in the (θ_{dx}, Ca) space at $t^* = 500$. Simulated conditions are designated by round grey dots. (Setup H, Table 3.2)

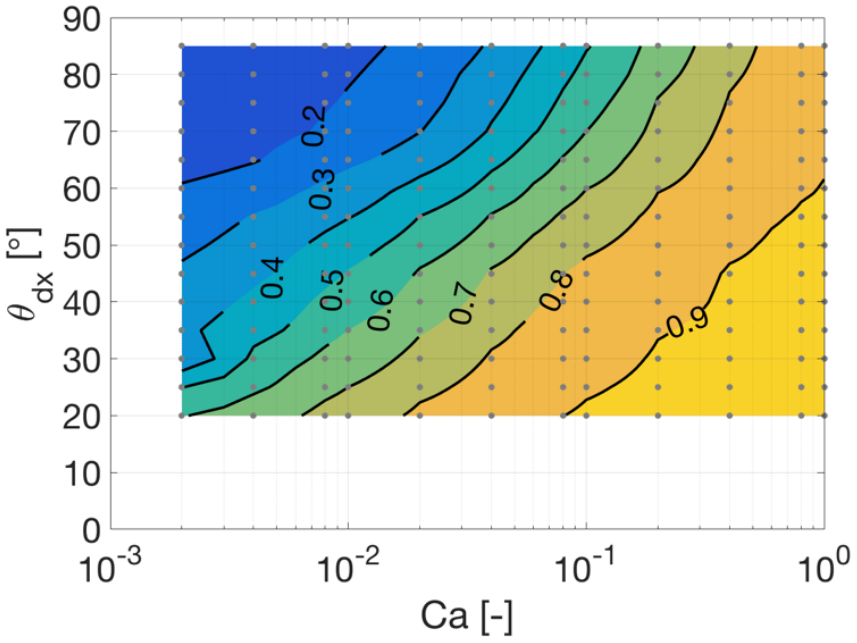

Figure 3-23: Wetted fraction contours α^*= 0.2, 0.3, 0.4, 0.5, 0.6, 0.7, 0.8, 0.9 in the (θ_{dx}, Ca) space at $t^* = 1000$. Simulated conditions are designated by round grey dots. (Setup H, Table 3.2)

the inner edge of the microlayer is found to move at a constant speed U_{cl} - see position of the contact point (black dots) and linear fit (red dashed lines) in Figure 3-24 below (Setup I, Table 3.2).

A thorough analysis of viscous sheet retraction dynamics can be found in [92]. In the simulation results presented here, we estimate the Ohnesorge number Oh to be very small compared to unity. Oh is defined as the ratio between viscous resistance holding the rim back to the surface tension force pushing it outwards:

$$Oh = \mu_l / \sqrt{\delta \rho_l \sigma} \tag{3.23}$$

$Oh << 1$ in all simulations presented here.

In this regime of low Oh, we estimate the characteristic time scale associated

with the initial retraction of the rim, $\tau_{inv}/t_c \approx 30$ (-) throughout all simulations:

$$\tau_{inv} = \sqrt{\rho_l H^3/\sigma} \tag{3.24}$$

with $H \approx 1\mu m$. Consequently, all results presented for $t^* > 200 >> \tau^*_{inv}$ are well past the initial retraction transient.

We define a capillary number Ca_{cl} based on the contact line velocity U_{cl}: $Ca_{cl} = \mu_l U_{cl}/\sigma$, and plot it in Figure 3-25 as a function of Ca, the macroscopic capillary number associated with bubble growth. Interestingly, we note that the capillary number of the contact line scales as the harmonic mean between the macroscopic capillary number Ca and a capillary number C_∞=0.081 obtained numerically, which represents the asymptotic value that the capillary number of the contact line approaches at high Ca:

$$Ca \to 1,\ (Ca >> C_\infty):\ Ca_{cl} \to C_\infty \tag{3.25}$$

In Figure 3-26 we plot the dimensionless velocity of the contact line $U^*_{cl} = Ca_{cl}/Ca$ as a function of Ca for convenience, and confirm that Ca_{cl} scales with Ca at low Ca:

$$Ca \to 0,\ (Ca << C_\infty):\ Ca_{cl} \propto Ca \tag{3.26}$$

- Scaling of Ca_{cl} with Ca for various θ_{dx}

  As the contact angle is decreased, the surface tension force pushing the liquid bulge is impeded, and the maximum asymptotic capillary number C_∞ that it reaches as Ca tends to unity is then also decreased, see Figures 3-27 and 3-28 (Setup J and K, resp., Table 3.2). In fact, as the contact angle tends to 0, the contact line velocity should also tend to zero, with no possible motion. In Figure 3-28, we report the variation of C_∞ obtained numerically with contact

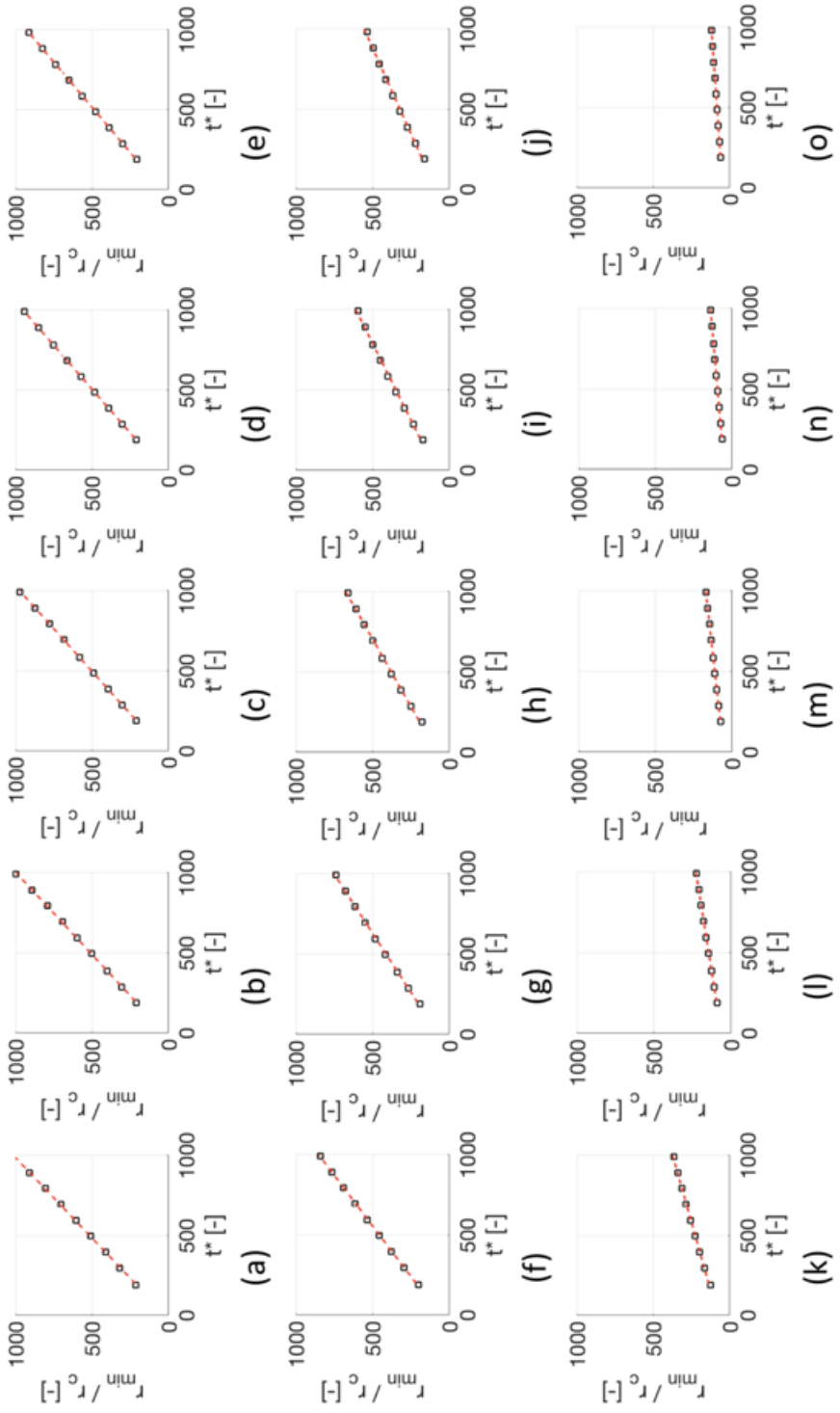

Figure 3-24: Time evolution of the contact point position at the wall, for θ_{dx}=90° (dx=100nm), and various Ca: Ca= 0.002 (a), 0.004 (b), 0.006 (c), 0.008 (d), 0.01 (e), 0.02 (f), 0.04 (g), 0.06 (h), 0.08 (i), 0.1 (j), 0.2 (k), 0.4 (l), 0.6 (m), 0.8 (n), 1.0 (o). (Setup I, Table 3.2).

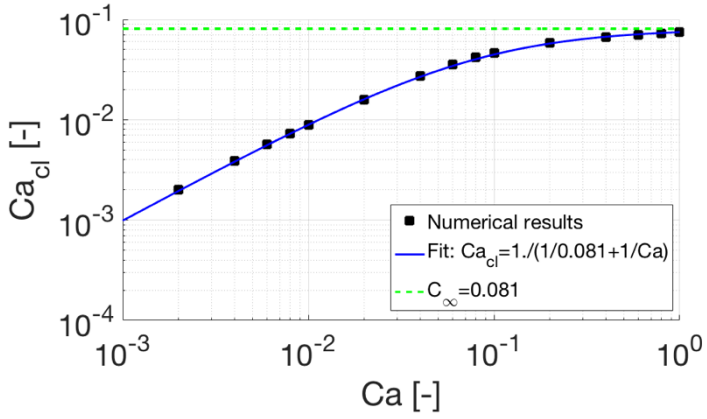

Figure 3-25: Capillary number Ca_{cl} (black dots) associated with the motion of the contact line (obtained numerically), as a function of the macroscopic capillary number Ca associated with bubble growth. The fit of the numerical results to a harmonic mean between two capillary numbers Ca and C_∞: $Ca_{cl} = 1/(1/C\_infty + 1/Ca)$ is provided (blue solid line). The constant C_∞ obtained during the fitting is also plotted (green dashed line) and corresponds to the asymptotic value Ca_{cl} tends to as $Ca \to 1$. Ca_{cl} scales with Ca at very low Ca ($Ca << 1$, $Ca < C_\infty$). (Setup I, Table 3.2).

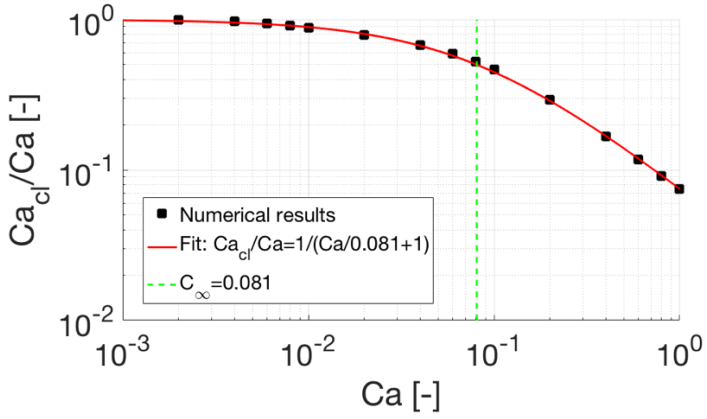

Figure 3-26: Dimensionless velocity of the contact line $U^*_{cl}(= Ca_{cl}/Ca)$ (black dots) associated with the motion of the contact line (obtained numerically), as a function of the macroscopic capillary number Ca associated with bubble growth. The fit of the numerical results to a harmonic mean between two capillary numbers Ca and C_∞: $Ca_{cl}/Ca = 1/(Ca/C_\infty + 1)$ is provided (red solid line). The constant C_∞ obtained during the fitting is also plotted (green dashed line) and corresponds to the asymptotic value Ca_{cl} tends to as $Ca \to 1$. Ca_{cl} scales with Ca at very low Ca ($Ca << 1$, $Ca < C_\infty$). (Setup I, Table 3.2).

angle, and find a cubic fit in the form of:

$$C_\infty = 0.02\theta_{\mathrm{dx}}^3, \text{ (with } \theta_{\mathrm{dx}} \text{ in rad)} \tag{3.27}$$

Such scaling is consistent with the asymptotic value: $C_\infty \to 0$ as $\theta_{\mathrm{dx}} \to 0$. At low Ca, Ca_{cl} scales as a Ca/C_0, with C_0 a constant obtained numerically that is unity for θ_{dx}=90°, and larger than unity as the contact angle is decreased, which is consistent with the motion of the contact line being impeded at lower contact angle. In Figure 3-29, we correlate our data to a simple linear dependence:

$$C_0 = 1 - 1.52\ (\theta_{\mathrm{dx}} - \pi/2), \text{ (with } \theta_{\mathrm{dx}} \text{ in rads)} \tag{3.28}$$

that is consistent with C_0=1 for $\theta_{\mathrm{dx}} = \pi/2\ [rad]$.

- Liquid build-up at the rim during microlayer formation. We here provide results on the shapes of bulges obtained for a fixed contact angle dx=90°(d$x = 100nm$), for a wide range of Ca - see Figures 3-30 to 3-39 (Setup L, Table 3.2).

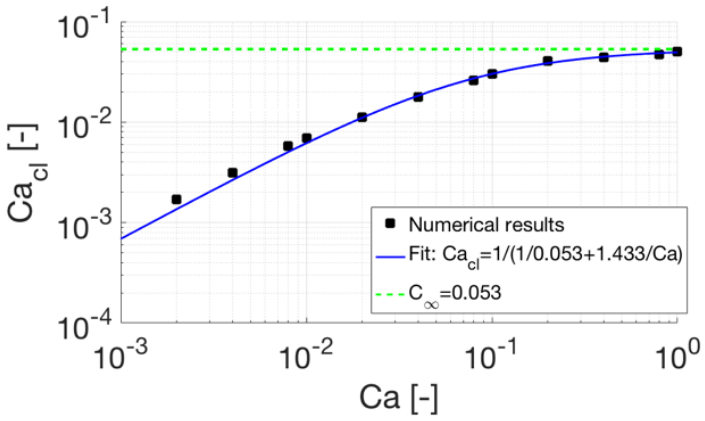

(a)

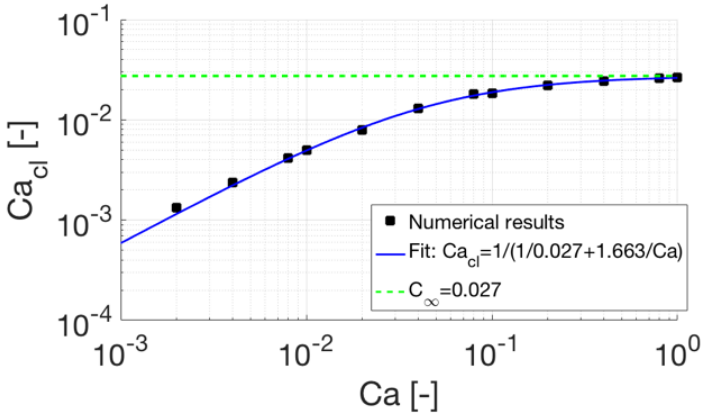

(b)

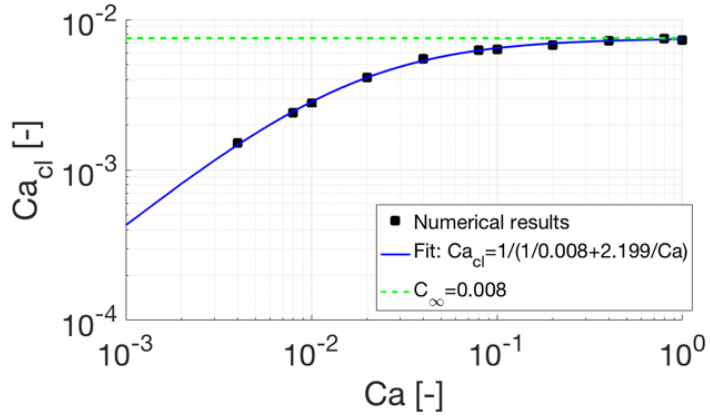

(c)

Figure 3-27: Capillary number Ca_{cl} (black dots) associated with the motion of the contact line (obtained numerically), as a function of the macroscopic capillary number Ca associated with bubble growth, for θ_{dx}=80°(a), 60°(b) and 40°(c). The fit of the numerical results Ca_{cl} with an harmonic mean between Ca and C_∞: $Ca_{cl} = 1/(1/C_\infty + C_0/Ca)$, with C_∞ and C_0 fitting parameters, is provided (blue solid line). The constant C_∞ obtained during the fitting is also plotted (green dashed line) and corresponds to the asymptotic value Ca_{cl} tends to as $Ca \to 1$. Ca_{cl} scales with Ca/C_0 at very low Ca ($Ca << 1, Ca/C_0 < C_\infty$). (Setup J, Table 3.2).

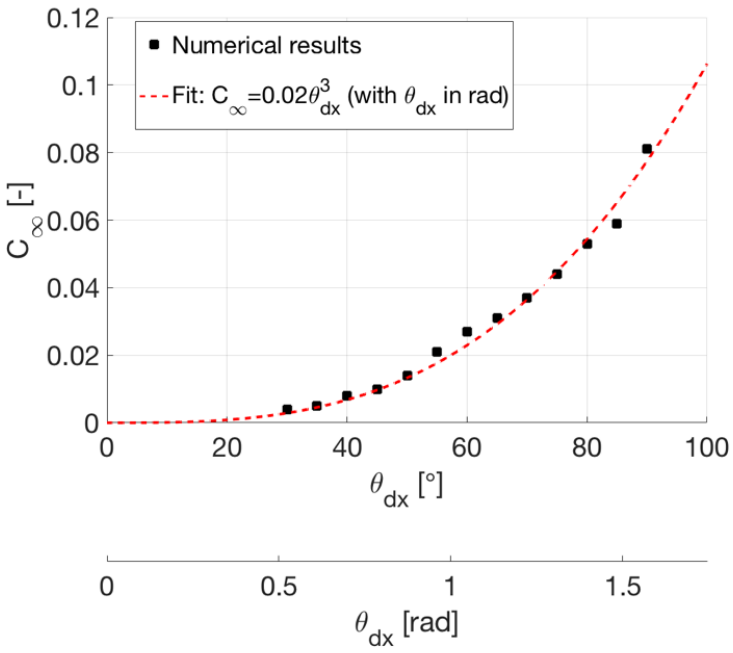

Figure 3-28: Asymptotic capillary number of the contact line C_∞ (black dots) as a function of θ_{dx} (dx=100nm), obtained from fitting numerical results on Ca_{cl} with an harmonic mean: $Ca_{cl} = 1/(1/C_\infty + C_0/Ca)$. A cubic fit (red dash line) seems to describe the data well, and converges asymptotically to 0 as Ca tends to 0 (the contact line would asymptotically stop moving as its contact angle approaches zero). (Setup K, Table 3.2).
[h!]

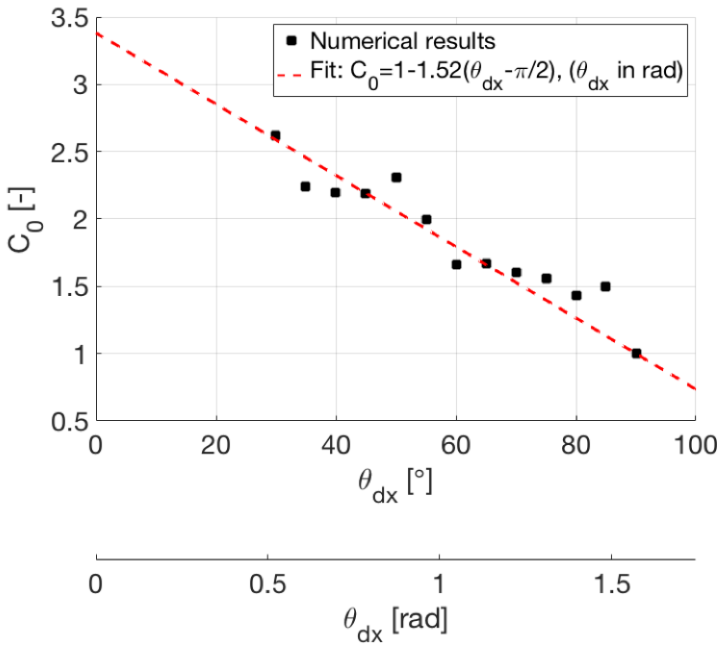

Figure 3-29: Weighting coefficient C_0 (black dots) as a function of θ_{dx} (dx=100nm), obtained from fitting numerical results on Ca_{cl} with a harmonic mean: $Ca_{cl} = 1/(1/C_\infty + C_0/Ca)$. A linear fit (red dash line) seems to describe the data well. (Setup K, Table 3.2).

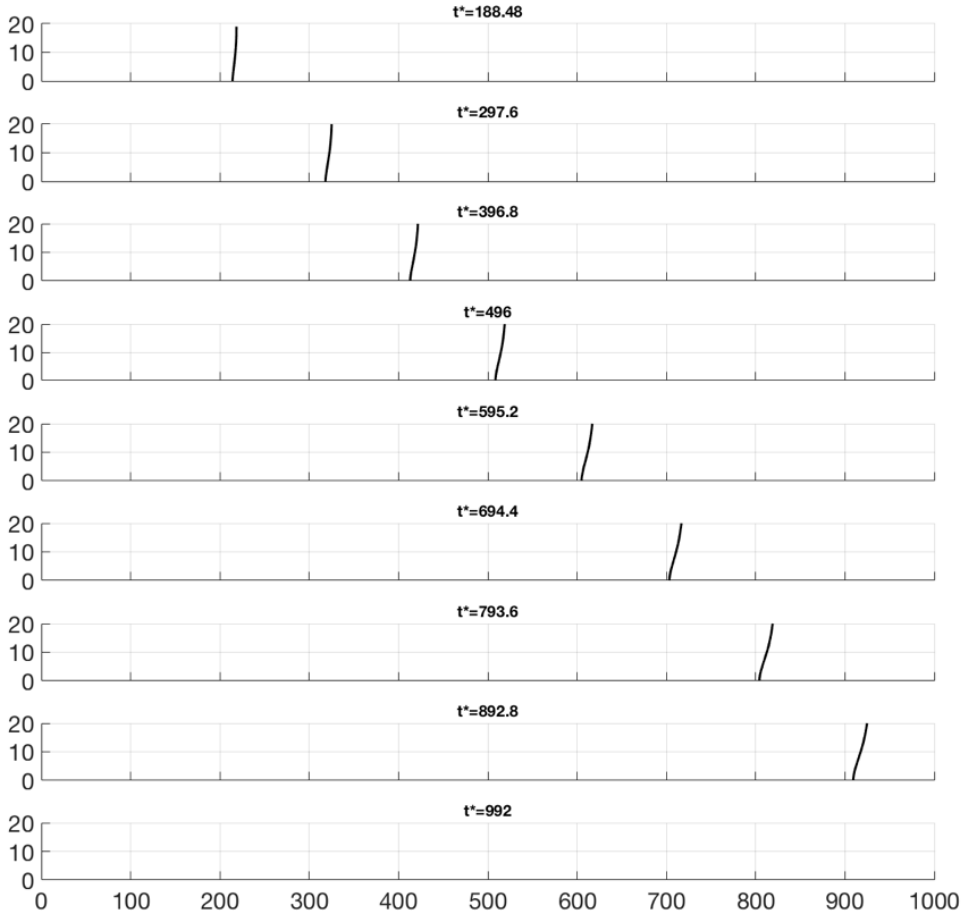

Figure 3-30: Time series of bulge formation: δ^* (y-axis), r^* (x-axis), for $\mathrm{d}x = 90°$ ($\mathrm{d}x = 100nm$) and Ca=0.002 (Setup L, Table 3.2).

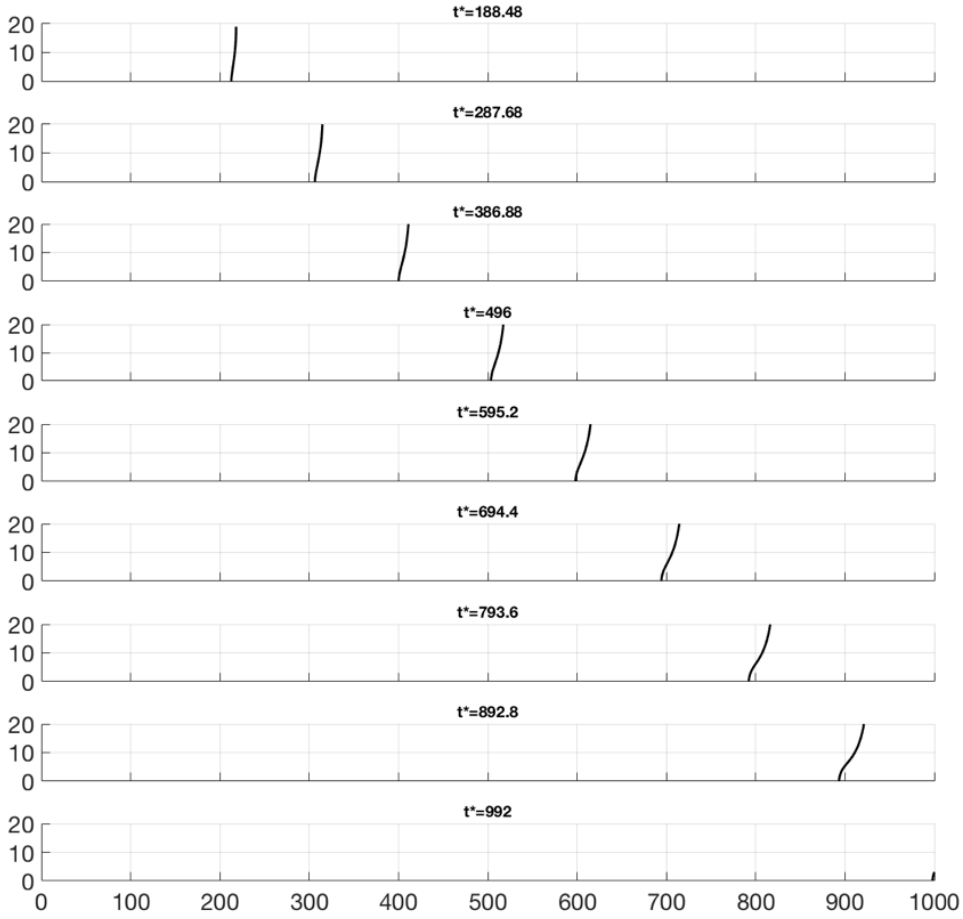

Figure 3-31: Time series of bulge formation: δ^* (y-axis), r^* (x-axis), for $\mathrm{d}x = 90°$ ($\mathrm{d}x = 100nm$) and Ca=0.004 (Setup L, Table 3.2).

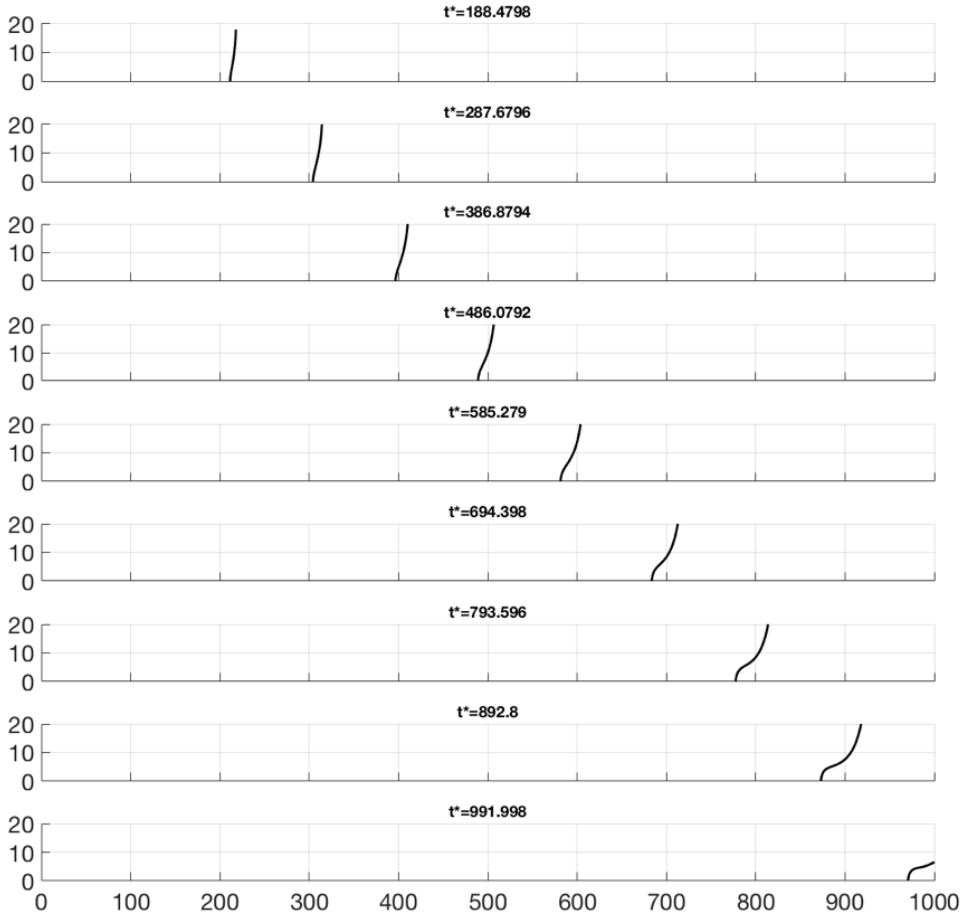

Figure 3-32: Time series of bulge formation: δ^* (y-axis), r^* (x-axis), for $\mathrm{d}x = 90°$ ($\mathrm{d}x = 100nm$) and Ca=0.006 (Setup L, Table 3.2).

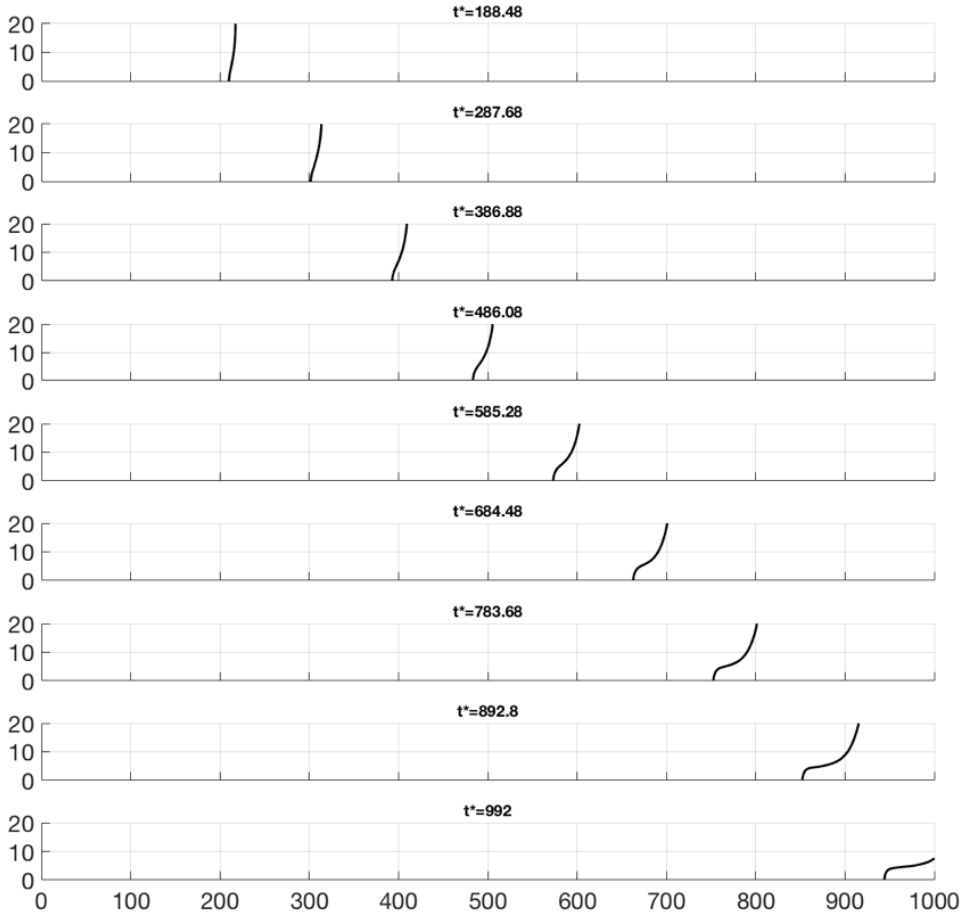

Figure 3-33: Time series of bulge formation: δ^* (y-axis), r^* (x-axis), for $\mathrm{d}x = 90°$ ($\mathrm{d}x = 100nm$) and Ca=0.008 (Setup L, Table 3.2).

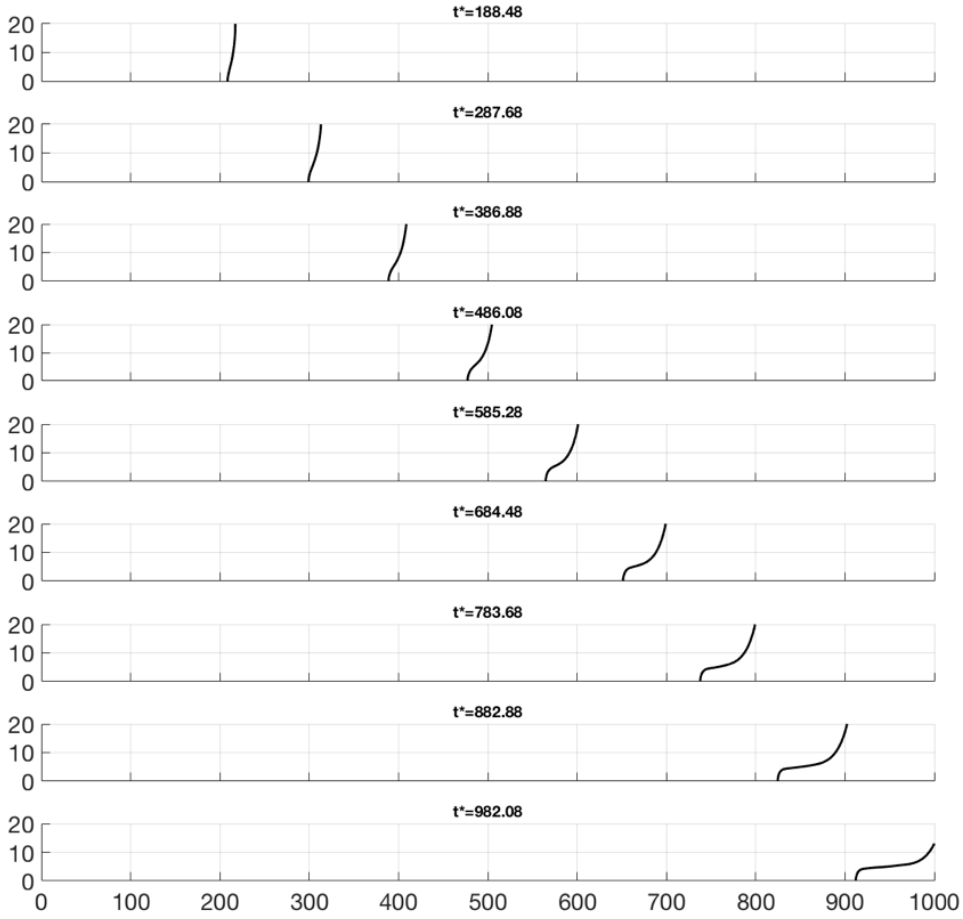

Figure 3-34: Time series of bulge formation: δ^* (y-axis), r^* (x-axis), for $\mathrm{d}x = 90°$ ($\mathrm{d}x = 100nm$) and Ca=0.01 (Setup L, Table 3.2).

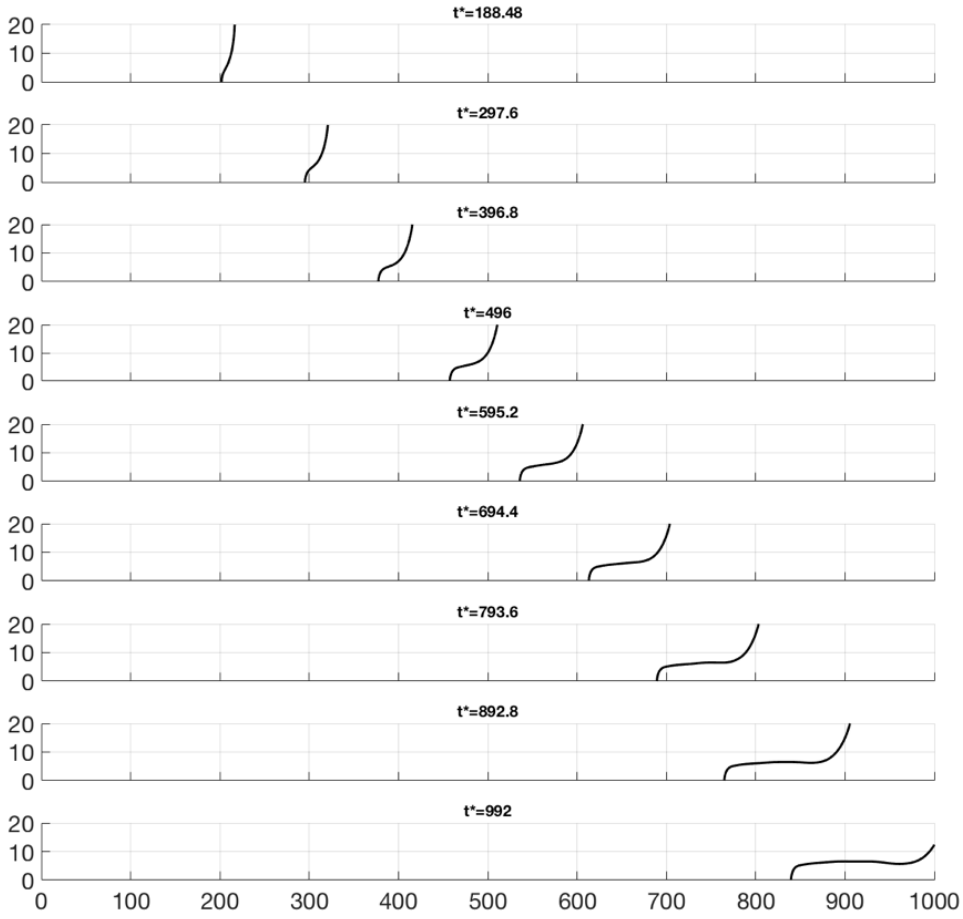

Figure 3-35: Time series of bulge formation: δ^* (y-axis), r^* (x-axis), for $\mathrm{d}x = 90°$ ($\mathrm{d}x = 100nm$) and Ca=0.02 (Setup L, Table 3.2).

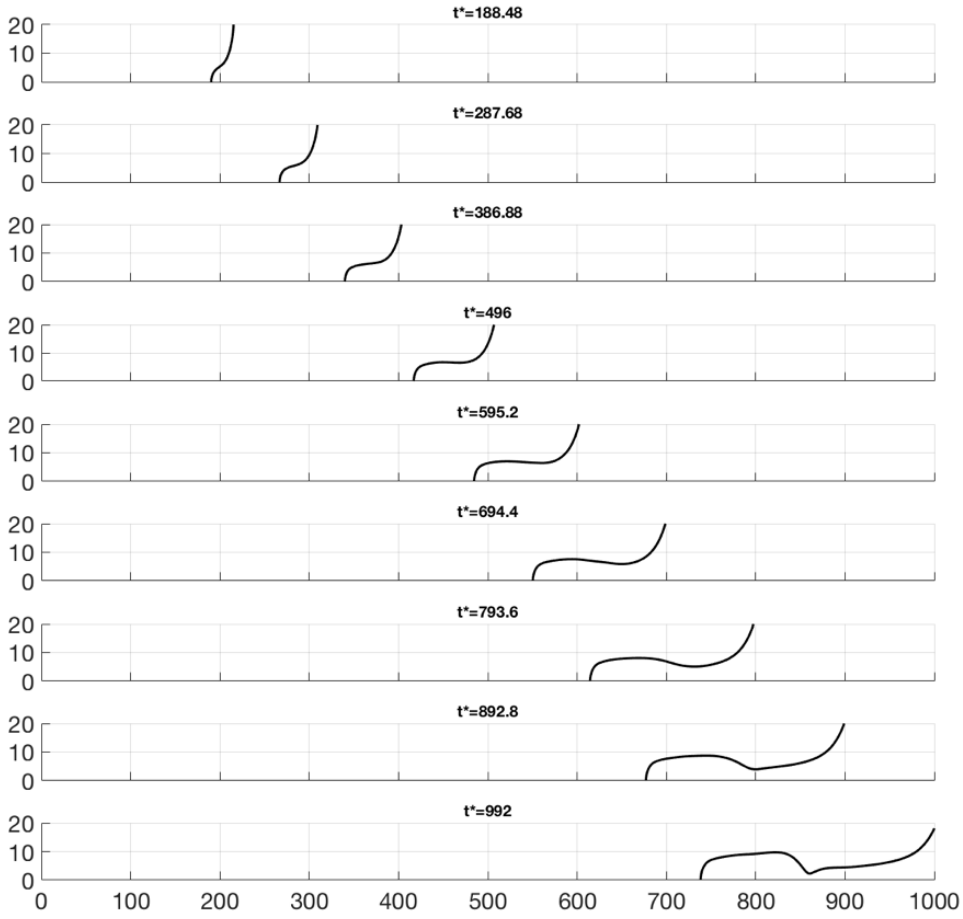

Figure 3-36: Time series of bulge formation: δ^* (y-axis), r^* (x-axis), for $\mathrm{d}x = 90°$ ($\mathrm{d}x = 100nm$) and Ca=0.04 (Setup L, Table 3.2).

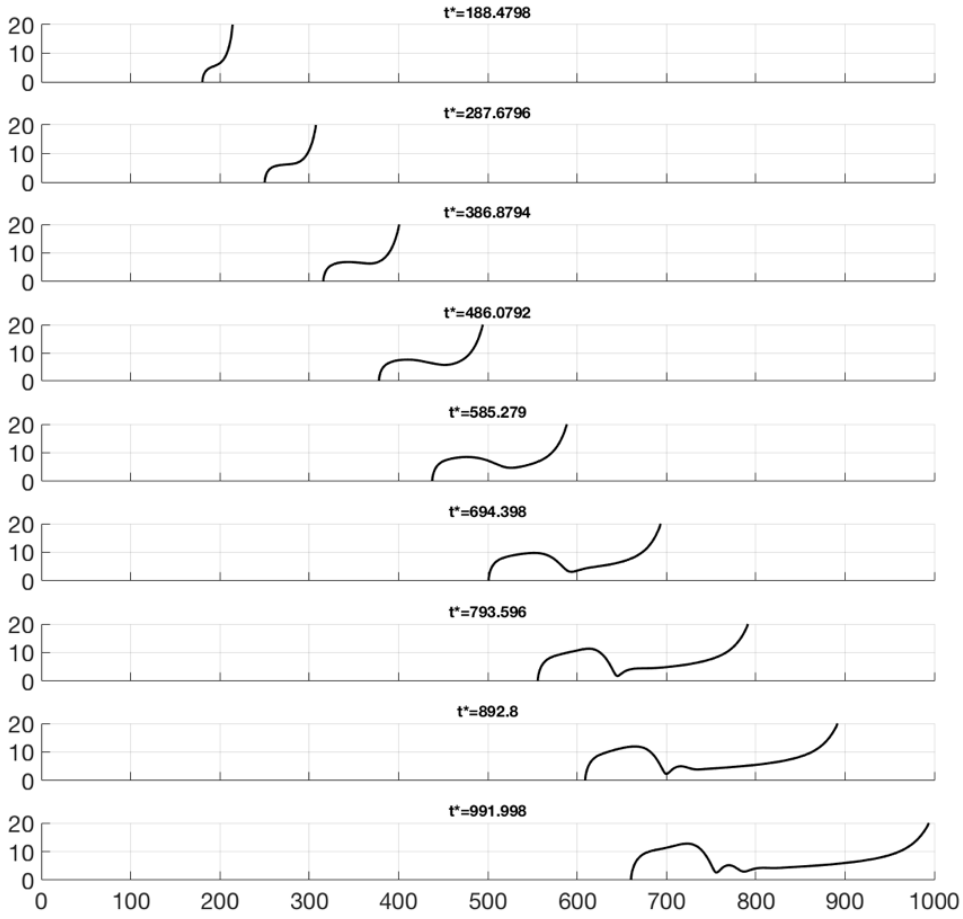

Figure 3-37: Time series of bulge formation: δ^* (y-axis), r^* (x-axis), for $\mathrm{d}x = 90°$ ($\mathrm{d}x = 100nm$) and Ca=0.06 (Setup L, Table 3.2).

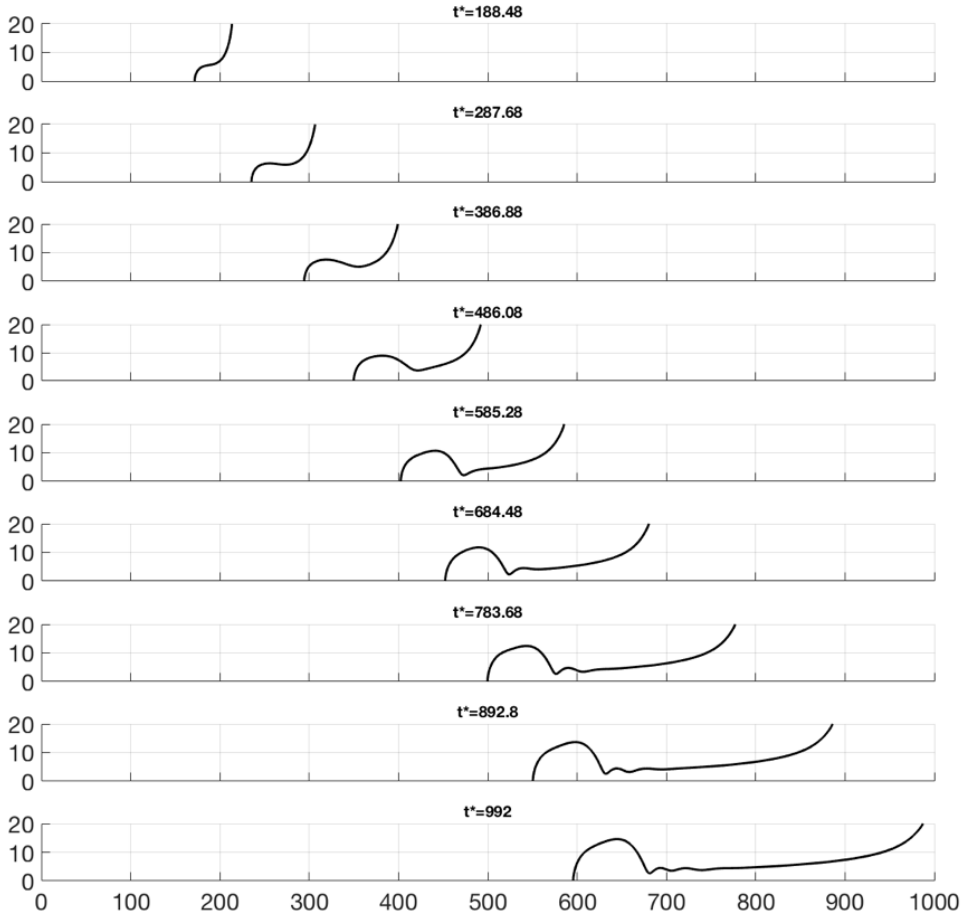

Figure 3-38: Time series of bulge formation: δ^* (y-axis), r^* (x-axis), for $\mathrm{d}x = 90°$ ($\mathrm{d}x = 100nm$) and Ca=0.08 (Setup L, Table 3.2).

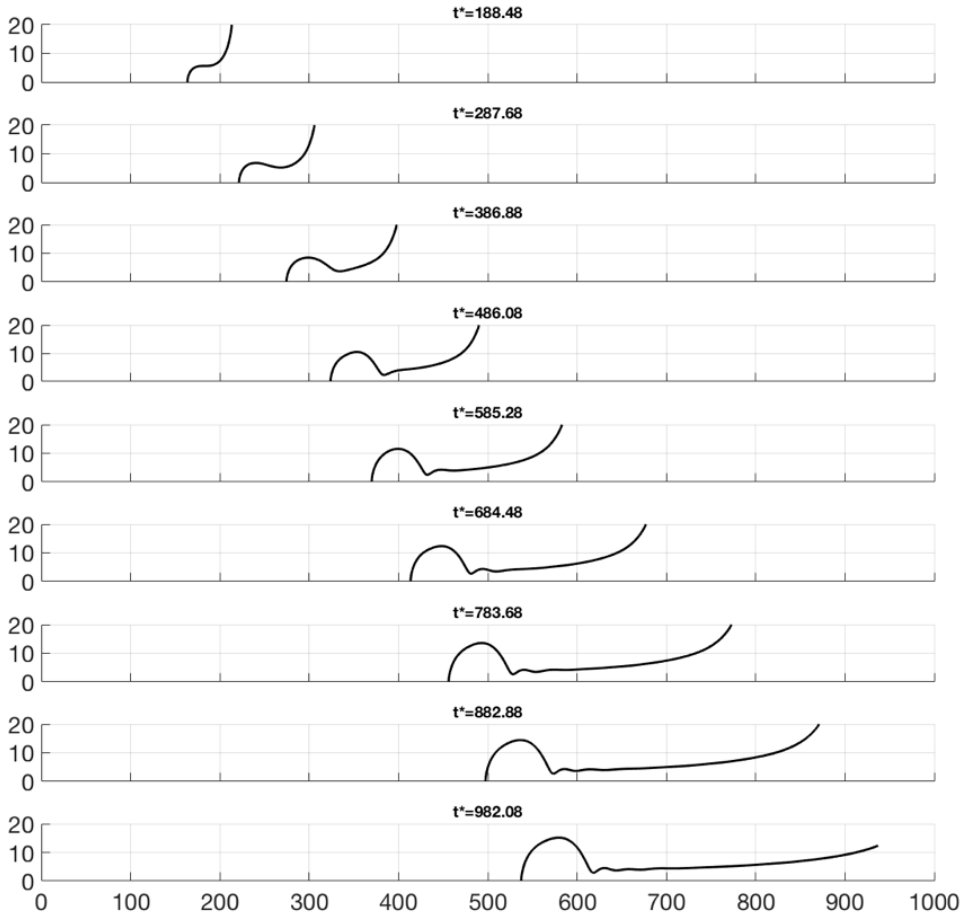

Figure 3-39: Time series of bulge formation: δ^* (y-axis), r^* (x-axis), for dx = 90° (d$x = 100nm$) and Ca=0.1 (Setup L, Table 3.2).

3.4.2 Linear shape of the extended microlayer

Scaling of $(\delta_0^*,\ C) = f(t^*, Ca)$

For times $t^* > 50$, the microlayer is well formed at the wall at it is possible to accurately fit the central region with a linear profile - see Figures 3-40, 3-41, 3-42 and 3-43 and in Appendix C:

$$\delta^* = \delta_0^* + \ Cr^* \tag{3.29}$$

Numerical results of microlayer shape at the wall can accurately be fitted to a

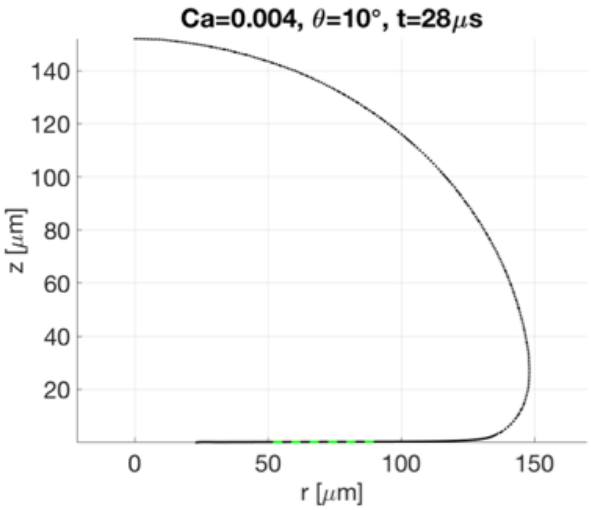

(a)

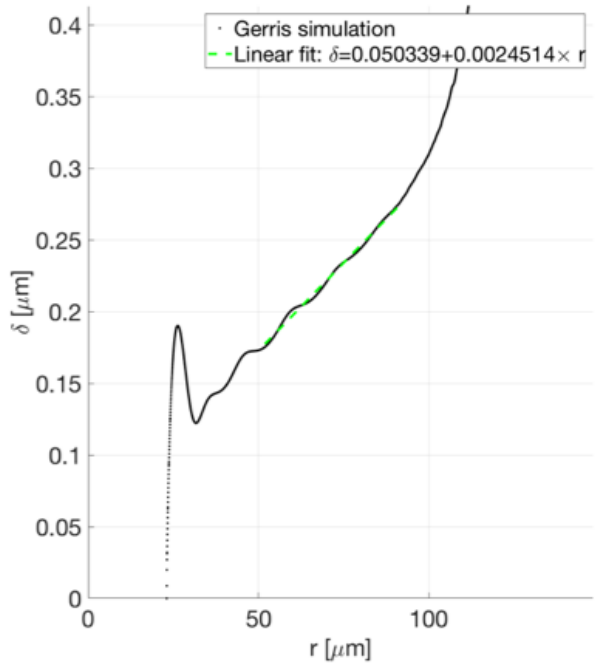

(b)

Figure 3-40: Profile (black dots) of the bubble (a) and microlayer (b), and the fitting performed in the central linear region (green dashed line), for Ca=0.004, dx = 10° (d$x = 1/32\mu m$).

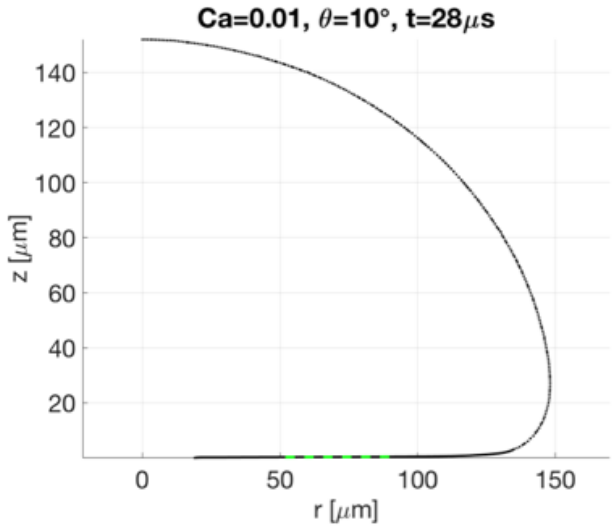

(a)

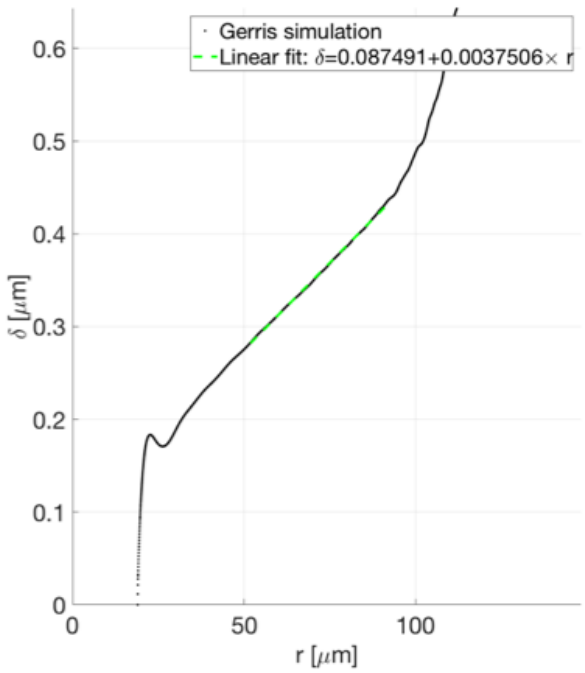

(b)

Figure 3-41: Profile (black dots) of the bubble (a) and microlayer (b), and the fitting performed in the central linear region (green dashed line), for Ca=0.004, dx = 10° (d$x = 1/32\mu m$).

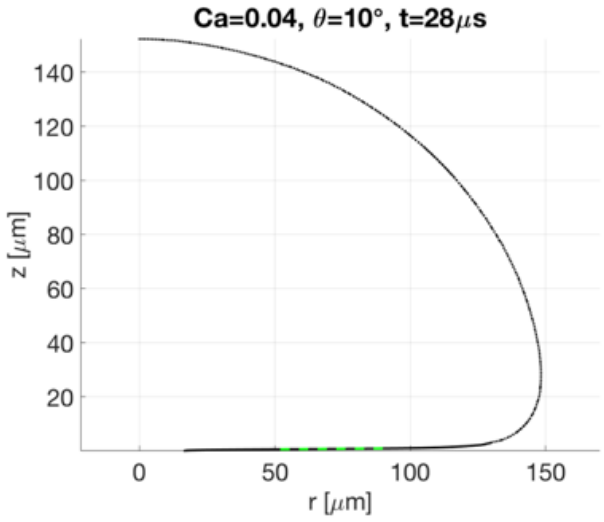

(a)

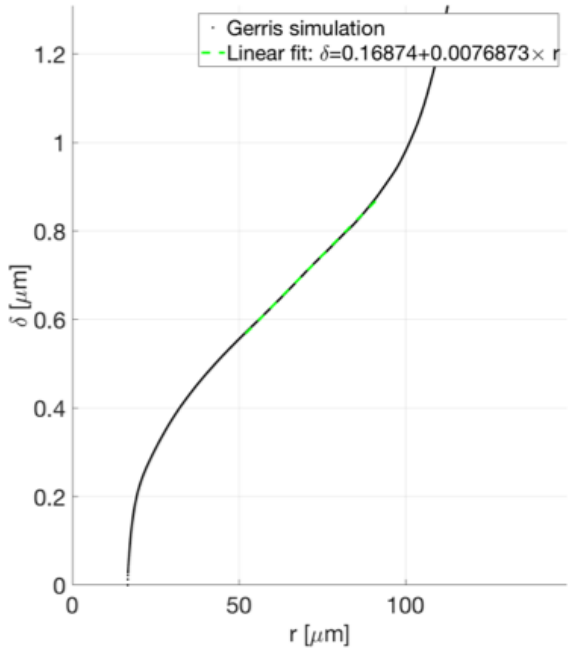

(b)

Figure 3-42: Profile (black dots) of the bubble (a) and microlayer (b), and the fitting performed in the central linear region (green dashed line), for Ca=0.004, dx = 10° (d$x = 1/32\mu m$).

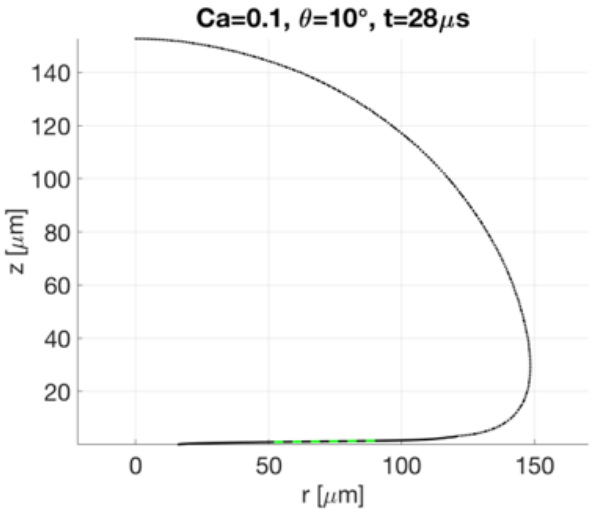

(a)

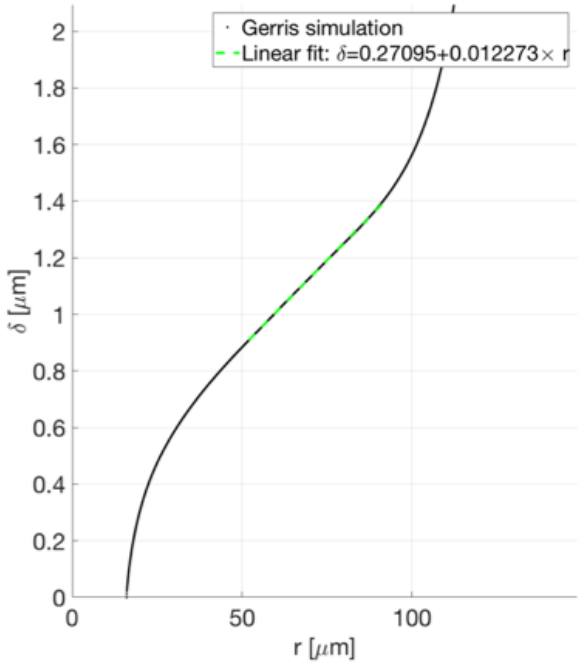

(b)

Figure 3-43: Profile (black dots) of the bubble (a) and microlayer (b), and the fitting performed in the central linear region (green dashed line), for Ca=0.004, dx = 10° (d$x = 1/32\mu m$).

linear profile in its central extended region. From this fitting of our numerical results, we obtain the scaling of both parameters ($\delta_0^*,\ C$) with Ca - see Figure 3-44 (a) and (b), respectively (Setup M, Table 3.2). Interestingly, both parameters scale with $\sqrt{\text{Ca}}$, which is consistent with qualitative trends discussed earlier: higher capillary numbers yield thicker layers. More specifically, we obtain:

$$\delta_0^*(t^* = 140) = 0.716\sqrt{\text{Ca}} \tag{3.30}$$

$$C(t^* = 140) = 0.042\sqrt{\text{Ca}} \tag{3.31}$$

Based on section 3.3.4 (Self-similarities in the central region), we obtain the general scaling with both time and Ca:

$$\begin{aligned} &\forall t^* > 50,\ \text{(no earlier fitting was reliable)},\ \forall \text{Ca} \in [10^{-3}, 0.1]: \\ &\qquad \delta_0^* = 0.716\sqrt{\text{Ca}}\sqrt{t^*/140} \end{aligned} \tag{3.32}$$

$$\begin{aligned} &\forall t^* > 50,\ \text{(no earlier fitting was reliable)},\ \forall \text{Ca} \in [10^{-3}, 0.1]: \\ &\qquad C = 0.042\sqrt{Ca}/\sqrt{t^*/140} \end{aligned} \tag{3.33}$$

Or more explicitly:

$$\begin{aligned} &\forall t^* > 50,\ \text{(no earlier fitting was reliable)},\ \forall \text{Ca} \in [10^{-3}, 0.1]: \\ &\qquad \delta_0^* = 0.06\sqrt{\text{Ca}}\sqrt{t^*} \end{aligned} \tag{3.34}$$

$$\begin{aligned} &\forall t^* > 50,\ \text{(no earlier fitting was reliable)},\ \forall \text{Ca} \in [10^{-3}, 0.1]: \\ &\qquad C = 0.5\sqrt{\text{Ca}}/\sqrt{t^*} \end{aligned} \tag{3.35}$$

We gain new insight on the actual y-intercept of the linear profile used to model the extended liquid microlayer in the central region underneath the bubble:

- At high Ca, $Ca = 0.1$, $t^* = 100$, $\delta_0/r_c = 0.2$: the y-intercept is not negligible compared to r_c

- At low Ca, $Ca = 0.001$, $t^* = 100$, $\delta_0/r_c = 0.02$: the y-intercept is negligible

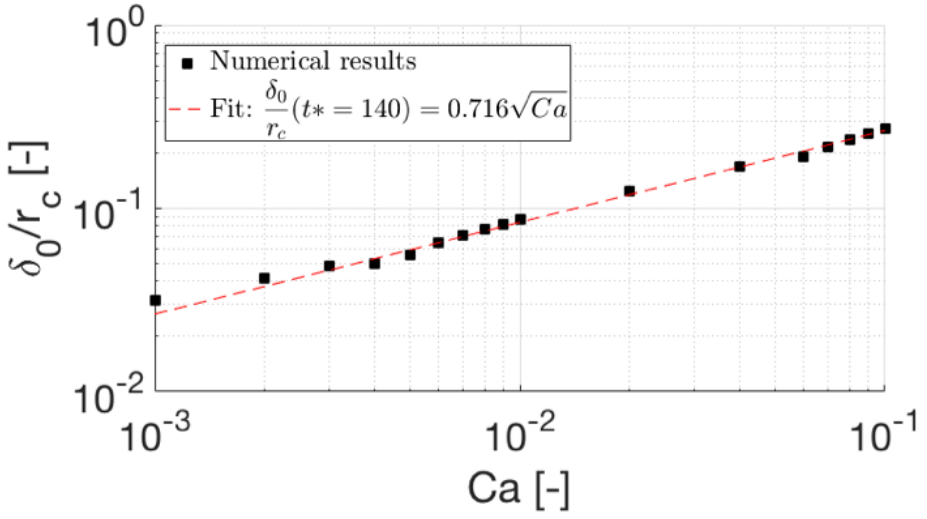

(a)

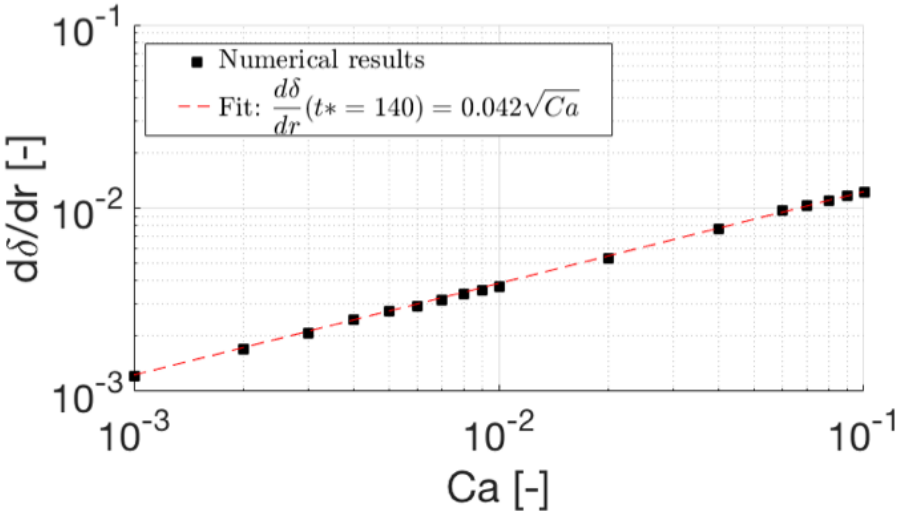

(b)

Figure 3-44: Scaling of δ_0/r_c(a) and C ($=d\delta/dr$) (b), the two dimensionless parameters (black dots) describing the central linear region of the extended microlayer, with $\sqrt{\text{Ca}}$ (dashed red line). $t^* = 140$, θ_{dx}=10°(dx=31.25nm). (Setup M, Table 3.2).

compared to r_c, and the linear profile could be modeled as a linear wedge of liquid extending from the origin (0,0).

Comparison with existing models and data

- Existing analytical model

  These results are consistent with [16] who obtained an analytical expression for the slope, noted C_{ana}, of the linear profile:

$$C_{ana} = C^{te}\sqrt{\nu_l t}/R_b, \quad \text{with } R_b = U_b t \text{ and } \nu_l = \mu_l/\rho_l. \tag{3.36}$$

  Rearranging Eq. 3.36, we obtain:

$$C_{ana} = C^{te}\sqrt{\mu_l t/(\rho_l U_b^2 t)} = C^{te}\sqrt{Ca\ t_c/t} = C^{te}\sqrt{\mathrm{Ca}}/\sqrt{t^*} \tag{3.37}$$

  with C^{te} in the range of 0.3-1.0 in [16].

- Existing experimental data

  Recent advances in microlayer thickness measurements at different radial locations and short time scales [114] uncovered two regimes based on Bond number Bo - see Figure 3-45, defined as:

$$\mathrm{Bo} = \rho_l r^2 U/t\sigma \tag{3.38}$$

  Rearrangement of Eq. 3.38, Bo yields:

$$\mathrm{Bo} = \rho_l U^2 t U/\sigma = Ut/r_c = t/t_c = t^* \tag{3.39}$$

  Results from [114] can be rearranged in the following form:

$$\mathrm{Bo} < 13\ (t^* < 13):\ C_{exp} = \delta/R_b = 0.13\sqrt{\mathrm{Ca}}/\sqrt{t^*}\mathrm{Bo}^{0.38} \tag{3.40}$$

  where C_{exp} denotes the slope of the microlayer profile in the central linear region.

$$\mathrm{Bo} \geq 13\ (t^* \geq 13):\ C_{exp} = 0.34\sqrt{\mathrm{Ca}}/\sqrt{t^*} \tag{3.41}$$

In practice, the time scale associated with this initial transient ($t^* < 13$) is very

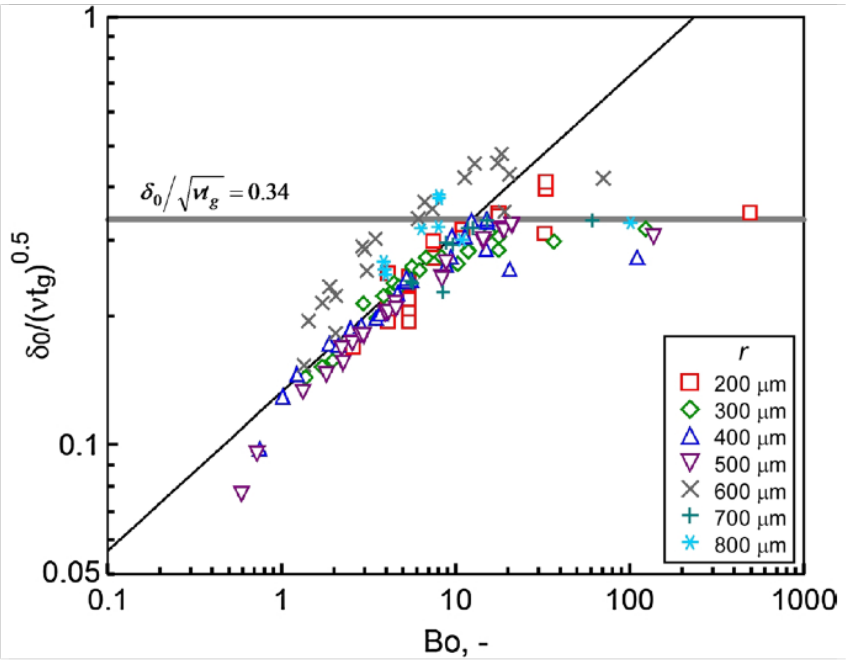

Figure 3-45: Initial microlayer thickness (made dimensionless with boundary layer thickness) versus Bond number [114]

small compared to the time scale of microlayer formation. In our simulations, microlayer formation lasts for tens of μs, which is over two order of magnitudes longer than the duration of the initial transient ($t^* = 13$ corresponds to $t = 0.65\mu s$). We use Eq. 3.41 to compare experimental results with our results obtained numerically, and confirm same functional form ($C \propto \sqrt{Ca}/\sqrt{t^*}$), and similar magnitudes: 0.34 (-) is obtained experimentally, 0.5 (-) is obtained numerically. Note experimental results spread between 0.25 and 0.5 (-) in Figure 3-45.

- Unpublished experimental data

  Most recent (and currently not published yet) experimental data from S. Jung & Prof. H. Kim, following previous work [46] [47], provides measurement of the microlayer shape (slope $C_{exp,2}$) for boiling water at 0.101MPa, $q'' = 209kW/m^2$,

$\Delta T_0 = 11.7°C$):

$$\begin{aligned} U_b(t = 0.41ms) &\approx 4.1\ (m/s) \\ C_{exp,2}(t = 0.41ms) &\approx 0.0039\ (-) \end{aligned} \tag{3.42}$$

The model presented above predicts $\hat{C}_{exp,2} = 0.0033$, a 16.5% difference with the measured slope $C_{exp,2}$. Note the prediction is sensitive to the bubble growth rate: for a change in U_b of 10%, the difference between predicted and measured slopes decreases from 16.5% to 7.2%. Also note that the uncertainty in the experimental measurement of the slope is not reported yet.

A remarkable result: microlayer slope independant of Ca

Rearranging Eq. (3.35) using $t^* = t/t_c = \rho_l U_b^3 t/\sigma$ and Ca=$\mu_l U_b/\sigma$ we obtain:

$$C = 0.5\sqrt{\mu_l/(\rho_l U_b^2 t)} = 0.5/\sqrt{t^{**}} \tag{3.43}$$

with $t^{**} = t/t_{c,2}$, and $t_{c,2} = \mu_l/(\rho_l U_b^2)$. Eq. (3.43) shows that the slope of the central region of the liquid microlayer that forms at the wall is independent of Ca - also shown in Figure 3-46. In practice, fluid properties (μ_l, ρ_l) are known. The bubble growth rate U_b then constitutes the single parameter needed to predict the slope of the liquid microlayer at the end of the inertia-limited phase of bubble growth during nucleate boiling, which is required in the initialization of current nucleate boiling simulations.

3.4.3 The extension radius r^*_{out}

We obtain from numerical simulations the radial location of the maximum of curvature at the interface, noted r_{out}, from which the thickness of the layer rapidly increases as it meets the macroscopic bubble cap at the bubble nose. The location of the maximum curvature can be normalized by the radius of the macroscopic bubble r_{max}, for various Ca in the range of 10^{-3} to 0.1, and times t^* from 40 to 200 - see Figure 3-47 (Setup M, Table 3.2). The normalized location r_{out}/r_{max} lies in the 0.9-0.95 range,

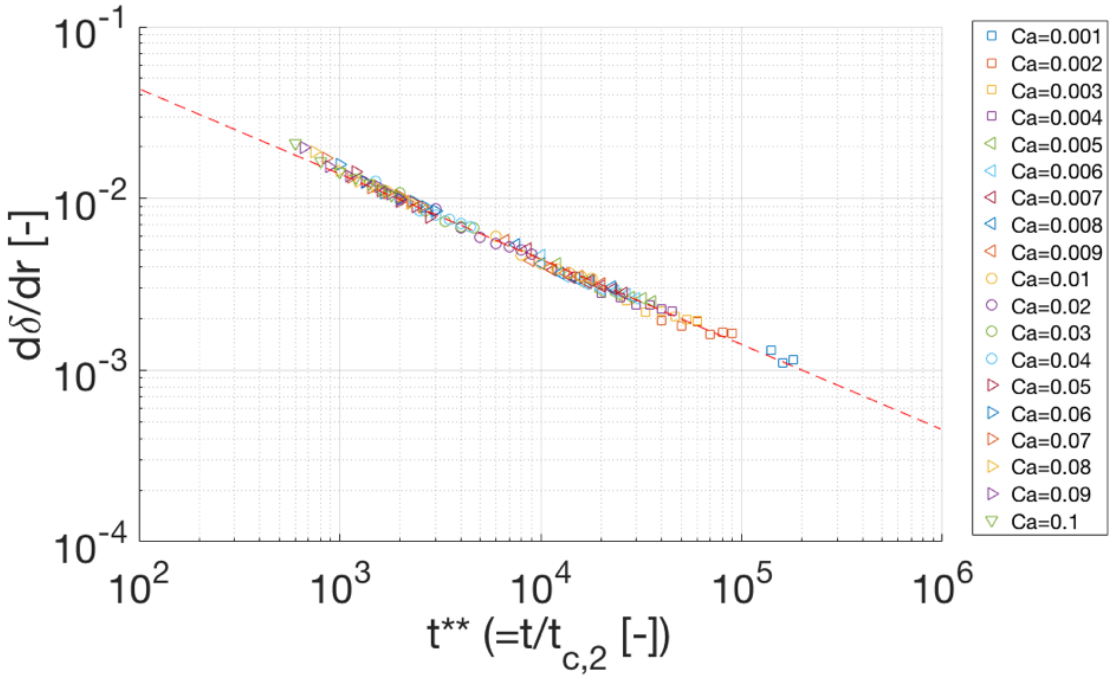

Figure 3-46: Plot of microlayer slope as a function of $t^{**} = t/\{\mu_l/(\rho_l U_b^2)\}$, for all simulated cases: Ca=0.001, 0.002, 0.003, 0.004, 0.005, 0.006, 0.007, 0.008, 0.009, 0.01, 0.02, 0.03, 0.04, 0.05, 0.06, 0.07, 0.08, 0.09, 0.1. Identical scaling with Cooper and Lloyd [16] ($C \propto 1/\sqrt{t^{**}}$) is obtained (dash line).

for all times t^* and Ca. The value of 0.9 is kept as a lower bound estimate. Using the characteristic length scale r_c, and since $r_{max} = R_{b,0} + U_b t$, we obtain an estimate of the dimensionless extension radius of the extended microlayer region:

$$r^*_{out} = (r_{out}/r_{max})(r_{max}/r_c) \approx 0.9(R_{b,0}/r_c + t^*) \tag{3.44}$$

3.5 Conclusions

In this work, we used Computational Fluid Dynamics with Interface Tracking Methods to numerically reproduce the hydrodynamics of bubble growth at a wall, and resolve the formation of the liquid microlayer at the wall with unprecedented resolution in space and time. The fluid considered was water in lab experiment and pressurized water reactor conditions. We identified the minimum set of dimensionless

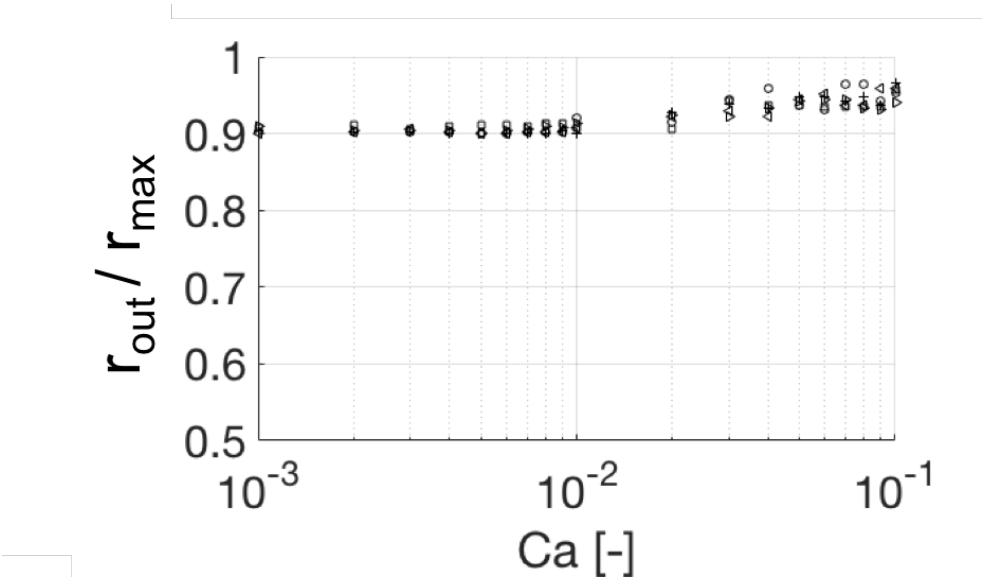

Figure 3-47: Radial location of the maximum of curvature at the interface r_{out}, normalized by the radial extension of the macroscopic bubble r_{max}, for various Ca in the range of 10^{-3} to 0.1, for times t^*=40 (squares), 80 (>), 120 (<), 160 (o), 200 (+). The normalized location lies in the 0.9-0.95 range for all t^* and Ca considered. (Setup M, Table 3.2).

parameters that controls microlayer formation, and reduced the parameter space for the conditions and fluids of interest:

$$\delta/r_c = f(r/r_c, t/t_c, Ca, \theta_{\mathrm{dx}}) \tag{3.45}$$

With δ the shape of the extended liquid microlayer.

We generated a large numerical database that discretizes the parameter space of interest, and built a generally applicable model for microlayer formation, to be used during the initialization of boiling simulations:

1. The wetted fraction underneath the bubble, $\alpha^* = (1-r_{min}/r_{max}) = f(\theta_{\mathrm{dx}}, t^*, Ca)$, informs the presence (or absence) of liquid microlayer underneath a growing bubble, for a given $(\theta_{\mathrm{dx}}, t^*, Ca)$ condition - see maps in Figure 3-18, 3-19, 3-20.

2. The central linear region of the microlayer $\delta^* = \delta_0^* + Cr^*$, for $r* \in [r_{min}^*, r_{out}^*]$, with r_{min}^* the position of the inner edge and r_{out}^* its extension radius:

$$\delta_0^* = 0.06\sqrt{Ca}\sqrt{t^*} \tag{3.46}$$

$$C = 0.5\sqrt{Ca}/\sqrt{t^*} \tag{3.47}$$

3. An estimate of the extension radius r_{out}^* of the liquid microlayer:

$$r_{out}^* \approx 0.9(R_{b,0}/r_c + t^*) \tag{3.48}$$

Comparison with previous work, both analytical [16] and experimental [114], show similar scaling of the central linear region, whose slope is found to be independent of Ca:

$$C = 0.5/\sqrt{t^{**}} \tag{3.49}$$

with $t^{**} = t/t_{c,2}$ and $t_{c,2} = \mu_l/(\rho_l U_b^2)$. Note that our numerical database is much broader than any experimental conditions previously explored.

In addition, this model provides an estimate of the extension radius of the extended microlayer, and maps of wetted fractions (based on hydrodynamics of the contact line) underneath the bubble at different times, and for the wide range of Ca and θ_{dx} (dx=100nm) of interest. Future work could further investigate additional effects such as thermal effects and mass transfer at the contact line that may modify the wetted fraction underneath the bubble. A physical mobility law $\theta = f(Ca)$ could also be used in replacement of the static contact angle used in this study.

This general model on microlayer formation resolves the initial and rapid phase of bubble growth in nucleate boiling, called inertia-controlled phase, which lasts a fraction of a milliseconds in the case of water at 0.101MPa. The following phase of

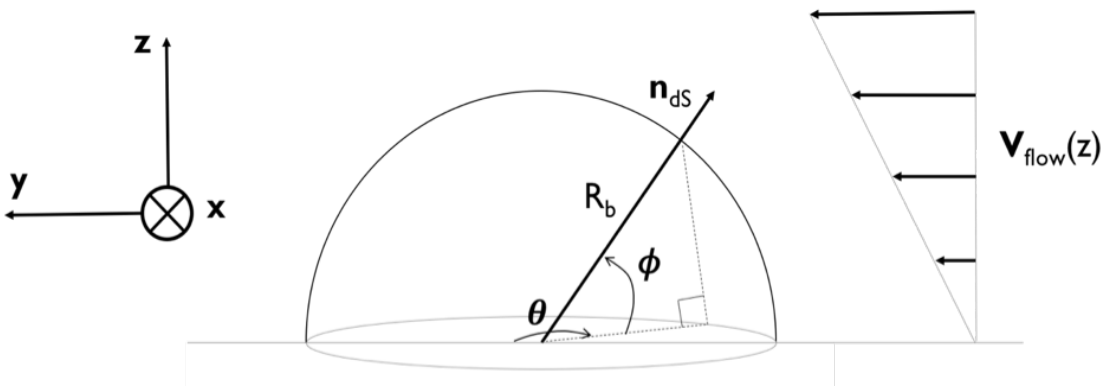

Figure 3-48: Sketch of the hemispherical bubble growing in the presence of an external flow

bubble growth, the thermal diffusion controlled phase, is much slower and lasts tens of milliseconds in the case of water at 0.101MPa. In practice, the present model allows initializing boiling simulations at the end of the rapid inertia-controlled phase of bubble growth during which the microlayer forms.

3.6 Towards a microlayer formation model in the presence of an external flow

In the presence of an external flow along the y-axis - see Figure 3-48, the dynamic pressure associated with the external flow may affects bubble growth dynamics. In an elementary surface dS at the interface, the superposition of forces normal to the interface can be written as:

$$\mathrm{d}\vec{F}_{\mathrm{withflow},\perp} = \mathrm{d}\vec{F}_{\mathrm{noflow},\perp} + \mathrm{d}\vec{F}_{\mathrm{flow},\perp} \tag{3.50}$$

with

$$\mathrm{d}\vec{F}_{\mathrm{noflow},\perp} = \frac{1}{2}\rho_l U^2_{b,\mathrm{noflow}}\ \mathrm{d}S\ \vec{n}_{\mathrm{d}S} \tag{3.51}$$

and

$$\mathrm{d}\vec{F}_{\mathrm{flow},\perp} = \frac{1}{2}\rho_l V^2_{\mathrm{flow}}\ \mathrm{d}S\ <\vec{n}_{\mathrm{d}S}\ .\ \vec{n}_{\mathrm{flow}}>\ \vec{n}_{\mathrm{d}S} \tag{3.52}$$

Expanding the scalar product we obtain:

$$\mathrm{d}\vec{F}_{\mathrm{withflow},\perp} = \frac{1}{2}\rho_l \; U^2_{b,\mathrm{noflow}}\{1 + (V_{\mathrm{flow}}/U_{b,\mathrm{noflow}})^2 cos(\theta)cos(\phi)\}\mathrm{d}S \; \vec{n}_{\mathrm{d}S} \tag{3.53}$$

3.6.1 Expansion velocity $U_{b,\mathbf{noflow}}$

Rayleigh [86] carried out the first analysis of bubble growth in an infinite pool of liquid. In general form, the bubble radius is controlled by the following governing differential equation:

$$\left(P_b - P_\infty\right)/\rho_l = R\ddot{R} + \frac{3}{2}\dot{R}^2 + 4\nu_l\frac{\dot{R}}{R} + \frac{2\sigma}{\rho_l R} \tag{3.54}$$

where P_b denotes the pressure within the bubble, P_∞ the far-field pressure, R the bubble radius, ν_l the kinematic viscosity of the liquid, ρ_l the density of the liquid, and σ the surface tension. An analytical solution exists for the special case of constant overpressure inside the bubble, when surface tension and liquid viscosity are neglected. The bubble radius R then increases linearly with time t:

$$R = \sqrt{\frac{2\Delta P}{3\rho_l}}t \tag{3.55}$$

In the inertia-driven growth phase, we consider the expansion velocity to be proportional to the square root of the pressure difference across the interface:

$$U_{b,\mathrm{noflow}} = \sqrt{\frac{2\Delta P}{3\rho_l}} \tag{3.56}$$

3.6.2 Effect of the flow in the vicinity of the wall

In the vicinity of the wall relevant to microlayer formation, $cos(\phi) \approx 1$ and Eq. (3.53) yields:

$$U_{b,\text{withflow}} = U_{b,\text{noflow}}\sqrt{1 + (V_{\text{flow}}/U_{b,\text{noflow}})^2\cos(\theta)},\ \text{if}\ (V_{\text{flow}}/U_{b,\text{noflow}})^2\cos(\theta) > -1$$
$$U_{b,\text{withflow}} = 0,\ \text{otherwise} \tag{3.57}$$

Qualitatively, we confirm:

- $U_{b,\text{withflow}} = U_{b,\text{noflow}}$ for $V_{flow} = 0$: no external flow
- $U_{b,\text{withflow}} \leq U_{b,\text{noflow}}$ for $\theta \in [\pi/2,\ 3\pi/2]$: growth at the front of the bubble slowed down by the flow
- $U_{b,\text{withflow}} \geq U_{b,\text{noflow}}$ for $\theta \in [-\pi/2,\ \pi/2]$: growth enhanced at the rear of the bubble

3.6.3 Flow induced by the growth of neighbor bubbles (velocities $\approx 1m/s$)

Boiling is initiated on so-called active cavities. In practical applications, and as the heat flux is increased, the number of such cavities also increases. As a result, the likelihood of bubbles growing near other bubbles is increased. Qualitatively with $V_{flow} \approx U_{b,\text{noflow}}$, we obtain that $U_{b,\text{withflow}}$ can range from 0 (no microlayer) to $\sqrt{2}U_{b,\text{noflow}}$. This is particularly relevant in the vicinity of neighbor bubbles, as qualitatively observed experimentally in Figure 3-49(courtesy of Matteo Bucci, 2016).

3.6.4 Forced convection in PWR

We here investigate the effect of the flow in PWR conditions on microlayer formation.

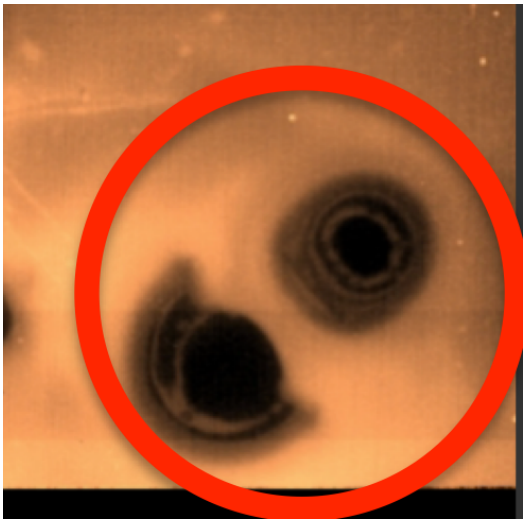

(a)

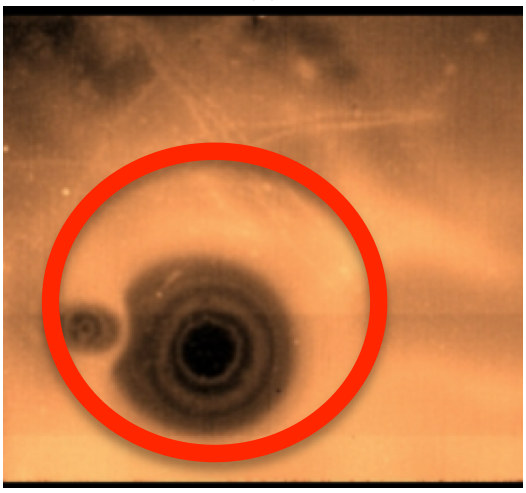

(b)

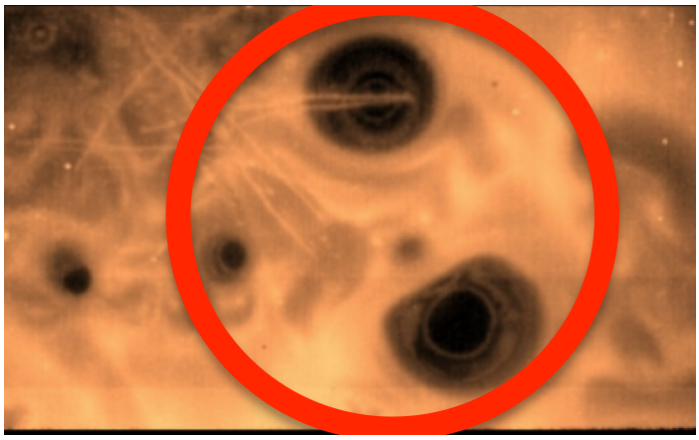

(c)

Figure 3-49: Qualitative Infra-Red observations of the boiling surface: when two neighbor bubbles grow next to each other, we note a front/rear asymmetry in the interference patterns underneath bubbles, and originating from the presence of the microlayer.

Geometric conditions

In pressurized water reactors, liquid water flows in fuel assemblies, which are square channels of side $214mm$. Each assembly contains a 17x17 array of cylindrical rods (e.g. 289 total rods) of diameter $D_{rod} = 9.5mm$. The cross section of the assembly can be divided in 289 unit cells each composed of one cylindrical rod and part of the surrounding coolant - see Figure 3-50 [104].

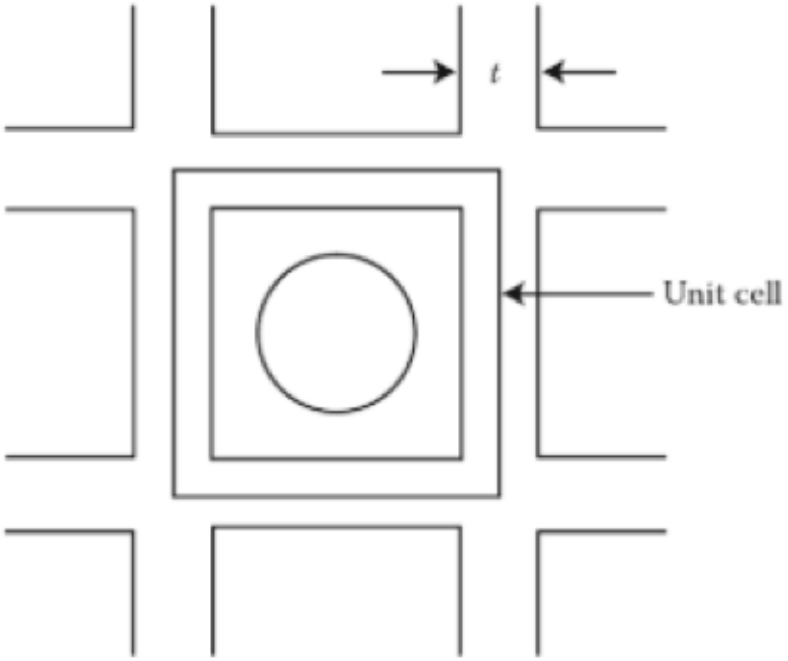

Figure 3-50: Definition of unit cell in PWR assembly [104]

Fluid properties

We consider the upper side of the fuel assembly, where the coolant in normal operating conditions is liquid water at approximately 604K and 15.5MPa. Liquid water properties at such conditions are as follow:

- Liquid water density ($T = 604K,\ P = 15.5MPa$): $\rho_l = 646.1kg/m^3$
- Liquid water viscosity ($T = 604K,\ P = 15.5MPa$): $\mu_l = 75.36E-6Pa.s$

Flow conditions

The cross sectional flow area in a unit cell is:

$$A_f = A_{\text{unit cell}} - A_{\text{rod}} = (158.46 - 70.88) = 87.58 \ (mm^2) \tag{3.58}$$

The wetted parameter P_w is simply the circumference of the outer-radius of the cylindrical rod:

$$P_w = D_{rod} = 29.85 \ (mm) \tag{3.59}$$

Hence the hydraulic diameter for the considered flow is:

$$D_h = 4A_f/P_w = 11.74 \ (mm) \tag{3.60}$$

The total mass flow rate in the assembly is $92.26kg/s$, which yields a mass flow rate $(dm/dt)_{\text{unit cell}}$ per unit cell:

$$(dm/dt)_{\text{unit cell}} = 92.26/289 = 0.32 \ (kg/s) \tag{3.61}$$

Based on fluid properties, we obtain the average velocity U in the unit cell:

$$U = (dm/dt)_{\text{unit cell}}/(\rho_l A_f) = 5.66 \ (m/s) \tag{3.62}$$

This yields a Reynolds number Re in the turbulent regime:

$$Re = \rho_l U D_h/\mu_l = 5.7E + 5 \ (-) \tag{3.63}$$

We here consider fresh rods (no oxidation), and estimate the friction coefficient f using the McAdams correlation [70] applicable in the conditions of interest, namely smooth surface and $Re = 5.7E + 5$:

$$f = 0.184Re^{-0.20} = 0.0130 \ (-) \tag{3.64}$$

Roughness of metal-oxide interface of fuel rods at different stages of oxidation can also be found at [84]. With an estimate of the friction factor, we then obtain the wall shear stress τ_w:

$$\tau_w = (f/4)\rho_l U^2/2 = 33.4\ (N/m^2) \tag{3.65}$$

And the shear velocity:

$$v_{z,0} = \sqrt{\tau_w/\rho_l} = 0.23\ (m/s) \tag{3.66}$$

with the characteristic length scale:

$$y_0 = \mu_l/(\rho_l v_{z,0}) = 0.51\ (m) \tag{3.67}$$

Using Martinelli's model [69] we obtain the turbulent velocity profile as a function of the position above the wall - see Figure 3-51:

$$\begin{aligned} 0 \leq y \leq 5y_0\ (=2.6\mu m),\ v_z(y) &= v_{z,0}(y/y_0) \\ 5y_0 \leq y \leq 30y_0\ (=15.4\mu m),\ v_z(y) &= v_{z,0}\{-3.05 + 5\ln(y/y_0)\} \\ y > 30y_0\ (=15.4\mu m),\ vz(y) &= v_{z,0}\{5.5 + 2.5\ln(y/y_0)\} \end{aligned} \tag{3.68}$$

This velocity distribution is only useful if we are able to estimate the region at the wall that affects microlayer formation at this high pressure of 15.5MPa. With such estimate of the thickness at the wall, we can obtain from the velocity profile the average velocity relevant to microlayer formation in PWR conditions. At atmospheric pressure, a thickness of tens of microns typically describes that region near the wall relevant to microlayer formation. At 15.5MPa, the size of bubbles is greatly diminished, and we expect that the extent of that region at the wall to be greatly diminished as well.

Average velocity in the near wall region relevant to microlayer formation

In the case of water at 0.101MPa the thickness of the microlayer δ_{max} is found in the range: $\delta_{max} \approx 1 - 10\mu m$ [46] [51] [54] [43], while bubble size is found in the millimeter range: $R_b \approx 1mm$. The ratio between the two scales is: $\delta_{max}/R_b \approx 10^{-3} - 10^{-2}$ $(-)$.

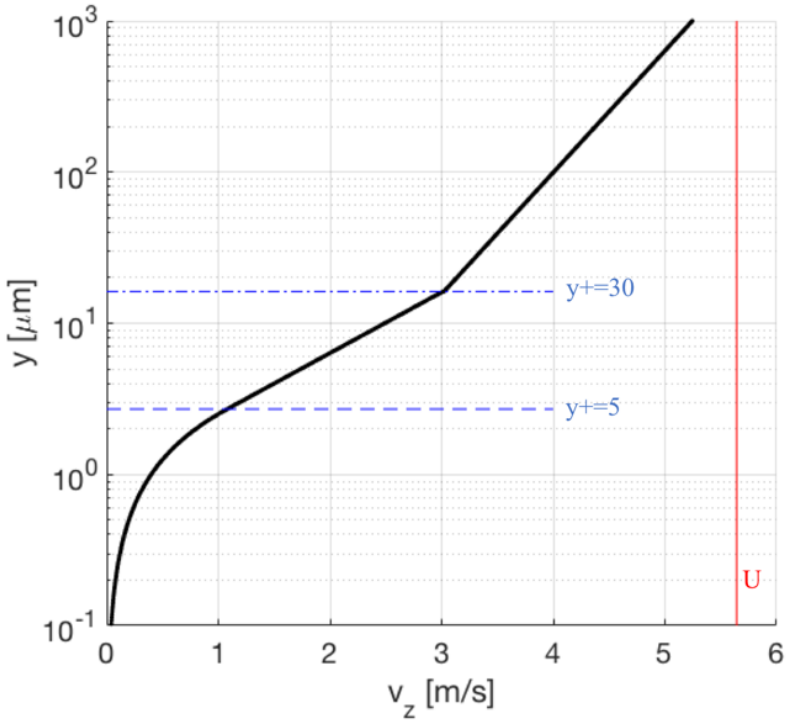

Figure 3-51: Turbulent velocity profile at the wall obtained for liquid water in PWR conditions [69].

In the case of water at 15.5MPa, we were not able to find any estimates of the height of the bubble nose (defined in Figure 3-12), but a review [102] provides estimates of the bubble size at 15.5MPa: $R_b \approx 0.1mm$ - see Table 3.4.
Assuming the ratio between the two scales δ_{max}/R_b remains similar, we obtain an estimate of the region near the wall relevant to microlayer formation at 15.5MPa:

$$\delta_{max}(15.5MPa) \approx 10^{-4} - 10^{-3}\ (mm) \tag{3.69}$$

With this estimate of the thickness δ_max relevant to microlayer formation at the wall at 15.5MPa, we can estimate the average velocity based on the turbulent velocity profile obtained earlier:

$$\begin{aligned} V_m(y \in [0; \delta_{max}]) &\approx 0.02 - 0.2\ (m/s) \\ U_{b,\text{noflow}} &\approx 0.1 - 10\ (m/s) \end{aligned} \tag{3.70}$$

in PWR conditions. The flow is expected to only affect a small fraction of activated cavities in PWR conditions.

3.6.5 Conclusions

We propose to extend the model for microlayer formation in the absence of external flow to include the effect of an external flow by adjusting the bubble growth rate $U_{b,\text{noflow}}$ by $U_{b,\text{withflow}}$:

$$U_{b,\text{withflow}} = U_{b,\text{noflow}}\sqrt{1 + (V_{\text{flow}}/U_{b,\text{noflow}})^2\cos(\theta)},\ \text{if}\ (V_{\text{flow}}/U_{b,\text{noflow}})^2\cos(\theta) > -1$$
$$U_{b,\text{withflow}} = 0,\ \text{otherwise} \tag{3.71}$$

Depending on the velocity of the external flow in the vicinity of the wall, compared with the bubble growth rate $U_{b,\text{noflow}}$ in the absence of flow, the effect of the flow can be:

- negligible ($V_{\text{flow}}/U_{b,\text{noflow}} << 1$), such as in most cases of steam bubbles growing in PWR conditions (high Re and high pressure).
- appreciable ($V_{\text{flow}}/U_{b,\text{noflow}} \approx 1$), such as in the case of the growth of neighbor bubbles
- dominant ($V_{\text{flow}}/U_{b,\text{noflow}} >> 1$), possibly achieved in the case of strong forced convection velocities (high Re) and large bubbles (low pressures).

Table 3.4: Review of available experimental data on bubble departure diameter in flow boiling [102].

Parameter	Sugrue et al.	Klausner et al.	Zeng et al.	Prodanovic et al.	Situ et al.	DEBORA	PWR hot channel
Fluid	Water	Refrigerant R113	Refrigerant R113	Water	Water	Refrigerant R12	Water
Orientation	0°, 30°, 45°, 60°, 90°, 180°[*]	Horizontal flow	Horizontal flow	Vertical upflow	Vertical upflow	Vertical upflow	Vertical upflow
Channel	Rect., D_e = 16.7 mm	Rect., D_e = 25 mm	Rect., D_e = 25 mm	Annular, D_e = 9.3 mm	Annular, D_e = 19.1 mm	Pipe, D_e = 19.2 mm	Rod Bundle, D_e = 11.8 mm
Mass flux (G) [kg/m^{2}s]	250–400	112–287	150–315	76.6–766	466–900	2000–3000	~3700
Heat flux (q'') [kW/m^2]	50, 100	11–26	5.8–16.8	200–1000	54–206	73, 76	1000–1400
Subcooling [°C]	10°, 20°	Saturation	Saturation	10°, 20°, 30°	2–20°	13–29°	10–30°
Pressure [kPa]	101, 202, 505	101	101	105–300	101	1460–2620	1550
Reynolds # $\frac{GD_i}{\mu_l}$	11,800–34,500	6000–17,000	8600–18,000	600–6000	2.9×10^4–5.7×10^4	3.05×10^5–4.47×10^5	~5.3×10^5
Froude # $\frac{G^2}{\rho_l^2 g D_i}$	0.42–1.06	1.4–3.5	6.2–17.8	0.7–7.0	6.2–12.5	22–54	~199
Typical Bubble Size (d_b)	0.23–1.0 mm	0.16–0.46 mm	0.19–0.46 mm	0.31–2.68 mm	0.15–0.61 mm	0.3–0.6 mm	~0.1 mm[a]
Contact angles	α = 91°, β = 8°	α = 45°, β = 36°	α = 45°, β = 36°	α = 45–75°, β = 40–70°	α^a = 55° β^a = 35°	None measured	α^b = 30–50° β^b = 5–15°
Boiling # $q''/h_{lg}G$	1.11×10^{-7}–8.49×10^{-5}	2.73×10^{-7}–1.66×10^{-6}	1.31×10^{-7}–7.99×10^{-7}	1.16×10^{-7}–5.79×10^{-6}	2.66×10^{-8}–1.96×10^{-7}	3.23×10^{-4}–4.36×10^{-4}	2.80×10^{-7}
Jakob # $\frac{c_{pl}(T_w - T_{sat})}{h_{lg}}$	0.0056–0.00934	0.089–0.11	0.036–0.08	0.0056–0.00934	0.0056–0.0187	0.976–1.33	0.0465
Eotvos (or Bond) # $\frac{\Delta\rho g d_b^2}{\sigma}$	0.008–0.159	0.027–0.226	0.038–0.226	0.015–1.148	0.003–0.059	2.3–4.6	0.0103
Morton # $\frac{g\mu_l^4 \Delta\rho}{\rho^2 \sigma^3}$	3.91×10^{-13}	9.18×10^{-11}	9.18×10^{-11}	1.28×10^{-12}	3.91×10^{-13}	2.6×10^{-11}–1×10^{-10}	5.95×10^{-12}
Weber # $\frac{G^2 d_b}{\rho_l \sigma}$	0.255–2.834	0.101–1.898	0.214–2.286	0.032–27.97	0.577–8.75	0.73x10^3–2.18×10^3	495.53

[*] Note 0° corresponds to a downward-facing horizontal heater, 90° is a vertical heater, and 180° is an upward-facing horizontal heater.

[a] Since contact angles were not measured, these values are an approximation suggested by Yeoh et al. Yeoh et al. (2008), specifically, an equilibrium bubble contact angle can be taken as 45°, and advancing and receding angles can be estimated as $\alpha = \theta + 10°$ and $\beta = \theta - 10°$.

[b] Assumed ranges. High pressure water on oxidized Zircaloy is well wetting.

Chapter 4

Experimental study of bubble growth rates at short time scales during nucleate pool boiling of water

4.1 Motivation

In the previous chapter, we conclude that liquid properties, namely liquid viscosity and density, as well as bubble growth rates at early times (tens of μs) control microlayer formation. While liquid water properties are well known, it is unclear how existing models on initial bubble growth rate [71] perform at very early times - see Figure 4-1.

In this chapter we discuss how to bridge this gap by modifying an existing pool boiling experiment at MIT to specifically measure bubble dynamics at very early times with unprecedented temporal and spatial resolutions.

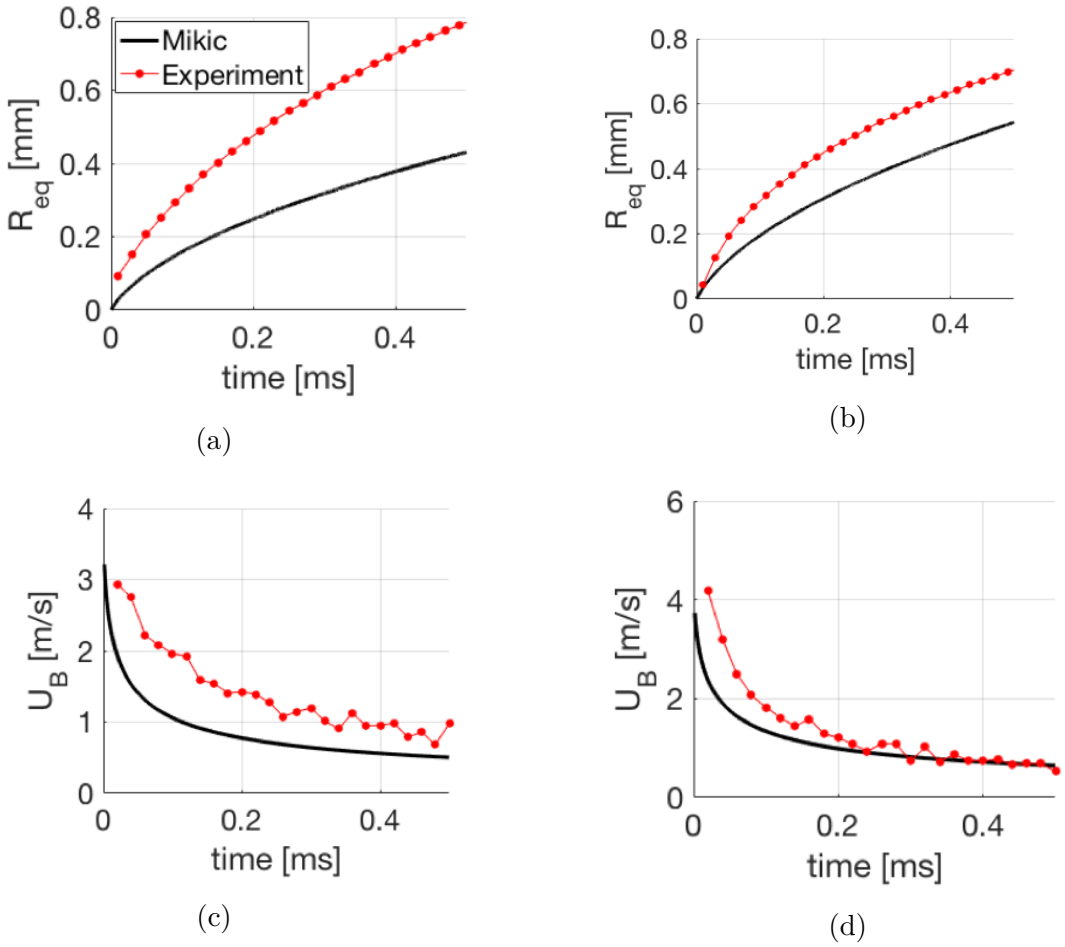

Figure 4-1: Experimental results (red dots) of equivalent bubble radius (a)(b) and bubble growth rates (c)(d) over time, in the case of water boiling in lab experiments (unpublished data, Kim 2016), and corresponding prediction from [71] (black solid line), for two experimental runs: $q" = 114kW/m^2$ and initial wall temperature $T_w = 109°C$ (a)(c), and $q" = 209kW/m^2$ and initial wall temperature $T_w = 111.7°C$ (b)(d).

4.2 Experimental setup

This work has been performed at the Green Lab at MIT with substantial help from Prof. Matteo Bucci, Dr. Reza Azizian, Guanyu Su, and Artyom Kossolapov.

4.2.1 Modification of existing pool boiling setup

A pool boiling experimental setup has been built and validated in [32], and improved in [24]. A pool boiling cell allows boiling water at saturated conditions at 0.101MPa,

while visualizing the boiling surface from the side through lateral windows of observation, and from underneath. A particularly thin Indium-Tin-Oxyde layer deposited on a transparent sapphire substrate serves as heater and allows observing the boiling surface from underneath using a high speed video camera - see Figure 4-2. The pur-

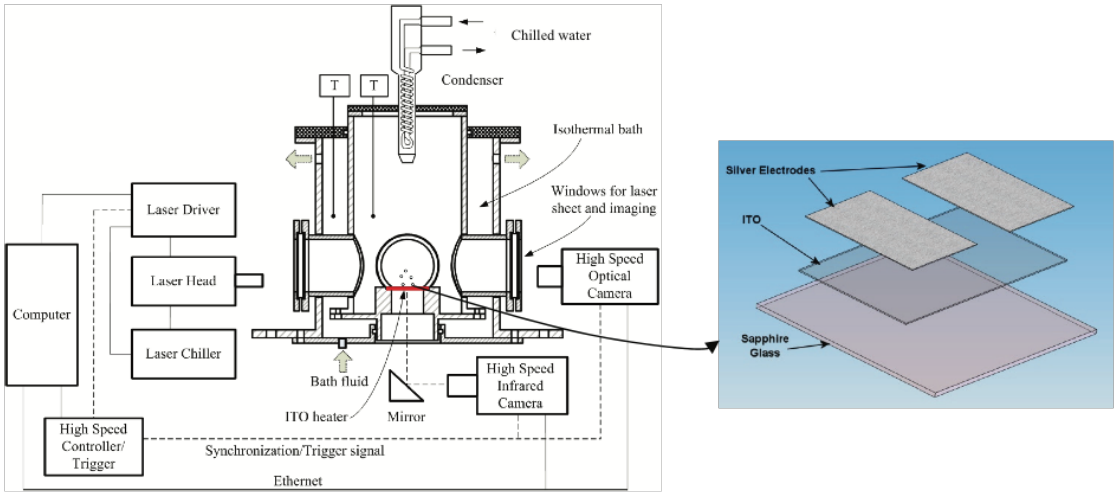

Figure 4-2: Pool boiling experiment setup (left) as in [24], and details on the heater composition (right)

pose of our experimental study is to achieve high resolution in time (tens of μs) and space (tens of μm) in measuring the bubble growth rates over time. In this particular case of initial bubble growth in saturated conditions, the bubble is fairly grows hemispherically. As a consequence, a side view of the bubble becomes equivalent to a bottom view of the bubble in order to obtain its radius over time.

As the frame rate used with the high speed video camera (HSV) is increased from a few thousands frames per second in [24] up to 160,000 frames per second (highest possible with the current camera, which yields a $6.25\mu s$ resolution), the need for sufficient lighting is dramatically increased: a powerful light is needed as close as possible to the boiling surface in order to minimize absorption from the liquid water and maximize contrast seen by the HSV. We modify the setup in [24] to allow lighting from the top, and imaging the bubble from the bottom, using the high speed video camera. In addition, we use a hot mirror at the bottom (which reflects part of the IR

light and transmit visible light) to allow gathering both the temperature distribution at the boiling surface, and the measurement of bubble growth, from the same window of observation underneath the boiling surface - see Figure 4-3, and Figure 4-4.

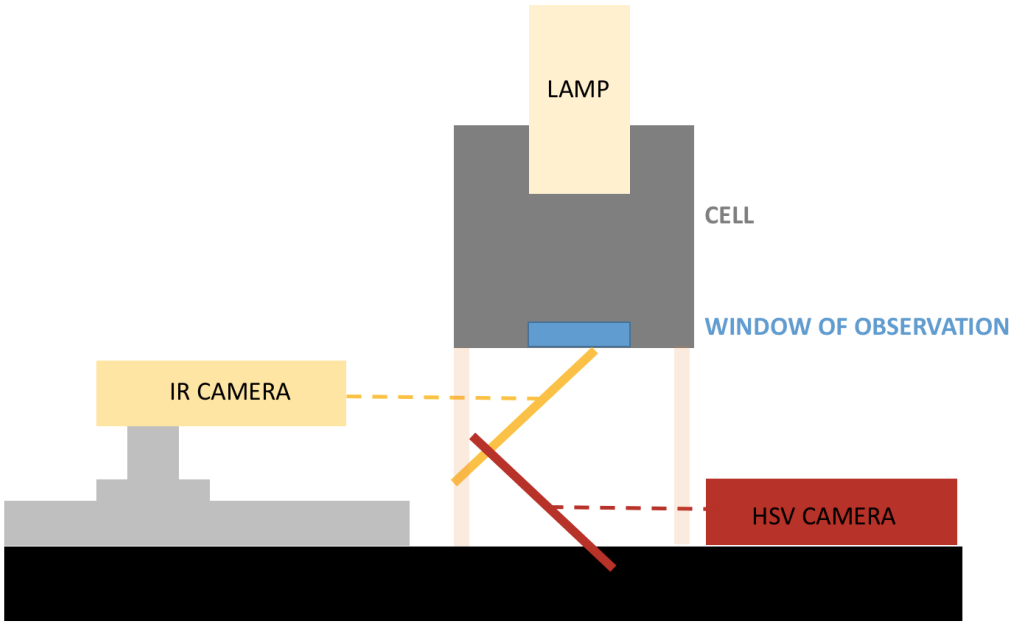

Figure 4-3: Modified pool boiling experimental setup from [24] to measure bubble growth rates at very early times with high resolution in time and space. We simultaneously measure the temperature distribution at the boiling surface.

4.2.2 Experimental procedure

Infra-Red (IR) camera calibration

The Infra-Red (IR) camera calibration is done in two steps:

1. Non-uniformity correction: each pixel on the IR camera sensor may have slightly different response to same IR light. In order to compensate for such non-uniformity on the IR sensor, we use two calibration procedures for which the IR image is uniform: 1) the image of a reflective metal representative of the IR image of the heater at room temperature, and 2) the image of a black body that emits same IR as heater at $50°C$.

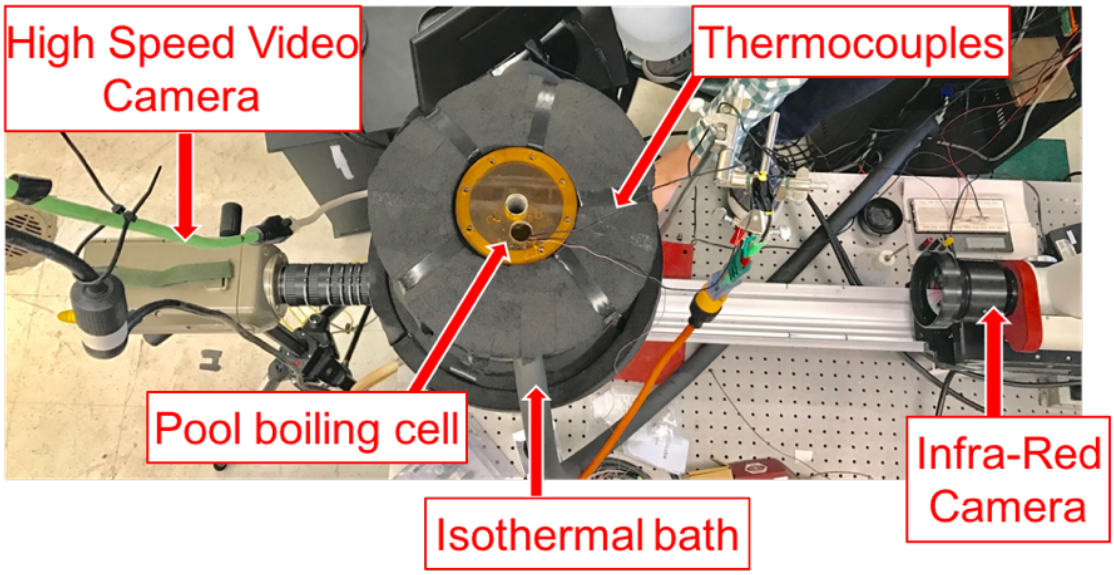

(a)

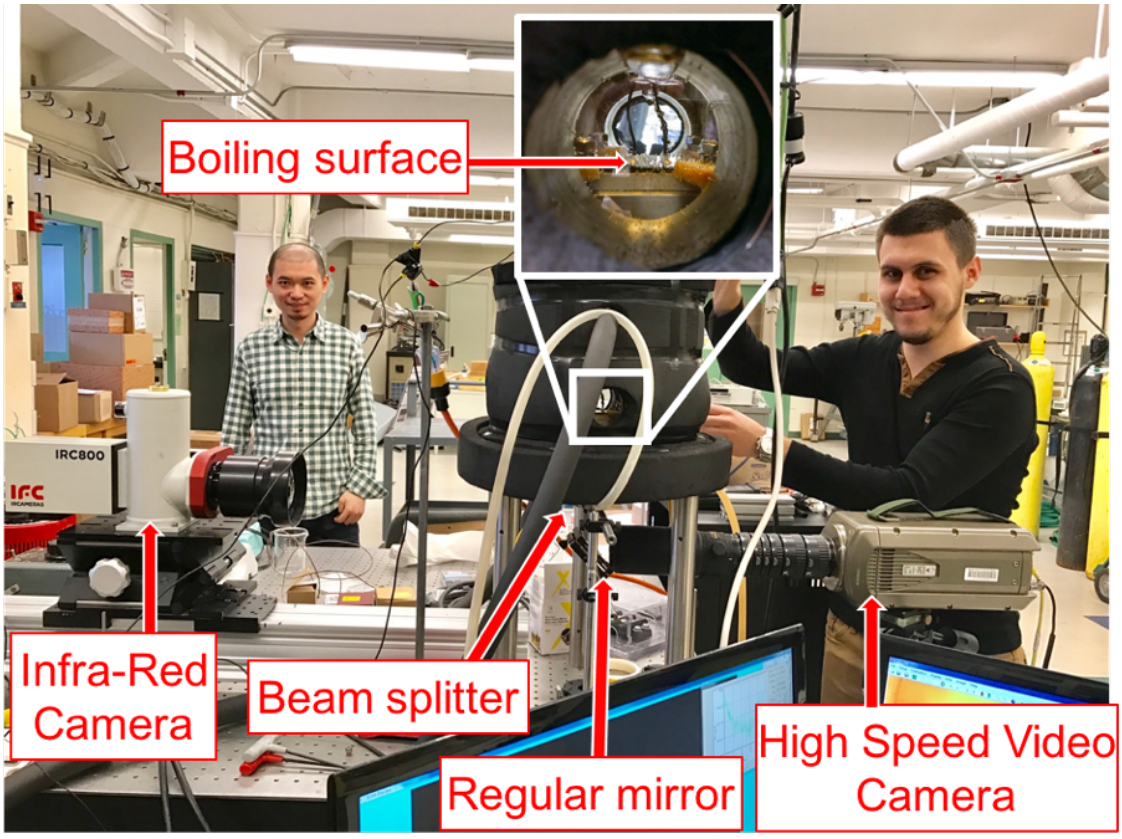

(b)

Figure 4-4: Top view (a) and side view (b) of the experimental setup

2. Calibration: turning radiation counts into a temperature measurement. Every $5°C$ we take a picture of the heater, and record the local temperature from a thermocouple in contact with the heater inside the boiling cell. The trace of temperature vs radiation counts is used to calibrate the IR camera through an in-house calibration model [9].

High Speed Video (HSV) camera calibration

Once the optical setup is finalized, we take a picture of an object of known dimensions with the HSV and deduce the resolution per pixel (for the given optical setup). With the use of extension rings, we obtain a resolution of $12.4\mu m$/pixel. At the rate of 130,000 frames per second, we reach a temporal resolution of $7.7\mu s$.

Synchronization of IR and HSV cameras

The synchronization of both cameras with the power generator is achieved using an (in-house) electronic circuit that triggers both cameras simultaneously at a respective recording rate of 2,500 (IR) and 130,000 (HSV) frames per second.

Experimental procedure

We heat up the DI water using an isothermal bath, to bring the liquid water from room temperature to saturation temperature. Two thermocouples are used to confirm the water is at saturation temperature: one in the bulk and one at the heater surface. We follow two steps:

1. Pre-boiling procedure.

   We perform a series of boiling tests (5min or longer) on the boiling surface to remove air entrapped in surface cavities (so-called degassing).

2. Boiling procedure.

   We initiate a step in voltage across the heater, while triggering synchronized recording of the boiling surface with HSV (130,000fps) and IR (2,500 fps). Properties of the heater are as follow: $R_{heater} = 4\Omega$, $S_{heater} = 2cm \times 0.9cm$.

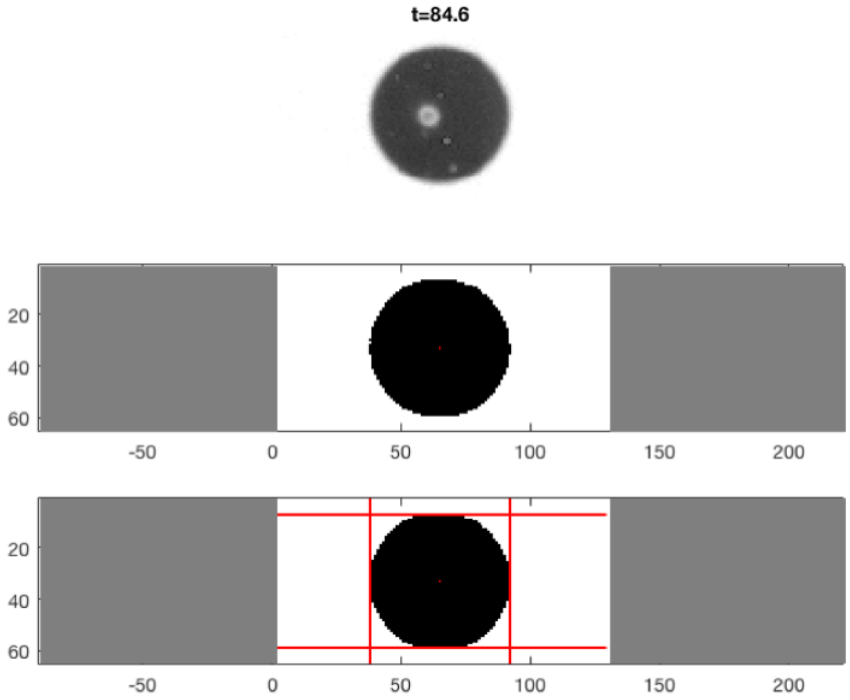

Figure 4-5: Typical result from HSV camera (top), processed into a black and white image (middle) centered around the apparent location of the nucleation site - see red dot. Top, bottom, left and right edges of the bubble interface are obtained from systematic image processing (red lines, bottom panel). X and Y-axis in middle and bottom panels refer to pixels from the centered HSV image (original image is a 256x128 pixel image). Heat flux is $q" = 555kW/m^2$, $t = 84.6\mu s$ after boiling incipience.

4.3 Experimental results and comparison with existing models

A typical result obtained at a heat flux of $q" = 555kWm^2$ from the HSV camera is shown in Figure 4-5.

We track four edges of the bubble interface over time to confirm its hemispherical growth and obtain its radius as a function of time - namely the top, bottom, right and left edges of the bubble, see Figure 4-5 bottom panel. The HSV window of observation is made of 256 pixels $\times$ 128 pixels. As the bubble grows on the heater surface, its edges reach the boundaries of the window of observation at different times, as shown

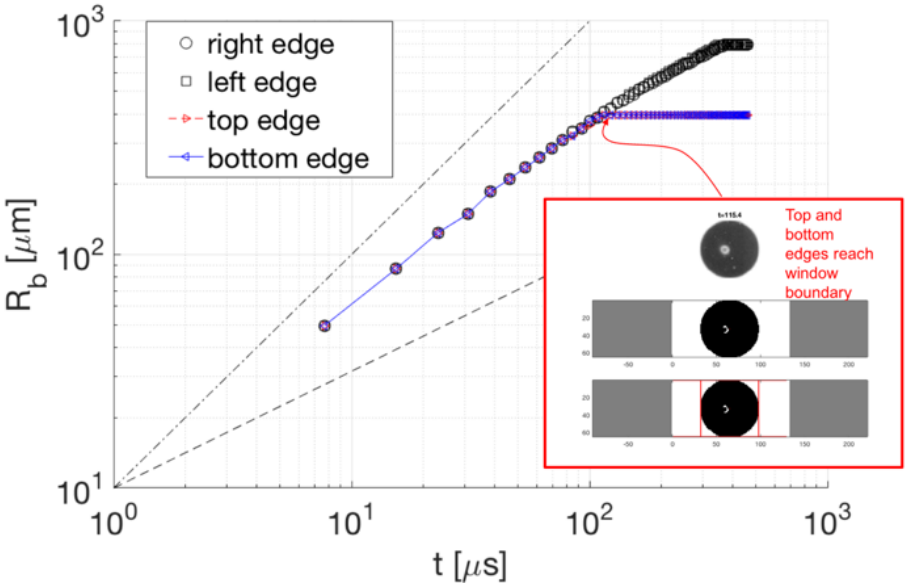

(a)

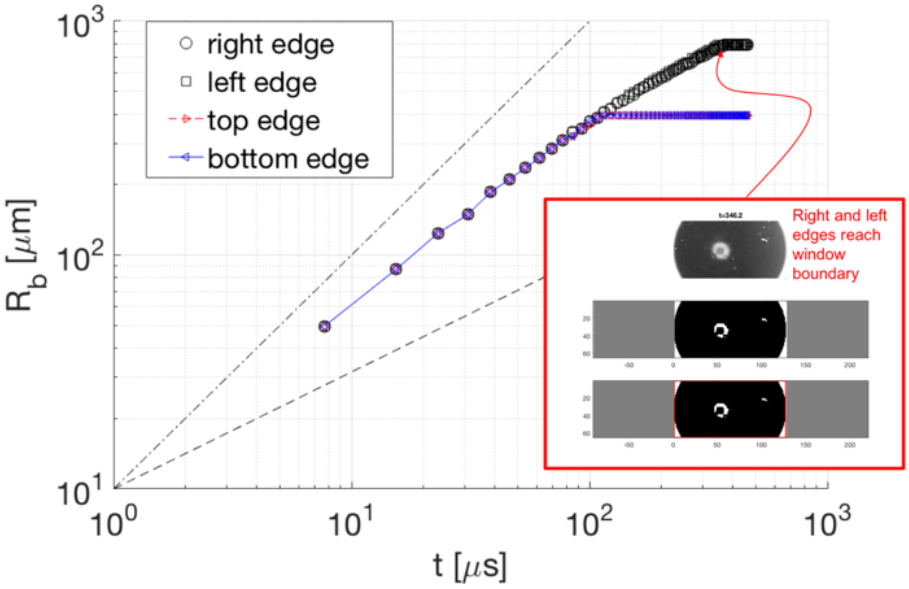

(b)

Figure 4-6: Details of post-processed HSV images that yield bubble radius as a function of time from all four edges, in the case of an imposed heat flux of $q" = 555kW/m^2$. Top and bottom edges of the bubble reach the boundary of the window of observation at $t \approx 115\mu s$ (a), while right and left edges of the bubble reach the boundary of the window of observation at $t \approx 350\mu s$ (b). Two scalings are added for reference: $R_b \propto t$ (dotted-dash line), indicated by Mikic theory [71] to describe the initial and rapid inertia-controlled phase of bubble growth, and $R_b \propto \sqrt{t}$ (dash line), that describes the later phase of slow thermally-controlled phase of bubble growth.

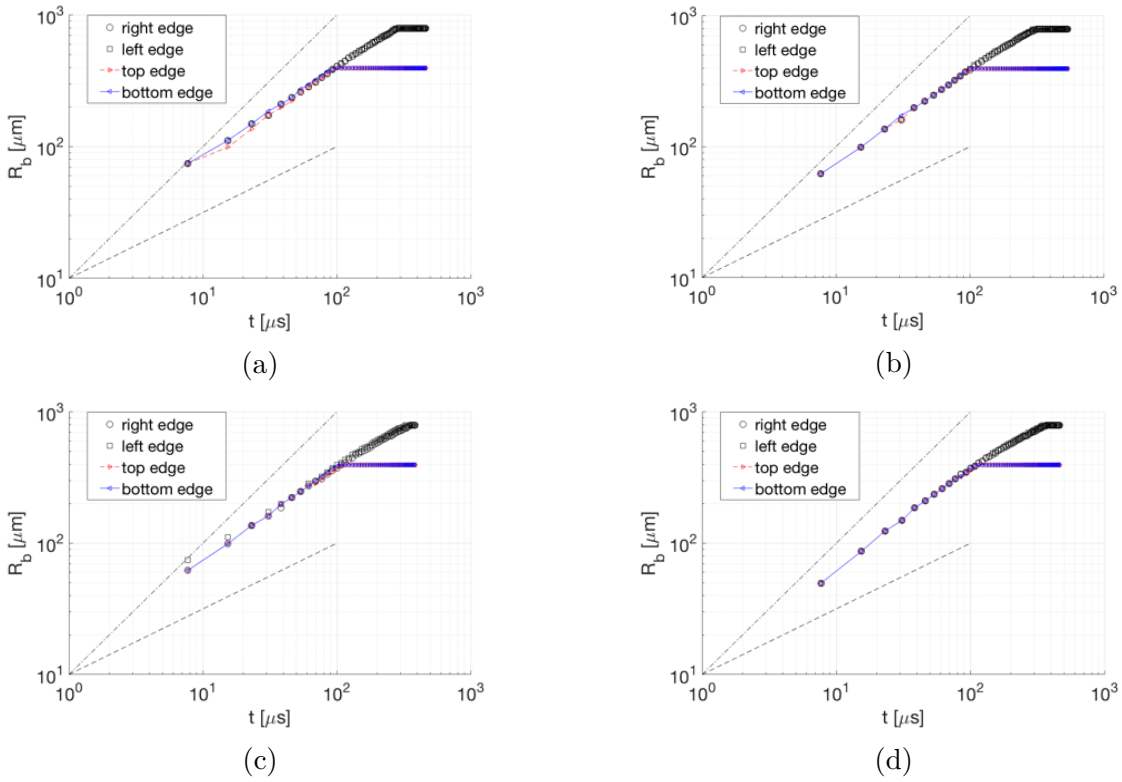

Figure 4-7: Bubble radius as a function of time, obtained from tracking all four bubble edges, for four heat fluxes: $q^{"} = 138kW/m^2$ (a), $272kW/m^2$ (b), $450kW/m^2$ (c) and $550kW/m^2$ (d). Two scalings are added for reference: $R_b \propto t$ (dotted-dash line), indicated by Mikic theory [71] to describe the initial and rapid inertia-controlled phase of bubble growth, and $R_b \propto \sqrt{t}$ (dash line), that describes the later phase of slow thermally-controlled phase of bubble growth.

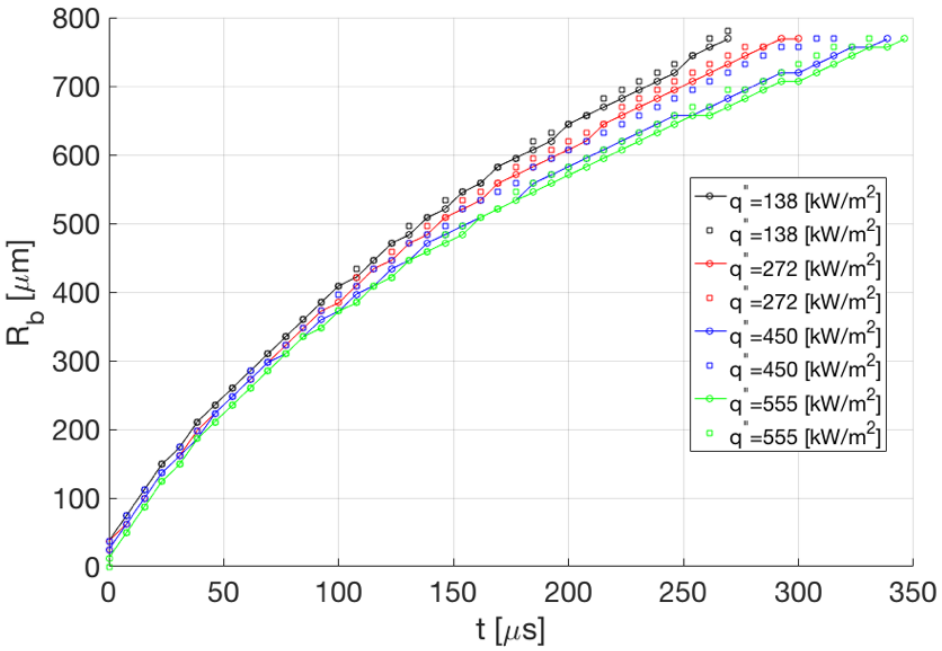

Figure 4-8: Bubble radius obtained from tracking side edges of the bubble (left edge: square symbol; right edge: circle symbol with line), and for all four heat fluxes $q" = 138kW/m^2,\ 272kW/m^2,\ 450kW/m^2$ and $550kW/m^2$.

in Figure 4-6: the top and bottom edges of the bubble are captured until $t \approx 115\mu s$, while right and left edges are captured for a longer period of time (the window is larger in the horizontal direction: 256 pixels vs. 128 pixels vertically), namely until $t \approx 350\mu s$.

Before these edges reach the boundaries of the window of observation, they reveal the exact same values of the bubble radius, which clearly indicates the hemispherical growth of the bubble. This result is generalized to the four heat fluxes investigated, see Figure 4-7: $q" = 138kW/m^2$ (a), $272kW/m^2$ (b), $450kW/m^2$ (c) and $550kW/m^2$ (d). Superheats at the inception of boiling are reported in Table 4.1.

Because of the shape of the window of observation, side edges allow tracking the bubble radius for longer times. We plot bubble radius obtained from tracking side edges of the bubble, and for all four heat fluxes in Figure 4-8, and in log-log format in Figure 4-9. In Figure 4-7 and Figure 4-9, two scalings are added for reference: $R_b \propto t$ (dotted-dash line), indicated by Mikic theory [71] to describe the initial and rapid

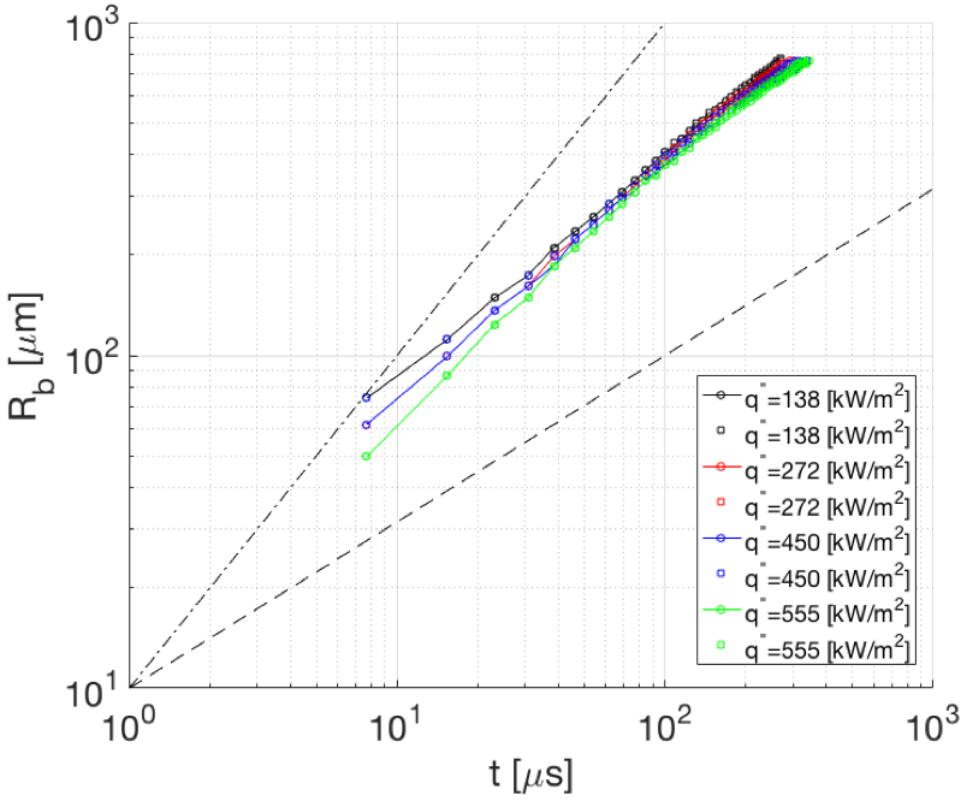

Figure 4-9: Bubble radius obtained from tracking side edges of the bubble (left edge: square symbol; right edge: circle symbol with line), and for all four heat fluxes $q" = 138kW/m^2$, $272kW/m^2$, $450kW/m^2$ and $550kW/m^2$. Two scalings are added for reference: $R_b \propto t$ (dotted-dash line), indicated by Mikic theory [71] to describe the initial and rapid inertia-controlled phase of bubble growth, and $R_b \propto \sqrt{t}$ (dash line), that describes the later phase of slow thermally-controlled phase of bubble growth.

inertia-controlled phase of bubble growth, and $R_b \propto \sqrt{t}$ (dash line), that describes the later phase of slow thermally-controlled phase of bubble growth.

The initial growth rate is found to indeed follow the $R_b \propto t$ scaling at short time scales for high heat flux ($555kW/m^2$), but not at lower heat fluxes. As the heat flux is decreased, the scaling exponent n describing $R_b \propto t^n$ ($t \to 0$), decreases from $n \approx 1$ ($555kW/m^2$) down to $n \approx 0.65$ ($138kW/m^2$). This result indicates that Mikic's theory may only be valid in the limit of high heat fluxes.

Table 4.1: Temperatures at the wall, underneath the bubble, at the incipience of boiling, for all four heat fluxes.

Test	$q^{"}$ (kW/m^2)	T_0 $(°C)$
1	138	121.4
2	272	121.7
3	450	121.8
4	550	122.1

4.4 Conclusions

We measure bubble dynamics at very early times of nucleate pool boiling of water at 0.101MPa (no subcooling) with unprecedented time and spatial resolutions: $12.4\mu m$/pixel spatial resolution and $7.7\mu s$ temporal resolution, respectively.

Results indicate that Mikic's theory [71], which predicts that bubble radius at very early times scales linearly with time ($R_b \propto t$), may only be valid in the limit of high heat fluxes, while the scaling is found to be much slower at lower heat fluxes. As the linear growth is not verified at low heat fluxes, time-varying growth rates could be used to further refine the simulation of bubble growth hydrodynamics and resolving microlayer formation at a wall.

Chapter 5

Direct computations of forced dewetting and moving contact lines

This chapter directly reflects results presented in the paper "Transition in a numerical model of contact line dynamics and forced dewetting" co-authored, in alphabetical order, with S. Afkhami, J. Buongiorno, S. Popinet, R. Scardovelli, and S. Zaleski, which was submitted to the Journal of Computational Physics and is available on ArXiv (arXiv:1703.07038) [1].

5.1 Motivation

During nucleate boiling, liquid is displaced by a growing bubble and wets the solid surface. The precise wetting mechanism taking place at the microscopic scale underneath the bubble determines whether the liquid microlayer forms or not. In general, wetting of solids by liquids can be found in a number of other applications, ranging from coating [18], tear films on the cornea [67] and CO2 sequestration [53]. However, despite this wide range of applications and interests, wetting mechanisms are only partially understood today.

In this section, we numerically study the fundamentals of forced dewetting, which corresponds to the situation where a fluid/fluid interface, such as the liquid/vapor

interface in boiling, is forced to move along a solid, such as the liquid/vapor interface moving along the solid substrate during microlayer formation. Depending on the balance between the surface tension force and the viscous force near the contact line, which is indicated by the capillary number Ca defined as:

$$Ca = \mu_l U_b / \sigma \tag{5.1}$$

forced dewetting can result in a receding contact line or on the formation of a thin film on the solid. This transition in forced dewetting can be described by a critical capillary number Ca_{cr} beyond which the imbalance between surface tension and viscous forces systematically leads to thin film formation, relevant to microlayer formation in nucleate boiling.

Lastly, in numerical simulations of moving contact lines the singularity at the contact line is removed by an implicit slip that comes from the finite size of the mesh at the wall (mesh size Δ), which allows the contact line to move along the no-slip solid boundary. As a consequence, numerical solutions of moving contact lines depend on mesh refinement [2], [111],[74]. In this chapter, we use results from direct computations of the forced dewetting transition, for which the apparent contact angle is known, and hydrodynamics theories, to propose a numerical procedure that enables mesh-independent results in moving contact line simulations.

5.2 Brief review of moving contact line theories and models

5.2.1 Singular flow geometry at contact line

The contact line region refers to the region close to the wall where the fluid/fluid interface separates wet regions from dry regions. In the case of a static meniscus at a wall, the fine balance between gravity and surface tension results in an equilibrium

shape governed by the capillary length:

$$l_c = \sqrt{\sigma/\{(\rho_1 - \rho_2)g\}} \tag{5.2}$$

where (ρ_1, ρ_2) refer to the density of the two fluids, σ the surface tension and g the gravitational constant. At the contact line where all three phases are in apparent contact, the equilibrium is determined by the balance of surface tension between the solid/fluid and fluid/fluid pairs. In the boiling scenario for example, the equilibrium contact angle $\theta_{\mathrm{d}x}$ is given by Young's law [116]:

$$cos(\theta_{\mathrm{d}x}) = (\sigma_{sv} - \sigma_{sl})/\sigma_{lv} \tag{5.3}$$

In practice, surfaces are not perfectly smooth and contact angle hysteresis is widely reported [28], where static solutions exist in a range of contact angles:

$$\theta_{receding} < \theta_{\mathrm{d}x} < \theta_{advancing} \tag{5.4}$$

When the relative velocity between the contact line and the solid is no longer zero, the static scenario no longer holds, and viscous forces add to the previously mentioned surface tension and gravity forces. In particular, Huh and Scriven [40] model the viscosity-dominated steady motion of a flat liquid/vapor interface on a flat solid with a 2D-Stokes flow, with a no-slip boundary condition at the solid surface. Corresponding stream lines are solution of the biharmonic equation:

$$\nabla^4 \Psi = 0 \tag{5.5}$$

see Figure 5-1, with four boundary conditions: no slip at the solid boundary, no shear stress at the free surface, and both solid and free surface impermeable. Under the assumption that the continuum description of the fluid flow still holds, they obtain

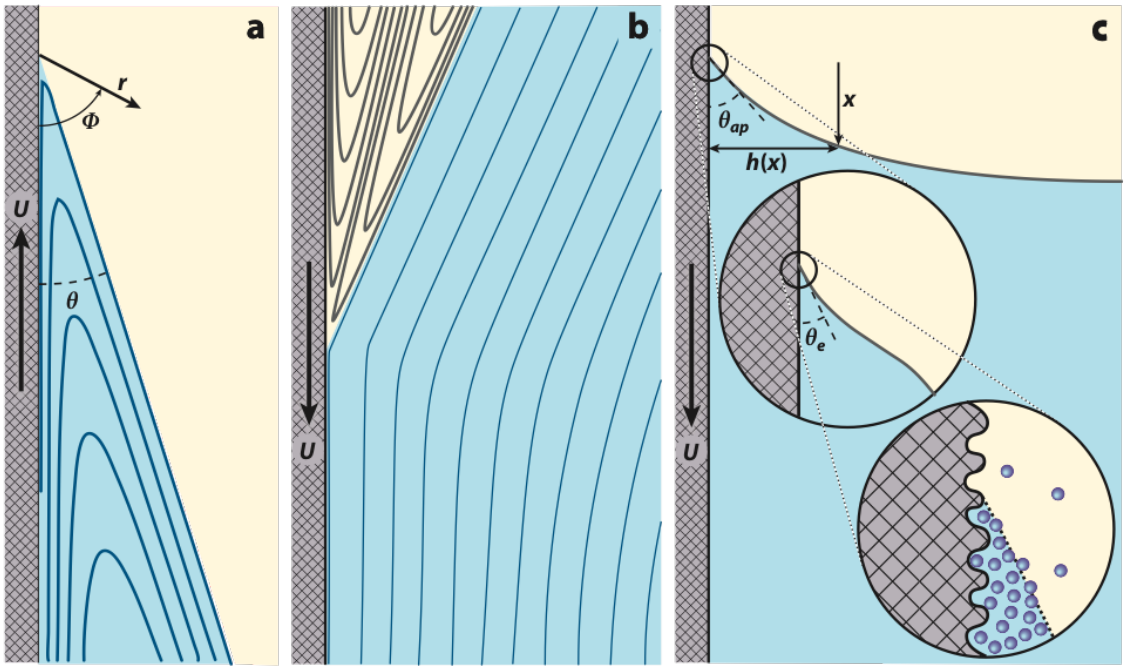

Figure 5-1: Figure from Snoeijer and Andreotti [97] showing streamlines in the vicinity of the contact line for a receding contact line (a) and an advancing contact line (b). In (c) the various scales are described, respectively: the apparent contact angle θ_{app} at the macroscopic scale, and the microscopic contact angle θ_e observed at the molecular scale.

the scaling of the shear stress with the distance r from the origin of the contact line:

$$\tau \propto 2\mu_1/r \tag{5.6}$$

which diverges at the contact point ($r \to 0$) and reveals the need to eliminate and regularize the non-integrable singularity at the contact line.

5.2.2 Multiscale modeling

Figure 5-1(c) shows the various scales and regions involved in contact line problems: the macroscopic region described by an apparent contact angle θ_{app} at distances to the contact line larger than the capillary length l_c, the microscopic region described by a nano to microscopic contact angle θ_e at molecular distances from the wall, and the intermediate mesoscopic region described by an angle $\theta(r)$ at distances to the

contact line smaller than the capillary length but larger than molecular length scales.

At the microscopic scale, a prediction of the slip occurring over the first few molecular layers above the solid substrate can be obtained from statistical physical theory of liquids to provide a slip length l_s [39]. In contrast, Molecular Kinetic Theory (MKT) introduces thermal fluctuations as key driving phenomena in the motion of contact lines [6], [7]: thermal activated processes can dominate capillary effect in controlling the motion of the contact line for scales below the thermal length $l_{thermal}$ defined as:

$$l_{thermal} = \sqrt{k_B T/\sigma} \tag{5.7}$$

At room temperature, $l_{thermal} \approx 0.1nm$.

At the mesoscopic scale, the bending of the interface is influenced by viscous effects. The balance between viscosity and surface tension in the limit of small angles can be modeled by the lubrication approximation, which leads to a third order differential equation for the interface profile h:

$$\frac{\mathrm{d}^3 h}{\mathrm{d}x^3} = \frac{3Ca}{h^2} \tag{5.8}$$

More generally, beyond the assumptions of the lubrication approximation, the wedge solution of Huh and Scriven can be extended to large contact angles where the contact angle at the mesoscopic scale is found to vary logarithmically with the distance to the contact line [17]:

$$G[\theta(r)] = G(\theta_e) - Ca\ln(r/\lambda) - Ca\frac{Q_i}{f(\theta_e, q)} + o(Ca) \tag{5.9}$$

where λ is a characteristic scale for microscopic effects, θ_e is the equilibrium angle, f and G defined in [17], and $q = \mu_2/\mu_1$ is the viscosity ratio. Q_i is an integration constant that is obtained by matching with the microscopic region and therefore depends on the microscopic region characteristics.

5.2.3 Wetting transition

In complete wetting conditions, one can control the deposition of a thin film on a solid by controlling the speed at which the solid is withdrawn from a bath of coating fluid. In such complete wetting scenario of the withdrawing plate, the contact line recedes and the thickness deposited h_{LLD} scales with $Ca^{2/3}$, see Landau and Levich [63] and Derjaguin [19] results:

$$h_{LLD} \propto l_c Ca^{2/3} \tag{5.10}$$

In the partially wetting scenario of the withdrawing plate, the contact line rise to a steady position without leaving any film behind, provided the capillary number is small, in particular smaller than a certain critical capillary number ($Ca < Ca_{cr}$). Above the critical capillary number, the imbalance between surface tension and viscous forces prevent any steady solution to exist, and a thin liquid film is entrained [7], [26], [94], [96].

5.2.4 Assumptions made in this work

In this work, we consider the solid surface to be smooth and the surface tension to be uniform in space and constant in time (no thermo-capillarity effect considered). We also do not consider evaporation at the contact line. Lastly, we only consider the asymptotic behavior $Ca \to 0$ where inertial effects are negligible.

5.3 Simulation of moving contact lines using Navier-Stokes solver with Volume-Of-Fluid (VOF) interface tracking method

5.3.1 Problem statement: forced dewetting

We consider the fundamental case of forced dewetting when a solid plate is withdrawn from a liquid reservoir at constant speed $V_s > 0$, as depicted in Figure 5-2. Domain side $L \approx 9l_c$ with l_c the capillary length. A no-slip boundary condition and a fixed contact angle, θ_Δ , i.e. the angle imposed numerically at the boundary in a simulation with grid size Δ, are prescribed at the substrate ($x = 0$). Symmetry boundary conditions are imposed on the right ($x = L$), top ($y = L$), and bottom ($y = 0$) boundaries of the domain. Results are confirmed to be insensitive to the choice of Re number:

$$Re = \rho_1 l_c V_s / \mu_1 \tag{5.11}$$

as well as computational domain size. We define another Reynolds number N_G, based on the on the wavelength of gravity waves L_{gw} traveling at the same speed as the withdrawing plate:

$$L_{gw} = \rho_1 V_s^2 / \{(\rho_1 - \rho_2)g\} \tag{5.12}$$

$$N_G = \rho_1 L_{wg} V_s / \mu_1 \tag{5.13}$$

N_G is related to Re, the capillary length Reynolds number:

$$Re = N_G^{1/2} / Ca^{1/2} \tag{5.14}$$

Simulation setups

We use the free code Gerris, previously described, for three different setups - see Table 5.1:

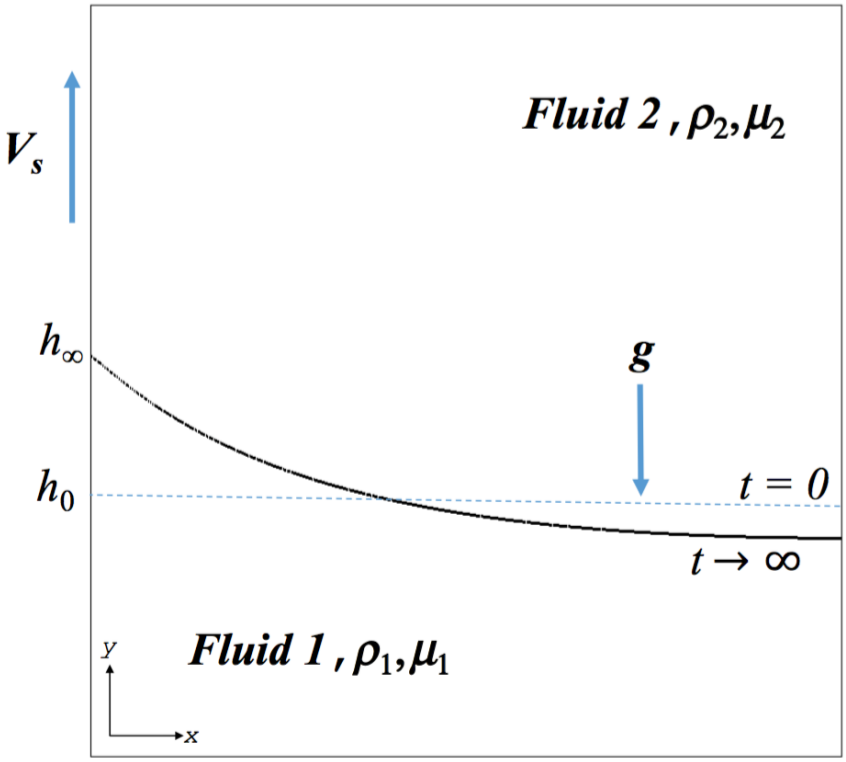

Figure 5-2: Schematic of the withdrawing plate, initially at $t = 0$, and at the stationary state $t \to \infty$.

- In Setup A, the number N_G is arbitrarily set to 25/64 (value corresponding to the arbitrary choices of $\rho_1 = 5$, $\rho_2 = 1$, $g = 16$, $\mu_1 = 1$, $V_s = 1$). Thus from Eq. (5.14) the Reynolds number based on l_c varies as:

$$Re = \frac{5}{8} Ca^{-1/2} \tag{5.15}$$

  The Reynolds number Re based on l_c increases as the capillary number is decreased. Varying the Reynolds number Re between 0 (Stokes approximation) and $Re = 3$ has no effect on the results, however increasing Re beyond this value introduces significant inertial effects and interface oscillations that modify the conclusions of our investigations.

- In Setup B, N_G is free to vary and the Reynolds number Re based on l_c is fixed to $Re = 1$.

- In Setup C, we keep Reynolds number Re and density ratio identical as in Setup B, but we increase the viscosity ratio to $\mu_1/\mu_2 = 50$.

Setup	N_G	Re	μ_1/μ_2	ρ_1/ρ_2
A	25/64	-	1	5
B	-	1	1	5
C	-	1	50	5

Table 5.1: Summary of the simulation Setups.

A specific discussion on the numerical methods employed can be found in [1].

Variation of contact angle with distance from contact line

In the neighborhood of the contact line, no specific choice of parameters is required except the equilibrium or static contact angle that is specified in the numerical model - see Figure 5-3. In this work, we apply the hydrodynamics theory to the study of the numerical model of contact line dynamics and forced dewetting without any special provisions for the contact line dynamics. Thus, we identify θ_e to θ_Δ, the numerically applied contact angle.

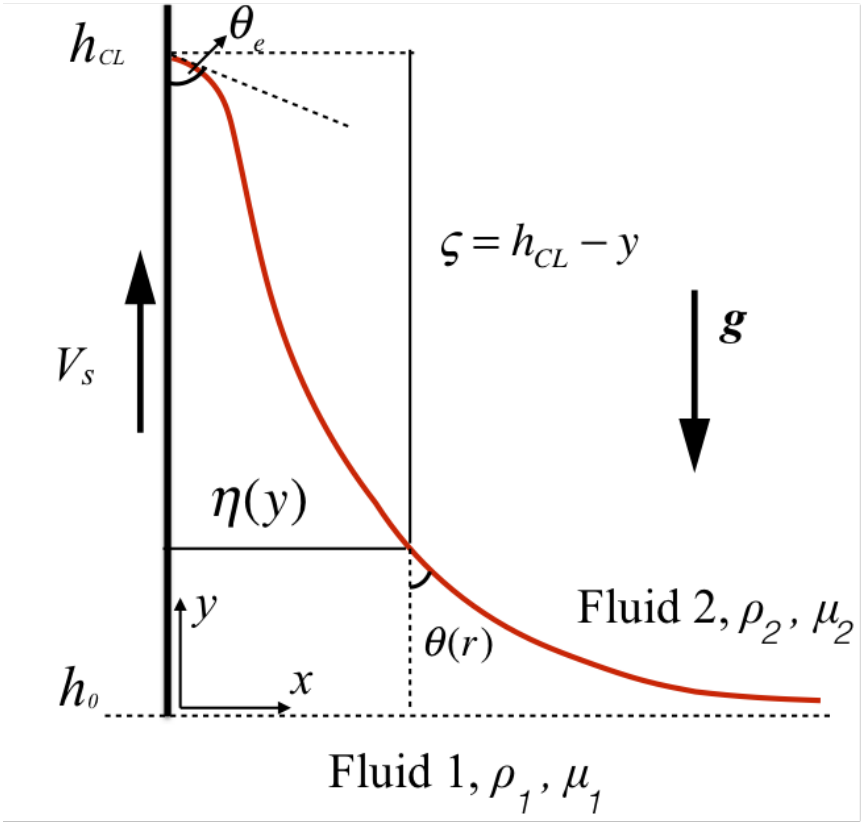

Figure 5-3: Sketch showing the variation of contact angle with distance from contact line: θ_e at the microscopic length scale λ, and $\theta(r)$ at length scale r.

5.3.2 Results: transition to film formation in forced dewetting

The time evolution of the contact line height h_{CL}, from its initial position h_0, and nondimensionalized by l_c, is show in Figure 5-4, for $Ca = 0.03$ and various mesh sizes (Δ/l_c) and contact angles (θ_Δ). Figure 5-4 shows that depending on Δ/l_c, different equilibrium configurations can be obtained. Also, it shows that when the contact angle is decreased, the contact line is raised to a new equilibrium height for the large grid sizes while a stationary meniscus cannot be achieved for the smallest grid size. In summary, we find two parameter ranges:

1. A stationary regime: as $\tau \to \infty$ the contact line motion along the substrate evolve to a steady state, where the nondimensional time τ is defined as:

$$\tau = V_s \; t \; / \; l_c \tag{5.16}$$

2. An unsteady regime: no steady state solution can be found and the contact line height continues to increase, covering the substrate by a film.

All results presented in this section are for Setup A, unless stated otherwise. We begin by presenting various scenarios characterized by different nondimensional grid sizes Δ/l_c, and the imposed contact angle, θ_Δ.

Stationary regime

Figure 5-5(a)-(d) show the nondimensional stationary contact line height $(h_\infty - h_0)/l_c$, where $h_\infty = h_{CL}(\tau \to \infty)$, as a function of the nondimensional mesh size, Δ/l_c, for various capillary numbers and for various contact angles, $90° \leq \theta_\Delta \leq 50°$. The results show the grid sizes where a stationary meniscus forms and no film is deposited on the substrate, for the range of considered contact angles. The results also show that the computed height of the contact line is a function of mesh size, and that for small enough contact angles, no steady state menisci can be attained when $\Delta/l_c \leq 0.014$. This lower limit of θ_Δ, for which steady state contact lines can be achieved, gets larger

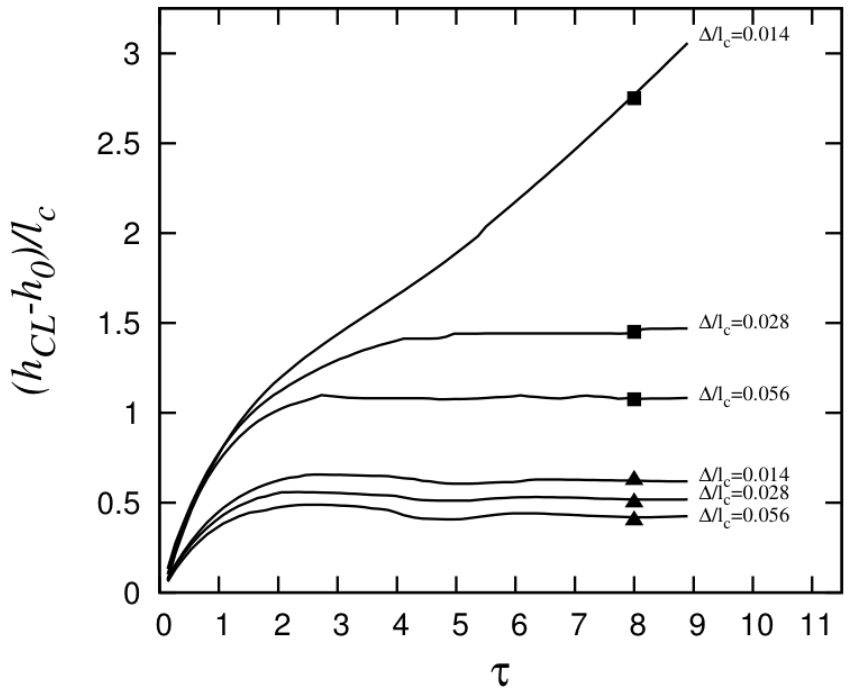

Figure 5-4: Contact line height as a function of time for $\theta_\Delta = 90°$ (triangles) and $\theta_\Delta = 60°$ (squares) at various mesh sizes Δ/l_c. For $\Delta/l_c = 0.014$ and $\theta_\Delta = 60°$, the contact line elevation continues increasing as τ increases. Ca = 0.03.

as Ca is increased. The results clearly depend on the chosen value for the smaller mesh size near the contact line, an effect that is expected and will be explained later in this chapter. This dependence of the results with mesh size becomes more marked as Ca is increased or θ_Δ is decreased.

Figure 5-6(a) provides an example of a stationary meniscus for $Ca = 0.043$, $\theta_\Delta = 90°$, and $\Delta/l_c = 0.014$ (for this set of parameters, $Ca_{cr} = 0.52$). The inset shows the magnified flow field and the pressure distribution. Figure 5-6(b) shows a magnified view of the contact line region and the computational mesh. The fine structure of the flow field and the pressure distribution in the contact line region are illustrated. As shown, large gradients of velocity and pressure necessitate a high mesh resolution around the contact line region. The interface is highly curved close to the contact line, leading to an intensified pressure gradient around that region, while the pressure gradient remains weak outside the vicinity of the contact line, leading to gentle bending of the interface away from the contact line.

Entrained film regime

The onset of film deposition, i.e. the forced dewetting transition, can be understood as when the balance between the surface tension and viscous forces close to the contact line region can no longer hold, resulting in wetting failure. Note that gravity only affects the macroscopic region of the meniscus, away from the contact line.
At the transition, we allow the computations to run for a very long time ($\tau >> 1$) in order to accurately determine whether or not the contact line can reach a stationary state. To obtain accurate numerical values of the transition Ca_{cr}, we compute the contact line instantaneous velocity (Figure 5-7(b)) from the time-evolution of its height (Figure 5-7(a)). Non-zero velocities in Figure 5-7(b) are clearly identified (see $\left|\frac{\mathrm{d}(h_{CL}/l_c)}{\mathrm{d}\tau}\right| \approx 0.1$) and correspond to the entrained film regime.

More specifically, contact line heights as a function of time is reported for various values of Ca in Figure 5-7, when $\theta_\Delta = 90°$ and $\Delta/l_c = 0.007$. At sufficiently small Ca a stationary meniscus can be reached, while for large Ca the contact line height keeps

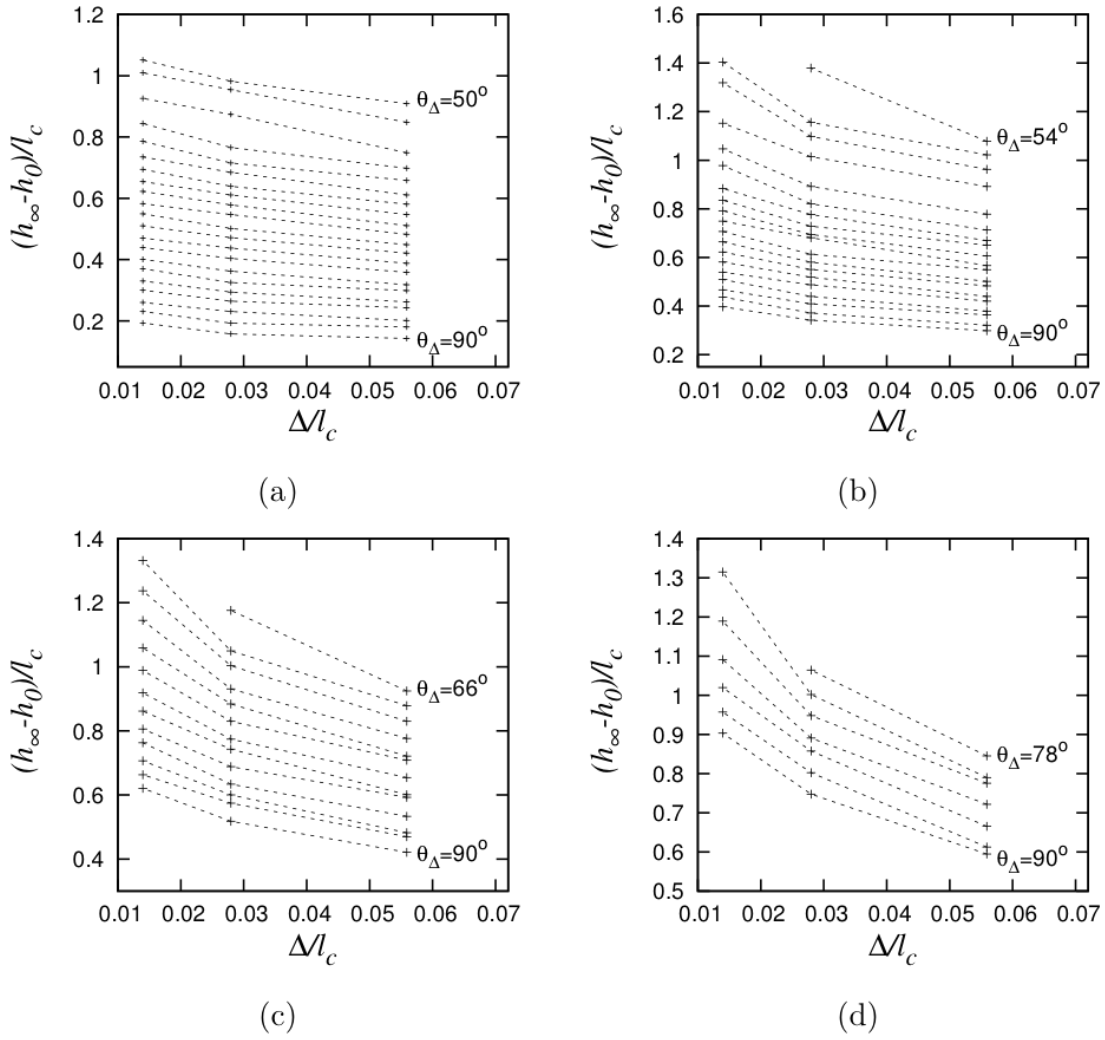

Figure 5-5: Nondimensional stationary contact line height, $(h_\infty - h_0)/l_c$, as a function of the nondimensional mesh size, Δ/l_c, for (a) Ca = 0.01, (b) Ca = 0.02, (c) Ca = 0.03, and (d) Ca = 0.04, for various contact angles, θ_Δ; the contact angle difference between each set is 2°. For (Ca, θ_Δ)=(0.02,54°), (0.03,66°), and (0.04,78°), no steady state menisci can be attained when $\Delta/l_c \leq 0.014$.

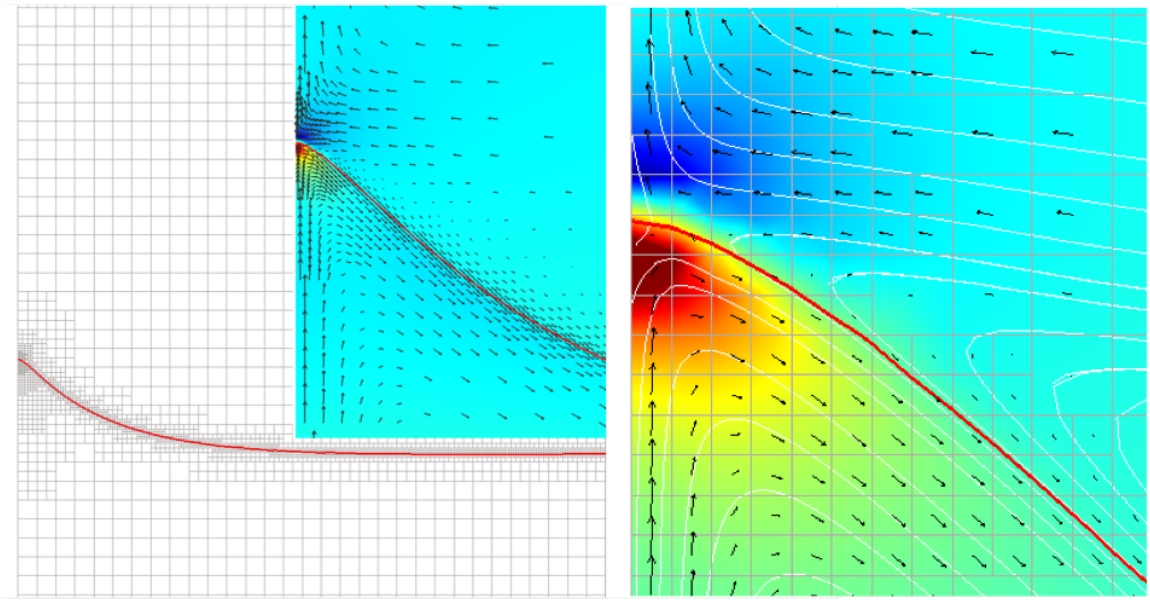

(a) (b)

Figure 5-6: (a) A stationary meniscus forms when $Ca < Ca_{cr}$ as $\tau \to \infty$.The inset shows the magnified flow field and the pressure distribution. $Ca = 0.043$, $\theta_\Delta = 90°$, and $\Delta/l_c = 0.014$. (b) A magnified view of the contact line region and the computational mesh. The fine structure of the flow field and the pressure distribution in the contact line region are illustrated. The pressure colors show the maximum (dark red) and minimum (dark blue) of the pressure distribution.

increasing. We pick the transition capillary number for which the relative velocity of the contact line, $\left|\frac{\mathrm{d}(h_{CL}/l_c)}{\mathrm{d}\tau}\right|$, does not go to zero as a function τ. This critical capillary number Ca_{cr} is depicted in red in Figure 5-7(a) and (b). Using the procedure above, we can therefore determine Ca_{cr} with a very good precision. Figure 5-8(a)-(b) show the contact line height, $(h_{CL} - h_0)/l_c$, as a function of nondimensional time τ, for two mesh sizes, Δ/l_c=0.028 and 0.014, when varying the wall contact angle $\theta_\Delta \in [50°;\ 80°]$, for a fixed Ca=0.03. The transition from a stationary meniscus not only depends on θ_Δ, but also on Δ/l_c. In particular, the transition occurs at a larger θ_Δ for smaller Δ/l_c. In the following sections, we investigate how the critical capillary number depends on contact angle and grid size. Figure 5-9 shows a typical evolution of the interface and the transition to the formation of a film deposited on the substrate, for $Ca = 0.048$, $\theta_\Delta = 90°$, and $\Delta/l_c = 0.014$ (for this set of parame-

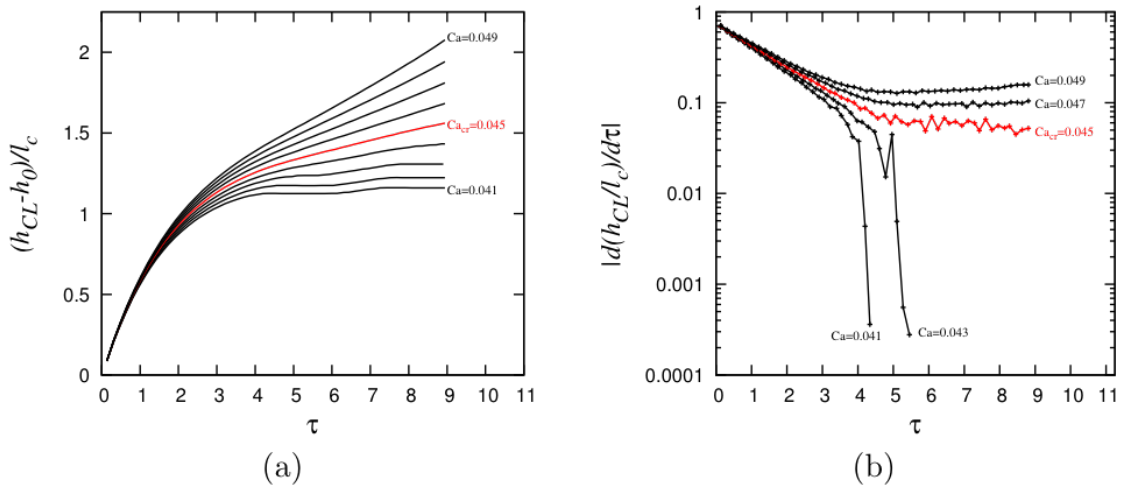

Figure 5-7: (a) Contact line height as function of time. The increment in Ca is 0.01 and the red line indicates the critical capillary number $Ca_{cr} = 0.045$. (b) Contact line velocity relative to the substrate velocity as a function of time. At the critical capillary number $Ca_{cr} = 0.045$, depicted in red, the transition occurs. $\theta_\Delta = 90°$ and $\Delta/l_c = 0.007$

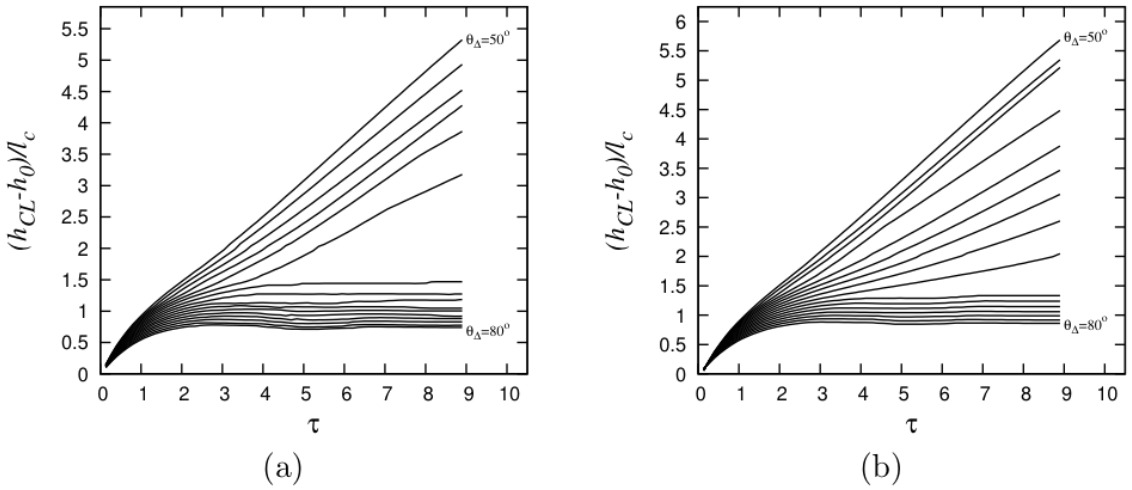

Figure 5-8: Contact line height as function of time for $\theta_\Delta \in [50°;\ 80°]$ and (a) $\Delta/l_c = 0.028$ and (b) $\Delta/l_c = 0.014$; the increment in θ_Δ is 2°. $Ca = 0.03$

ters, $Ca_{cr} = 0.024$). The insets of Figure 5-9 show the magnified flow field and the pressure distribution, as well as a magnified view of the contact line region and the flow streamlines. The fine structure of the flow field and the pressure distribution in the contact line region are illustrated. The results reveal the strong pressure gradients close to the contact line region: when capillary forces can no longer balance this strong pressure gradient, wetting failure occurs and a film is deposited on the substrate.

Figure 5-10 shows Ca_{cr} as a function of Δ/l_c for a range of θ_Δ for all three Setups: A, B, and C. The symbols are direct simulation results and the solid lines are drawn to guide the eye through a set of points corresponding to the same θ_Δ. In the next section, by systematically investigating the influence of θ_Δ and Δ/l_c on Ca_{cr}, we will develop an improved understanding of the onset of wetting failure. We study the effects of the contact angle and the grid size on Ca_{cr} and give the scaling of it with Δ/l_c. We also note that our results indicate that the transition coincides with an apparent contact angle $\theta_a = 0$, defining the "apparent contact angle" as the angle at the inflection point, (i.e. where the interface curvature becomes zero).

Figure 5-11 shows the dependence of the curvature (nondimensionalized by l_c) as a function of the nondimensional vertical distance of the interface from the contact line, defined as

$$\zeta/l_c = (h_{CL} - y)/l_c \tag{5.17}$$

(see Figure 5-3) for $\theta_\Delta = 60^\circ$ and $\Delta/l_c = 0.014$, and $Ca = Ca_{cr} = 0.024$. The results are plotted for τ =6.9 (shortly after the film is formed). The angle $\theta(\zeta/l_c)$ that the interface makes with the substrate is also plotted (red symbols), along with the curvature plot (black symbols), as a function of ζ/l_c. It is clear from these results that $\theta(\zeta/l_c) = 0$ coincides with $\kappa(\zeta/l_c) = 0$, confirming that contact angle is indeed 0 at the transition.

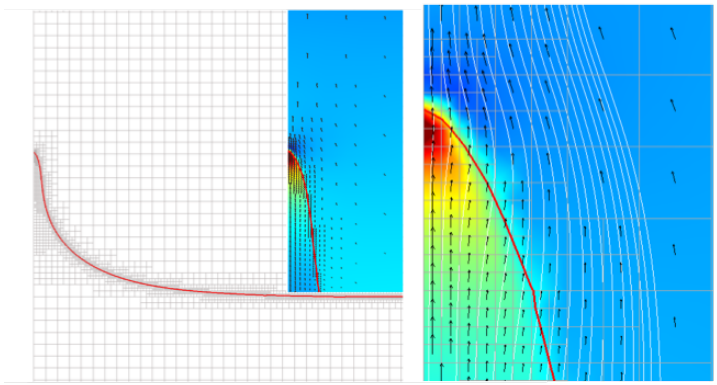

(a)

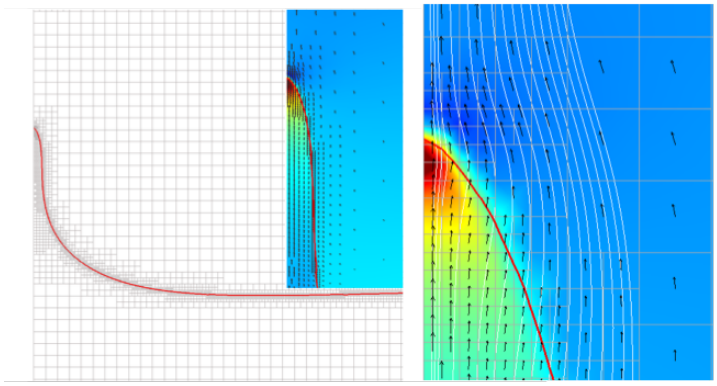

(b)

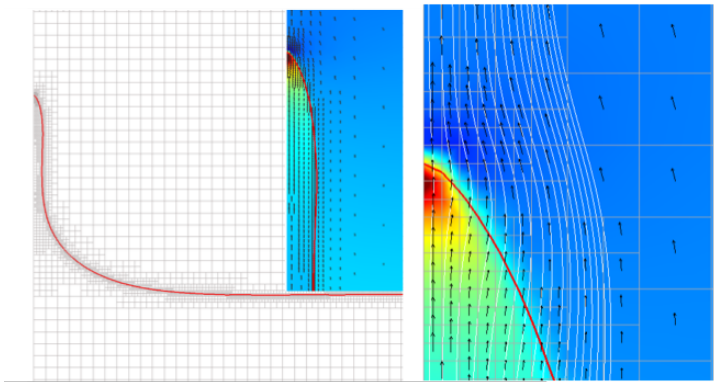

(c)

Figure 5-9: Time evolution of the interface for $Ca > Ca_{cr}$ at $\tau = 4$ (a), 4.8 (b), 5.9 (c). The insets show the magnified flow field and the pressure distribution. Right panels show a magnified view of the contact line region and the computational mesh; The fine structure of the flow field and the pressure distribution in the contact line region are illustrated. $Ca = 0.048$, $\theta_\Delta = 90°$, and $\Delta/l_c = 0.014$. The pressure colors show the maximum (dark red) and minimum (dark blue) of the pressure distribution

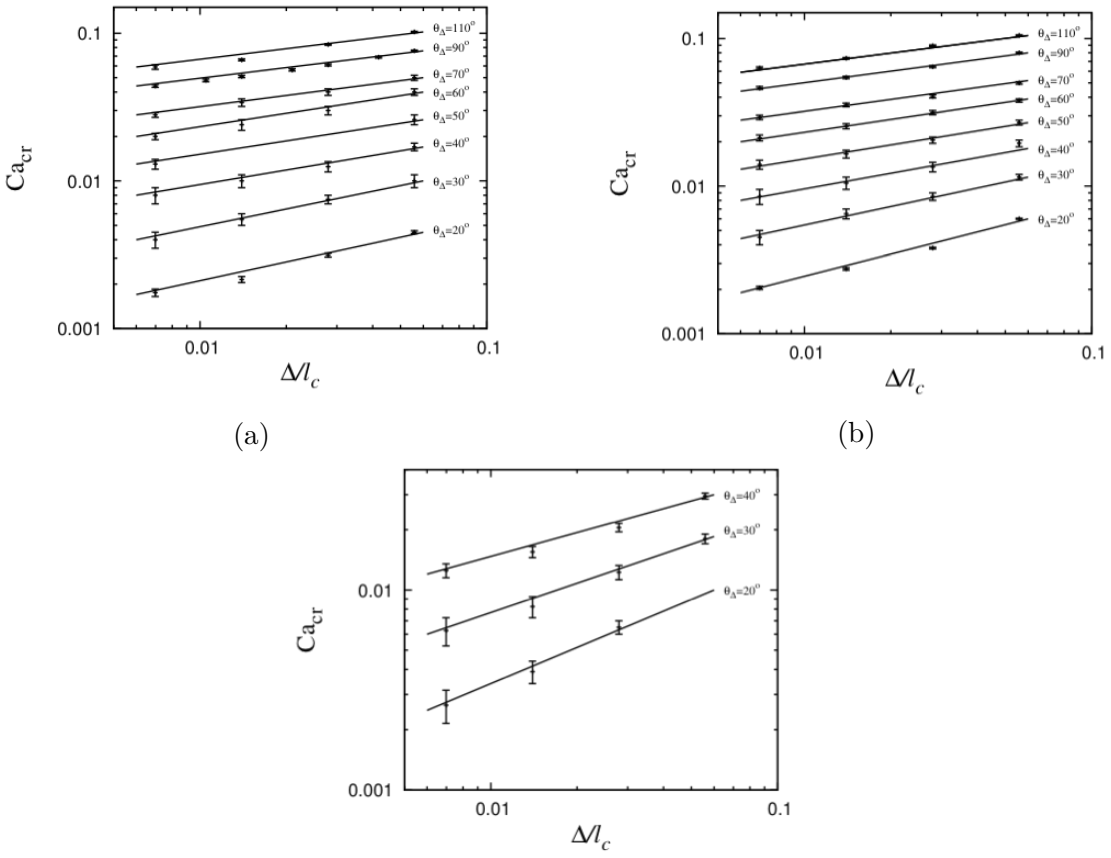

Figure 5-10: Plot of Ca_{cr} as a function of Δ/l_c for a range of θ_Δ for all three Setups: A (a), B (b), and C (c). Symbols present the numerical results and the solid lines are drawn to guide the eye.

5.4 Multiscale modeling of the contact line and critical capillary number for microlayer formation

To interpret our numerical results, we will proceed by analogy with the theory of [26] [12]. This theory is valid for small equilibrium contact angles, large viscosity and density ratios and a specific slip length model but we will use the theory of Cox [17] and an analogy to extend it to finite angles and arbitrary viscosity ratios.

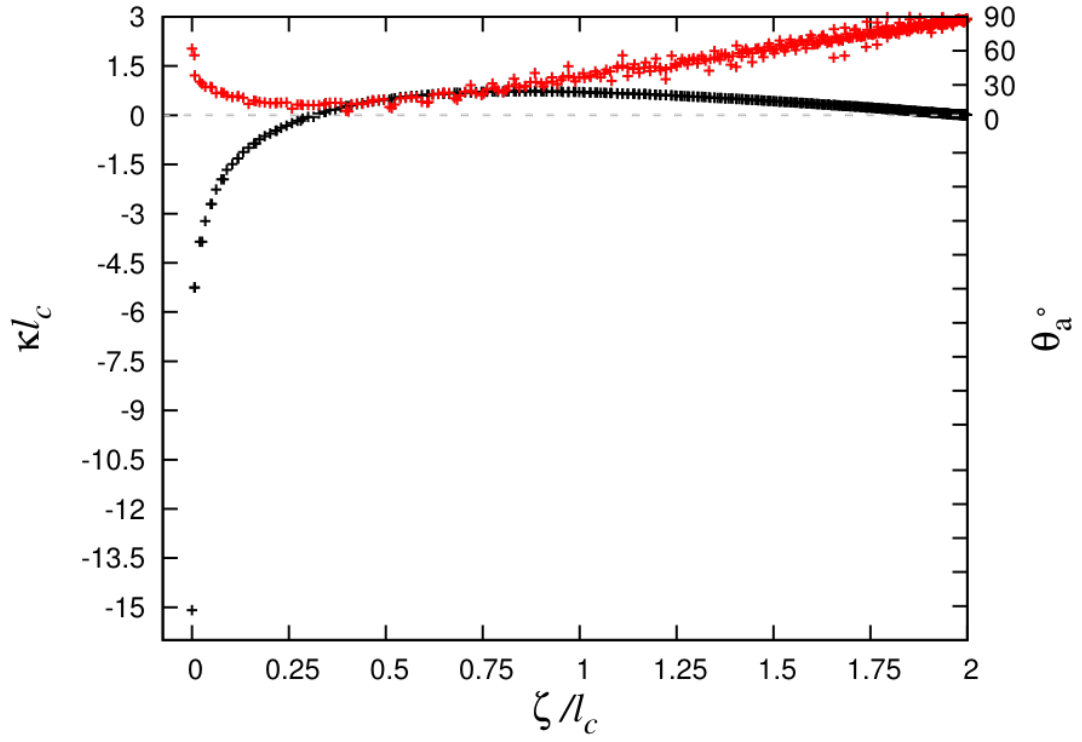

Figure 5-11: Dimensionless curvature κl_c (black symbols) as a function of the nondimensional vertical distance of the interface from the contact line ζ/l_c, for $\theta_\Delta = 60°$ and $\Delta/l_c = 0.014$, and $Ca = Ca_{cr} = 0.024$, at $\tau = 6.9$. Note $\theta(\zeta) \simeq 0$ where the curvature also becomes zero, at the inflexion point.

5.4.1 Hydrodynamic theory of the dynamic contact line and the dewetting transition

The problem is analyzed by asymptotic matching of three different regions:

1. A region I near the contact line, where microscopic effects dominate in the physical reality and numerical effects dominate in our simulations. The analysis of region I is straightforward, as we make no assumptions about it except that it provides a kind of initial condition for integrating in region II, and that as the velocity of the withdrawing plate and the capillary number go to zero, the angle relaxes to the equilibrium angle.

2. An intermediate region II, where continuum mechanics hold, with surface tension balancing viscous forces, any slip effects are small and gravity effects are negligible. Region II may further be divided into two subregions, a region IIa where the angle is large and a region IIb where the angle is small. The matching between regions IIb and III is performed at a small angle. In region II, we assume that the bending, while present, is relatively small so that the fluid fills approximately a linear wedge. In that case the fluid that fills the wedge flows according to the wedge solution of Huh and Scriven [40]. This gives a theory for the interface shape as described below. The theory is valid throughout region II, including region IIb, but in region IIb we can also use lubrication theory.

3. An outer region III, where viscous effects are negligible and surface tension balances gravity. The solution in region III is the famous static meniscus solution [64]. It gives in particular the curvature at the boundary of regions II and III as a function of a contact angle (which is not the microscopic contact angle but an angle that is "apparent" or "seen from region III") which is undetermined in the static analysis. By letting the contact angle be zero as discussed above one obtains a curvature of $\sqrt{2}/l_c$.

Film solution in region II

Cox's solution [17] in his "intermediate region" identifies with our region II, and his solution (Eq. 5.9) provides a universal description of the dependence of $\theta(r)$ on Ca, to the leading order, without any specification of the slip model or any necessity to calculate the details of the macroscopic flow in the outer region. Voinov introduces a microscopic length r_m [106] [107]:

$$r_m = \lambda \exp[f(\theta_e, q)/Q_i] \tag{5.18}$$

where $(r_m,\ \theta_e)$ are the characteristics of the microscopic region and provide a general description of the intermediate region:

$$G(\theta) = G(\theta_e) - Ca\ \ln(r/r_m) \tag{5.19}$$

We note $\eta(\zeta)$ the local thickness of the film. Then the angle $\theta \sim \eta'(\zeta)$ is the slope of the film, also noted $\eta' = d\eta/d\zeta$, and reduces in the case of small angles to:

$$\eta'(\zeta)^3 \sim 9G(\theta_e) - 9Ca\ \ln(\zeta/r_m) \tag{5.20}$$

which yields:

$$\eta'(\zeta) \sim [9G(\theta_e)]^{1/3}\left[1 - \frac{Ca}{G(\theta_e)}\ln(\zeta/r_m)\right]^{1/3} \tag{5.21}$$

valid in the limit of small Ca.

Film solution in region IIb-III

- Film slope in region IIb-III.

  We can match film profiles in region II and region III at the boundary between the two regions, the inflection point, using the thin film approximation - see Eq (5.8), whose solutions $h = (3Ca)^{1/3}H$ were obtained by Duffy and Wilson [25] introducing the Airy functions $(Ai,\ Bi)$, and two arbitrary constants $(\alpha,\ \beta)$:

  $$H = 1/\{\alpha Ai + \beta Bi\}^2 \tag{5.22}$$

  With such analytical solution of the layer profile, it becomes possible to obtain the slope:

  $$\eta'(\zeta) \sim \{9Ca\ \ln[\pi/(2^{2/3}\beta^2\zeta)]\}^{1/3} \tag{5.23}$$

  and the curvature κ (or η"(ζ)) of the interface. By matching slopes in II (Eq. 5.21) and III (Eq. 5.23), we eliminate β:

  $$\beta^2 \sim \frac{\pi}{2^{2/3}r_m}\exp\left[-\frac{G(\theta_e)}{Ca}\right] \tag{5.24}$$

- Film curvature in region IIb-III.

  The smallest possible curvature is reached when the Airy function assumes its global maximum $Ai(s_{max}) \approx 0.53$ with $s_{max} \approx -1.0$, s_{max} and β being two parameters describing the particular solution, which also yields an expression of the critical curvature:

$$\kappa_{\infty,cr} \approx (3Ca)^{1/3} \left[2^{1/6}\beta/(\pi Ai(s_{max}))\right]^2 \tag{5.25}$$

  or similarly, the curvature at the critical capillary number:

$$\kappa_{\infty} \approx (3Ca_{cr})^{1/3} \left[2^{1/6}\beta/(\pi Ai(s_{max}))\right]^2 \tag{5.26}$$

- Film curvature in region III:

$$\kappa_{\infty} \approx \sqrt{2}/l_c \tag{5.27}$$

  which yields by matching curvatures between IIb (Eq. 5.26) and III (Eq. 5.27):

$$\frac{3^{1/3}2^{-5/6}}{\pi Ai^2(s_{max})} \frac{Ca_{cr}^{1/3} l_c}{r_m} \exp\left[-\frac{G(\theta_e)}{Ca_{cr}}\right] = 1 \tag{5.28}$$

Gauge function ϕ

The microscopic length r_m can be obtained by dimensional analysis. In models that only have one single length scale ℓ, such as slip-length models, the only dimensionally correct solution is to assume $r_m = \ell/\phi$ where ϕ is a function of the other dimensionless parameters of the model, such as θ_Δ and q. In the numerical case where the only length scale is Δ and in the limit $Ca << 1$ and $\Delta << l_c$, we represent the microscopic scale r_m as:

$$r_m = \Delta/\phi \tag{5.29}$$

where the "gauge function" ϕ is a non-dimensional measure of the amplitude of the numerical effects on the film near the contact line. Combining Eq. 5.28 and Eq. 5.29

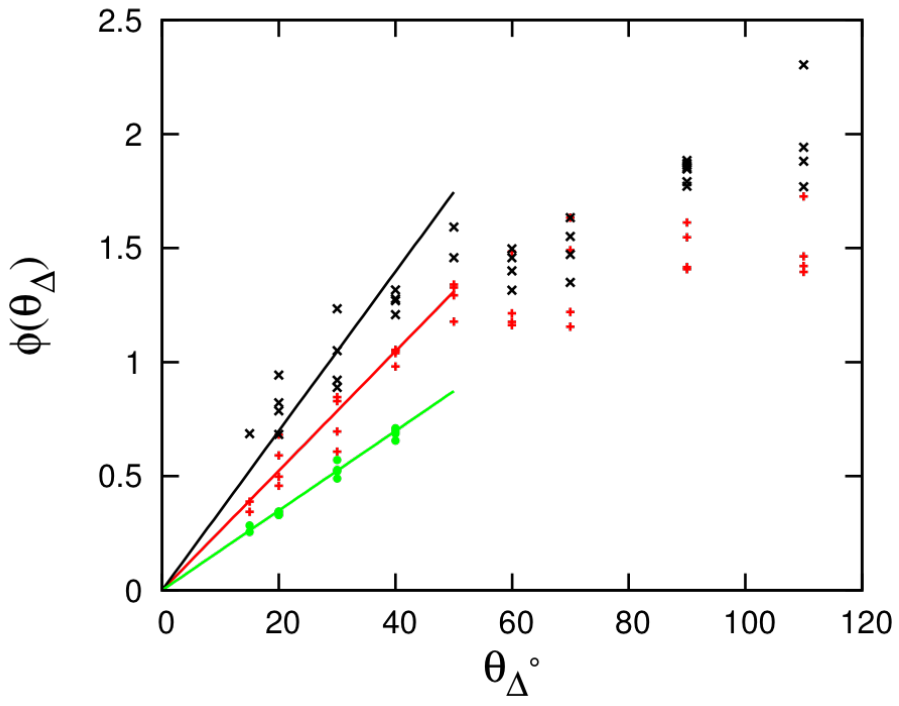

Figure 5-12: The gauge function ϕ plotted using expression (5.30) in the text, Setups A ($\times$), B ($+$), and C ($\bullet$). Solid lines are $f(x) = 2x$ (–), $f(x) = 1.5x$ (–), and $f(x) = x$ (–) (with x measured in radian). For a given angle θ_Δ, the various values of ϕ correspond to the various values of the grid size Δ.

we obtain:

$$\phi(\theta_\Delta) = \frac{\pi Ai^2(s_{max})}{3^{1/3}2^{-5/6}} \frac{\Delta}{Ca_{cr}^{1/3} l_c} \exp\left[\frac{G(\theta_\Delta)}{Ca_{cr}}\right] \tag{5.30}$$

Note that we can use our knowledge of Ca_{cr} obtained for a wide range of $(\Delta/l_c, \theta_\Delta)$ to compute the gauge function ϕ, for all three Setups A, B and C - see Figure 5-12.

5.4.2 Comparison with other predictions

Comparison: numerical model vs. physical model

It is interesting to compare the above, purely numerical results, to the situation with physical models of the contact line region obtained by other authors.

Eggers [26] started with several slip-length models. For the usual Navier slip con-

dition with slip length λ, he obtained the internal solution for interface slope η':

$$\eta'(\zeta) = \theta_e - \frac{3Ca}{\theta_e^2}\ln\left(\frac{\zeta \mathrm{e}\theta_e}{3\lambda}\right) \tag{5.31}$$

For $\theta << 1$ and $q = 0$, it can be shown that

$$G(\theta) \sim \theta^3/9 \tag{5.32}$$

which, combined with Eq. 5.21, yields:

$$\eta'(\zeta) \sim \theta_e - \frac{3Ca}{\theta_e^2}\ln\left[\frac{\zeta\phi(\theta_e)}{\lambda}\right] \tag{5.33}$$

By comparing Equations 5.31 and 5.33, we obtain:

$$\phi(\theta_e) = \mathrm{e}\theta_e/3 \tag{5.34}$$

Using Eq. 5.32This leads to

$$\kappa_\infty \sim \frac{\mathrm{e}}{18^{1/3}\pi Ai^2(s_{max})}\frac{Ca_{cr}^{1/3}\theta_e}{\lambda}\exp\left(-\frac{\theta_e^3}{9Ca_{cr}}\right) \tag{5.35}$$

which agrees with [26], [27], [12] except for a factor of "e" which was not carried over from Eq. 5.31.

Interpretation: numerical slip

An equivalence between the numerical model and the slip length model with $\theta_e = \theta_\Delta$ can be obtained if the numerical length scale $r_m = \Delta/\phi(\theta_\Delta)$ is equalled to the length scale $3\lambda/(\mathrm{e}\theta_e)$ that appears in Eq. 5.33. Then using the small angle approximation $\phi(\theta_\Delta) \simeq a\theta_\Delta$, and $a \approx 1.5$ from Figure 5-12 for setup B at $q = 1$, one obtains the equivalent slip length $\lambda = \mathrm{e}\Delta/(3a) \simeq 0.6\Delta$. Thus our numerical model may be viewed as having an effective slip of the order of a grid cell.

5.5 Outline of a procedure for mesh-independent computations

5.5.1 Previous work: "AZB" model [3]

In the computation of a number of problems involving dynamics contact lines, such as droplet spreading, drop impact or drop sliding on inclined plates, the result typically varies with grid resolution because of hydrodynamic effects. In [3], two of the authors of the present work [1] (S. Afkhami and S. Zaleski) suggested a manner (hereafter called the "AZB" model) of compensating for this hydrodynamic effect, by adjusting the numerical contact angle with the grid resolution. The theory was deemed applicable in the range defined by Sheng and Zhou [95], that is $q = 1$ and $|\cos\theta| < 0.6$. The resulting expression for the variation of the numerical contact angle was

$$\cos(\theta_\Delta) - \cos(\theta_a) = 5.63Ca\ln\left(\frac{2K}{\Delta}\right) \tag{5.36}$$

where K is a constant having the dimension of a length, and θ_a is a reference angle that parameterizes, together with K, the "AZB" model. If for a given Ca, K, and θ_a, the grid size and θ_Δ are varied in accordance with Eq. 5.36, then the grid dependence of the simulations is reduced. There is no universal choice for K. Instead, the pair K and θ_a needs to be fixed from experimental observations or theoretical models of the contact line, so that θ_a is an approximation of the angle at the length scale K, provided K lies in the region of the validity of Cox's theory, that is region II in the present work, or the equivalent of region II for a given problem.

5.5.2 Present work: generalization of "AZB" model to wide range of Ca and θ [1]

The AZB approach defines a length scale K analogous to the microscopic length r_m. Assuming that $K = r_m$ is constant misses the effect of the gauge function ϕ that appears as $r_m = \Delta/\phi(\theta_a)$ and therefore $K/\Delta = 1/\phi(\theta_a)$. In addition, the AZB ap-

proach is limited to $q = 1$ and $|\cos\theta| < 0.6$.

Generalizing "AZB" model

To overcome these limitations, we can use the general approach of Cox, see Eq. 5.19:

$$G(\theta) = G(\theta_\Delta) - Ca \ln\left[\frac{r}{\Delta/\phi(\theta_\Delta)}\right]. \tag{5.37}$$

In particular, the hydrodynamics theory predicts that simulations should be independent of grid size if for a given reference angle θ_a and a reference length $K = r_a$ we constrain the numerical angle θ_Δ to vary with grid size as follows:

$$G(\theta_\Delta) = G(\theta_a) - Ca \ln\left[\frac{\Delta/\phi(\theta_\Delta)}{r_a}\right] \tag{5.38}$$

provided Δ lies in or "below" region II, and that $\Delta \ll l_{out}$, $Ca << 1$ and $Re = \mathcal{O}(1)$ where the subscript *out* indicates the outer or region III length scale at which the theory approach is not valid anymore. This can be seen by summing Eq. (5.37) and Eq. (5.38) to obtain:

$$G(\theta) = G(\theta_a) - Ca \ln\left(\frac{r}{r_a}\right), \tag{5.39}$$

Limitations of present model

We list below some limitations of the present model, in terms of Ca and Re:

1. $Ca < Ca_{cr}$: too large values of Ca lead to a paradox. The model Eq. 5.39, with specified θ_a, r_a, leads to a value of Ca_{cr} given by Eq. 5.28 with the substitution $\theta_e = \theta_a$ and $r_m = r_a$. If $Ca > Ca_{cr}$, then the choice of reference values θ_a, r_a is inconsistent and a different numerical approach including some sort of thin film modeling should be used instead; this is beyond the scope of this paper.

2. Even if $Ca < Ca_{cr}$ but Ca is still not very small, values of Δ that are too large or too small compared to r_a lead to $\theta_\Delta < 0$ or $> \pi$, albeit these "critical" values

of Δ increase or decrease exponentially as $\exp(\pm 1/Ca)$. Thus there is again a range in which the model can be used. In order to be useful when Ca is not very small, the value of r_a should not be too different from the values of Δ used in practice.

3. The asymptotic limit in which the developments are valid is $Ca \to 0$. Perturbations of higher order in the small parameter Ca would create non-convergence effects.

4. Similarly, the procedure for grid-independent computations will be valid if inertial effects are negligible in the corresponding range of scales, that is: $Re(\Delta) = \rho_1 V_s \Delta/\mu_1 \ll 1$ and $Re(r_a) = \rho_1 V_s r_a/\mu_1 \ll 1$.

5.6 Conclusions

We focus on the problem of forced dewetting transition of a partially wetting plate withdrawn from a reservoir using direct numerical simulations. We provide a numerical dataset for critical capillary number, Ca_{cr}, at which the dewetting transition occurs, as a function of the mesh size, Δ, and the numerically-imposed equilibrium contact angle, θ_Δ. Using the asymptotic hydrodynamic theory of the vicinity of the contact line and matching it to the static theory of menisci, we derive an equation for the effect of Δ and θ_Δ on the larger-scale regions of the simulation. The critical capillary number is then predicted by an implicit equation for Ca_{cr}. This equation contains an unknown gauge function ϕ that characterizes the contact line dynamics and is akin to a coefficient that determines the amount of slip. This gauge function is specific to the numerical model used. Our numerical simulations allow to quantify this "numerical slip" and confirm that it varies linearly with the grid size Δ.

We suggest a manner in which simulations can be made convergent upon grid refinement, despite the singularity at the contact line. This involves adjusting the numerical contact angle as a function of the grid size. This adaptation of the contact

angle involves the numerical gauge function ϕ and improves in several ways over the AZB model in [3]. Indeed it is valid for arbitrary angles and viscosity ratios. However the gauge function ϕ is not known, except for the cases treated in this paper: i) for a specific contact angle numerical procedure, or ii) a Navier slip model. Thus the applicability of the grid-independent model may be limited.

The perspectives of this work are a systematic determination of the gauge function ϕ for a range of contact line models used in practice and the verification of the procedure for grid-independent computations in a number of flows. Such grid independent simulation could in turn be used to analyze the results of experiments on contact line dynamics.

Chapter 6

Conclusions and future directions

6.1 Summary and conclusions

Boiling is one of the most efficient modes of heat transfer: in Boiling Water Reactors (BWR) boiling is the primary mode of heat transfer in the reactor core to accommodate very high heat fluxes; in Pressurized Water Reactors (PWR) subcooled flow boiling can occur in hot sub-channels.

6.1.1 Sensitivity study on boiling simulations

We first confirm through a sensitivity study the need for accurate modeling of microlayer formation to initialize boiling simulations and to reproduce physical boiling dynamics (chapter 2). We focus on the simulation of a single vapor bubble growing at a heated wall, under saturated pool boiling conditions at atmospheric pressure. Our results confirm the strong sensitivity of simulated bubble growth rates to initial microlayer shape and extension in boiling simulations. We also discuss how fluid properties influence the actual contribution of microlayer evaporation to bubble growth and wall heat transfer, and confirm our results are consistent with experimental data for water and FC-72.

6.1.2 A generally applicable model for microlayer formation

Then, we build the first generally applicable model for microlayer formation through direct computations of the hydrodynamics of bubble growth at the wall for a wide range of conditions and fluids, including water at 0.101MPa (lab experiments) and 15.5MPa (PWR) (chapter 3). We identified the minimum set of dimensionless parameters that controls microlayer formation, and reduced the parameter space for the conditions and fluid of interest:

$$\delta/r_c = f(r/r_c, t/t_c, Ca, \theta_{\mathrm{dx}}) \tag{6.1}$$

With δ the shape of the extended liquid microlayer. We generated a large numerical database that discretizes the parameter space of interest, and built a generally applicable model for microlayer formation, to be used during the initialization of boiling simulations:

1. The wetted fraction underneath the bubble, $\alpha^* = (1-r_{min}/r_{max}) = f(\theta_{\mathrm{dx}}, t^*, Ca)$, informs the presence (or absence) of liquid microlayer underneath a growing bubble, for a given $(\theta_{\mathrm{dx}}, t^*, Ca)$ condition - see maps in Figure 3-18, 3-19, 3-20.

2. The central linear region of the microlayer $\delta^* = \delta_0^* + Cr^*$, for $r* \in [r^*_{min}, r^*_{out}]$, with r^*_{min} the position of the inner edge and r^*_{out} its extension radius:

$$\delta_0^* = 0.06\sqrt{Ca}\sqrt{t^*} \tag{6.2}$$

$$C = 0.5\sqrt{Ca}/\sqrt{t^*} \tag{6.3}$$

3. An estimate of the extension radius r^*_{out} of the liquid microlayer:

$$r^*_{out} \approx 0.9(R_{b,0}/r_c + t^*) \tag{6.4}$$

Comparison with previous work, both analytical [16] and experimental [114], show similar scaling of the central linear region, whose slope is found to be independent of Ca:

$$C = 0.5/\sqrt{t^{**}} \tag{6.5}$$

with $t^{**} = t/t_{c,2}$ and $t_{c,2} = \mu_l/(\rho_l U_b^2)$

In addition, this model provides an estimate of the extension radius of the extended microlayer, and maps of wetted fractions (based on hydrodynamics of the contact line) underneath the bubble at different times, and for the wide range of Ca and θ_{dx} (dx=100nm) of interest. Future work could further investigate additional effects such as thermal effects and mass transfer at the contact line that may modify the wetted fraction underneath the bubble. A physical mobility law $\theta = f(Ca)$ could also be used in replacement of the static contact angle used in this study.

Lastly, we investigate the effect of an external flow on microlayer formation. Depending on the velocity of the flow in the vicinity of the wall, compared with the bubble growth rate $U_{b,\mathrm{noflow}}$ in the absence of flow, we find that the effect of the flow can be:

- negligible ($V_{\mathrm{flow}}/U_{b,\mathrm{noflow}} << 1$), such as in most cases of steam bubbles growing in PWR conditions (high Re and high pressure).
- appreciable ($V_{\mathrm{flow}}/U_{b,\mathrm{noflow}} \approx 1$), such as in the case of the growth of neighbor bubbles
- dominant ($V_{\mathrm{flow}}/U_{b,\mathrm{noflow}} >> 1$), possibly achieved in the case of strong forced convection velocities (high Re) and large bubbles (low pressures).

This general model on microlayer formation resolves the initial and rapid phase of bubble growth in nucleate boiling, called inertia-controlled phase, which lasts a fraction of a milliseconds in the case of water at 0.101MPa. The following phase of bubble growth, the thermal diffusion controlled phase, is much slower and lasts tens

of milliseconds in the case of water at 0.101MPa. In practice, the present model allows initializing boiling simulations at the end of the rapid inertia-controlled phase of bubble growth during which the microlayer forms.

6.1.3 Measurements of bubble growth rates during inertia-controlled growth phase

In addition, we modify an existing experimental pool boiling setup to measure with unprecedented accuracy initial bubble growth rates needed to predict microlayer formation (chapter 4). We measure bubble dynamics at very early times of nucleate pool boiling of water at 0.101MPa (no subcooling) with unprecedented time and spatial resolutions: $12.4\mu m$/pixel spatial resolution and $7.7\mu s$ temporal resolution, respectively. Results indicate that Mikic's theory [71], which predicts that bubble radius at very early times scales linearly with time ($R_b \propto t$), may only be valid in the limit of high heat fluxes, while the scaling is found to be much slower at lower heat fluxes. As the linear growth is not verified at low heat fluxes, time-varying growth rates could be used to further refine the simulation of bubble growth hydrodynamics while resolving microlayer formation at a wall.

6.1.4 A numerical procedure based on hydrodynamics theory to obtain mesh-independent results in moving contact line simulations

Lastly, we develop a numerical procedure based on hydrodynamics theories to obtain mesh-independent results in moving contact line simulations for a wide range of contact angles and viscosity ratios (chapter 5). In particular, we use direct computations of the transition to a Landau-Levich-Derjaguin film in forced dewetting to inform the onset of microlayer formation in nucleate boiling. We focus on the problem of forced dewetting transition of a partially wetting plate withdrawn from a reservoir using direct numerical simulations. We provide a numerical dataset for critical capillary

number, Ca_{cr}, at which the dewetting transition occurs, as a function of the mesh size and the numerically-imposed equilibrium contact angle θ_Δ. Using the asymptotic hydrodynamic theory of the vicinity of the contact line and matching it to the static theory of menisci, we derive an equation for the effect of θ_Δ and on the larger-scale regions of the simulation. The critical capillary number is then predicted by an implicit equation for Ca_{cr}. This equation contains an unknown gauge function that characterizes the contact line dynamics and is specific to the numerical model used. Our numerical simulations allow quantification of this "numerical slip" and confirm that it varies linearly with the grid size.

We suggest a manner in which simulations can be made convergent upon grid refinement, despite the singularity at the contact line. This involves adjusting the numerical contact angle as a function of the grid size. This adaptation of the contact angle involves the numerical gauge function and generalizes the AZB model in [2]. Indeed, it is valid for arbitrary angles and viscosity ratios.

6.2 Future directions

6.2.1 Boiling simulations

Additional mechanisms could be included in boiling simulations proposed in this thesis, in particular to approach the industrial situation of interest: namely perform conjugate heat transfer simulations that couple the wall boundary with microlayer evaporation. In addition, higher heat fluxes could be explored, where multiple sites are activated and multiple bubbles could be simulated at the boiling surface, which would inform the area of influence of individual bubbles.

6.2.2 Microlayer formation

3D simulations of microlayer formation with flow could be performed, and would require the implementation of a 3D model of contact angle in numerical simulations, which has been done recently in [2] using an older version of Gerris. Additional

measurements of microlayer thickness as a function of time for various heat fluxes and flow conditions could further validate the models proposed in this thesis. In practice, higher resolution in time and space and wider ranges of fluids and conditions are needed to complete the experimental validation.

6.2.3 Moving contact line simulations

Additional and systematic determination of the gauge function for a range of contact line models that are used in practice would allow the verification of the procedure we propose in chapter 5 for grid-independent computations. Such grid independent simulations could in turn be used to analyze the results of experiments on contact line dynamics, including the onset of microlayer formation in nucleate boiling. Lastly, further calibrating numerics of moving contact lines with experiments is still needed to unlock the possibility to perform predictive simulations.

Appendix A

TransAT user-defined functions

A.1 userglobal.h

```
#ifndef _USERGLOBAL_H
#define _USERGLOBAL_H
#include "userglobal_prototype.h"
#include <vector>
#include <stdio.h>

class UserGlobal:public UserGlobal_Prototype
{
 private:
   //----------------------------------------
   // add your classes here
   // to have access during the simulation
   //----------------------------------------

 public:
   //--------------//
   // entry points //
   //--------------//
```

```
   FILE *ofwall, *subcells,*indexwall, *surfaces, *onlywall;
   UserGlobal();

   // every time step before solver
void User_processing_beforesolver();

   // for different variables before solving
void User_adjust_linear_system(char*);

   // adjust cpgl
void User_adjust_material_properties();

   // add source term to temperature
   // member data (store ii, mdot, area)
int jv_constantTw, jv_marching, shape_flat, shape_linear, Constant_Tw;
double r_bubble, r_bubblep, r_film;

struct mdotarea {
   int index;
   double mdot, areagl, avgthick;
};

static const int ncell = 100; //extra points within a macro delta x

std::vector<mdotarea> microlayer;
std::vector<double> delta_ROC, y_validation, microarea_validation,
    microarea_value;
std::vector<double> mlthick, mlthickp, ynn_validation, index_wall;

void add_mdot_source_temperature();

   // deallocation
```

```
   ~UserGlobal();
};


#endif
```

A.2 userglobal.cxx

```
#include "userglobal.h"
   #include "userglobal_prototype.h"
   #include "user_interface.h"
   #include "cppinterface.h"
   #include <iostream>
   #include <stdio.h>
   #include <cmath>
   #include <cstring>




   UserGlobal::UserGlobal(){
   // ****************************** output booleans *****************
   // jv scheme
   jv_constantTw=1;
   jv_marching=0;

   //  shape
   shape_flat=0;
   shape_linear=1;

   // constant Tw
```

```
Constant_Tw=1;
// ****************************** end of booleans *****************

double *hei;
set_pointer(&hei  ,"hembed");
int    nijk    = get_integer("nijk");
double hsupport = get_double("hsupport");
y_validation.resize(nijk);
index_wall.resize(nijk);
ynn_validation.resize(nijk);
mlthick .resize(nijk); // current thickness
mlthickp.resize(nijk); // next thickness
microarea_value.resize(nijk);
microarea_validation.resize(nijk);
} //end: constructor




UserGlobal::~UserGlobal(){
} //end: destructor



void UserGlobal:: User_processing_beforesolver() {
double extension_ratio=0.90;
int nijk=get_integer("nijk");
int NI=get_integer("ni") ;
int NJ=get_integer("nj");
int NIJ=NI*NJ;
double time, dtime;
double lambl, rhol, rhov, rholv, hfg, hsupport, tsat;
```

```
double *phi, *y, *x, *z,*mdot, *ycor, *xcor, *T;
double *areagl, *deltaei, *cellvol, *hei, *deltagl;
int timestep;
int ii, i, j, k, outf;
bool aei;

timestep = get_integer("timestep");
outf     = get_integer("output_frequency");
time     = get_double("time");
dtime    = get_double("dtime");


//FLUID PROPERTIES
lambl = get_double("lambl");
rhol= get_double("rhol");
rhov= get_double("rhog");
rholv=rhol-rhov;
hfg      = get_double("latent");
tsat     = get_double("tsat");

if (timestep == 1) {
      fprintf(stderr,"lambl %f\n",lambl);
      fprintf(stderr,"rhol %f\n",rhol);
      fprintf(stderr,"rhov %f\n",rhov);
      fprintf(stderr,"rholv %f\n",rholv);
      fprintf(stderr,"hfg %f\n",hfg);
      fprintf(stderr,"tsat %f\n",tsat);
}

// ****************************** SIMULATION PROPERTIES ********
//intial microlayer linear shape properties
double d0, dou, dT0, rmax, s;
```

```
d0   = 1.7e-9; // absorbed layer thickness
s    = 0.01;   // intial slope from rdry = 0 to contact line
dT0  = 9.0;    // wall superheat to rema[ii] constant
dou  = 3.e-6; // flat thickness
set_pointer(&phi ,"levelset");
set_pointer(&T ,"temperature");
set_pointer(&z ,"cellcenterz");
set_pointer(&y ,"cellcentery");
set_pointer(&x ,"cellcenterx");
set_pointer(&ycor,"cellcornery");
set_pointer(&xcor,"cellcornerx");
set_pointer(&mdot ,"mdot");
set_pointer(&areagl ,"areagl");
set_pointer(&deltaei,"deltaembed");
set_pointer(&deltagl,"discdel");
set_pointer(&cellvol,"cellvolume");
set_pointer(&hei  ,"hembed");
aei = get_logical("activate_embedded_interface");
// bubble outer edge radius *********
r_bubble = r_bubblep;
if (aei) {
   double avgy, avgn;
        avgy = 0.0;
        avgn = 0.0;
   for (ii=0; ii < NJ; ii++) {
   avgy = avgy + y[ii]*deltaei[ii]*deltagl[ii]*cellvol[ii];
   avgn = avgn + deltaei[ii]*deltagl[ii]*cellvol[ii];
   }
        r_bubblep = avgy/avgn;
}
rmax = extension_ratio*r_bubblep;
// intialize the microlayer thickness at t = 0
```

```
// (store the indexes for the wall boundary -- get length)
int curr=0;
for (unsigned ii=0; ii < nijk; ++ii) {
   if ( hei[ii]>0&&hei[ii]<1.0 && x[ii]<0 && y[ii]<1.5e-3 && z[ii]==0){
      index_wall[curr]=ii;
      curr=curr+1;
   }
}

int length_wall=curr-1; // validated
mlthick.resize(length_wall*(ncell+1));
mlthickp.resize(length_wall*(ncell+1));

// first time step
if (timestep == 1) {
   r_film = 0.0;
      for (unsigned ii=0; ii<nijk; ++ii) {
         mlthick[ii]= d0; // curr starts at 0: (curr-0)*..
         mlthickp[ii]= d0;// ncell +1 points in each intervall
             ..*(ncell+1)

      }
      for (unsigned jj=0; jj<length_wall; ++jj) {
         int ii=index_wall[jj];
         int iip=index_wall[jj+1];
         double dr = (ycor[iip]-ycor[ii]);
         double rr = ycor[ii];
         for (unsigned nn = 0; nn < (ncell+1); ++nn) {
         mlthick[(jj)*(ncell+1)+nn]= d0; // curr starts at 0: (curr-0)*..
         mlthickp[(jj)*(ncell+1)+nn]= d0;// ncell +1 points in each
             intervall ..*(ncell+1)
         }
```

```
        if (rr < 1.5e-3) {
           if (shape_flat==0 && shape_linear==1){
              y_validation[jj]=y[ii];
              for (unsigned nn = 0; nn < (ncell+1); ++nn) {
                 double dr_nn = (ycor[ii+NI]-ycor[ii])/(ncell+1);
                 mlthick [(jj)*(ncell+1)+nn]= d0+s*(rr+nn*dr_nn);
                 mlthickp[(jj)*(ncell+1)+nn] =d0+s*(rr+nn*dr_nn);
                 ynn_validation[(jj)*(ncell+1)+nn]=rr+nn*dr_nn;
              }
           }
         r_film = std::max(r_film,rr);
        } // end of radial extension limit
      } // end of for loop over all index
   r_bubble = r_bubblep;
} // end first time step

else{
fprintf(stderr,"timestep>1");
 // LATER then first time step else {
      for (unsigned jj=0; jj<length_wall+1; ++jj) {
         for (unsigned nn = 0; nn < (ncell+1); ++nn) {
              mlthick [(jj)*(ncell+1)+nn] = mlthickp[(jj)*(ncell+1)+nn];
         } // end loop on subcells
      } // end loop over boundary cells
   //} // end condition of EI
} // end condition on timestep


if(timestep==1){
char fname3[32];
sprintf(fname3,"index_wall.dat");
indexwall= fopen(fname3,"w");
```

```
fprintf(indexwall,"x[ii], y[ii], z[ii]\n");
index_wall.resize(3,0);
for (unsigned jj=0; jj<length_wall; ++jj) {
   int ii=index_wall[jj];
    for (unsigned nn = 0; nn < (ncell+1); ++nn) {
      fprintf(indexwall,"%.3g %.3g %.3g \n", x[ii], y[ii], z[ii]);
   }
}//end for
fclose(indexwall);
fprintf(stderr,"length wall\n");
}
double r_film_new;
r_film_new = r_film;
// ****************************** UPDATE MDOT AT BOUNDARY
    *****************
double t1=time;
double r_inner, router;
double dy, ymid, dyc, ymidc;
double s_nn, dr_nn, y_nn;
double Vi, Vip;
//reset vector
microlayer.clear();
mdotarea triplet;
   for (unsigned jj=0; jj<length_wall; ++jj) {
      int ii=index_wall[jj];
      int iip=index_wall[jj+1];
      if (ycor[ii] < 1.5e-3) {
              double microarea, jv, s_validation;
              microarea = 0.5*(pow(ycor[iip],2)-pow(ycor[ii],2) );
            fprintf(stderr,"%.3g \n", microarea);
            jv = 0.0;
            s_validation=0.0;
```

```
   double avgt = 0.0;

// *LOOP SUBCELLS ***********************************
   for (unsigned nn = 0; nn < (ncell+1); ++nn) {
   double dnow, dnewsqr, dtemp, dnew;
   y_nn = ycor[ii]+(nn)*(ycor[iip]-ycor[ii])/(ncell+1);
   dr_nn = (ycor[iip]-ycor[ii])/(ncell+1);
   s_nn =0.5*(pow(y_nn+dr_nn,2)-pow(y_nn,2) );
   s_validation=s_validation+s_nn;
   dnow    = mlthick[(jj)*(ncell+1)+nn];

      if (Constant_Tw==1){
         dtemp   = std::max(383. - tsat,0.0);
      }
      else {
         dtemp   = std::max(T[ii] - tsat,0.0);
      }
      // * JV SCHEME **********************************
      if(jv_constantTw==1 &&jv_marching==0){
         dnewsqr = std::max( pow(dnow,2)
             -2.0*lambl*dtemp*dtime/(rhol*hfg),pow(d0,2));
         dnew = sqrt(dnewsqr);
      }

      // forward in time
      if ( jv_constantTw==0 && jv_marching==1){
         double delta_ROCiinn=-lambl*dtemp/(rhol*hfg*dnow);
         dnew=std::max(dnow+delta_ROCiinn*dtime,d0);
      }
      // *end of JV SCHEME ****************************

      mlthickp[(jj)*(ncell+1)+nn]= dnew;
```

```
                double davg = 0.5*(dnow+dnew);
                avgt = avgt + davg;
                if (davg > d0) {
                   jv = jv + lambl*dtemp/(dnow*hfg)*s_nn;
                }
             }
             //* END LOOP ON SUBCELLS**************************
        jv = jv / microarea;
        //microarea = 1e-12;
        //jv=1e12;
        //T[ii]=500;
        mdot[ii]  = mdot[ii]  + jv ;
        areagl[ii] = areagl[ii] + microarea;
        // ****************************** Store variables*********
        triplet.index = ii;
           triplet.mdot  = jv;
           triplet.areagl = microarea;
           triplet.avgthick = avgt;
           microlayer.push_back(triplet);
     } // end limitation on radial extension
  } // end loop on wall cells


// ****************************** OUTPUT SECTION
    ******************************
timestep = get_integer("timestep");
char fname[32];
sprintf(fname,"m_test-%05d.dat", timestep);
ofwall= fopen(fname,"w");

for (unsigned jj=0; jj<length_wall+1; ++jj) {
   int ii=index_wall[jj];
```

```
    for (unsigned nn = 0; nn < (ncell+1); ++nn) {
      fprintf(ofwall,"%.3g %d %d %d %.3g %.3g %.3g %.3g %.3g \n", time,
          ii, (jj)*(ncell+1)+nn, nn, x[ii], y[ii],
          mlthick[(jj)*(ncell+1)+nn], T[ii], mdot[ii]);
   }
}//end for
fclose(ofwall);




}; // End Before Solver
//
    ********************************************************************************
void UserGlobal:: User_adjust_linear_system(char* varname){
   if (strcmp(varname,"temperature") == 0) {
   add_mdot_source_temperature();
   }
};
//
    ********************************************************************************
void UserGlobal:: User_adjust_material_properties(){

double *cpgl, *rhof, *cvol;
int *blk;
int ii;
double mdot, areagl, term, rhol, cpl;
set_pointer(&cpgl,"heatcapacity");
set_pointer(&rhof,"rhofluid");
set_pointer(&cvol,"cellvolume");
set_pointer(&blk,"block");
rhol = get_double("rhol");
```

```
cpl  = get_double("cpl");
double small = get_double("small");

for (int i = 0; i < microlayer.size(); i++){
   ii = microlayer[i].index;
   areagl = microlayer[i].areagl;
   double liqvol = areagl*microlayer[i].avgthick;
   double rcp = (1-blk[ii])*rhof[ii]*cpgl[ii]
        +blk[ii]*( rhof[ii]*cpgl[ii]*cvol[ii]
             +rhol*cpl*liqvol)/(cvol[ii]+liqvol+small);
   double rho = (1-blk[ii])*rhof[ii]
        +blk[ii]*( rhof[ii]*cvol[ii]
          +rhol*liqvol)/(cvol[ii]+liqvol+small);
   cpgl[ii] = rcp/rho;
   rhof[ii] = rho;
}
};
//*************************************************************************************
void UserGlobal:: add_mdot_source_temperature(){

if (Constant_Tw==1){
}
else{
   double *tissu, *hei, *x, *y, *z, *phi, *tissp, *temp, *aw;
   double latent, tsat;
   int ii;
   double mdot, areagl, term, term2;
   set_pointer(&tissu ,"issu");
   set_pointer(&tissp ,"issp");
   set_pointer(&hei ,"hembed");
   set_pointer(&temp ,"temperature");
   set_pointer(&aw  ,"westcoeff");
```

```
    set_pointer(&x ,"cellcenterx");
    set_pointer(&y ,"cellcentery");
    set_pointer(&z ,"cellcenterz");
    set_pointer(&phi ,"levelset");
    latent = get_double("latent");
    tsat   = get_double("tsat");
     fprintf(stderr,"----INSIDE TEMP LOOP: SIZE=%.3g",microlayer.size());
    for (int i = 0; i < microlayer.size(); i++){
          ii     = microlayer[i].index;
             mdot   = microlayer[i].mdot;
             areagl = microlayer[i].areagl;
             term   = mdot*areagl*latent;//*hei[ii];
             term2  = mdot*areagl*latent*hei[ii];
          fprintf(stderr,">>>>>>>>> %.3g %.3g %.3g %.3g
              %.3g\n",temp[ii],phi[ii], x[ii], y[ii], z[ii]);
       if (term>0.0){
          tissp[ii] = tissp[ii] - term/temp[ii];
       }
    }
  }
  };
```

Appendix B

Pressure boundary at the bubble root to reproduce bubble growth hydrodynamics at the wall

We here present a method we initially proposed and tested to reproduce the hydrodynamics of bubble growth at the wall, but that we dropped for the reasons explained later in this section. Rayleigh [86] carried out the first analysis of bubble growth in an infinite pool of liquid. In general form, the bubble radius is controlled by the following governing differential equation:

$$\left(P_b - P_\infty\right)/\rho_l = R\ddot{R} + \frac{3}{2}\dot{R}^2 + 4\nu_l\frac{\dot{R}}{R} + \frac{2\sigma}{\rho_l R} \tag{B.1}$$

where P_b denotes the pressure within the bubble, P_∞ the far-field pressure, R the bubble radius, ν_l the kinematic viscosity of the liquid, ρ_l the density of the liquid, and σ the surface tension. An analytical solution exists for the special case of constant overpressure inside the bubble, when surface tension and liquid viscosity are neglected. The bubble radius R then increases linearly with time t:

$$R = \sqrt{\frac{2\Delta P}{3\rho_l}}t \tag{B.2}$$

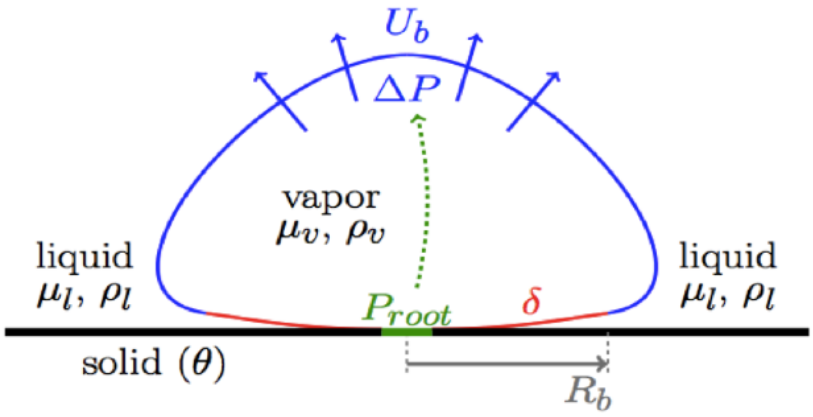

Figure B-1: A pressure boundary condition at the base of the bubble is proposed to drive and control bubble growth, and resolve the dynamics of microlayer formation at the wall.

In the inertia-driven growth phase, we consider the expansion velocity to be proportional to the square root of the pressure difference across the interface:

$$U_{b,\text{noflow}} = \sqrt{\frac{2\Delta P}{3\rho_l}} \tag{B.3}$$

We consider a pressure boundary condition at the bubble root to drive and control the growth of a bubble at a constant rate U_b - see sketch of methodology in Figure B-1 and computational domain in Figure B-2. In the results presented in Figure B-3, a constant pressure of $50kPa$ is imposed at the bubble root, whose mouth radius is set to be 10 microns. The contact angle with the wall is held constant in time at 10° for a finest mesh size at the wall of $156nm$. Early profiles (in red) show how the interface rearranges from its initial shape. Note that the bubble is initialized at the wall with an angle greater than the boundary contact angle. Then the shape rearranges to a hemispherical shape (in blue) and the bubble shape remains hemispherical as it grows further (black profiles). After the first $5\mu s$, the bubble outer diameter reaches a few tens of microns at the wall. The equivalent radius of the simulated bubble as a function of time in Figure B-4 indicates that the methodology is able to control the bubble growth rate, and reproduce hydrodynamics of bubble growth. Results

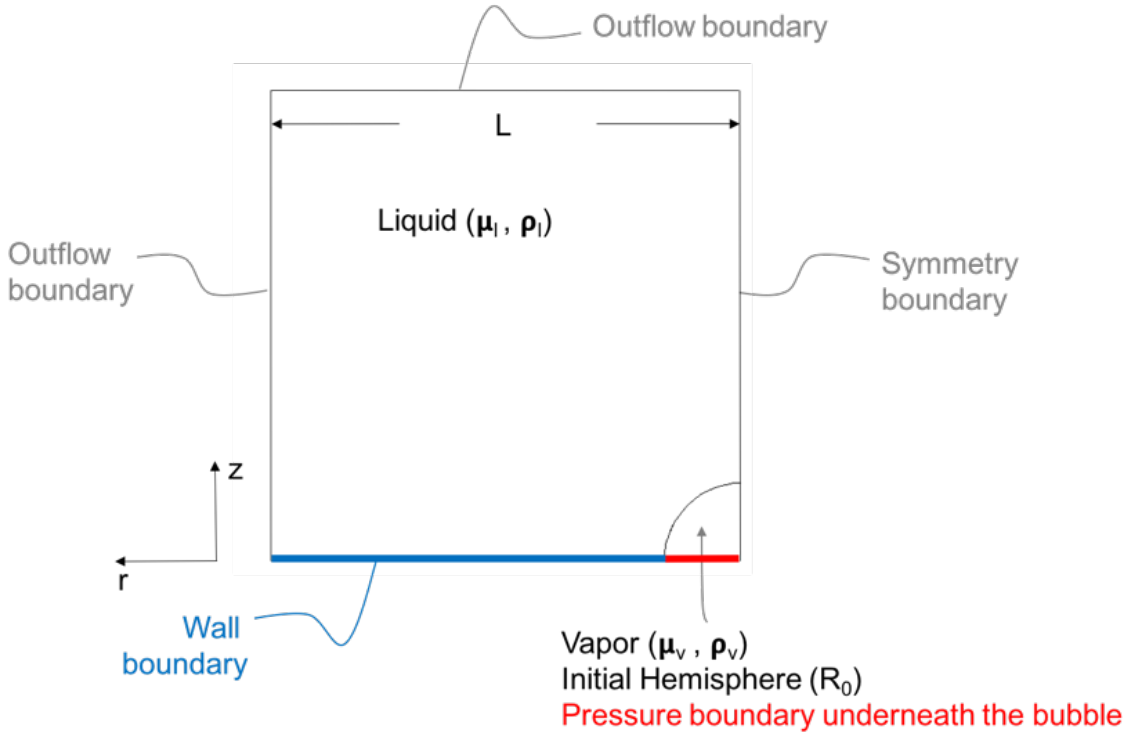

Figure B-2: Computational domain implementing a pressure boundary condition at the bubble root (red) to drive and control bubble growth at a wall (in blue). The domain is axisymmetric of side $120\mu m$.

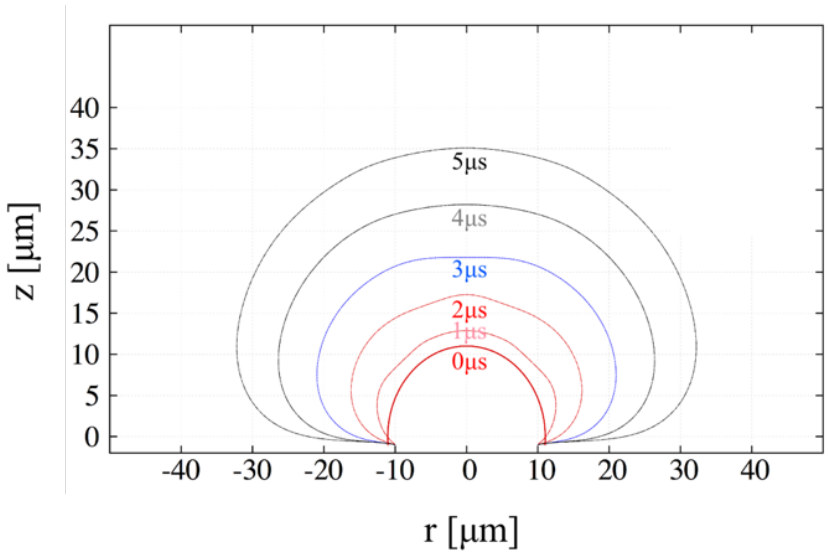

Figure B-3: Interface of a steam bubble growing at a wall under 50kPa overpressure at its root, Ca=0.03,$\theta_{dx} = 10°$ (dx=156nm).

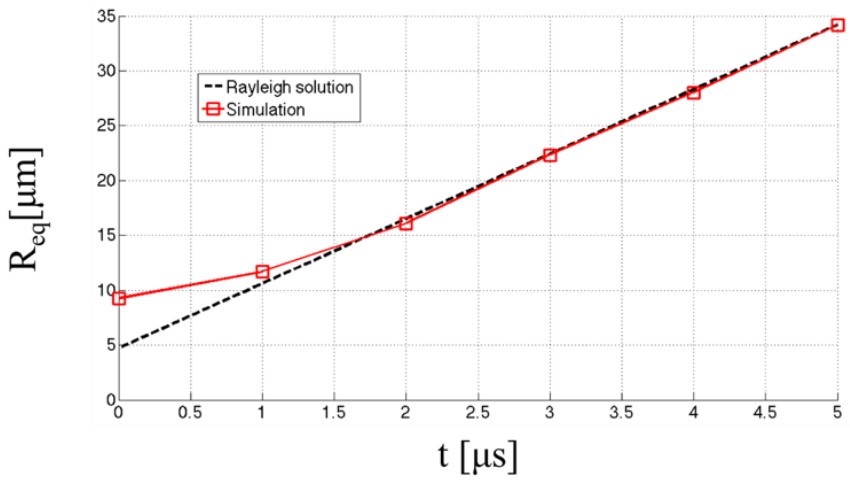

Figure B-4: Equivalent radius of the simulated bubble (red square with solid line) as a function of time, and the reference Rayleigh solution (dashed black line).

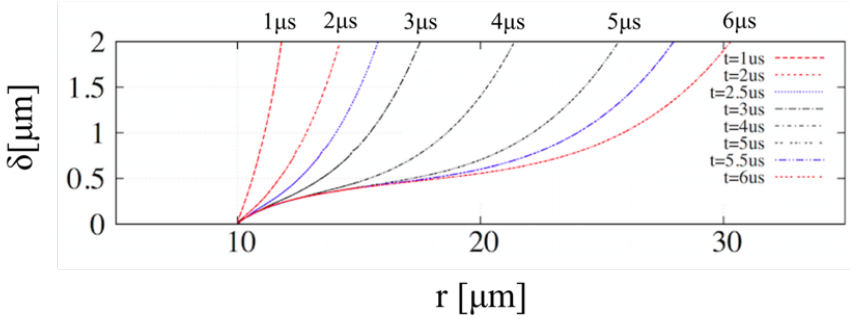

Figure B-5: Dynamics of microlayer formation at the wall under 50kPa overpressure at its root, Ca=0.03,$\theta_{dx} = 10°$ (dx=156nm).

indicate the dynamics of a thin micro-metric microlayer that forms at the wall for the first few micro-seconds - see Figure B-5.

The methodology requires further work to sustain hemispherical growth at longer simulation times and was abandoned for now: the very low viscosity in the vapor phase failed to diffuse momentum in the radial direction in the computational setup explored - see Figure B-7. As the bubble grows, and as its outer-edge moves further and further away from the bubble root where the overpressure boundary condition is imposed, the norm of the velocity field indicates the formation of a jet in the vertical direction - see Figure B-8, that was later found to disappear if the viscosity

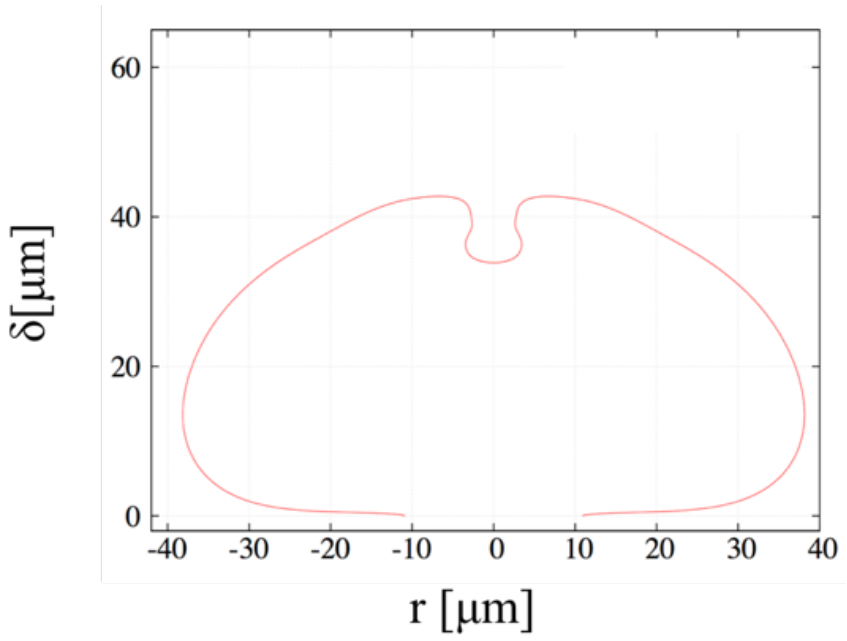

Figure B-6: Shape of the simulated bubble at t=6μs. Note the non-hemispherical shape of the interface (deformation at the top of the bubble cap) that indicates the methodology failed to reproduce the desired growth.

ratio were increased towards unity. The plot of pressure along the axis of rotation $P(r = 0, z)$ in Figure B-9 reveals that the pressure build up is in the liquid phase, well past the position of the liquid-vapor interface, also shown in Figure B-8. The non-hemispherical growth profile obtained no longer reproduces the desired bubble growth characteristics, and this methodology was abandoned.

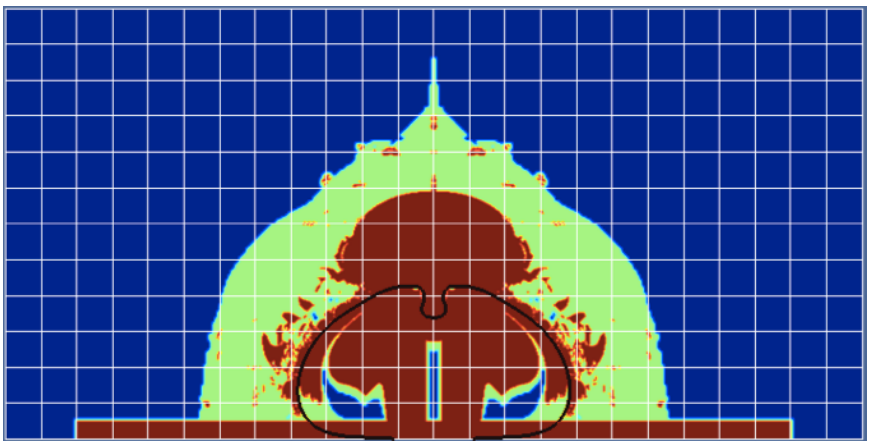

Figure B-7: Details of the mesh size distribution in the domain at t=6μs. The domain is refined in region of high vorticity, as well as at the wall where the microlayer is expected to form (see red regions, dx=156nm), and coarsened elsewhere (blue regions, dx=625nm). White lines show computational boxes of side 10μm. The axis of symmetry is vertical in the center, the simulations are axisymmetric.

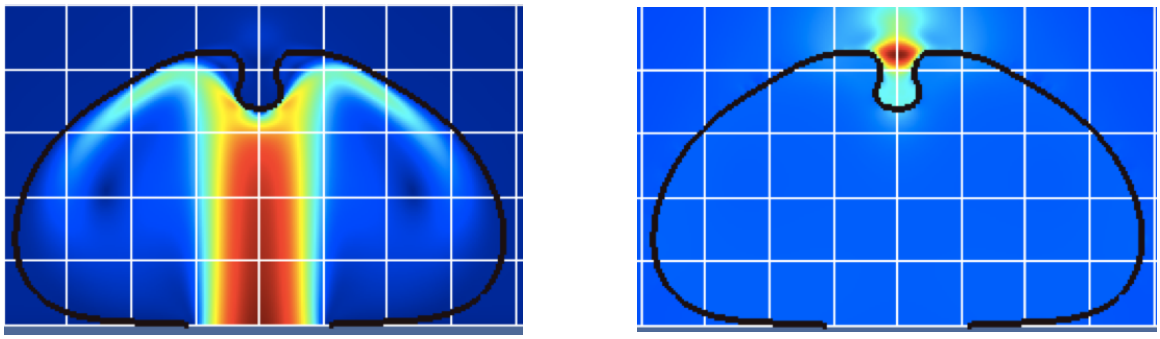

(a) (b)

Figure B-8: Details of the distribution of the norm of the velocity (a) (blue: 0m/s, red: 370m/s) and pressure difference (b) (blue: 0Pa, red: 250kPa) in the vicinity of the bubble at t=6μs.

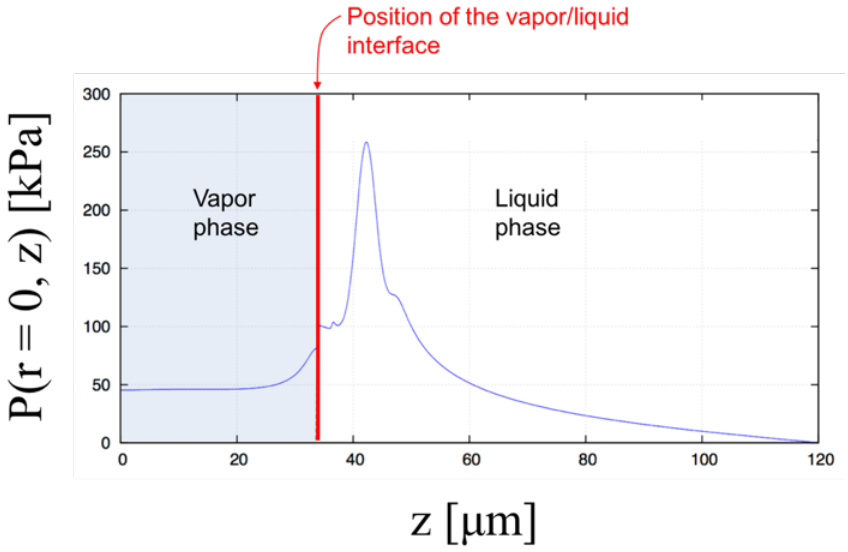

Figure B-9: Details of the pressure profile along the axis of symmetry (r=0). The separation between the vapor phase and the liquid phase is indicated by the red vertical line.

Appendix C

Details of the simulated microlayer and its linear shape

Profiles of the bubble (left) and microlayer (right) (black dots), and the fitting performed in the central linear region (green dashed line), for $Ca \in [0.001;\ 0.1]$ and $\theta_{\mathrm{d}x} = 10^{\circ}$ (dx=$1/32\mu m$), at $t^* = 140$.

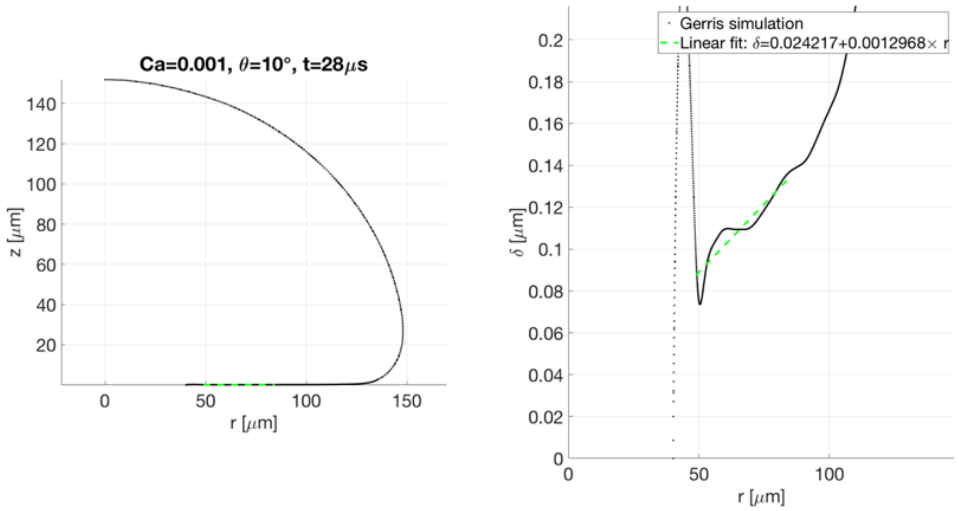

Figure C-1: Profile (black dots) of the bubble (left) and microlayer (right), and the fitting performed in the central linear region (green dashed line), for Ca=0.001, $\theta_{dx} = 10^{\circ}$ (dx=$1/32\mu m$), at $t^* = 140$.

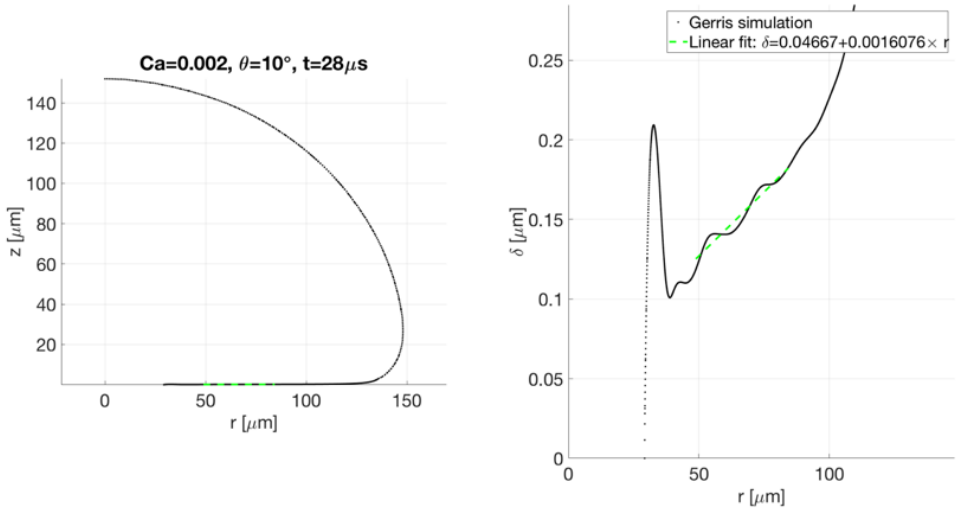

Figure C-2: Profile (black dots) of the bubble (left) and microlayer (right), and the fitting performed in the central linear region (green dashed line), for Ca=0.002, $\theta_{dx} = 10^{\circ}$ (dx=$1/32\mu m$), at $t^* = 140$.

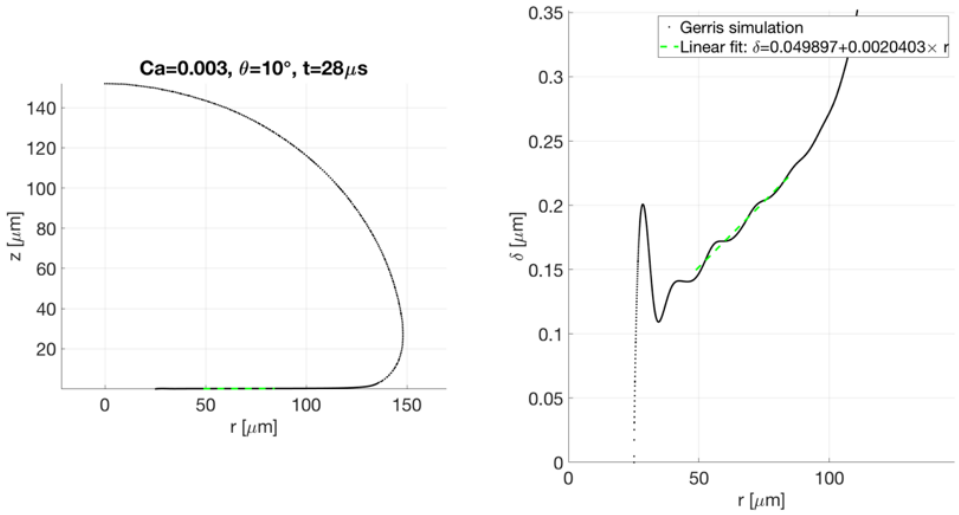

Figure C-3: Profile (black dots) of the bubble (left) and microlayer (right), and the fitting performed in the central linear region (green dashed line), for Ca=0.003, $\theta_{dx} = 10^{\circ}$ (dx=$1/32\mu m$), at $t^* = 140$.

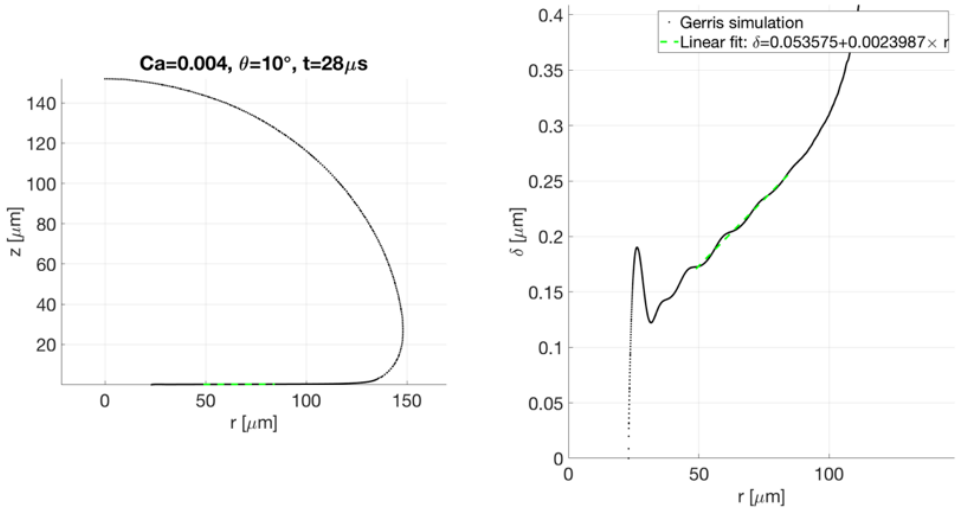

Figure C-4: Profile (black dots) of the bubble (left) and microlayer (right), and the fitting performed in the central linear region (green dashed line), for Ca=0.004, $\theta_{dx} = 10^{\circ}$ (dx=$1/32\mu m$), at $t^* = 140$.

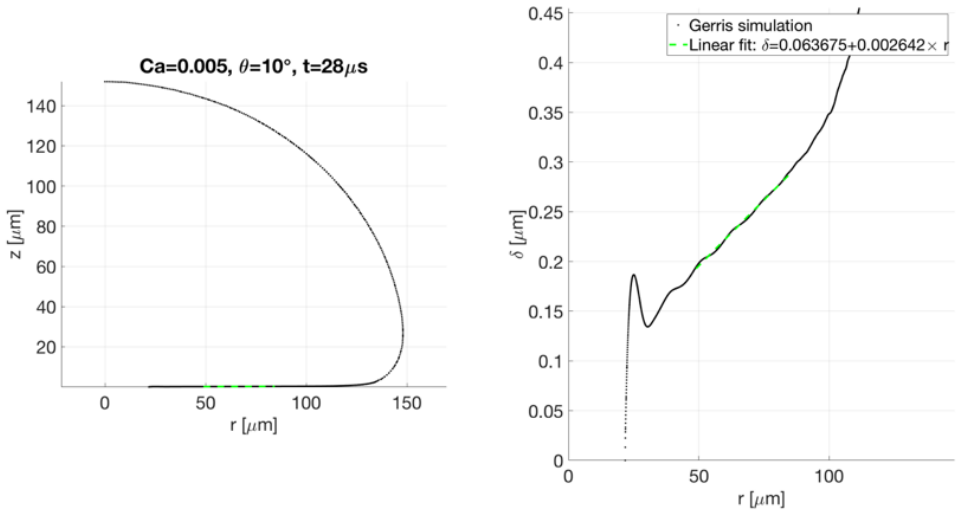

Figure C-5: Profile (black dots) of the bubble (left) and microlayer (right), and the fitting performed in the central linear region (green dashed line), for Ca=0.005, $\theta_{dx} = 10^\circ$ (dx=$1/32\mu m$), at $t^* = 140$.

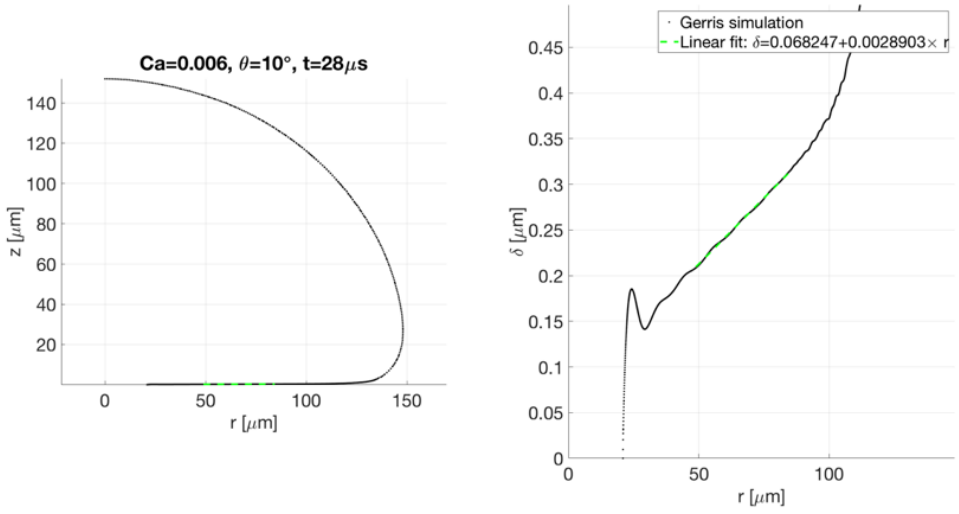

Figure C-6: Profile (black dots) of the bubble (left) and microlayer (right), and the fitting performed in the central linear region (green dashed line), for Ca=0.006, $\theta_{dx} = 10^\circ$ (dx=$1/32\mu m$), at $t^* = 140$.

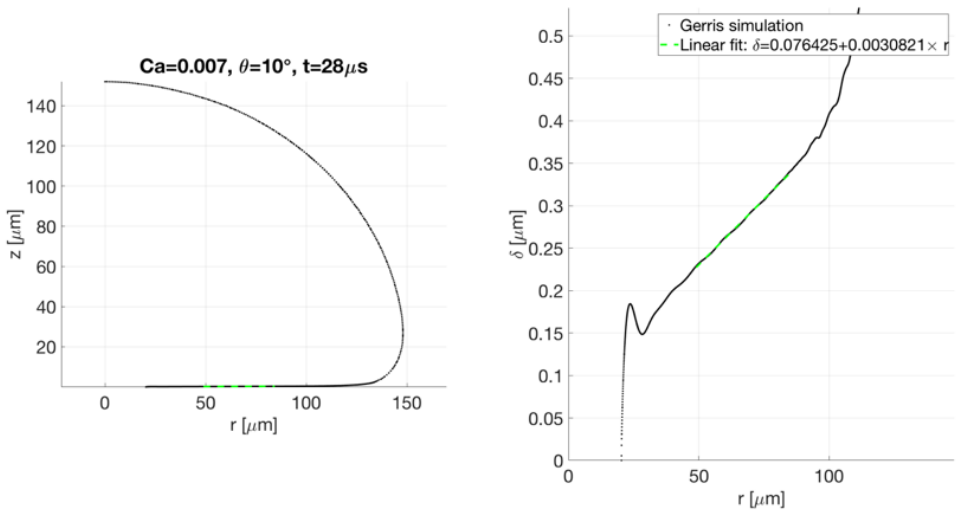

Figure C-7: Profile (black dots) of the bubble (left) and microlayer (right), and the fitting performed in the central linear region (green dashed line), for Ca=0.007, $\theta_{dx} = 10^{\circ}$ (dx=$1/32\mu m$), at $t^* = 140$.

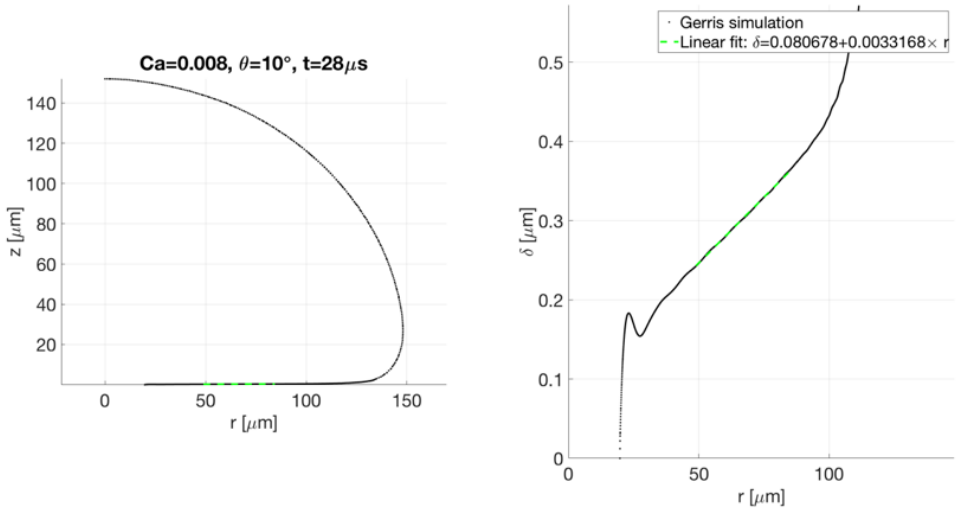

Figure C-8: Profile (black dots) of the bubble (left) and microlayer (right), and the fitting performed in the central linear region (green dashed line), for Ca=0.008, $\theta_{dx} = 10^{\circ}$ (dx=$1/32\mu m$), at $t^* = 140$.

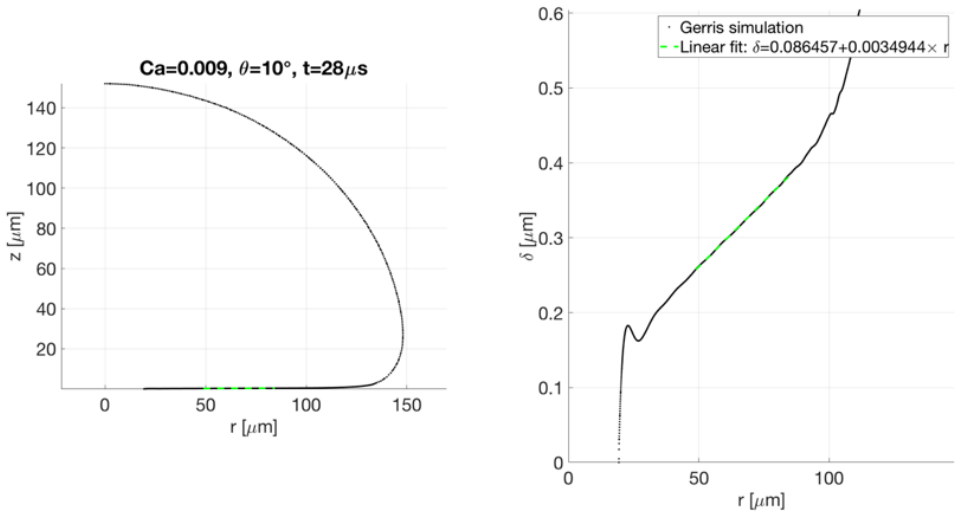

Figure C-9: Profile (black dots) of the bubble (left) and microlayer (right), and the fitting performed in the central linear region (green dashed line), for Ca=0.009, $\theta_{dx} = 10°$ (dx=$1/32\mu m$), at $t^* = 140$.

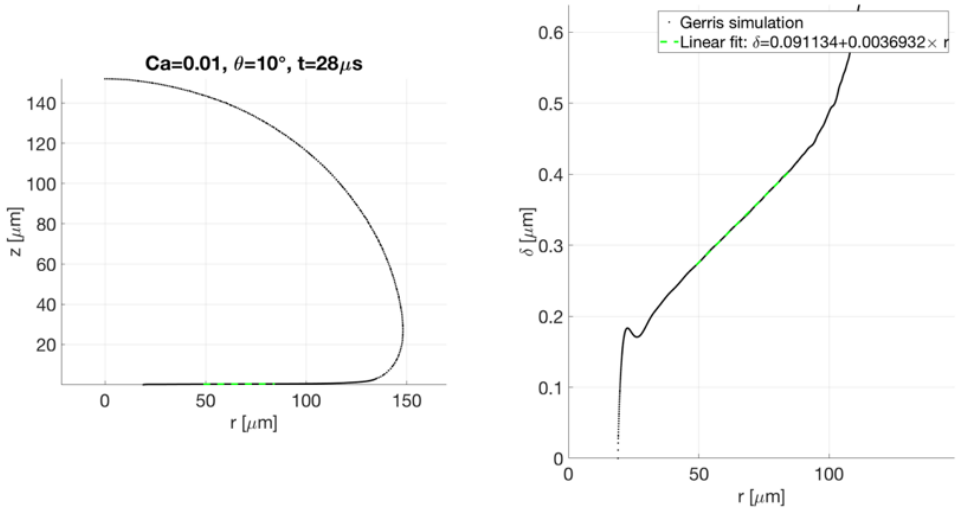

Figure C-10: Profile (black dots) of the bubble (left) and microlayer (right), and the fitting performed in the central linear region (green dashed line), for Ca=0.01, $\theta_{dx} = 10°$ (dx=$1/32\mu m$), at $t^* = 140$.

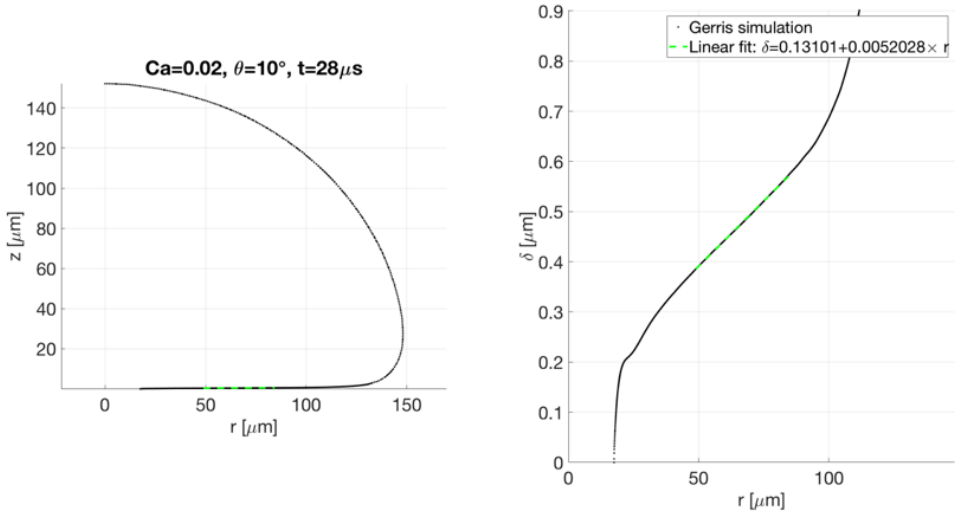

Figure C-11: Profile (black dots) of the bubble (left) and microlayer (right), and the fitting performed in the central linear region (green dashed line), for Ca=0.02, $\theta_{dx} = 10^\circ$ (dx=$1/32\mu m$), at $t^* = 140$.

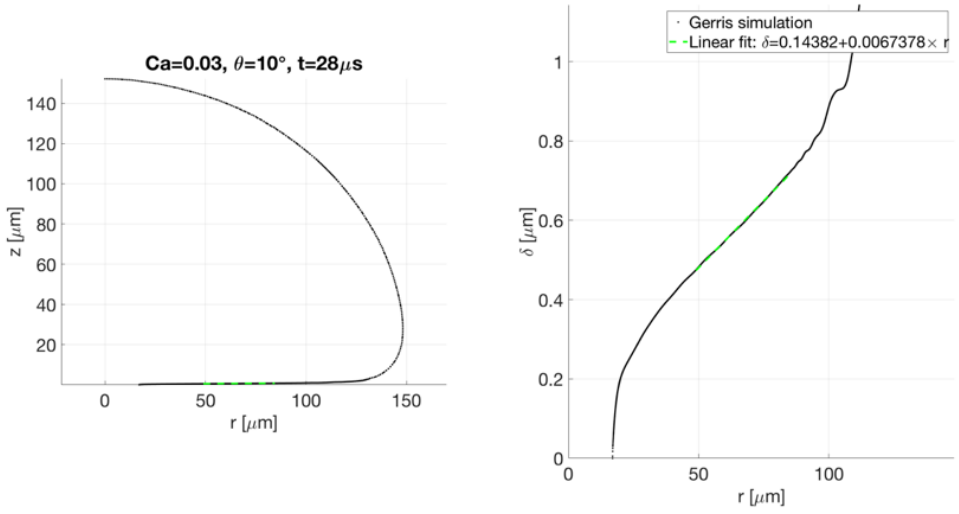

Figure C-12: Profile (black dots) of the bubble (left) and microlayer (right), and the fitting performed in the central linear region (green dashed line), for Ca=0.03, $\theta_{dx} = 10^\circ$ (dx=$1/32\mu m$), at $t^* = 140$.

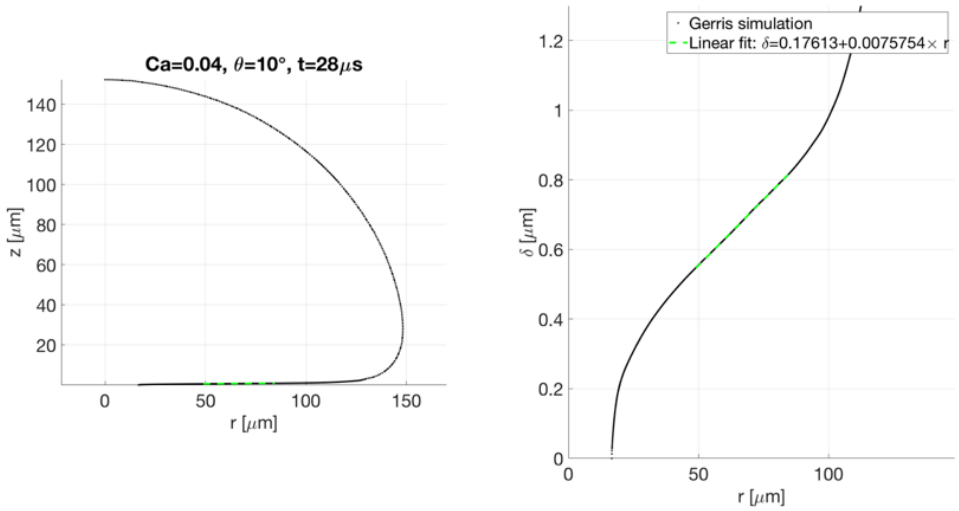

Figure C-13: Profile (black dots) of the bubble (left) and microlayer (right), and the fitting performed in the central linear region (green dashed line), for Ca=0.04, $\theta_{dx} = 10^\circ$ (dx=$1/32\mu m$), at $t^* = 140$.

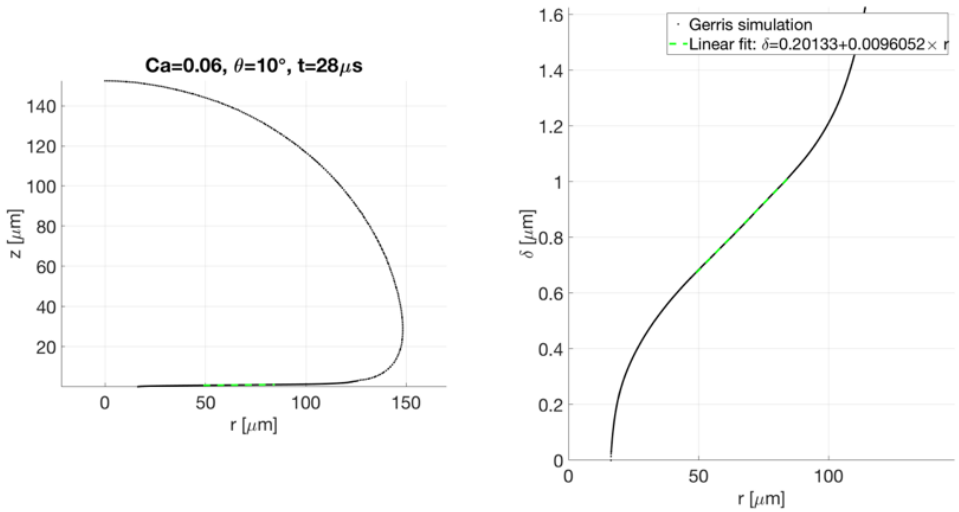

Figure C-14: Profile (black dots) of the bubble (left) and microlayer (right), and the fitting performed in the central linear region (green dashed line), for Ca=0.06, $\theta_{dx} = 10^\circ$ (dx=$1/32\mu m$), at $t^* = 140$.

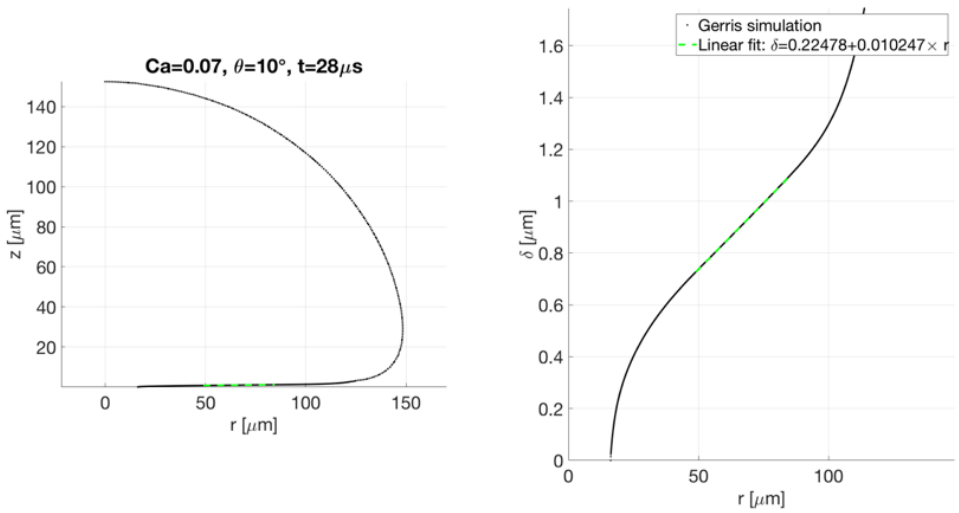

Figure C-15: Profile (black dots) of the bubble (left) and microlayer (right), and the fitting performed in the central linear region (green dashed line), for Ca=0.07, $\theta_{dx} = 10^\circ$ (dx=$1/32\mu m$), at $t^* = 140$.

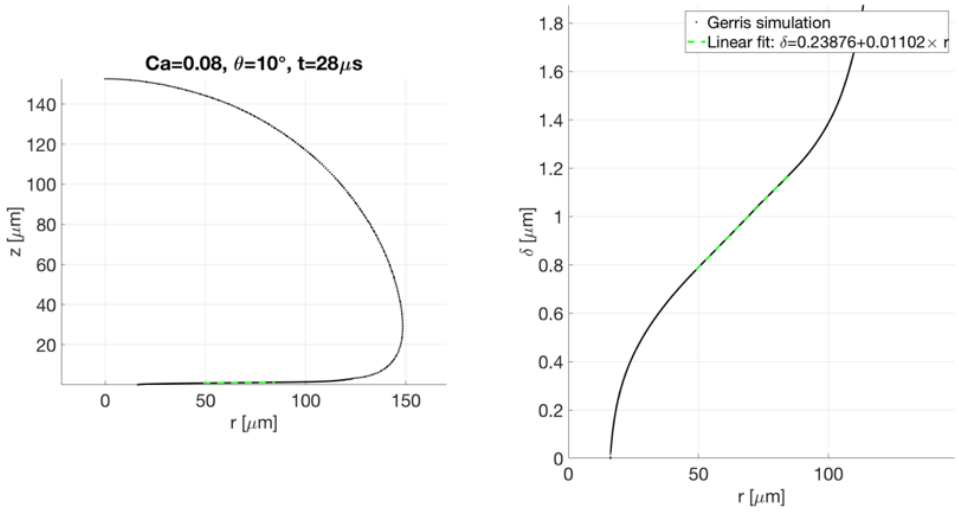

Figure C-16: Profile (black dots) of the bubble (left) and microlayer (right), and the fitting performed in the central linear region (green dashed line), for Ca=0.08, $\theta_{dx} = 10^\circ$ (dx=$1/32\mu m$), at $t^* = 140$.

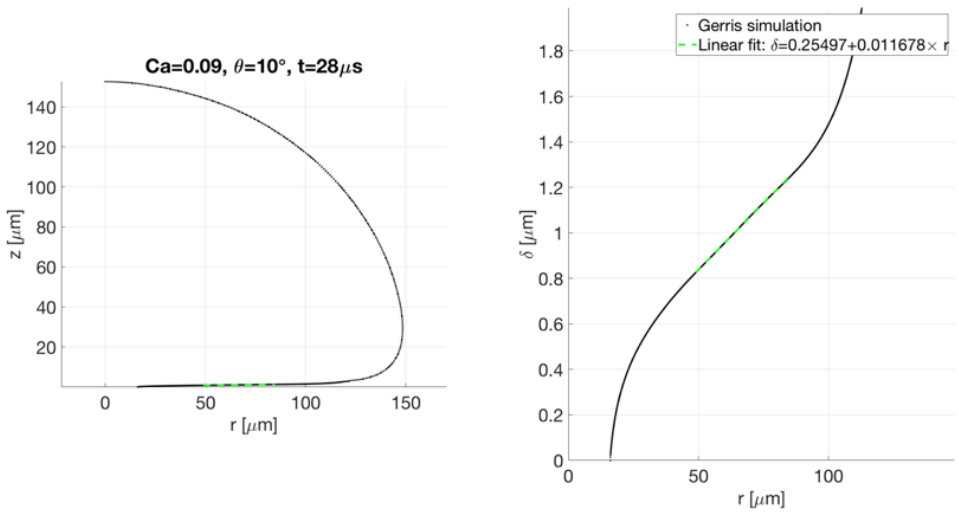

Figure C-17: Profile (black dots) of the bubble (left) and microlayer (right), and the fitting performed in the central linear region (green dashed line), for Ca=0.09, $\theta_{dx} = 10^\circ$ (dx=$1/32\mu m$), at $t^* = 140$.

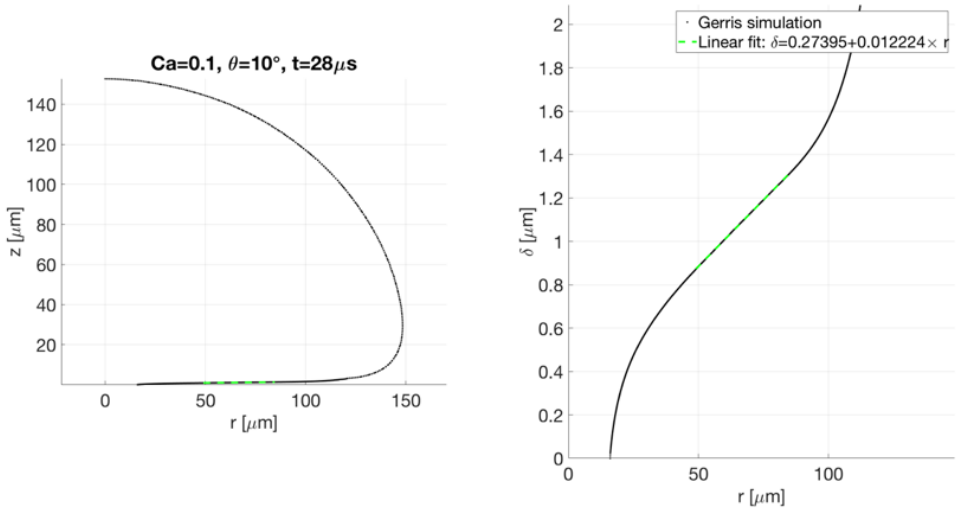

Figure C-18: Profile (black dots) of the bubble (left) and microlayer (right), and the fitting performed in the central linear region (green dashed line), for Ca=0.1, $\theta_{dx} = 10^\circ$ (dx=$1/32\mu m$), at $t^* = 140$.

Bibliography

[1] S Afkhami, J Buongiorno, A Guion, S Popinet, R Scardovelli, and S Zaleski. Transition in a numerical model of contact line dynamics and forced dewetting. *arXiv preprint arXiv:1703.07038*, 2017.

[2] S. Afkhami and M. Bussmann. Height functions for applying contact angles to 3D VOF simulations. *International Journal for Numerical Methods in Fluids*, 61(8):827–847, 2009.

[3] S Afkhami, Stephane Zaleski, and M Bussmann. A mesh-dependent model for applying dynamic contact angles to vof simulations. *Journal of Computational Physics*, 228(15):5370–5389, 2009.

[4] Gilou Agbaglah, Christophe Josserand, and Stéphane Zaleski. Longitudinal instability of a liquid rim. *Physics of Fluids*, 25(2):022103, 2013.

[5] Sajjad Bigham and Saeed Moghaddam. Role of bubble growth dynamics on microscale heat transfer events in microchannel flow boiling process. *Applied Physics Letters*, 107(24):244103, 2015.

[6] Terence D. Blake. The physics of moving wetting lines. *Journal of Colloid and Interface Science*, 299(1):1–13, 2006.

[7] Terence D. Blake and K. J. Ruschak. A maximum speed of wetting, 1979.

[8] Michael P Brenner and Denis Gueyffier. On the bursting of viscous films. *Physics of Fluids*, 11(3):737–739, 1999.

[9] Matteo Bucci, Andrew Richenderfer, Guan Yu Su, Thomas McKrell, and Jacopo Buongiorno. A mechanistic IR calibration technique for boiling heat transfer investigations. *International Journal of Multiphase Flow*, 83:115–127, 2016.

[10] Edgar Buckingham. On physically similar systems; illustrations of the use of dimensional equations. *Physical Review*, 4(4):345, 1914.

[11] Jacopo Buongiorno, David G Cahill, Carlos H Hidrovo, Saeed Moghaddam, Aaron J Schmidt, and Li Shi. Micro-and nanoscale measurement methods for phase change heat transfer on planar and structured surfaces. *Nanoscale and Microscale Thermophysical Engineering*, 18(3):270–287, 2014.

[12] Tak Shing Chan, Jacco H. Snoeijer, and Jens Eggers. Theory of the forced wetting transition. *Physics of Fluids*, 24(7), 2012.

[13] David M. Christopher and Lu Zhang. Heat transfer in the microlayer under a bubble during nucleate boiling. *Tsinghua Science and Technology*, 15(4):404–413, 2010.

[14] J. N. Chung, Tailian Chen, and Shalabh C. Maroo. A review of recent progress on nano/micro scale nucleate boiling fundamentals. *Frontiers in Heat and Mass Transfer*, 2(2), 2011.

[15] NV Churaev. The effect of adsorbed layers on van der waals forces in thin liquid films. *Colloid & Polymer Science*, 253(2):120–126, 1975.

[16] MG Cooper and AJP Lloyd. The microlayer in nucleate pool boiling. *International Journal of Heat and Mass Transfer*, 12(8):895–913, 1969.

[17] RG Cox. The dynamics of the spreading of liquids on a solid surface. part 2. surfactants. *Journal of Fluid Mechanics*, 168:195–220, 1986.

[18] Anton a. Darhuber, Sandra M. Troian, Jeffrey M. Davis, Scott M. Miller, and Sigurd Wagner. Selective dip-coating of chemically micropatterned surfaces. *Journal of Applied Physics*, 88(9):5119, 2000.

[19] B.V. Derjaguin. On the thickness of a layer of liquid remaining on the walls of vessels after their emptying, and the theory of the application of photoemulsion after coating on the cine film (presented by academician A.N. Frumkin on July 28, 1942). *Progress in Surface Science*, 43(1-4):129–133, may 1993.

[20] Vijay K Dhir, Hari S Abarajith, and Ding Li. Bubble Dynamics and Heat Transfer during Pool and Flow Boiling. *Heat Transfer Engineering*, 28(7):608–624, 2007.

[21] Vijay K. Dhir, Gopinath R. Warrier, and Eduardo Aktinol. Numerical Simulation of Pool Boiling: A Review. *Journal of Heat Transfer*, 135(6):061502, 2013.

[22] VJ Dhir. Simulation of boiling: How far have we come! In *Proceedings of 7th ECI International Conference on Boiling Heat Transfer, Florianópolis, Brazil, May*, pages 3–7, 2009.

[23] VK Dhir. Boiling heat transfer. *Annual Review of Fluid Mechanics*, 30(1):365–401, 1998.

[24] X. Duan, B. Phillips, T. McKrell, and J. Buongiorno. Synchronized high-speed video, infrared thermometry, and particle image velocimetry data for validation of interface-tracking simulations of nucleate boiling phenomena. *Experimental Heat Transfer*, 26(2-3):169–197, 2013.

[25] B.R. R Duffy and S.K. K Wilson. A third-order differential equation arising in thin-film flows and relevant to Tanner's Law. *Applied Mathematics Letters*, 10(3):63–68, 1997.

[26] Jens Eggers. Toward a description of contact line motion at higher capillary numbers. *Physics of Fluids*, 16(9):3491–3494, 2004.

[27] Jens Eggers. Contact line motion for partially wetting fluids. *Physical Review E*, 72(6):061605, 2005.

[28] H. B. Eral, D. J C M 'T Mannetje, and J. M. Oh. Contact angle hysteresis: A review of fundamentals and applications, 2013.

[29] Asghar Esmaeeli and Gretar Tryggvason. Computations of film boiling. Part I: Numerical method. *International Journal of Heat and Mass Transfer*, 47(25):5451–5461, 2004.

[30] GE Foltz and RB Mesler. The measurement of surface temperatures with platinum films during nucleate boiling of water. *AIChE Journal*, 16(1):44–48, 1970.

[31] Ming Gao, Lixin Zhang, Ping Cheng, and Xiaojun Quan. An investigation of microlayer beneath nucleation bubble by laser interferometric method. *International Journal of Heat and Mass Transfer*, 57(1):183–189, 2013.

[32] Craig Douglas Gerardi. *Investigation of the pool boiling heat transfer enhancement of nano-engineered fluids by means of high-speed infrared thermography.* PhD thesis, Massachusetts Institute of Technology, 2009.

[33] Lindsey Anne Gilman. *Development of a general purpose subgrid wall boiling model from improved physical understanding for use in computational fluid dynamics.* PhD thesis, Massachusetts Institute of Technology, 2014.

[34] I Golobic, J Petkovsek, M Baselj, A Papez, and DBR Kenning. Experimental determination of transient wall temperature distributions close to growing vapor bubbles. *Heat and Mass Transfer*, 45(7):857–866, 2009.

[35] Leonardo Gordillo, Gilou Agbaglah, Laurent Duchemin, and Christophe Josserand. Asymptotic behavior of a retracting two-dimensional fluid sheet. *Physics of Fluids*, 23(12):122101, 2011.

[36] A Guion, D Langewisch, and J Buongiorno. On the Liquid Microlayer Underneath a Vapor Bubble Growing at a Heated Wall. *International Conference on Multiphase Flow*, pages 1–13, 2013.

[37] Robert C Hendricks and Robert R Sharp. Initiation of cooling due to bubble growth on a heating surface. 1964.

[38] Narayan B Hospeti and Russell B Mesler. Deposits formed beneath bubbles during nucleate boiling of radioactive calcium sulfate solutions. *AIChE Journal*, 11(4):662–665, 1965.

[39] David M. Huang, Christian Sendner, Dominik Horinek, Roland R. Netz, and Lydric Bocquet. Water slippage versus contact angle: A quasiuniversal relationship. *Physical Review Letters*, 101(22), 2008.

[40] Chun Huh and L. E. Scriven. Hydrodynamic model of steady movement of a solid/liquid/fluid contact line. *Journal of Colloid And Interface Science*, 35(1):85–101, 1971.

[41] HH Jawurek. Simultaneous determination of microlayer geometry and bubble growth in nucleate boiling. *International Journal of Heat and Mass Transfer*, 12(8):843IN1847–846IN2848, 1969.

[42] Yu Yan Jiang, Hiroshi Osada, Masahide Inagaki, and Nariaki Horinouchi. Dynamic modeling on bubble growth, detachment and heat transfer for hybrid-scheme computations of nucleate boiling. *International Journal of Heat and Mass Transfer*, 56(1):640–652, 2013.

[43] RL Judd. Laser interferometric investigation of the microlayer evaporation phenomenon. *Journal of Heat Transfer*, page 89, 1975.

[44] RL Judd and KS Hwang. A comprehensive model for nucleate pool boiling heat transfer including microlayer evaporation. *ASME J. Heat Transfer*, 98(4):623–629, 1976.

[45] Satbyoul Jung and Hyungdae Kim. An experimental method to simultaneously measure the dynamics and heat transfer associated with a single bubble during nucleate boiling on a horizontal surface. *International Journal of Heat and Mass Transfer*, 73:365–375, 2014.

[46] Satbyoul Jung and Hyungdae Kim. An experimental method to simultaneously measure the dynamics and heat transfer associated with a single bubble during nucleate boiling on a horizontal surface. *International Journal of Heat and Mass Transfer*, 73:365–375, 2014.

[47] Satbyoul Jung and Hyungdae Kim. An experimental study on heat transfer mechanisms in the microlayer using integrated total reflection, laser interferometry and infrared thermometry technique. *Heat Transfer Engineering*, 36(12):1002–1012, 2015.

[48] Damir Juric and Grétar Tryggvason. Computations of boiling flows. *International Journal of Multiphase Flow*, 24(3):387–410, 1998.

[49] Satish G Kandlikar. History, advances, and challenges in liquid flow and flow boiling heat transfer in microchannels: a critical review. *Journal of Heat Transfer*, 134(3):034001, 2012.

[50] Chirag R Kharangate and Issam Mudawar. Review of computational studies on boiling and condensation. *International Journal of Heat and Mass Transfer*, 108:1164–1196, 2017.

[51] Hyungdae Kim and Jacopo Buongiorno. Detection of liquid–vapor–solid triple contact line in two-phase heat transfer phenomena using high-speed infrared thermometry. *International Journal of Multiphase Flow*, 37(2):166–172, 2011.

[52] Jungho Kim. Review of nucleate pool boiling bubble heat transfer mechanisms. *International Journal of Multiphase Flow*, 35(12):1067–1076, 2009.

[53] Elizabeth Harper Kimbrel, Anna L. Herring, Ryan T. Armstrong, Ivan Lunati, Brian K. Bay, and Dorthe Wildenschild. Experimental characterization of nonwetting phase trapping and implications for geologic CO<inf>2</inf> sequestration. *International Journal of Greenhouse Gas Control*, 42:1–15, 2015.

[54] L D Koffman and M S Plesset. Experimental observations of the microlayer in vapor bubble growth on a heated solid. *Journal of Heat Transfer*, 105(3):625–632, 1983.

[55] LD Koffman and MS Plesset. Experimental study of microlayer formed during vapour bubble growth on the heated solid surface. *Trans ASME J Heat Transf*, 105, 1983.

[56] Christian Kunkelmann. *Numerical Modeling and Investigation of Boiling Phenomena*. PhD thesis, Darmstadt, 2011.

[57] Christian Kunkelmann, Khalid Ibrahem, Nils Schweizer, Stefan Herbert, Peter Stephan, and Tatiana Gambaryan-Roisman. The effect of three-phase contact line speed on local evaporative heat transfer: Experimental and numerical investigations. *International Journal of Heat and Mass Transfer*, 55(7):1896–1904, 2012.

[58] Christian Kunkelmann and Peter Stephan. CFD Simulation of Boiling Flows Using the Volume-of-Fluid Method within OpenFOAM. *Numerical Heat Transfer, Part A: Applications*, 56(8):631–646, 2009.

[59] Christian Kunkelmann and Peter Stephan. Modification and extension of a standard volume-of-fluid solver for simulating boiling heat transfer. In *Proc. 5th European Conference on Computational Fluid Dynamics ECCOMAS CFD2010, Lisbon, Portugal*, 2010.

[60] Tomoaki Kunugi. Brief review of latest direct numerical simulation on pool and film boiling. *Nuclear Engineering and Technology*, 44(8):847–854, 2012.

[61] N Kurul and Mm Z Podowski. Multidimensional effects in forced convection subcooled boiling. In *Proceedings of the Ninth International Heat Transfer Conference*, volume 2, pages 19–24. Hemisphere Publishing New York, 1990.

[62] Sreeyuth Lal, Yohei Sato, and Bojan Niceno. Direct numerical simulation of bubble dynamics in subcooled and near-saturated convective nucleate boiling. *International Journal of Heat and Fluid Flow*, 51:16–28, 2015.

[63] L. Landau and B. Levich. Dragging of a Liquid by a Moving Plate. *Acta Physicochimica U.R.S.S.*, 17(1-2):42–54, 1942.

[64] L D Landau and E M Lifshitz. *Fluid Mechanics*, volume 6. 1987.

[65] Dustin R Langewisch. *Application of the polynomial chaos expansion to multiphase CFD: a study of rising bubbles and slug flow*. PhD thesis, Massachusetts Institute of Technology, 2014.

[66] Woorim Lee, Gihun Son, and Han Young Yoon. Direct numerical simulation of flow boiling in a finned microchannel. *International Communications in Heat and Mass Transfer*, 39(9):1460–1466, 2012.

[67] Longfei Li, R. J. Braun, K. L. Maki, W. D. Henshaw, and P. E. King-Smith. Tear film dynamics with evaporation, wetting, and time-dependent flux boundary condition on an eye-shaped domain. *Physics of Fluids*, 26(5), 2014.

[68] Raj M Manglik. On the advancements in boiling, two-phase flow heat transfer, and interfacial phenomena. *Journal of Heat Transfer*, 128(12):1237–1242, 2006.

[69] RC t Martinelli and DB Nelson. Prediction of pressure drop during forced circulation boiling of water. *Trans. Asme*, 70(6):695–702, 1948.

[70] William McAdams. Heat Transmission, 1954.

[71] BB Mikic, WM Rohsenow, and P Griffith. On bubble growth rates. *International Journal of Heat and Mass Transfer*, 13(4):657–666, 1970.

[72] Saeed Moghaddam and Ken Kiger. Physical mechanisms of heat transfer during single bubble nucleate boiling of fc-72 under saturation conditions-i. experimental investigation. *International Journal of Heat and Mass Transfer*, 52(5):1284–1294, 2009.

[73] Franklin D Moore and Russell B Mesler. The measurement of rapid surface temperature fluctuations during nucleate boiling of water. *AIChE Journal*, 7(4):620–624, 1961.

[74] JA Moriarty and LW Schwartz. Effective slip in numerical calculations of moving-contact-line problems. *Journal of Engineering Mathematics*, 26(1):81–86, 1992.

[75] I Mudawar and TM Anderson. Parametric investigation into the effects of pressure, subcooling, surface augmentation and choice of coolant on pool boiling in the design of cooling systems for high-power-density electronic chips. *Journal of Electronic Packaging*, 112(4):375–382, 1990.

[76] A Mukherjee and VK Dhir. Study of lateral merger of vapor bubbles during nucleate pool boiling. *Transactions of the ASME-C-Journal of Heat Transfer*, 126(6):1023–1039, 2004.

[77] A Mukherjee, SG Kandlikar, and ZJ Edel. Numerical study of bubble growth and wall heat transfer during flow boiling in a microchannel. *International Journal of Heat and Mass Transfer*, 54(15):3702–3718, 2011.

[78] Abhijit Mukherjee and Satish G Kandlikar. Numerical study of single bubbles with dynamic contact angle during nucleate pool boiling. *International Journal of Heat and Mass Transfer*, 50(1):127–138, 2007.

[79] C Narayanan, D Chatzikyriakou, J Buongiorno, and D Lakehal. Evaluation of Level-Set Based Phase-Change Models in TransAT, Including Test Case 3b. Technical report, 2013.

[80] Chidambaram Narayanan, Siju Thomas, and Djamel Lakehal. Statistical Modelling of Bubble Nucleation and Heat Transfer Using Interface Tracking in Transat Cmfd Code. *Proceedings of the 8Th International Conference on Nanochannels, Microchannels and Minichannels, 2010, Pts A and B*, pages 79–84, 2011.

[81] B. Niceno, Y. Sato, A. Badillo, and M. Andreani. Multi-scale modeling and analysis of convective boiling: Towards the prediction of CHF in rod bundles. *Nuclear Engineering and Technology*, 42(6):620–635, 2010.

[82] William F Noh and Paul Woodward. Slic (simple line interface calculation). In *Proceedings of the Fifth International Conference on Numerical Methods in Fluid Dynamics June 28–July 2, 1976 Twente University, Enschede*, pages 330–340. Springer, 1976.

[83] Yasuo Ose and Tomoaki Kunugi. Development of a boiling and condensation model on subcooled boiling phenomena. *Energy Procedia*, 9:605–618, 2011.

[84] P. Platt, V. Allen, M. Fenwick, M. Gass, and M. Preuss. Observation of the effect of surface roughness on the oxidation of Zircaloy-4, 2015.

[85] Stéphane Popinet. An accurate adaptive solver for surface-tension-driven interfacial flows. *Journal of Computational Physics*, 228(16):5838–5866, 2009.

[86] Lord Rayleigh. VIII. On the pressure developed in a liquid during the collapse of a spherical cavity. *Philosophical Magazine Series 6*, 34(200):94–98, 1917.

[87] Alexey Rednikov and Pierre Colinet. Singularity-free description of moving contact lines for volatile liquids. *Physical Review E*, 87(1):010401, 2013.

[88] Y. Sato, S. Lal, and B. Niceno. Computational fluid dynamics simulation of single bubble dynamics in convective boiling flows. *Multiphase Science and Technology*, 25(2-4), 2013.

[89] Yohei Sato and Bojan Niceno. A depletable micro-layer model for nucleate pool boiling. *Journal of Computational Physics*, 300:20–52, 2015.

[90] Yohei Sato and Bojan Niceno. A depletable micro-layer model for nucleate pool boiling. *Journal of Computational physics*, 300:20–52, 2015.

[91] Yohei Sato and Bojan Niceno. Nucleate pool boiling simulations using the interface tracking method: Boiling regime from discrete bubble to vapor mushroom region. *International Journal of Heat and Mass Transfer*, 105:505–524, 2017.

[92] Nikos Savva and John WM Bush. Viscous sheet retraction. *Journal of Fluid Mechanics*, 626:211–240, 2009.

[93] Ruben Scardovelli and Stéphane Zaleski. Direct numerical simulation of free-surface and interfacial flow. *Annual Review of Fluid Mechanics*, 31(1):567–603, 1999.

[94] R. V. Sedev and J. G. Petrov. The critical condition for transition from steady wetting to film entrainment. *Colloids and Surfaces*, 53(1):147–156, 1991.

[95] Ping Sheng and Minyao Zhou. Immiscible-fluid displacement: Contact-line dynamics and the velocity-dependent capillary pressure. *Physical Review A*, 45(8):5694–5708, 1992.

[96] Jacco H. Snoeijer. Free-surface flows with large slopes: Beyond lubrication theory. *Physics of Fluids*, 18(2), 2006.

[97] Jacco H Snoeijer and Bruno Andreotti. Moving contact lines: scales, regimes, and dynamical transitions. *Annual Review of Fluid Mechanics*, 45:269–292, 2013.

[98] Gihun Son and Vijay K Dhir. A level set method for analysis of film boiling on an immersed solid surface. *Numerical Heat Transfer, Part B: Fundamentals*, 52(2):153–177, 2007.

[99] Gihun Son and Vijay K Dhir. Numerical simulation of nucleate boiling on a horizontal surface at high heat fluxes. *International Journal of heat and Mass transfer*, 51(9):2566–2582, 2008.

[100] P Stephan and J Hammer. A new model for nucleate boiling heat transfer. *Heat and Mass Transfer/Waerme-und Stoffuebertragung*, 30(2):119–125, 1994.

[101] Peter Stephan and Jürgen Kern. Evaluation of heat and mass transfer phenomena in nucleate boiling. *International Journal of Heat and Fluid Flow*, 25(2):140–148, 2004.

[102] R Sugrue and J Buongiorno. A modified force-balance model for prediction of bubble departure diameter in subcooled flow boiling. *Nuclear Engineering and Design*, 305:717–722, 2016.

[103] GI Taylor and DH Michael. On making holes in a sheet of fluid. *Journal of Fluid Mechanics*, 58(04):625–639, 1973.

[104] Neil E Todreas and Mujid S Kazimi. *Nuclear Systems: Thermal Hydraulic Fundamentals*, volume 1. CRC press, 2012.

[105] SJD Van Stralen, MS Sohal, R Cole, and WM Sluyter. Bubble growth rates in pure and binary systems: combined effect of relaxation and evaporation microlayers. *International Journal of Heat and Mass Transfer*, 18(3):453–467, 1975.

[106] O. V. Voinov. Hydrodynamics of wetting. *Fluid Dynamics*, 11(5):714–721, 1976.

[107] Oleg V. Voinov. Wetting: Inverse Dynamic Problem and Equations for Microscopic Parameters. *Journal of Colloid and Interface Science*, 226(1):5–15, 2000.

[108] Hao Wang, Suresh V. Garimella, and Jayathi Y. Murthy. An analytical solution for the total heat transfer in the thin-film region of an evaporating meniscus. *International Journal of Heat and Mass Transfer*, 51(25-26):6317–6322, 2008.

[109] Gopinath R Warrier and Vijay K Dhir. Heat transfer and wall heat flux partitioning during subcooled flow nucleate boiling: a review. *Journal of Heat Transfer*, 128(12):1243–1256, 2006.

[110] P. C. Wayner, Y. K. Kao, and L. V. LaCroix. The interline heat-transfer coefficient of an evaporating wetting film. *International Journal of Heat and Mass Transfer*, 19(5):487–492, 1976.

[111] O. Weinstein and L. M. Pismen. Scale Dependence of Contact Line Computations. *Mathematical Modelling of Natural Phenomena*, 3(1):98–107, jul 2008.

[112] O Weinstein and LM Pismen. Scale dependence of contact line computations. *Mathematical Modelling of Natural Phenomena*, 3(1):98–107, 2008.

[113] Tomohide Yabuki and Osamu Nakabeppu. Heat transfer mechanisms in isolated bubble boiling of water observed with mems sensor. *International Journal of Heat and Mass Transfer*, 76:286–297, 2014.

[114] Tomohide Yabuki and Osamu Nakabeppu. Microlayer formation characteristics in pool isolated bubble boiling of water. *Heat and Mass Transfer*, pages 1–6, 2016.

[115] LT Yeh. Review of heat transfer technologies in electronic equipment. *Transactions of the ASME-P-Journal of Electronic Packaging*, 117(4):333–339, 1995.

[116] T. Young. An Essay on the Cohesion of Fluids. *Philosophical Transactions of the Royal Society of London*, 95(0):65–87, 1805.

[117] DL Youngs. Time-dependent multi-material fluid dynamics, edited by kw morton and mj baines, 1982.

[118] An Zou, Ashish Chanana, Amit Agrawal, Peter C Wayner Jr, and Shalabh C Maroo. Steady state vapor bubble in pool boiling. *Scientific Reports*, 6, 2016.

[119] An Zou, Dhirendra P. Singh, and Shalabh C. Maroo. Early Evaporation of Microlayer for Boiling Heat Transfer Enhancement. *Langmuir*, 32(42):10808–10814, 2016.